# Development of Heterodyne Receiver Technology for Sub-millimetre Wavelength Astronomy


Andre Hector
The Queen's College
University of Oxford

A thesis submitted for the degree of
*Doctor of Philosophy*

Michaelmas 2021

# Statement of Originality

I hereby declare that the work presented in this thesis has been carried out by myself at the University of Oxford and the Rutherford Appleton Laboratory between 2013 – 2021. Every effort has been made to clearly indicate any contribution made by others with reference to relevant literature and acknowledgement of collaboration and discussion. No part of this thesis has been submitted for any degree, diploma or other qualification at the University of Oxford or elsewhere.

Andre Hector

*December 2021*

# Acknowledgements

First and foremost, I would like to thank my project supervisors: Professors Brian Ellison, Mike Jones and Angela Taylor for all their advice, support and patience over the years. Without you none of this would have been possible so thank you for your tireless guidance and endless encouragement. I would also like to thank Dr. Byron Alderman, Dr. Jamie Leech and Dr. Diego Pardo for always being approachable and helpful whenever I've needed less formal academic assistance. A special thanks goes out to Mark Merritt for his help and enthusiasm whenever pesky E-Beam equipment decided to misbehave. In addition, I am deeply grateful to Andy Stokes, Joe Tacon and Mike Tacon from the Physics Mechanical Workshop for their constant assistance and willingness to put up with (and work from) some of my finer "technical" drawings! Furthermore, the efforts of Tony Lynas-Gray must be acknowledged for delivering the best and most enjoyable Graduate lecture course that anyone could have asked for, which was a true highlight of my first year in Oxford. In addition, I would like to express my sincere gratitude to Ashling Morris and Lance Miller for their exceptional pastoral care and support which went far above and beyond any obligation.

I would also like to thank all of my friends and peers that I was lucky enough to meet during my graduate studies. A special mention goes out to Olivier A, Ricarda B, Andrea C, John G (for always losing so graciously at Mario Kart), Peter H, Ben P, Alfie T and Simon Z. It has been an absolute joy to spend time and carry out my studies with you. However, this recognition would not be complete without the mention of Vin A, Rory B, Nick G, Izzy H, Patrick L, Tom L, Andreas M, Alex S, Dustin S, Tom S, James W, Sam W, Tom W, Tomoki Y and David Z for providing, at times, a much needed outlet from academic endeavours and being great company during those chilly morning outings.

Further to the above, I am deeply indebted to my undergraduate supervisor, Stewart Boogert - a friend, mentor and guru of all things physics and programming for always having time for me, his infectious enthusiasm for science and for inspiring me to pursue my interest in astronomy. As well as this, my undergraduate internship supervisors Jon Goff, Dan Porter and Mechthild Enderle deserve a special mention for a truly wonderful experience of scientific research. In addition, I would also like to thank my close friends from before my time in Oxford. In particular: Adam B, David B, Alex C, Josh C, Sam D, Angelo F, Fouad H, Rob H, Aaron J, Sarah K, Ash L, Kayleigh M, Krishna M, Stuart M, Belinda S, Luke S, Pete S, Harriet V and everyone in PA - thank you all for being awesome!

Finally, I would like to thank my family; my parents, my sister Clair and my brothers Phil and Kev for their unconditional love, boundless encouragement and utmost faith over the years - I couldn't have done it without you.

# Abstract

Superconductor-Insulator-Superconductor (SIS) mixers are regularly employed as the detectors of choice in sub-millimetre wavelength astronomy receivers due to their unparalleled sensitivity, stable operation and ability to capture both amplitude and phase of incoming signals which is necessary to perform high-resolution spectroscopic observations. With the advent of telescopes such as the Atacama Large Millimetre/sub-millimetre Array (ALMA) which are set to explore the field for the foreseeable future, there is considerable interest in developing the technological capabilities employed by such facilities.

The work presented in this thesis has therefore focused on the development of coherent, heterodyne receiver technology at sub-millimetre wavelengths for potential applications such as the upgrade of current, ground based observatories.

In particular, the harmonic content of Local Oscillator reference sources has been investigated and shown to play an important role in both the noise performance of heterodyne receivers and the spectral content of their output IF band.

Furthermore, successful design, optimisation, fabrication and testing of $THz$ frequency feed horns has led to the demonstration of a novel, smooth walled horn design that presents an attractive alternative to the more complex corrugated feed horn structure for antenna deployment in sub-mm wavelength receivers. A three section horn design operating between $780 - 950\ GHz$ has been shown to exhibit excellent measured far-field beam patterns which closely resemble the predicted performance down to $\sim -30\ dB$ and a two section design employed in a four pixel feed horn array has been shown to operate between $1300 - 1500\ GHz$.

In addition, a novel E-Beam lithography fabrication process has been developed for the production of Schottky barrier diodes to be used in high frequency multiplier and mixer components. This process has demonstrated the ability to create the ohmic pad layer, sub-micron anodes and the suspended air-bridge of the device which are necessary for efficient performance at sub-mm wavelengths. Initial RF testing of the diodes as frequency multipliers has produced excellent results between $225 - 330\ GHz$.

Finally the development of a prototype, heterodyne receiver, *based on double side band SIS mixer* with a novel optical design that operates between $800 - 900\ GHz$ has been presented and shown to exhibit very encouraging noise temperature characteristics of $\sim 340\ K$ at $880\ GHz$. This system is due to be tested at even higher frequencies with the aim of pushing its detection capabilities into the supra-Terahertz regime.

# Contents

# List of Figures

# List of Tables

# Chapter 1

# Introduction

## 1.1 Sub-millimetre Wavelength Astronomy

The sub-millimetre part of the electromagnetic spectrum remains relatively unexplored, which is part of the reason why it is a highly interesting area of study. The major difficulty in observing radiation in this part of the spectrum comes from the fact that the astronomical signal is very weak and so highly sensitive receivers are required. Nonetheless, there is great interest in observing sub-mm radiation because a significant amount of energy produced by stars and galaxies in the visible part of the spectrum is absorbed by surrounding interstellar dust and re-emitted at far infrared and sub-mm wavelengths. At certain wavelengths many interesting sites such as giant, dense molecular clouds with masses of around $10^6$ $M_\odot$ become transparent, providing the possibility to peer into their cores where new stars and planetary systems are being born (Shu et al., 1987). These Giant Molecular Clouds (GMCs) mainly consist of molecular Hydrogen ($H_2$) which drives star formation but does not strongly emit since it lacks a permanent dipole moment. Despite this, it is still possible to probe the physical conditions, such as density, temperature and dynamics, of these clouds by studying the spectral lines of different molecular species which are abundant in the sub-mm domain such as rotational ladder lines from Carbon Monoxide (CO) molecules (Wilson et al., 1970).

Apart from spectroscopic measurements, there is also great interest in performing broad-band continuum observations of cold interstellar dust with temperatures below $\sim 100$ $K$ to study cooling mechanisms that lead to the condensation of gaseous molecules and the

formation of protostars.

As well as acquiring knowledge about cool objects in the local universe, such as GMCs which have their black-body radiation peaks in the sub-mm part of the electromagnetic spectrum, there is also an interest in studying the unexplored Terahertz ($THz$) domain which is important for extra galactic observations of some of the earliest galaxies with light curves that have been red-shifted into the $THz$ regime (Solomon et al., 1992).

By studying highly redshifted, ultra-luminous galaxies such as the ones discovered by the Sub-millimetre Common User Bolometer Array (SCUBA) of the James Clerk Maxwell Telescope (JCMT) and the Herschel Space Telescope, as well as the highly red-shifted spectra of atomic species like [C II] and [N II], it is possible to learn about star and galaxy formation processes at early cosmological epochs. For example, [C II] (157 $\mu m$) and [N II] (122 and 205 $\mu m$) are forbidden fine-structure lines that are the brightest emission lines from the ISM at around 100 $\mu m$. As such, they are good tracers of ISM density and star formation rate. Since carbon has an ionisation potential that is slightly lower than that of hydrogen, it is easily ionised by any Lyman-alpha photons present. Therefore [C II] traces "neutral" as well as ionised material, even though the carbon itself has to be ionised for [C II] to exist. Nitrogen, on the other hand, has a larger ionisation potential than hydrogen so needs a strong ionising environment (e.g. UV radiation from stars) for [N II] to exist and thus traces ionised material only. The ratio of the two can then give electron density, for example. At high redshift ($z \simeq 4 - 7$) such lines are redshifted to sub-mm wavelengths, which allows the physical parameters that they trace to be probed across cosmic time (Lee et al., 2019). By combining such information with local observations of the same lines, it may be possible to discover new information about the overall evolution of the universe from high redshifts to the present day.

## 1.2 The Atacama Large Millimetre/sub-millimetre Array

Currently, the largest sub-millimetre astronomy project in the world is the Atacama Large Millimetre/sub-millimetre Array (ALMA). It is located at an altitude of 5000 metres above sea level on the Chajnantor plateau in the Atacama desert in Chile. This location was chosen

because of its extremely dry atmosphere which, for 25 % of the time, has a precipitable water vapour (PWV) column of just 0.7 $mm$ (Bustos et al., 2014). Such a dry site is required because atmospheric water vapour strongly attenuates the incident sky signal at a number of different frequencies. The ALMA telescope itself is an astronomical interferometer which consists of 54 twelve-metre and 12 seven-metre diameter radio telescopes. An image of a selection of these dishes, obtained from Malin & European Southern Observatory (2013), is presented in Figure 1.1(a). Such a setup allows ALMA to observe the universe in 10 different frequency bands spanning the range of $35 - 950\ GHz$, or a wavelength range of $0.3 - 8.5\ mm$. These 10 bands are defined by the atmospheric transmission windows at the Chajnantor plateau, which can be seen in more detail in Figure 1.1(b).

(a) An image of the ALMA telescope dishes on the Chajnantor plateau beneath a starry night sky. The Large and Small Magellanic Clouds can also be seen.

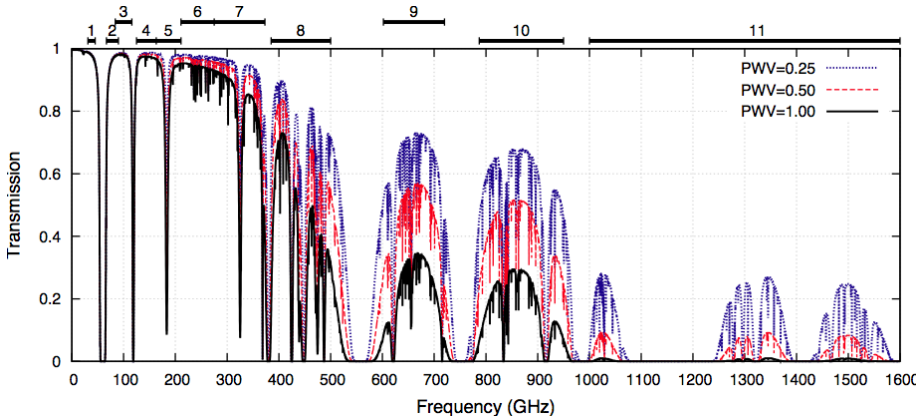


(b) The atmospheric transmission windows on the Chajnantor plateau at an altitude of $\sim 5000\ m$ which define the ALMA bands, shown for PWV columns of 0.25, 0.5 and 1.0 $mm$. The frequency range of each band is shown along the top. Obtained from: `https://almascience.eso.org/`

Figure 1.1: An image of the ALMA interferometer along with the atmospheric transmission bands at the Chajnantor plateau.

It can be seen from Figure 1.1(b) that signal transmission through the atmosphere deteriorates sharply above $\sim 300\ GHz$ at the ALMA site, with maximum transmission not exceeding $\sim 25 - 30$ % at frequencies surpassing the 1000 $GHz$ mark. This further points to the need for modern telescopes to utilise highly sensitive receiver technologies if sub-mm wavelength radiation is to be observed, even at some of the driest sites on the planet.

To that end, ALMA can achieve an angular resolution of 0.005" ($\sim 10$ times better than Hubble) allowing for parsec scale objects to be resolved at a distance of $\sim 40\ Mpc$. This may be employed to study the structure of astronomical sources such as Active Galactic Nuclei (AGN), for example. In addition, with a total collecting area of 6492 $m^2$, the ALMA interferometer exhibits significantly higher sensitivity than other sub-mm facilities such as the James Clerk Maxwell Telescope (JCMT) or the SubMillimetre Array (SMA). As such, the combination of its location and available infrastructure provides the perfect platform for future development of astronomical instrumentation operating in the sub-mm regime.

Even though there are a number of ground based, sub-mm telescopes already in existence such as the Atacama Pathfinder EXperiment (APEX), the SMA and the JCMT, the arrival of ALMA is surely one of the most exciting recent events to occur in the field of sub-mm astronomy due to the fact that this observatory promises to facilitate the exploration of the field for decades to come and exceed the sensitivity, resolution and scientific achievements of its predecessors.

## 1.3 Principle of Detection

Sub-millimetre radiation can be detected using two methods. First there is direct, or incoherent, detection where a change in the resistance of a material due to the absorption of a photon by an electron can be exploited to detect the presence of external radiation. This type of detection is sensitive to the total incident power coming into the detector but it lacks the ability to preserve phase information and as such is only relevant to single dish telescopes. The Hot Electron Bolometer (HEB) is an example of such a detector.

The second method of detection is known as coherent detection and this technique has the advantage of being able to preserve both the amplitude and the *phase* information of

incident radiation. This is necessary for interferometry, which requires the complex voltage from each antenna to be preserved so that they can be cross-correlated to form the interferometric visibility. In addition, coherent detection is also required to carry out high-resolution spectroscopic measurements. In general, modern, multiple-dish sub-mm telescopes employ non-linear coherent detectors, with one example being the Superconductor-Insulator-Superconductor (SIS) mixer which will be discussed in more detail in Section 1.4.

The coherent detection method is also particularly useful because of the down conversion, or heterodyning, of high frequency signals that it provides. This technique allows two signals with similar frequencies to be combined, or mixed, in a highly non-linear device, such as a Schottky diode or an SIS mixer, to create signals at frequencies which are the sum and difference of the two original signals and which also preserve the original signal phase.

It is common to refer to the frequency of the astronomical signal as the "Radio Frequency" ($\omega_{RF}$), while the larger amplitude, laboratory-produced reference tone is known as the "Local Oscillator" frequency ($\omega_{LO}$). Combining these together in a mixer, leads to a new, "Intermediate Frequency" ($\omega_{IF}$) signal being produced.

This concept of mixing can be understood with the diagram in Figure 1.2, which illustrates some of the main components of a heterodyne receiver and also depicts how the astronomical signal is combined with a Local Oscillator using a beamsplitter before being coupled into a mixing device with the use of an antenna.

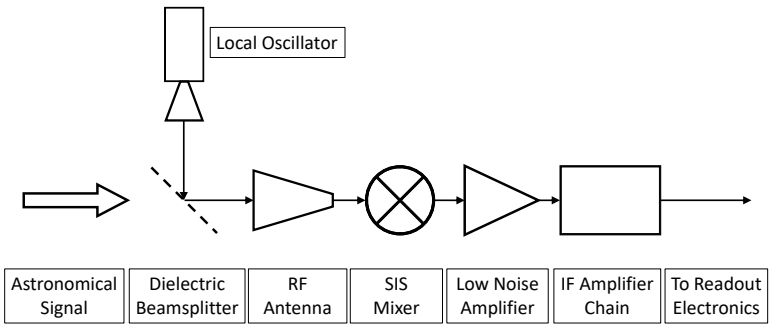


Figure 1.2: A typical, millimetre-wave heterodyne receiver setup.

To understand the concept of heterodyne mixing and down-conversion, consider two

sinusoidal voltages, $V_{RF}\sin(\omega_{RF}t)$ and $V_{LO}\sin(\omega_{LO}t)$, applied to a non-linear device such that the output current is proportional to the square of the applied voltage. In this example the output current will be

$$\begin{aligned} I(\omega) &\propto (V_0 + V_{RF}\sin(\omega_{RF}t) + V_{LO}\sin(\omega_{LO}t))^2 \\ &\propto \frac{V_{RF}^2}{2} + \frac{V_{LO}^2}{2} + V_0^2 + V_{RF}V_{LO}\cos(\omega_{RF} - \omega_{LO})t \\ &\quad - V_{RF}V_{LO}\cos(\omega_{RF} + \omega_{LO})t + ... \end{aligned} \tag{1.1}$$

where $V_0$ is the DC bias voltage. From Equation 1.1 it can be seen that after mixing, there are signals that flow at the sum and difference frequencies of the two input tones but given that, in general, frequency *down*-conversion is required, the Intermediate Frequency (IF) is usually defined as $\omega_{IF} = |\omega_{RF} - \omega_{LO}|$. This expression for $\omega_{IF}$ thus implies that a basic heterodyne receiver is sensitive to input signals on either side of the LO frequency, $\omega_{LO}$. The range of frequencies above $\omega_{LO}$ that the mixer will down-convert is known as the Upper Side Band (USB) while the frequency range below $\omega_{LO}$ that the mixer responds to is known as the Lower Side Band (LSB). This sensitivity to both the USB and LSB around $\omega_{LO}$ is known as Double Side Band (DSB) operation and leads to both side bands being down-converted, or "mapped", into a common IF band during the heterodyne process. This results in signals from both the USB and LSB overlapping and appearing in the IF band which, depending on the intended receiver application, can either be a benefit (e.g. a broader receiver bandwidth when performing continuum observations) or a setback (e.g. added noise or even spectral signature confusion when observing spectral lines). In the case where having both the USB and LSB mapped into the same IF band is undesired, it is possible to separate the side bands using 90° hybrid couplers, two separate mixers (along with their respective IF electronics chains) and by exploiting the phase preservation property of the down-conversion process. This process is known as side band separation and is shown schematically in Figure 1.3 (Ellison, 2021). It can be seen that this technique separates the side bands into two, separate output channels - one for the USB and the other for the LSB. This enables the full receiver bandwidth to be utilised while allowing for easier identification and analysis of spectral features. However, it should be noted that one of the

drawbacks of such a setup is increased system complexity (since two mixers and two IF chains are required) which results in greater costs.

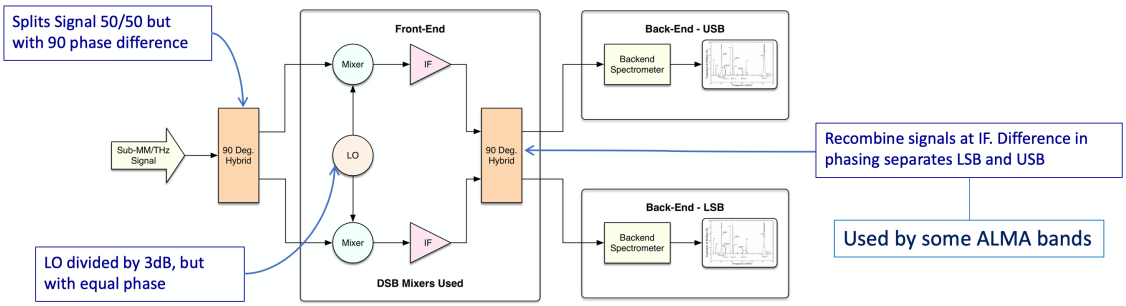


Figure 1.3: A schematic diagram showing side band separation in a typical heterodyne receiver setup (Ellison, 2021).

Apart from the fact that the heterodyne technique preserves the phase of the input signals which allows for side band separation, another advantage of this method of down-conversion is that it is possilbe to scan a wide range of RF frequencies by simply varying the LO frequency. In addition, the down-conversion of a high frequency signal reduces transmission losses and enables Low Noise Amplifiers (LNAs), which are challenging to construct for high frequency operation, to be used to further amplify a weak astronomical signal. Unwanted tones which arise as a result of mixing can usually be filtered out, either with the use of filters or by the intrinsic capacitence of the SIS junction. However, as will de demonstrated in Chapter 2, their origin must be well understood.

## 1.4 SIS Mixers

The Superconductor-Insulator-Superconductor (SIS) mixer is one example of a highly non-linear device used in sub-mm astronomy for the coherent detection of electromagnetic radiation. It is used on eight out of the ten ALMA bands with the remaining two employing High Electron Mobility Transistor (HEMT) technology. While HEMT low noise amplifiers work well at the lower frequency bands of up to $\sim 100\ GHz$, above this frequency the transistor noise rapidly increases making them less viable at sub-millimetre wavelengths (Yassin et al., 2014). In addition, the superconducting nature and principle of operation of SIS mixers makes them preferred over alternatives such as Schottky diode mixers due to their increased

sensitivity, which is achieved through a sharper non-linearity in their current-voltage characteristic as well as inherently lower levels of additional noise.

An SIS junction consists of two layers of a superconducting material such as Niobium (Nb), separated by a very thin (few tens of Angstroms) insulating layer, e.g. Aluminium Oxide (AlOx), to form a sandwich-like structure as shown in Figure 1.4. These junctions are employed in sub-mm detectors, not only because they are highly sensitive to incoming radiation but also due to their reliable stability of operation (Tucker, 1979).

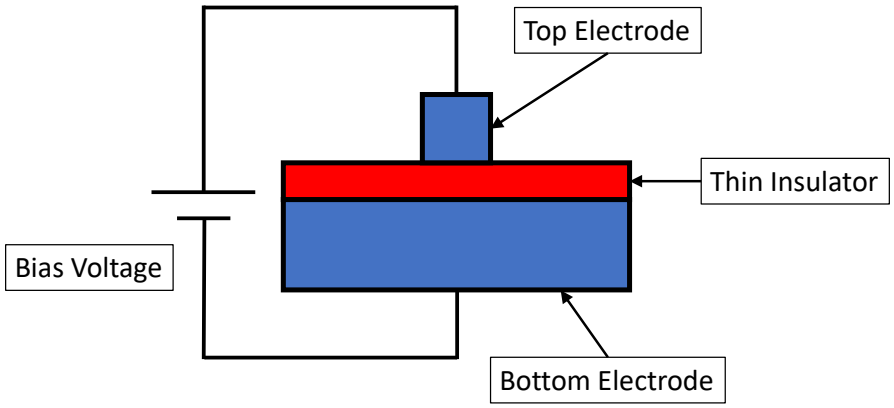


Figure 1.4: SIS junction schematic cross section. The DC bias voltage is applied to the junction through the on-chip circuit.

The non-linearity in the current-voltage (I-V) curve arises due to the superconducting property of the materials and the quasi-particle tunnelling of electrons across the insulating barrier. In a normal metal, all the conduction electrons act as fermions and obey Fermi-Dirac statistics and the Pauli exclusion principle. However, when certain metals such as niobium are cooled below a critical temperature, $T_c$ ($\sim$ 9.2 $K$ for Nb), they undergo a superconducting phase transition after which it is energetically favourable for electrons with anti-parallel spins close to the Fermi level to form Cooper pairs through a phonon interaction with the crystal lattice. These Cooper pairs have properties more akin to bosons and as such obey Bose-Einstein statistics which allows them to condense into the same, lower, energy level. This phenomenon, described in 1957 by Bardeen, Cooper and Schrieffer in their (BCS) theory of superconductivity (Bardeen et al., 1957), leads to the development of an energy gap ($\Delta$) above and below the Fermi level as can be seen in the two density of states diagrams in Figure 1.5.

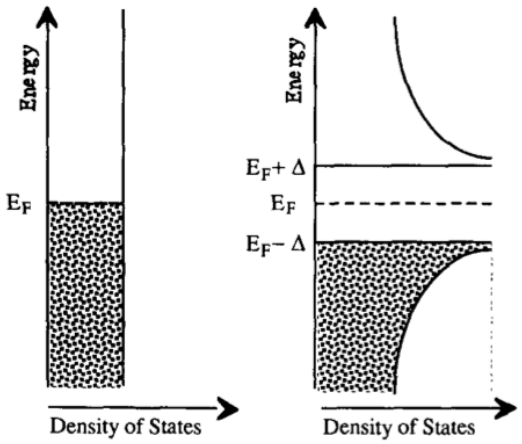


Figure 1.5: Schematic diagram of the density of states as a function of energy for a normal (left) and a superconducting (right) metal at $T = 0\ K$. Reproduced from Wengler (1992).

Cooper pairs cannot exist above the critical temperature $T_c$, because their binding energy, $2\Delta$, is quite weak, typically on the order of a few millielectron volts ($meV$). Below $T_c$ however, some of the Cooper pairs can be broken through the absorption of electromagnetic radiation with energy greater than $2\Delta$, or via the absorption of thermal energy. If a Cooper pair is broken, two quasi-particle electrons are created which behave similarly to normal electrons except for the fact that they have an energy gap in their density of states around the Fermi energy as shown in Figure 1.5.

These quasi-particles become extremely useful in the SIS junction when two superconductors form a sandwich structure with a thin insulating barrier between them. The barrier is thin enough to allow the wavefunction describing the particles on one side of the junction to have a non-zero probability amplitude on the other side, thus allowing quasi-particles and Cooper pairs to tunnel across the barrier. This tunnelling leads to the flow of current across the SIS junction (Tucker, 1979; Wengler, 1992).

A simple way to explain and understand the phenomenon of quasi-particle tunnelling is to consider Cooper pairs on one side of an SIS junction being broken by applying a DC bias voltage ($V_b$) across the SIS junction which exceeds $2\Delta/e$. In general the DC gap voltage across the junction can be written as (Tucker, 1979; Wengler, 1992)

$$V_{gap} = \frac{\Delta_1 + \Delta_2}{e} \tag{1.2}$$

where $\Delta_1$ and $\Delta_2$ are the superconductor gap energies on either side of the insulating barrier and $e$ is the electron charge. In the case that the two superconductors are identical (i.e. $\Delta_1 = \Delta_2$), the gap voltage becomes simply $V_{gap} = 2\Delta/e$. Therefore, if $V_b > V_{gap}$, Cooper pairs will be broken on one side of the SIS junction and tunnel into the conduction band of the superconductor on the other side of the SIS junction, which will result in the flow of current as shown schematically and graphically in Figure 1.6.

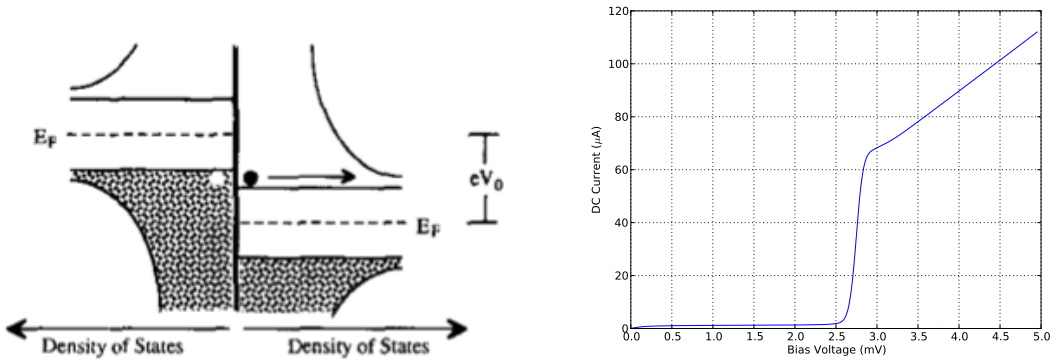


(a) Density of states diagram for an SIS junction with $V_b$ just greater than $V_{gap}$. A quasiparticle has tunnelled from left to right (Wengler, 1992).

(b) Experimental un-pumped I-V curve showing a strong non-linearity resulting from the flow of tunnelling current.

Figure 1.6: Quasi-particle tunnelling and the resulting current-voltage (I-V) curve from an SIS junction.

Figure 1.6(a) shows a schematic diagram of an SIS junction with a bias voltage applied to it that just exceeds the gap voltage. This causes the energy levels of the left-hand side superconductor to be shifted with respect to the right-hand side up to such a point that the quasi-particle electrons in the valence band of the left-hand side superconductor have equal energy to the conduction band of the right-hand side superconductor, at which point they tunnel across as there is a higher density of unoccupied states in the right-hand side superconductor. This results in a sharp increase in the flow of current across the junction, as can be seen in Figure 1.6(b), where there is only leakage current up to $V_b < V_{gap}$ due to thermally excited quasi-particles (Tucker, 1979). Once $V_b$ reaches $V_{gap}$, a large number of quasi-particles tunnel across, resulting in the sharp non-linearity in the I-V curve. As $V_b$ is increased further, it can be seen that the I-V characteristic becomes linear again. This is due to the fact that the increased density of energy states exists only around the energy gap

of the superconductors and as the Fermi level of the two superconductors is shifted further away from each other, the density of states on both sides of the junction tends towards that of a normal metal. By looking at an un-pumped I-V curve, it is possible to estimate the width of the energy gap of the SIS junction by looking at the voltage where the sharp non-linearity appears. In the case of the curve shown in Figure 1.6(b), this corresponds to a gap voltage of approximately $V_{gap} \sim 2.7\ mV$, or radiation with a frequency of $\sim 650\ GHz$. This is reasonable for a Niobium/Aluminium-Oxide/Niobium junction at a temperature of $\sim 4.6\ K$.

It is also possible for current to flow through the junction when $V_b < V_{gap}$. This is known as "photon-assisted" quantum tunnelling because it requires the presence of external electromagnetic radiation. If the SIS mixer is illuminated with photons of frequency $\nu$, then tunnelling current will be observed below $V_{gap}$ as long as the condition $nh\nu + eV_b > eV_{gap}$ is satisfied, where $h$ is Planck's constant and $n$ is an integer number corresponding to the number of photons absorbed. The idea of photon-assisted quantum tunnelling can be better understood from Figure 1.7 and is further explained in Tucker (1979).

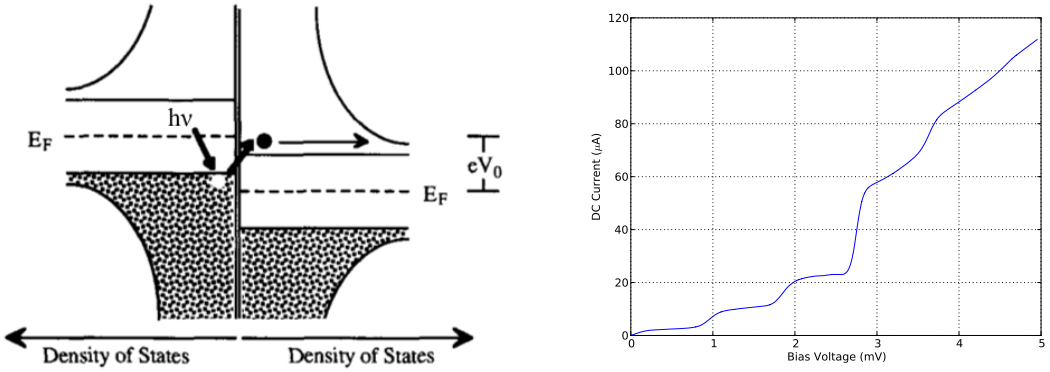


(a) Schematic diagram to illustrate photon-assisted tunnelling in an SIS junction when $V_b$ is less than $V_{gap}$ (Wengler, 1992).

(b) Experimental pumped I-V curve showing photon steps and the flow of current at $V_b < V_{gap}$ due to photon-assisted tunnelling.

Figure 1.7: Photon-assisted quasi-particle tunnelling and the resulting I-V curve from an SIS junction.

In Figure 1.7(a), $V_b$ across the junction is such that the quasi-particles in the left-hand side superconductor do not quite have enough energy to tunnel into the right-hand side superconductor. However, in the presence of external photons with frequency $\nu$ such that

$nh\nu + eV_b > V_{gap}$, a quasi-particle electron in the left-hand superconductor can absorb a photon, thus increasing its energy and allowing it to tunnel across into the right-hand side superconductor. This results in an I-V curve as shown in Figure 1.7(b) where there are clear "photon steps" before the sharp non-linearity. The first photon step is immediately to the left of the non-linearity and corresponds to one absorption event taking place where as the second photon step requires for two photons to be absorbed within the coherence time of the system, hence the lower current. The frequency of radiation being absorbed by the SIS junction can also be estimated by measuring the width of the photon steps, while the gradient of the first photon step determines whether the junction is showing inductive or capacitative behaviour. However, the crucial property of SIS mixers is their highly non-linear I-V characteristic below the superconducting phase transition temperature. It is this feature that makes them viable heterodyne detectors at sub-mm wavelengths.

## 1.5 Receiver Noise Measurement and Estimation Techniques

### 1.5.1 The Y-Factor Method

One of the most frequently employed techniques to quantify the experimental performance of an SIS receiver is known as the "Y-Factor" method. This involves estimating the noise power ($P_N$) of a mixer by measuring its output power at two different input power levels, $P^{in}_{hot}$ and $P^{in}_{cold}$. The input power for such measurements is usually provided by radiating loads at different physical temperatures. In a laboratory environment, it is common to use a room temperature ($\sim 293\ K$), "hot" load and a "cold" load with a physical temperature of $\sim 77\ K$, which corresponds to the boiling point of liquid nitrogen. The mixer noise power can approximately be related to its equivalent noise temperature, $T_N$, through $P_N = k_B T_N \delta\nu$ where $k_B$ is the Boltzmann constant and $\delta\nu$ is the bandwidth of the receiver. The measured noise power is subsequently given by (e.g. Kerr et al. (1997))

$$P_N = \frac{P^{in}_{hot} - Y P^{in}_{cold}}{Y - 1}, \qquad \text{which is equivalent to} \qquad T_N = \frac{T_{hot} - Y T_{cold}}{Y - 1} \tag{1.3}$$

where $T_{hot}$ and $T_{cold}$ are the thermal noise temperatures of the hot and cold loads respectively. Assuming the loads to be perfect black-bodies (i.e. that their emissiviities are 1) and in the limit of the Rayleigh-Jeans approximation (i.e. $h\nu/k_BT << 1$), these can be approximated by the physical temperature of the loads. The "Y-Factor" in Equation 1.3 is given by $Y = \frac{P^{out}_{hot}}{P^{out}_{cold}}$ where $P^{out}_{hot} = G_C\left(P^{in}_{hot} + P_N\right)$, $P^{out}_{cold} = G_C\left(P^{in}_{cold} + P_N\right)$ and $G_C$ is the conversion gain of the mixer.

### 1.5.2 Callen and Welton Noise Temperature Correction

While it is possible to approximate the noise temperatures of the hot and cold loads ($T_{hot}$ and $T_{cold}$) using their physical temperatures in the Rayleigh-Jeans limit, a little more care must be taken when working with frequencies and/or load temperatures such that the relation $h\nu/k_BT << 1$ no longer holds. In such cases, the noise temperatures of the loads ought to be determined from their respective noise powers, which are given by the dissipation-fluctuation (or generalised Nyquist) theorem of Callen and Welton (Callen & Welton, 1951) as

$$P^{C\&W} = k_BT\delta\nu\left(\frac{\frac{h\nu}{k_BT}}{\exp\left(\frac{h\nu}{k_BT}\right)-1}\right) + \frac{h\nu\delta\nu}{2} \tag{1.4a}$$

$$= \frac{h\nu\delta\nu}{2}\coth\left(\frac{h\nu}{2k_BT}\right). \tag{1.4b}$$

The first term on the Right Hand Side (RHS) of Equation 1.4a corresponds to the Planck radiation law that can be used to compute thermal noise power in a bandwidth $\delta\nu$ about frequency $\nu$ ($\delta\nu << \nu$), radiated into a single mode by a black-body at physical temperature $T$ (Kerr et al., 1997). The second term on the RHS of Equation 1.4a adds an additional half photon per unit frequency to the total radiated noise power and takes into account the zero-point fluctuation noise which is associated with the incoming source radiation, rather than the receiver itself (Devyatov et al., 1986). While these zero-point quantum fluctuations deliver no exchangeable power, the receiver can nevertheless develop them to

quite measurable levels and omitting this term from the calculation would underestimate the *true* noise power of the source loads and overestimate the noise temperature of the receiver.

From Equation 1.4, the noise temperature (noise power per unit bandwidth) of a black-body radiator at physical temperature $T$ can be determined by dividing the noise power ($P^{C\&W}$) by $k_B\delta\nu$ which leads to

$$T^{C\&W} = T\left(\frac{\frac{h\nu}{k_BT}}{\exp\left(\frac{h\nu}{k_BT}\right)-1}\right) + \frac{h\nu}{2k_B} \tag{1.5a}$$

$$= \frac{h\nu}{2k_B}\coth\left(\frac{h\nu}{2k_BT}\right). \tag{1.5b}$$

In the limit of small $h\nu/k_BT$, the Callen and Welton noise power tends to the Rayleigh-Jeans result ($P^{C\&W} \rightarrow P^{R-J} = k_BT\delta\nu$), while the Callen and Welton noise temperature simply tends to the physical temperature of the black-body ($T^{C\&W} \rightarrow T^{R-J} = T$). However, this result no longer holds as either the frequency of the incoming radiation increases and/or the physical temperature of the source loads decreases, because the relative contribution of the zero-point fluctuation noise (second term on the RHS of Equations 1.4a and 1.5a) grows with increasing frequency and decreasing load temperature. For example, if the noise temperature of a receiver operating at 230 $GHz$ were to be measured using the "Y-Factor" method with hot and cold loads at physical temperatures of 293 $K$ and 77 $K$ respectively, the difference in hot and cold load noise temperatures calculated using the Callen and Welton expression (Equation 1.5) and estimated with the Rayleigh-Jeans approximation would be $\sim 0.035$ $K$ for the hot load ($T_{hot}^{C\&W} \simeq 293.035$ $K$, $T_{hot}^{R-J} = 293.0$ $K$) and $\sim 0.132$ $K$ for the cold load ($T_{cold}^{C\&W} \simeq 77.132$ $K$, $T_{cold}^{R-J} = 77.0$ $K$). Then, for a measured Y-Factor of e.g. 3.0, the difference in receiver noise temperature according to Equation 1.3 would be $\sim 0.181$ $K$. This is a fairly small discrepancy because the combination of measurement frequency and load temperature chosen is such that $h\nu/k_BT << 1$ and the noise temperature contribution of the zero-point fluctuations is small relative to the thermal radiation of the loads. However,

if the noise temperature of the same receiver were to be measured again at 230 $GHz$ but this time using a 293 $K$ hot and a 4 $K$ cold load, then the noise temperature difference of the cold load when calculated using the Callen and Welton expression and estimated with the Rayleigh-Jeans approximation would be $\sim 2.27\ K$ ($T_{cold}^{C\&W} \simeq 6.27\ K$, $T_{cold}^{R-J} = 4.0\ K$). This, in turn, would lead to a receiver noise temperature that is $\sim 3.39\ K$ higher when calculated using the Rayleigh-Jeans approximation, assuming a measured Y-Factor of 3.0 once again. The difference in this result is now significantly greater and illustrates the importance of including the zero-point fluctuation noise in calculations of $T_N$ when working outside the Rayleigh-Jeans limit.

In a similar manner, if the measurement frequency were increased to 800 $GHz$ and hot/cold loads of 293/77 $K$ were used, the difference in hot and cold load noise temperatures calculated using the Callen and Welton expression (Equation 1.5) and estimated with the Rayleigh-Jeans approximation would be $\sim 0.42\ K$ for the hot load ($T_{hot}^{C\&W} \simeq 293.42\ K$, $T_{hot}^{R-J} = 293.0\ K$) and $\sim 1.59\ K$ for the cold load ($T_{cold}^{C\&W} \simeq 78.59\ K$, $T_{cold}^{R-J} = 77.0\ K$). The receiver noise temperature in this example would then be $\sim 2.18\ K$ higher if the Rayleigh-Jeans approximation was used to compute it and a measured Y-Factor of 3.0 was once more assumed. The results of these examples are neatly summarised in Table 1.1.

| $\nu\ (GHz)$ | $T_{hot}\ (K)$ | | | $T_{cold}\ (K)$ | | | $T_N\ (K)$ | | |
|---|---|---|---|---|---|---|---|---|---|
| | *C&W* | *R-J* | $\Delta T_{hot}$ | *C&W* | *R-J* | $\Delta T_{cold}$ | *C&W* | *R-J* | $\Delta T_N$ |
| 230 | 293.035 | 293.0 | 0.035 | 77.132 | 77.0 | 0.132 | 30.819 | 31.0 | 0.181 |
| 230 | 293.035 | 293.0 | 0.035 | 6.27 | 4.0 | 2.27 | 137.11 | 140.50 | 3.39 |
| 800 | 293.42 | 293.0 | 0.42 | 78.59 | 77.0 | 1.59 | 28.82 | 31.0 | 2.18 |

Table 1.1: A comparison of load and receiver noise temperatures when calculated using the Callen and Welton expression and estimated with the Rayleigh-Jeans approximation for different measurement frequencies and cold load physical temperatures. A Y-Factor of 3.0 has been assumed to calculate $T_N$ using Equation 1.3.

As such, it should be explicitly stated that all of the receiver noise temperatures presented in Chapter 5, which is concerned with the development of SIS receivers approaching $THz$ frequencies, were computed using the Callen and Welton expression (Equation 1.5b) for the effective noise temperature of black-body loads, rather than using the Rayleigh-Jeans approximation. This is particularly relevant to the measurements presented in Figures 5.13

and 5.19, which show receiver noise temperature measured between $\sim 600 - 700\ GHz$ and $\sim 800 - 900\ GHz$ respectively and thus the $h\nu/k_BT << 1$ condition no longer applies.

### 1.5.3 Separating the RF System, SIS Junction and IF Components

It can be seen that the "Y-Factor" measurement estimates the noise temperature of the entire receiver including the SIS junction, the RF optics as well as the noise contribution of the IF chain. In order to get a better understanding of the contribution made by all the various components in the receiver, it is possible to model the system as a cascaded circuit of discrete elements. By doing this, the receiver noise temperature can be expressed using a modified version of the Friis expression (Friis, 1944) which is given by

$$T_N = T_1 + \frac{T_2}{G_1} + \frac{T_3}{G_1 G_2} + ... + \frac{T_n}{G_1 G_2 + ... + G_{n-1}} \tag{1.6}$$

where $T_1, T_2, ... T_n$ is the noise temperature and $G_1, G_2, ... G_{n-1}$ the gain of each component in the chain respectively assuming a perfect impedance match between them. From this, the conversion gain of the receiver can be expressed as $G_C = G_1 G_2 ... G_n$ while the effective noise temperature for passive components (such as the RF optics) can be expressed by $T_{passive} = \left(\frac{1}{G} - 1\right) T$, where $T$ corresponds to the physical temperature and $1/G$ is the attenuation, or loss.

A convenient way to estimate the noise temperature of the receiver in practice is to approximate the system using its three major sub-systems; namely the RF system, the SIS junction and the IF part of the receiver. This is schematically illustrated in Figure 1.8 and allows Equation 1.6 to be simplified as

$$T_N = \left(\frac{1}{G_{RF}} - 1\right) T_{RF} + \frac{T_{SIS}}{G_{RF}} + \frac{T_{IF}}{G_{RF} G_{SIS}} \tag{1.7}$$

which assumes a very large gain for the first stage cryogenic IF amplifier that makes the noise contribution from further components in the receiver chain negligible. In addition, the RF contribution in Figure 1.8 (and Equation 1.7) is modelled to arise from all the components before the SIS junction (such as the optics and transmission lines) while the

IF noise comes from the different amplification stages and components after the junction.

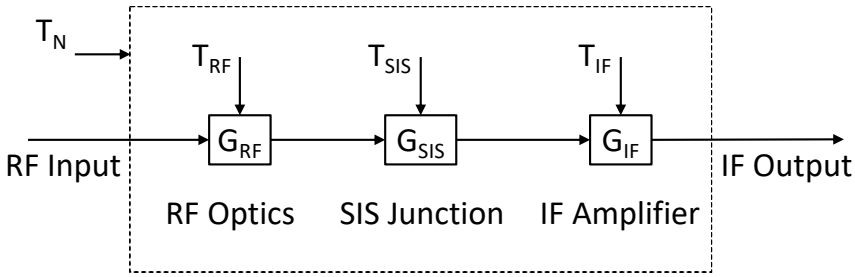


Figure 1.8: Schematic diagram of the main receiver sub-systems that contribute to the overall noise temperature.

### 1.5.4 Estimating the RF Noise Contribution

The RF noise contribution to the overall system noise temperature can be experimentally estimated by rewriting Equation 1.7 as

$$T_N = T' + \frac{T_{IF}}{G_{RF}G_{SIS}}, \qquad \text{where} \qquad T' = \left(\frac{1}{G_{RF}} - 1\right) T_{RF} + \frac{T_{SIS}}{G_{RF}} \tag{1.8}$$

represents the total RF contribution of all the components in front of the SIS junction, including the junction noise itself. By considering a load placed in front of the mixer at temperature $T_{in}$, the output power per unit instantaneous bandwidth can be expressed as $P_{out}(T_{in}) = k_B\,(T_N + T_{in})\,G_C$, with $G_C = G_{RF}G_{SIS}G_{IF}$. Then substituting in for $T_N$ using Equation 1.8 leads to $P_{out}(T_{in}) = k_B\,(T' + T_{in})\,G_C + k_B T_{IF} G_{IF}$. By plotting $P_{out}$ as a function of $T_{in}$, it is possible to obtain a straight line with a gradient of $k_B G_C$ and y-axis intercept of $k_B T_{IF} G_{IF}$.

The gain of the mixer ($G_{SIS}$) is highly sensitive to the LO input power, while the mixer noise ($T_{SIS}$) varies slowly with pump level below the peak of the gain (Ke & Feldman, 1994). Therefore, assuming that $T_{SIS}$ does not change dramatically below the peak of the mixer gain, it is possible to plot a set of straight lines by gradually adjusting the LO pump level such that $T_{in} = T_{in}^{hot}$ and $T_{in} = T_{in}^{cold}$ are the two data points which define the straight line. Since all of these lines will intersect at $T_{in} = -T'$, with $P_{out} = k_B T_{IF} G_{IF}$, this provides a practical way to graphically estimate the RF system noise contribution and is illustrated in

the plot in Figure 1.9.

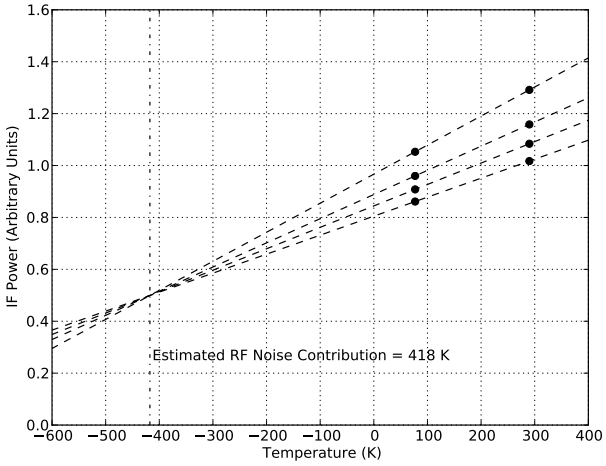


Figure 1.9: An example of the intersecting lines method being used to estimate the RF system noise contribution at 880 $GHz$.

### 1.5.5 Estimating the Mixer Gain and IF Noise Contribution

It is possible to experimentally estimate the mixer conversion gain by using the shot noise property of the SIS junction itself (Woody et al., 1985). For an unpumped junction, the shot noise can be expressed as (Rogovin & Scalapino, 1974)

$$T_{shot} = \frac{1}{2k_B} eI_{DC}R_{dyn} \coth\left(\frac{eV_b}{2k_BT_{phys}}\right), \tag{1.9}$$

where $I_{DC}$ is the DC tunnelling current, $R_{dyn}$ the dynamic impedance of the junction and $T_{phys}$ the physical temperature of the junction at bias voltage $V_b$. The tunnelling current above the gap increases in an approximately linear manner, with the IF output in this region being generated by the shot noise of the junction itself. Since in the linear part of the DC I-V curve the hyperbolic cotangent term in Equation 1.9 (Rogovin & Scalapino, 1974) is $\sim 1$, it can be simplified to

$$T_{shot} \simeq \frac{eI_{DC}R_N}{2k_B} + constant \simeq 5800 \times V_b + constant \tag{1.10}$$

with $R_N$ representing the junction's normal resistance, bias voltage given by $V_b = I_{DC}R_N$ and the gradient of the line being approximately equal to 5.8 $K/mV$. Dividing this by

the measured gradient of the IF output curve (resulting from an unpumped DC I-V curve) above the gap voltage which is in *Arbitrary Units/mV* (since the IF power output scale depends on the IF chain configuration and is thus, initially, unknown and arbitrary) leads to a scaling factor, $X_{IF}$, in $K/AU$. The gain of the IF chain is then given by the inverse of this quantity, $G_{IF} = \frac{1}{X_{IF}}$ (in $AU/K$), as it represents the measured IF system output power with reference to a known shot noise power of the junction at the IF input port. It should be noted that if an isolator is used between the mixer and the IF amplifier, the noise added by the IF amplifier would be of the LNA looking into a 50 Ω source impedance (i.e. the isolator). However, if no isolator is used in front of the IF amplifier then the noise added by the IF amplifier, measured with the described method, would be of the LNA looking into a source impedance equal to $R_N$ (i.e. the normal resistance of the SIS mixer). Therefore, the noise of the LNA depends on the source impedance and can be significantly different if terminated into 50 Ω, $R_N$ or the output impedance of the SIS mixer. In particular, for an SIS mixer cascaded directly with the IF amplifier where the optimum mixer bias is half a photon step below the gap voltage, the source impedance for the IF amplifier depends on the IF output impedance of the SIS, which in general is much greater than $R_N$.

It is now possible to write an expression for the power difference produced by the SIS mixer at its output port by considering a simplified, two component system which consists only of the SIS mixer and an IF amplifier. Assuming that the Rayleigh-Jeans approximation still applies, the difference in output power of the mixer and the IF amplifier in response to hot and cold loads can be written as

$$P_{mix}^{out} = G_{mix} k_B \left(T_{hot}^{in} - T_{cold}^{in}\right), \qquad \text{and} \qquad P_{IF}^{out} = k_B \left(T_{hot}^{out} - T_{cold}^{out}\right), \tag{1.11}$$

where $G_{mix}$ is given by the product of $G_{RF}$ and $G_{SIS}$, rather than just the gain of the junction itself. Because the gain of the amplifier, $G_{IF}$ has already been determined, it is now possible to estimate the mixer conversion gain using

$$G_{IF} = \frac{P_{IF}^{out}}{P_{mix}^{out}} = \frac{T_{hot}^{out} - T_{cold}^{out}}{G_{mix}\left(T_{hot}^{in} - T_{cold}^{in}\right)}, \quad \text{leading to} \quad G_{mix} = \frac{1}{G_{IF}} \times \frac{T_{hot}^{out} - T_{cold}^{out}}{T_{hot}^{in} - T_{cold}^{in}}. \tag{1.12}$$

In addition, the noise contribution of the IF sub-system can also be estimated using the shot noise of the SIS junction, since the noise current does not begin to flow before a specific voltage, $V_{sh}$ is reached. This voltage can be determined by extrapolating the linear part of the unpumped DC I-V curve of the junction back to the voltage axis ($y = 0$) intercept as described in detail by Woody et al. (1985). At this voltage, the junction does not contribute any shot noise to the system which means that the IF power output must also be zero. Therefore, by performing a similar extrapolation on the IF curve and measuring the output power at $V_{sh}$ of the IF curve, it is possible to estimate the additional system noise generated by the IF system itself. This technique can be seen in the plot in Figure 1.10.

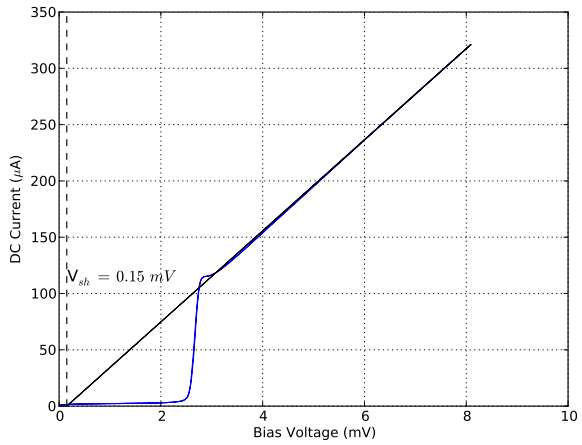


(a) Unpumped I-V curve showing the shot voltage extrapolation, $V_{sh}$.

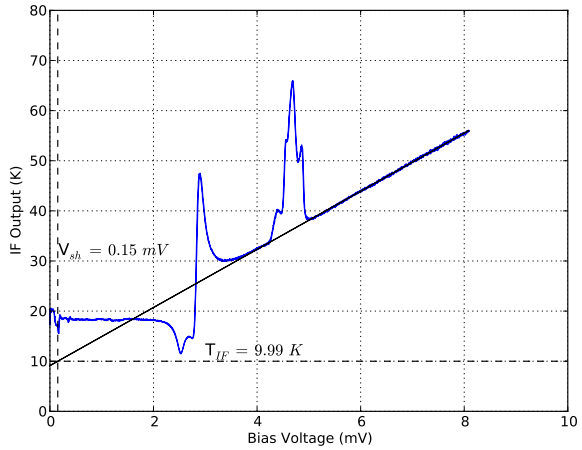


(b) Corresponding IF curve showing the IF system noise contribution, $T_{IF}$ at the shot voltage, $V_{sh}$.

Figure 1.10: An example of the shot noise extrapolation technique being used to determine the IF system noise contribution.

## 1.6 Thesis Outline

Given the recent development of the novel field of sub-millimetre wavelength astronomy and because there is scientific interest in carrying out astronomical observations at frequencies approaching and even exceeding 1 $THz$, there is motivation to upgrade and develop the technological capabilities of high frequency radio telescopes to facilitate these observations in years to come. Therefore, the work presented in this thesis will focus on addressing some of the technological issues facing such telescopes with the key objectives and results presented in each Chapter given below:

- Chapter 2: This chapter will focus on the harmonic content of Local Oscillator (LO) sources and how this can affect receiver performance in terms of noise and spectral output. It will be shown that it is possible for RF signals to be down-converted into the IF band multiple times by pumping an SIS mixer using a commercially available, but spectrally impure LO operating between $\sim 190 - 260$ $GHz$. This will cause the same spectral line to appear at several locations in the IF spectrum leading to the presence of highly confusing spectral artefacts.

  The generation of unwanted LO harmonics will be shown to affect receiver performance in terms of both noise and spectral content, thus requiring close attention when receivers employing such sources are used for astronomical observations. The key outcomes of this work have been published in Hector et al. (2015a).

- Chapter 3: The work here will focus on the design, fabrication and far-field beam pattern measurement of a number of smooth-walled, multiple-flare-angle-discontinuity feed horns operating in the $THz$ regime. These feeds will be shown to exhibit high-quality simulated beam patterns between $780 - 950$ $GHz$ and $1300 - 1500$ $GHz$, the latter of which is well into the supra-Terahertz regime. Using, a robust direct machining technique for the fabrication process it is possible to manufacture any number of such feeds quickly and efficiently, thus making it suitable for applications such as the production of high-frequency focal plane arrays. Finally, far-field radiation pattern measurement of the horns will show that by ensuring the dimensions of the

fabricated horns are within $\sim$ 10 $\mu m$ of the design specifications, it is possible to create feeds with excellent experimental beam patterns which closely resemble their theoretical predictions. This makes such horns highly attractive antenna alternatives to the more complex corrugated feed horn structure at Terahertz frequencies. The major results of this Chapter have been published in Hector et al. (2015b) and Hector et al. (2017).

- Chapter 4: This part of the thesis will demonstrate the use of Electron-Beam (E-Beam) lithography to fabricate Schottky barrier diodes for high radio frequency applications. The E-Beam system will be shown to successfully write all of the metallic layers of the device, including the development of a novel bi-layer resist process for the creation of a suspended air-bridge which is necessary for the successful operation of such diodes at high radio frequencies. A selection of fabricated diodes will be presented which will exhibit encouraging I-V characteristics before RF measurements demonstrate these diodes to be excellent frequency multipliers and effective LO sources in the $225-330\ GHz$ range. These measurements give validity to the E-Beam technique and provide a platform on which further iterations of the fabrication process can be pursued and optimised with the ultimate aim of delivering components suitable for astronomy applications at $THz$ frequencies.

- Chapter 5: The Chapter will present the development of a prototype heterodyne receiver suitable for $THz$ frequency operation. A major novel feature of this system is that all of the RF and most of the LO signal coupling optics are inside a Pulse Tube Cooled cryostat, which helps to reduce RF losses. Furthermore, the system employs an internally mounted cryogenic cold load for more sensitive Y-factor noise temperature measurements. This receiver will be shown to have reasonable performance between $600-700\ GHz$ before being tested between $800-900\ GHz$ using a Nb/AlN/NbN twin tunnel junction SIS mixer combined with a custom feed horn. The twin junction SIS mixer, which was supplied by colleagues from the Kapteyn Astronomical Institute in the Netherlands, enables broadband receiver performance and helps tune out parasitic junction capacitance. Here, it will be shown to exhibit very good noise temperature

performance once beamsplitter losses and a waveguide dimension mismatch have been taken into account. The results of these tests have been published in Tan et al. (2018).

- Chapter 6: Finally, a summary of work contained in this thesis will be presented emphasising the necessity and importance of carrying out such a project. A brief description of future work that is necessary to further advance this research will also be given.

# Chapter 2

# The Origin of Harmonics and Multiple Signals in a 230 GHz LO

## 2.1 Introduction

Heterodyne frequency down conversion is a commonly-used technique for performing high-resolution spectroscopic observational radio astronomy. The heterodyne frequency conversion process combines an incident Radio Frequency (RF) astronomical signal with a local reference frequency source (Local Oscillator, LO) tone, in a highly non-linear mixing device, such as a Superconductor-Insulator-Superconductor (SIS) tunnel junction. The mixer in turn generates an Intermediate Frequency (IF) output, which is substantially lower in frequency than the RF and LO input signals. This allows for subsequent low noise amplification, signal processing and production of the astronomical signal power spectrum. When combined, the mixer, LO and IF components form a heterodyne receiver system, the likes of which have been employed on a number of sub-millimetre wave telescopes such as the Atacama Large Millimetre/sub-millimetre Array (ALMA), the James Clerk Maxwell Telescope (JCMT) and the Herschel Space Observatory, which used a heterodyne receiver on its HIFI (Heterodyne Instrument for the Far Infrared) spectrometer.

The LO is a key device within the receiver system. It must, for instance, provide sufficient power to "pump" the mixer, be stable in frequency and amplitude as well as

also possessing a broad tuning range. Additionally, it is essential that the LO signal is spectrally pure; i.e., spurious harmonic content is of sufficiently low amplitude to avoid spectral contamination and system noise degradation.

The presence of spurious frequency tones emanating from a harmonically generated LO signal can significantly degrade the performance of an SIS tunnel junction mixer (e.g. Zhou et al. (2012)). The existence of such tones is often revealed by distorted I-V curves obtained when pumping an SIS device with the LO.

However, LO spectral purity is difficult to specify for near-quantum-limited receiver systems and is often overlooked as a parameter when defining the LO chain. Determining the purity of an LO source is therefore important, as the harmonic content can mix with the RF input signal and result in unwanted parts of the RF spectrum being down converted into the IF band. This degrades the receiver sensitivity and could also introduce confusing spectral artefacts.

The work in this chapter explores this effect by using a commercially available 230 $GHz$ LO source to investigate its harmonic content and correlate unusual features identified in an LO-pumped, SIS mixer I-V curve with the direct measurement of LO tones made via a Fourier Transform Spectrometer (FTS) and a spectrum analyser.

The results show that intermixing frequency products are generated within the first, low frequency stage of the LO chain and these unwanted signals are then converted to higher frequencies through subsequent stages of LO amplification and frequency up-conversion.

Furthermore, the chapter describes SIS mixer noise temperature measurements carried out with a Yttrium Iron Garnet (YIG) oscillator in an attempt to use the superior stability of a YIG source, compared to a Voltage Controlled Oscillator (VCO), to improve the receiver noise temperature.

The work concludes with SIS mixer and spectrum analyser measurements which show that it is indeed possible to down convert higher order LO harmonics into the IF band and that these tones lead to unwanted spectral signals, especially when combined with a “test” spectral line produced with a second LO.

The experimental techniques and results obtained from the different LO experiments performed are described in detail in the following sections.

## 2.2 SIS Mixer Measurements at 230 GHz

The work in this chapter came about as a result of carrying out SIS mixer noise temperature measurements between $\sim 190 - 260\ GHz$ and observing unusual features in the normally "step-like" pumped I-V curves as well as elevated noise temperatures across a range of LO frequencies. The experimental setup used for carrying out the measurements described here is shown in Figure 2.1(a) while a schematic diagram of the receiver system can be seen in Figure 2.1(b).

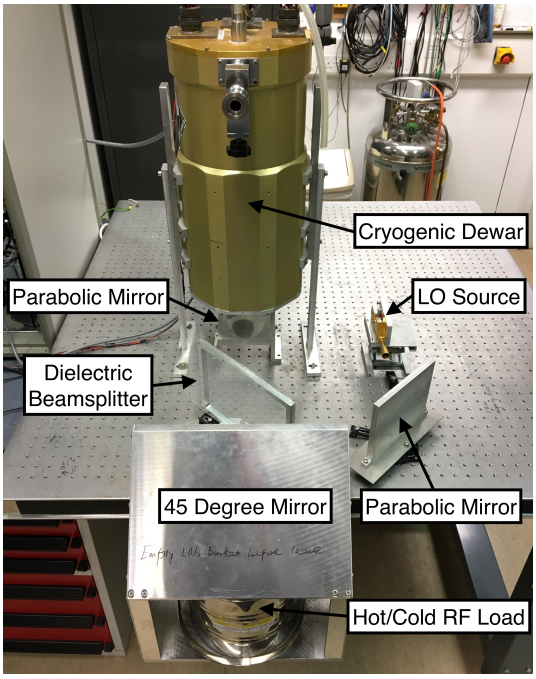


(a) Experimental setup for performing SIS mixer measurements at $\sim 230\ GHz$.

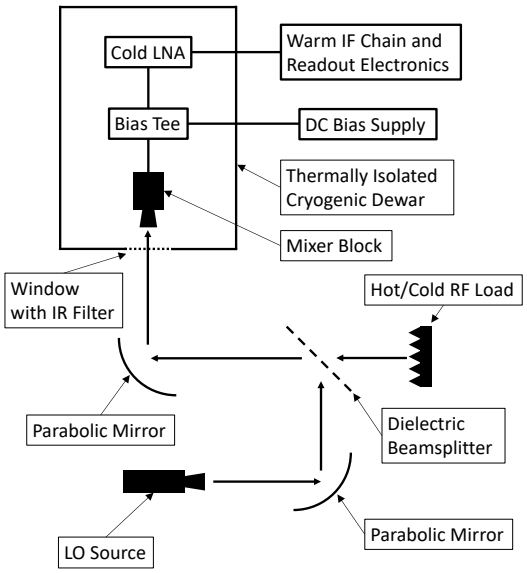


(b) Schematic diagram of a typical heterodyne receiver system.

Figure 2.1: Experimental setup and schematic diagram showing a $\sim 230\ GHz$ heterodyne receiver system.

The mixer, containing a Niobium/Aluminium-Oxide/Niobium SIS tunnel junction, is located within the thermally isolated dewar which needs to be pre-cooled using liquid Nitrogen. Once a pre-cool has been carried out (which usually takes $1 - 2$ days), a Helium transfer can be performed which brings the temperature inside the dewar down to around $4\ K$. This is approximately half the superconducting transition temperature of Niobium ($T_c \sim 9.2\ K$) and allows the use of the non-linear, superconducting properties of the material for the down conversion of high frequency signals.

The LO source is mounted on the optical table and directed into the mixer with the use of parabolic mirrors and a Mylar beamsplitter as shown in Figure 2.1. The RF signal, which couples in transmission through the beamsplitter, is provided by the ambient black-body radiation in the room as well as the black-body radiation emitted by a liquid Nitrogen reservoir. Thus, by placing a bucket of liquid Nitrogen beneath the 45 degree mirror, the RF signal temperature can be varied between a "Hot" (290 $K$) and a "Cold" (77 $K$) load.

This experimental setup can be used to obtain pumped I-V and corresponding IF curves which make it possible to determine the noise temperature ($T_{rec}$) of the receiver system. This is an important measurement because it is a direct way of quantifying the sensitivity of the instrument.

The noise temperature can be experimentally determined from the receiver output IF power measured at two different input power levels $P_{hot}$ and $P_{cold}$, which correspond to the hot and cold black-body loads with temperatures $T_{hot}$ and $T_{cold}$ respectively. Equation 2.1 (e.g. Kerr et al. (1997)) gives the relationship used to calculate the receiver noise temperature using this technique.

$$T_{rec} = \frac{T_{hot} - YT_{cold}}{Y - 1} \tag{2.1}$$

The Y-factor in Equation 2.1 ($Y = P_{hot_{IF}}/P_{cold_{IF}}$) is the ratio of the two IF output powers while $T_{hot} = 290\ K$ (ambient room temperature) and $T_{cold} = 77\ K$ (boiling point of liquid Nitrogen) are the thermal noise temperatures of the hot and cold loads respectively. In the limit that $h\nu/k_BT << 1$, where $h$ is Planck's constant, $\nu$ is the measurement frequency and $k_B$ the Boltzmann constant, the Rayleigh-Jeans approximation applies and the thermal noise temperature of a black-body at physical temperature $T$ can be approximated by $T$. Since at 230 $GHz$, with $T_{cold}^{phys} = 77\ K$, the difference between the physical and thermal noise temperature of the cold load as calculated using the Callen and Welton law (Kerr et al., 1997) is just 0.17 %, the Rayleigh-Jeans condition holds and it is possible to approximate the thermal noise temperatures of both loads using their physical temperatures.

An example of a clean, pumped I-V and corresponding IF curve obtained at 220.5 $GHz$ with the aforementioned setup, is shown in Figure 2.2.

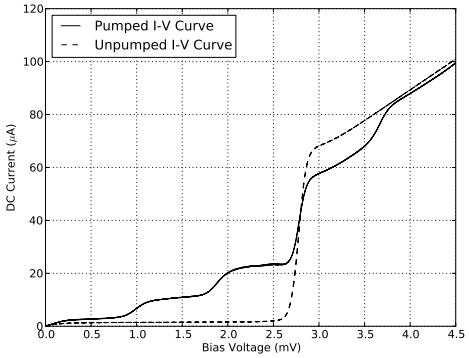


(a) Pumped I-V curve showing well defined photon steps at 220.5 $GHz$.

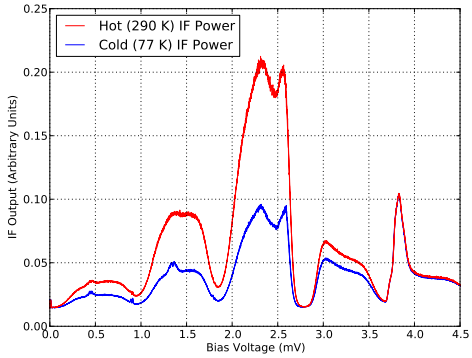


(b) IF power output in the presence of hot and cold black-body loads at 220.5 $GHz$. Measured $T_{rec} = 68.5\ K$.

Figure 2.2: A clean pumped I-V and corresponding IF curve at 220.5 $GHz$ obtained using the experimental setup shown in Figure 2.1(a).

The IF power output in the presence of hot and cold black-body loads can be seen in Figure 2.2(b). By taking the ratio of these powers and using Equation 2.1, the Double Side Band (DSB) receiver noise temperature has been calculated to be $T_{rec} = 68.5\ K$ at a pump frequency of 220.5 $GHz$. These results give an example of good receiver performance, with an acceptable noise temperature and a clean pumped I-V curve showing a well defined photon step structure.

On the other hand, Figure 2.3 provides an example of a distorted pumped I-V and its corresponding IF curve.

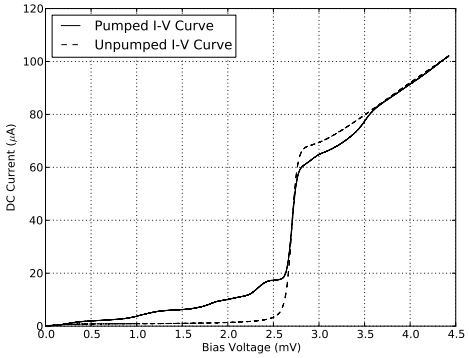


(a) Pumped I-V curve showing distorted, poorly defined photon steps at 198.0 $GHz$.

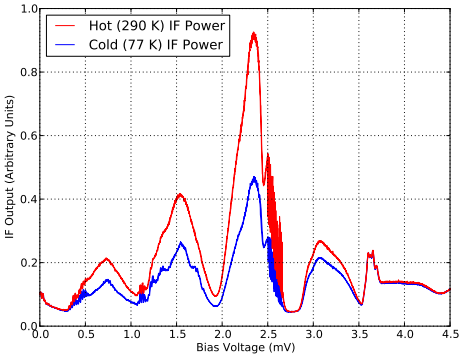


(b) IF power output in the presence of hot and cold black-body loads at 198.0 $GHz$. Measured $T_{rec} = 119.7\ K$.

Figure 2.3: A distorted pumped I-V and corresponding IF curve at 198.0 $GHz$ obtained using the experimental setup shown in Figure 2.1(a).

It can be seen from Figure 2.3(a) that the pumped I-V curve, with the LO set to 198.0 $GHz$, shows a poorly defined photon step structure as well as an unusual feature prior to the sharp non-linearity at $\sim 2.7\ mV$. Furthermore, the receiver noise temperature at 198.0 $GHz$, with a distorted pumped I-V curve, has been measured to be $T_{rec} = 119.7\ K$. This is 51.2 $K$ (75 %) higher than the result at 220.5 $GHz$ and $\sim 100\ K$ higher than the "state-of-the-art" SIS receiver measurements at these frequencies which can achieve DSB noise temperatures as low as $\sim 20\ K$ (Kerr et al., 2014), just $\sim 2$ times the quantum limit given by $T_{QL} = h\nu/k_B$.

The features observed in Figure 2.3(a) would not be present if the mixer were pumped with a pure LO source tone, as is likely to be the case in the results shown in Figure 2.2.

Additional I-V curves with a similar structure to the one seen in Figure 2.3(a) were obtained across a significant fraction of the LO frequency band of operation between $\sim 180 - 270\ GHz$ (Zhou, 2013), implying a variable nature to the LO harmonic content.

These results prompted an investigation into the frequency output of the LO chain being used to pump the SIS mixer. Direct measurements of the LO spectral output were initially made via a Fourier Transform Spectrometer (FTS) and later using a spectrum analyser combined with a range of solid-state, millimetre-wave external mixers which enabled frequencies up to 500 $GHz$ to be tested. The FTS and spectrum analyser measurements were carried out at the Rutherford Appleton Laboratory (RAL), while measurements of the pumped I-V and IF curves were made using a fin-line SIS mixer at Oxford's Superconducting Detectors Group laboratory.

## 2.3 Fourier Transform Spectrometer Measurements

The Fourier Transform Spectrometer (FTS) measurement system consists of a Martin-Puplett interferometer (Martin & Puplett, 1970), a power detector such as a Golay cell (Golay, 1947) and a signal modulator (e.g. optical chopper) that is connected to a lock-in amplifier. The system is capable of probing the spectral content of an LO (or other source of electromagnetic radiation) across a wide frequency range by acquiring an interferogram of the incoming LO signal and then performing a Fourier Transform on it. The Martin-Puplett

interferometer used in this setup is similar to the Michelson interferometer except that it uses a wire grid polariser (rather than a half-silvered mirror) to split the incident beam into two orthogonal polarisations. The system also employs two "rooftop" mirrors in the beam path to flip the polarisation of the two signals by 90° so that they can be recombined having travelled a different path length within the interferometer. The recombined signal, which is elliptically polarised with ellipticity dependent on the path difference between the two orthogonal polarisations, is turned into plane-polarised radiation via a polariser before being modulated by the optical chopper and detected at the Golay cell. An image of the experimental setup showing the Martin-Puplett interferometer that was used for the LO tests described in this section can be seen in Figure 2.4.

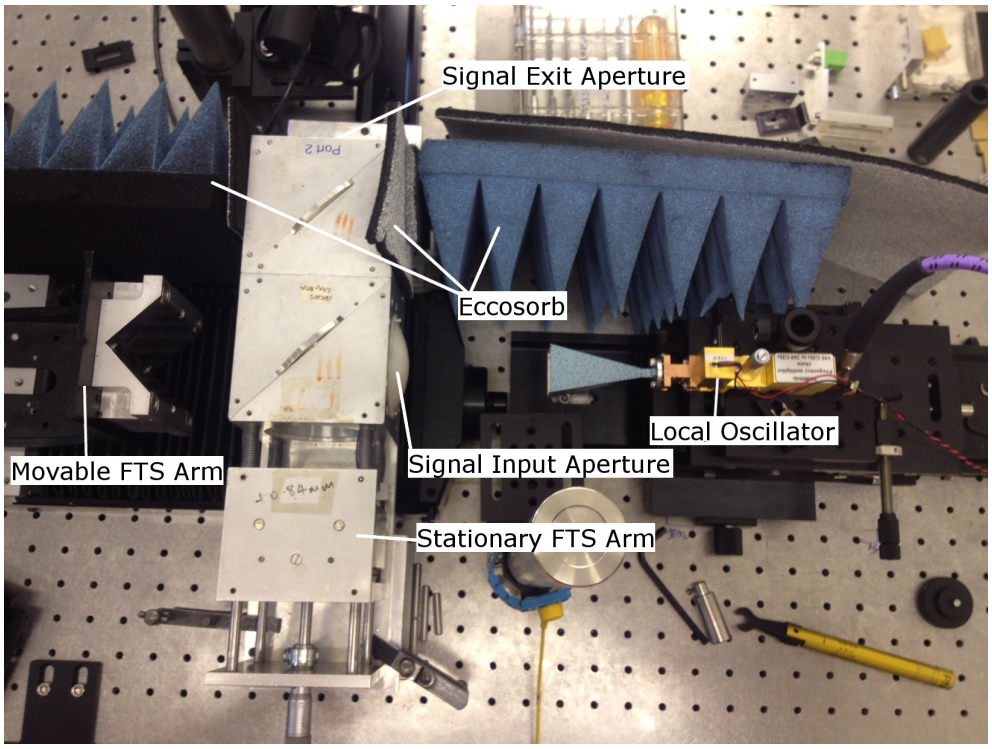


Figure 2.4: Experimental setup for LO measurements using the FTS.

The LO under investigation during these experiments was supplied by Radiometer Physics GmbH (RPG) and will henceforth be referred to as the "RPG LO". It consists of a synthesiser-driven active frequency multiplier which takes a low frequency ($\sim 10-15\ GHz$) input tone and multiplies it by a factor of 6 to up-convert it to $\sim 60-90\ GHz$. This signal is then amplified and multiplied by 3 using a tripler to bring it to $\sim 180-270\ GHz$.

This results in an overall multiplication factor of 18 from the original fundamental input frequency. The chain also contains a tunable waveguide attenuator between the sextupler and the amplifier which can be used to limit the amount of power entering the amplifier and thus prevent damage to the component. A schematic diagram of the LO chain is given in Figure 2.5.

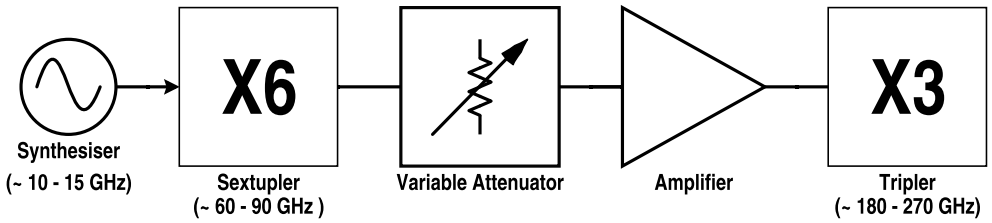


Figure 2.5: Schematic diagram of the RPG LO being tested.

### 2.3.1 RPG LO FTS Measurements

The initial FTS measurements were carried out with the LO set up as shown in Figure 2.5 but with the addition of a smooth-walled feed horn at the output of the tripler. The DC voltage required to operate the low frequency sextupler and amplifier of this LO is + 7 $V$ while a power level of +8 to +10 $dBm$ is required from the synthesised source. When powered up, the LO draws $\sim 0.64$ $A$ of current.

The source was initially tested at frequencies of 223.2 and 228.6 $GHz$ as these should both be well within the band of operation of the LO and also because 223.2 $GHz$ had previously been tested on the FTS (Zhou, 2013) and found to contain multiple unwanted harmonics so it was interesting to try to recreate this spectrum.

The FTS was initially set up to provide a spectral resolution of 0.5 $GHz$ and a measurement frequency range extending up to 400 $GHz$. The signal modulation frequency was set to 10 $Hz$, due to the relatively slow response time of the Golay cell detector. The FTS spectral output from these measurements at 223.2 and 228.6 $GHz$ is shown in Figure 2.6.

The results suggest that the FTS spectrum does contain tones that correspond to the LO frequencies being tested. However, in addition to these there are a number of harmonics also present in the spectrum (mainly around the frequency of the LO) which are separated

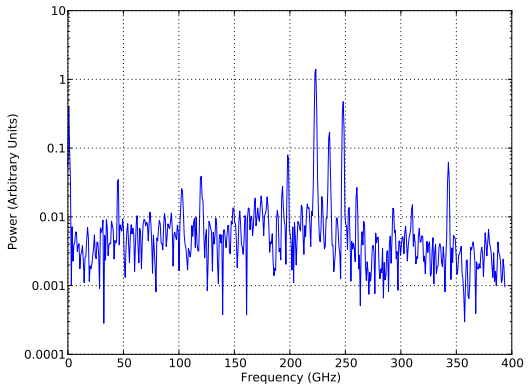


(a) FTS measurement at 223.2 $GHz$ showing a contaminated spectrum with harmonics present at 198.4, 223.2, 235.6, 248.0 and 260.4 $GHz$. Tones are also present at $\sim$ 45, 103, 120 and 342 $GHz$.

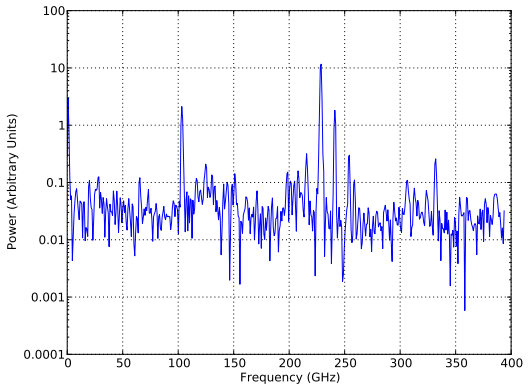


(b) FTS measurement at 228.6 $GHz$ showing a contaminated spectrum with harmonics present at 215.9, 228.6, 241.3 and 254.0 $GHz$. Tones are also present at $\sim$ 103 and 332 $GHz$.

Figure 2.6: FTS spectral output at 223.2 and 228.6 $GHz$ using a measurement frequency range of 400 $GHz$. Both sets of data show a highly contaminated spectrum with multiple harmonics present. The amplitude of uncertainties is on the scale of the noise floor fluctuation in the measurements, which is clearly visible in each plot.

from the desired frequency by the fundamental, low frequency tone going into the sextupler from the signal synthesiser, namely $\nu_{synth}$ = 12.4 (223.2/18) $GHz$ and $\nu_{synth}$ = 12.7 (228.6/18) $GHz$. As well as this, further tones can be seen at $\sim$ 45, 103, 120 and 342 $GHz$ in Figure 2.6(a) and $\sim$ 103 and 332 $GHz$ in Figure 2.6(b) which do not correspond to multiples of the fundamental input tone.

One explanation for these spurious tones, is that they could be the result of aliasing which can occur when a signal is under sampled. The condition required to avoid the negative effects of aliasing is given by Equation 2.2 and is known as the Nyquist criterion (Nyquist, 1928; Shannon, 1949).

$$\nu_s \geq 2\nu \tag{2.2}$$

This relationship states that in order to be able to correctly reproduce a signal of frequency $\nu$, it must be sampled at a frequency $\nu_s$ which is greater than or equal to $2\nu$. Since the complete spectral content of the LO source was unknown, the measurement in Figure 2.6 was repeated but with the step size of the movable FTS arm reduced from $3.8 \times 10^{-4}$ $m$ to $1.5 \times 10^{-4}$ $m$, thereby increasing the sample rate and the measurement range in the

frequency domain to $\sim 1000\ GHz$. This allowed testing of the idea that the spurious tones were indeed caused by under sampling, with the results shown in Figure 2.7. It can be seen from these measurements that the spurious tones present in Figure 2.6 have disappeared which supports the idea that they were caused by aliasing or "frequency folding". However, it is still evident that the LO frequency spectrum is contaminated with multiple harmonics around the LO tuning frequency.

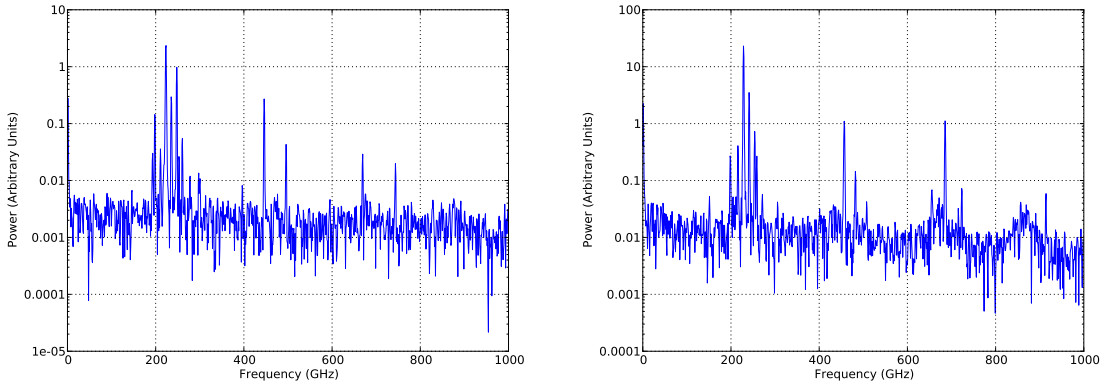


(a) FTS measurement at 223.2 $GHz$ showing a contaminated spectrum with harmonics present around the tuning frequency of the LO.

(b) FTS measurement at 228.6 $GHz$ showing a contaminated spectrum with harmonics present around the tuning frequency of the LO.

Figure 2.7: FTS spectral output at 223.2 and 228.6 $GHz$ using a measurement frequency range of 1000 $GHz$. Both sets of data show highly contaminated spectra but without the spurious tones due to aliasing observed in Figure 2.6. The amplitude of uncertainties is on the scale of the noise floor fluctuation in the measurements, which is clearly visible in each plot.

To try and pinpoint the origin of the harmonics present in the FTS spectrum shown in Figure 2.7, the tripler component was removed and the source tested again on the FTS to see if the harmonics might be originating from the low frequency stage of the LO. The resulting frequency with the tripler removed was $\nu_{LO} = 76.2\ (228.6/3)\ GHz$ and the results can be seen in Figure 2.8.

This measurement was carried out with the sampling frequency set to 1000 $GHz$ to try to eliminate any possibility of confusing alias tones being present in the spectrum. This also meant that the measurement frequency range was 1000 $GHz$ and it can be seen from Figure 2.8(a) that the frequency of the highest signal in the spectrum (the $6^{th}$ harmonic of the 76.2 $GHz$ signal) is 457.2 $GHz$, which is below $f_s/2$. This should mean that all the tones seen in Figure 2.8 are real. A zoomed in version of these results is shown in Figure 2.8(b),

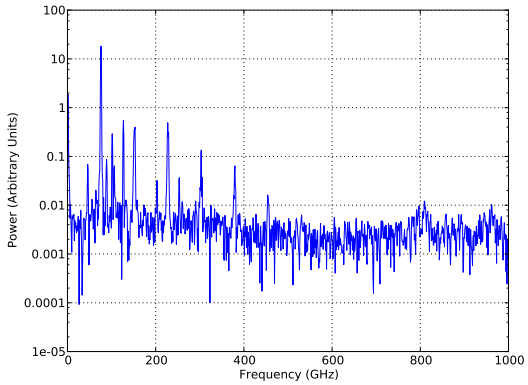


(a) FTS measurement at 76.2 $GHz$ showing multiple tones around the LO frequency but otherwise a clean spectrum.

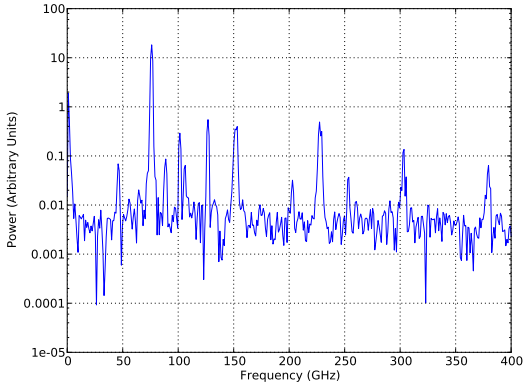


(b) Zoomed in version of the measurement in Figure 2.8(a). Frequency is limited at 400 $GHz$ to give a clearer view of the tones present in the spectrum.

Figure 2.8: FTS spectral output with the LO tripler removed at 76.2 $GHz$ using a measurement frequency range (and sampling rate) of 1000 $GHz$. There are no tones due to aliasing present in these results but harmonics of the fundamental synthesiser frequency are observed in the spectrum. The amplitude of uncertainties is on the scale of the noise floor fluctuation in the measurements, which is clearly visible in each plot.

with the Frequency range limited to 400 $GHz$. It is interesting to see that there are tones present in this spectrum at 76.2 $GHz$ (the signal frequency), $n\times$76.2 $GHz$ (harmonics of the signal frequency) and 46.2/106.2 $GHz$ (the LO sideband harmonics). However, additional tones can also be seen at 88.9, 101.6 and 127.0 $GHz$. These signals correspond to the $7^{\text{th}}$, $8^{\text{th}}$ and $10^{\text{th}}$ harmonics of the fundamental synthesiser input frequency (12.7 $GHz$) and support the idea that the origin of the LO harmonics, such as the ones seen in Figure 2.7 which may be responsible for a degraded SIS receiver sensitivity, is in the intermixing of the fundamental, synthesised input tone within the first, low frequency multiplier stage of the LO.

Following on from these results, an attempt was made to clean up the spectral output of the LO by adding a low-pass filter with a cutoff frequency of $\sim$ 130 $GHz$ after the amplifier, which had been measured to have a transmission of $\sim -25$ $dB$ at 150 $GHz$ and $\sim -65$ $dB$ at 220 $GHz$ (Henry, 2014). This was mainly done as a sanity check on the FTS measurement system to make sure that the spectra it produced from the acquired interferogram data were accurate. The result of an FTS measurement with the addition of the low-pass filter and the LO frequency again set to 76.2 $GHz$ is shown in Figure 2.9.

By comparing these results with the measurements in Figure 2.8(b), it seems that the

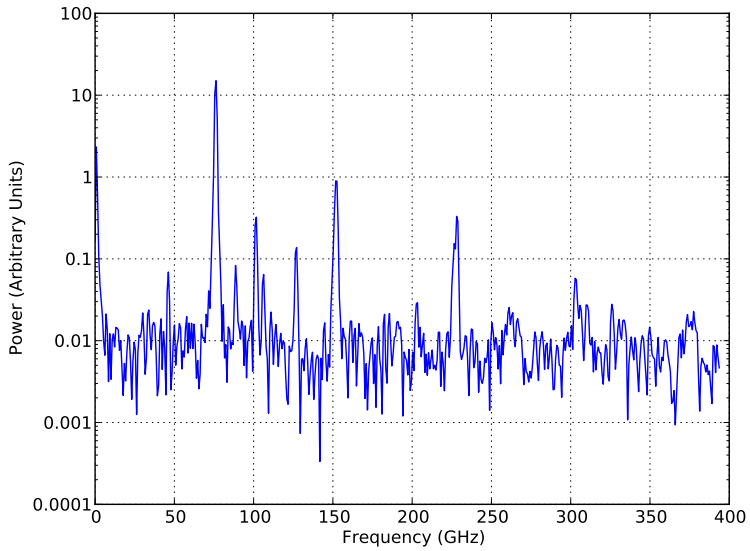


Figure 2.9: FTS spectral output at 76.2 $GHz$ with the LO tripler removed. In addition, a low-pass filter was used after the LO amplifier. The measurement is very similar to the one in Figure 2.8(b) suggesting that the filter had little effect on the tones seen in the spectrum. The amplitude of uncertainties is on the scale of the noise floor fluctuation in the measurement, which is clearly visible in the plot.

addition of the filter had very little effect on the presence of harmonics above 130.0 $GHz$. While the $7^{\text{th}}$ and $8^{\text{th}}$ harmonics of the fundamental synthesiser frequency are still expected to be present, the $2^{\text{nd}}$, $3^{\text{rd}}$ and $4^{\text{th}}$ harmonics of the 76.2 $GHz$ signal ought to have been reduced by the addition of the filter. However, only the amplitude of the $10^{\text{th}}$ harmonic of the fundamental tone (127.0 $GHz$) is significantly lower in Figure 2.9 compared to Figure 2.8(b), while the amplitude of the other tones, especially the one at 152.4 $GHz$ which should have been reduced by the filter, has barely changed.

Given that the addition of the low-pass filter had no significant effect on the presence of tones in the FTS spectrum (as shown in Figure 2.9), an experiment to check the validity of the software that the FTS system was using in order to Fourier Transform the LO signal was carried out. This led to an independent test of the Fourier Transform of the experimentally obtained interferogram using Python's Fast Fourier Transform (FFT) module (SciPy, 2017) as well as a test using a Discrete Fourier Transform (DFT) function that was written by the author. Furthermore, the interferogram acquired by the FTS was itself modelled and Fourier Transformed to check that it would produce peaks at the points seen in the measurements,

thus confirming that the tones observed in the FTS output were indeed present and not a manifestation of a software malfunction. The results of these tests are shown in Figure 2.10. The plot in Figure 2.10(a) shows the FTS FT of the interferogram ($\nu_{LO} = 76.2\ GHz$, no tripler, low-pass filter - same data as in Figure 2.9) as well as the results of the independent FFT/DFT tests carried out. The two sets of data agree very well thus suggesting that the FTS Fourier Transform software is working correctly. The plot in Figure 2.10(b) again shows the FTS FT of the interferogram as well as an FT of an interferogram that was modelled to closely resemble the experimental one acquired by the FTS. Here again the results agree closely suggesting that the interferogram acquired by the FTS does indeed contain the tones seen in its spectral output.

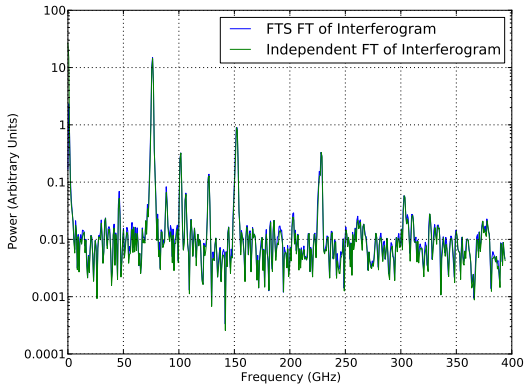


(a) FTS measurement at 76.2 $GHz$ with an overlay of the independent FT results carried out on the experimental interferogram data. Results match very well suggesting that FTS software is working correctly.

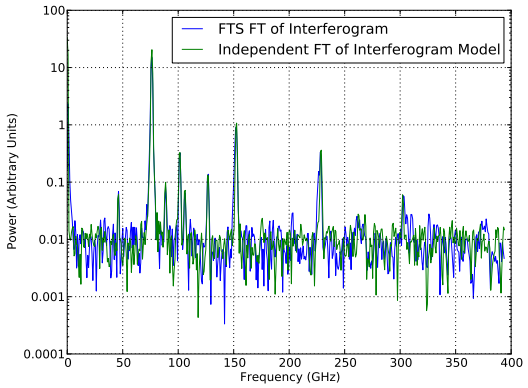


(b) FTS measurement at 76.2 $GHz$ with an overlay of the independent FT results carried out on simulated interferogram data. Good agreement suggesting that the tones seen in the spectral output are present in the interferogram acquired by the FTS.

Figure 2.10: FTS spectral output at 76.2 $GHz$ (no tripler, low-pass filter present) with (a) an independent Fourier Transform of the experimentally obtained interferogram as well as (b) a Fourier Transform of a simulated interferogram that closely matched the experimental data. The amplitude of uncertainties is on the scale of the noise floor fluctuation in the measurements, which is clearly visible in each plot.

These results provided confidence that the FTS software was working correctly and the issue may have been with the filter. However, as this was not the primary purpose of the investigation and the FTS results could now be interpreted reasonably well, the tripler was reinstalled onto the LO and a FTS measurement carried out at 198.0 $GHz$. This was the problematic frequency that produced the highly distorted pumped I-V curve in Figure 2.3(a) and an elevated receiver noise temperature. The result of this measurement is

presented in Figure 2.11 and it can be seen that the spectrum is highly contaminated with harmonics around the LO tuning frequency of 198.0 $GHz$, with most of the tones separated by integer multiples of 11.0 $GHz$, i.e. the fundamental low frequency tone produced by the VCO source. The measurements performed with the LO tripler removed showed that these tones are likely to be generated by the intermixing of the fundamental tone in the low frequency amplifier stage of the LO. The proximity of these harmonics to the LO signal frequency is likely to be responsible for distorted pumped I-V curves, elevated SIS receiver noise temperature measurements and, as will be shown in Section 2.7, confusing spectral artefacts in the IF spectra of SIS mixer experiments.

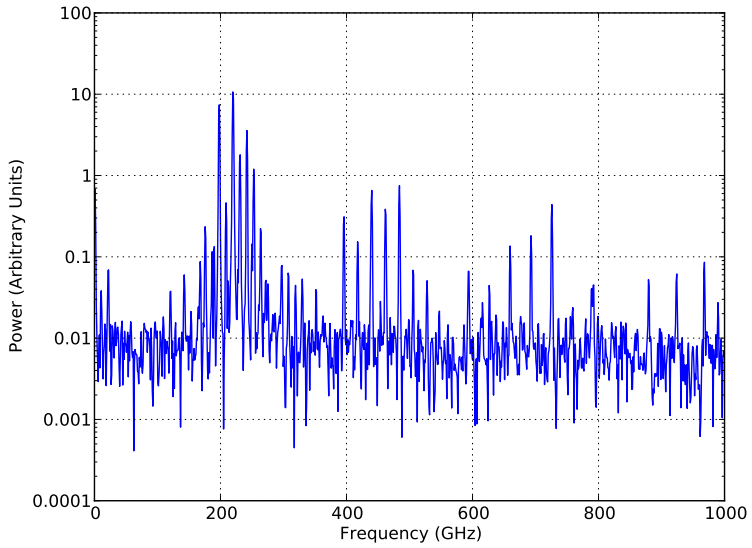


Figure 2.11: FTS spectral output at 198.0 $GHz$ using a measurement frequency range of 1000 $GHz$. The measurement shows a contaminated spectrum with harmonics present at 11.0 $GHz$ intervals around the signal frequency of the LO. The amplitude of uncertainties is on the scale of the noise floor fluctuation in the measurement, which is clearly visible in the plot.

All of the FTS measurements covered in this section provided a strong indication of the presence of unwanted tones in the output signal of the RPG LO. However, in some cases the acquired spectra proved ambiguous to interpret with tone confusion arising from effects such as signal aliasing. Thus, although providing strong evidence of the presence of harmonics, uncertainties in the FTS measurements meant it was worthwhile to check the spectral output of the LO source using an alternative measurement technique.

This led to an approach being taken in which external solid-state mixers, obtained from Radiometer Physics GmbH (RPG), and used in conjunction with a Rhode and Schwarz spectrum analyser, were used to directly measure the LO spectral output. These mixers enabled the direct measurement of frequencies up to 500 $GHz$ and the experiments performed with this configuration are described in more detail in Section 2.4.

## 2.4 Spectrum Analyser Measurements at RAL

The measurements described in this section were carried out with a Rohde & Schwarz FSU26 spectrum analyser. This instrument was used in conjunction with a series of external, solid-state sub-millimetre wave mixers which enabled quick acquisition of spectra across a frequency range of $40 - 500$ $GHz$ without the need to obtain an interferogram or carry out a Fourier Transform. The experimental setup used is shown in Figure 2.12.

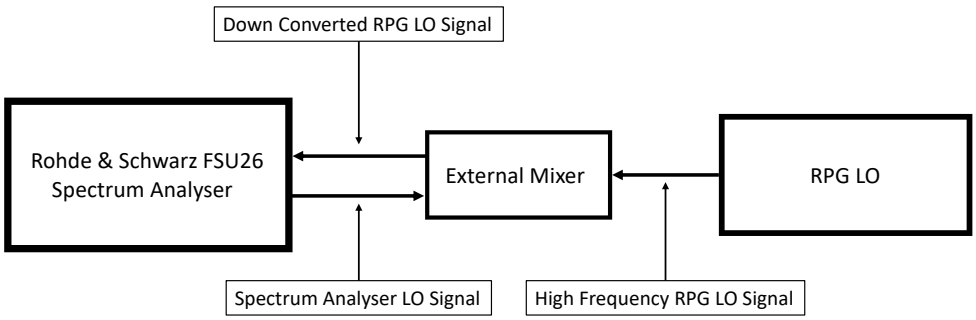


Figure 2.12: Schematic diagram showing the experimental setup used for the Rohde & Schwarz spectrum analyser measurements.

A high frequency signal produced by the RPG LO enters the external mixer via a waveguide flange connection while a signal produced by one of the higher order harmonics of the spectrum analyser's internal LO is coupled to the mixer via a SubMiniature version A (SMA) connector from the other side. The resulting, down converted signal then leaves the mixer via a second SMA port before being processed by the spectrum analyser.

By default, all of the mixer products are displayed. However, down converted signals

from unwanted harmonics of the internal LO can be removed using the "Signal ID" and "Auto ID" functions. Signal ID performs and displays two measurements, one with the LO frequency shifted by 2×IF/Harmonic Number. Any spectral components that are frequency shifted correspond to image products or mixer products from another harmonic. Auto ID identifies these shifted signals and removes them from the display by comparing the difference in amplitude between the two sweeps at every frequency point. If the difference is greater than a specific threshold value, they are removed. This was done for all of the measurements described in this section.

The RPG LO, complete with the frequency tripler, was tested via the spectrum analyser at a frequency of 198.0 $GHz$ and the results are shown in Figure 2.13.

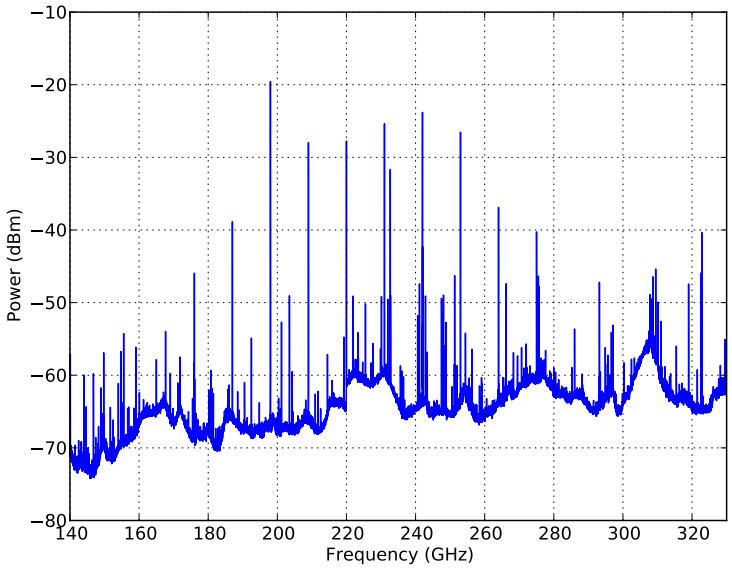


Figure 2.13: Spectrum analyser output at 198.0 $GHz$ using a combination of high frequency external mixers. The measurement shows a contaminated spectrum with large amplitude harmonics present at 11.0 $GHz$ intervals around the signal frequency of the LO.

Examination of this measurement shows that the LO source is indeed producing multiple tones of significant amplitude (within $5 - 10$ $dB$ of the 198.0 $GHz$ signal), which are separated in frequency from the desired 198.0 $GHz$ harmonic by integer multiples of 11.0 $GHz$. It can also be seen that there are more frequency components visible in the spectrum analyser measurement in Figure 2.13 than in the FTS measurement in Figure 2.11. This is because the spectrum analyser is more sensitive and has a higher dynamic range

than the FTS. As such, some of the lower amplitude tones produced at the output of the tripler component of the LO are being lost in the noise floor of the FTS measurement in Figure 2.11 but can be seen more clearly in the spectrum analyser result in Figure 2.13. However, it should also be noted that the the six brightest ($> 30\ dBm$) tones in Figure 2.13 (198.0, 209.0, 220.0, 231.0, 242.0 and 253.0 $GHz$) are also clearly visible in Figure 2.11. This supports the FTS measurement in Figure 2.11 and provides an independent confirmation of the spectrum obtained by the FTS. Furthermore, it will be shown in Section 2.6 that the presence of the additional, large amplitude tones around 198.0 $GHz$ seen in Figures 2.11 and 2.13 is caused by multiple large amplitude tones emanating from the sextupler, which are up converted by the non-linear tripler component of the LO. It is then possible for these tones to enter the SIS mixer input port and contribute to a distorted pumped I-V curve, such as the one shown in Figure 2.3(a).

To verify the hypothesis that the additional tones observed in Figure 2.13 were produced by the low frequency stage of the LO (as suggested by the FTS measurements in Figure 2.8, for example) or whether the tripler component was responsible for the production of the harmonics, a second spectrum analyser measurement was performed with the tripler removed. This experiment was done with two, lower frequency, external mixers while keeping the LO set to $198.0/3 = 66.0\ GHz$. While previous FTS measurements with the tripler removed were carried out with the LO set to $228.6/3 = 76.2\ GHz$, these were based upon the work of another student that had previously measured the RPG LO on the FTS at that frequency (Zhou, 2013) while the author of this thesis was primarily concerned with investigating the behaviour of the LO at 198.0 $GHz$, which produced the distorted pumped I-V curve shown in Figure 2.3(a), a significantly elevated receiver noise temperature at that frequency and highly contaminated LO output spectra as seen both in the FTS measurement in Figure 2.11 as well as the spectrum analyser measurement in Figure 2.13. This has, in effect, already been explained in the main narrative text of this chapter but is being emphasised here to avoid any potential confusion or ambiguity. As such, the spectrum analyser measurement of the RPG LO with the tripler component removed was carried out at a frequency of $198.0/3 = 66.0\ GHz$. The result can be seen in Figure 2.14.

If the tripler was the component solely responsible for the unwanted harmonics, then the

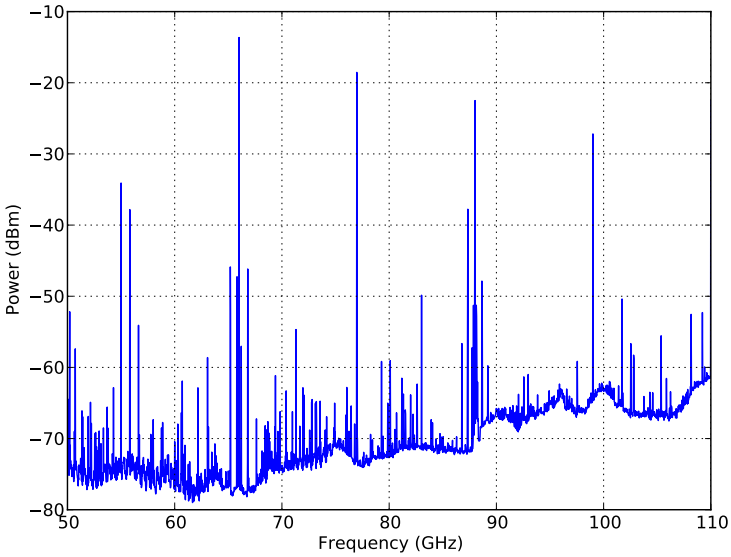


Figure 2.14: Spectrum analyser output at 66.0 $GHz$, with the LO tripler removed using a combination of external mixers. Similar to Figure 2.13, the result shows a contaminated spectrum with large amplitude harmonics present at 11.0 $GHz$ intervals around the signal frequency of the LO.

plot in Figure 2.14 would show a tone centred at 66.0 $GHz$, and no other significant tones. However, again there is evidence of harmonics around 66.0 $GHz$ separated in frequency by integer multiples of 11.0 $GHz$, which is the fundamental frequency going into the sextupler from the VCO source. This result demonstrates that intermixing of the fundamental tone takes place in the sextupler and leads to the production of undesired harmonics which are separated by integer multiples of the fundamental frequency.

This is further shown by the fact that it is possible to pump an SIS mixer with the signal synthesiser set to a particularly low fundamental frequency of 6.9 $GHz$. This is interesting because $6.9 \times 6 = 41.4$ $GHz$, which is just above the waveguide cut off (40 $GHz$) of the amplifier but quite far outside of its range of operation ($75 - 110$ $GHz$). Even so, if the 41.4 $GHz$ tone had enough power to pump the mixer, it would be 124.2 $GHz$ by the time it was tripled which is well below the mixer's frequency band of operation. The fact that it is possible to pump the SIS mixer with the signal synthesiser set to 6.9 $GHz$ suggests that the LO is producing higher order harmonics and these are consequently pumping the mixer. To test whether the LO was indeed producing such tones when set to a fundamental frequency of 6.9 $GHz$, it was tested on the spectrum analyser using external mixers over

the frequency range of $40 - 110\ GHz$ and with the tripler removed. The results of this measurement can be seen in Figure 2.15.

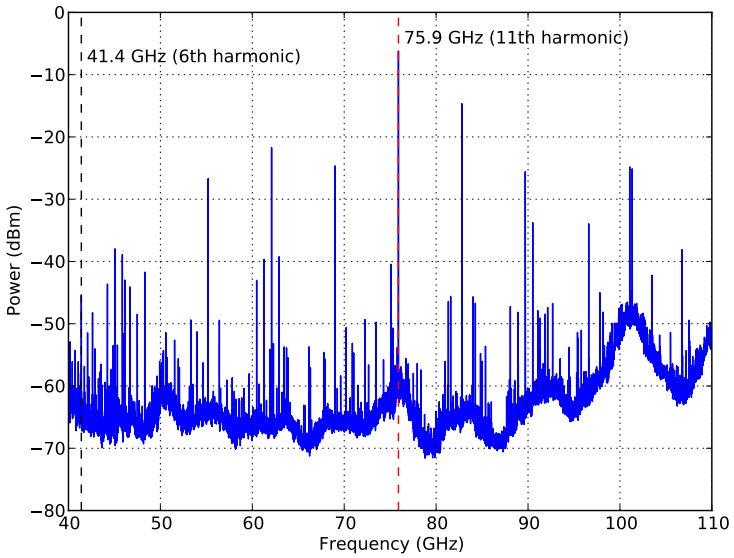


Figure 2.15: Spectrum analyser measurement between $40 - 110\ GHz$. LO set to 41.4 $GHz$ with the tripler removed. Tones separated by multiples of 6.9 $GHz$ are believed to result from the low frequency multiplication chain of the LO.

It is evident from Figure 2.15 that the desired tone of 41.4 $GHz$ (the $6^{\text{th}}$ harmonic of the fundamental) is quite low with an amplitude of $\sim -45\ dBm$. The $11^{\text{th}}$ harmonic however, at 75.9 $GHz$, has an amplitude of $\sim -7\ dBm$ and this is the tone which is most likely pumping the mixer. Additionally, it is worth noting that the entire spectrum is contaminated with harmonics separated by 6.9 $GHz$ which, once again, shows that undesired tones are being generated by the sextupler before being amplified (if within the operating band of the amplifier) and tripled.

The spectrum analyser measurements described in this section demonstrate that the spectral content of the RPG LO is highly contaminated with large amplitude harmonics that originate in the low frequency multiplier of the LO. These results support the initial FTS investigations carried out and the presence of the additional tones can lead to confusing spectral artefacts as well elevated SIS receiver noise temperatures. Given that these unwanted tones were present when the LO was being driven with a VCO source, measurements of SIS receiver noise temperature were also carried out using a more stable, YIG oscillator. The results of these tests are briefly outlined in Section 2.5.

## 2.5 YIG Oscillator Measurements

A Yttrium Iron Garnet (YIG) Oscillator is a type of microwave frequency signal generator that provides very low phase noise, multi-octave frequency tuning as well as excellent tuning linearity (Micro Lambda Wireless Inc., 2018).

Such a generator contains a YIG "sphere" that is manufactured from a synthesised YIG crystal. A YIG crystal is grown in a process similar to silicon but once fabricated it must further be diced, tumbled, ground and polished in order to produce a small sphere, $\sim 0.5\ mm$ in diameter.

For applications such as an oscillator, the YIG sphere is mounted on the end of a thermally conductive rod (typically made of Beryllium) which acts as a tuning stick for orienting the YIG sphere in its resonant circuit. As well as this, the rod works as a thermal conductor connected to a proportional heater which keeps the YIG sphere at a constant temperature, as its frequency stability is temperature dependent.

The ferrite properties of the YIG crystal mean that it resonates at microwave frequencies when placed in a DC magnetic field. This resonance is directly proportional to the strength of the magnetic field and increases at a rate of 2.8 $MHz$ per Gauss of applied field (Castetter, 2018). The magnetic field can be generated by an electromagnet and "tuned" using a variable current. By increasing the current, the strength of the magnetic field is increased along with the frequency of resonance of the YIG sphere. This relationship continues until the structure magentically saturates which limits the upper frequency that can be generated using a YIG based system. Oscillators with upper frequencies in excess of 50 $GHz$ have been produced but given the commercial availability of inexpensive frequency doublers, YIG oscillator manufacturers have discontinued fundamental oscillators above 26.5 $GHz$ (Micro Lambda Wireless Inc., 2018).

A coupling structure, or "coupling loop", is added around the YIG sphere to couple RF energy and form a high Q microwave tank circuit. This allows the system to be used as a low phase noise signal generator for microwave and sub-mm applications.

For the experiments covered in this section, an MLSP-8020 YIG based oscillator (purchased from Micro Lambda Wireless Inc.) was used to supply the RPG LO with a fun-

damental input signal. The aim was to compare the SIS receiver performance when the RPG LO was driven using either the YIG source or an Anritsu MG3692B $2 - 20\ GHz$ VCO thereby testing whether the superior phase noise provided by the YIG would have an impact on the noise temperature of the receiver or the spectral purity of the RPG LO.

The power output of the YIG was initially checked to make sure it could provide enough power to drive the LO across its frequency range of operation, between $8 - 20\ GHz$. This was done using an Anritsu ML2487A power meter connected to the RF output of the YIG and the results are presented in Figure 2.16.

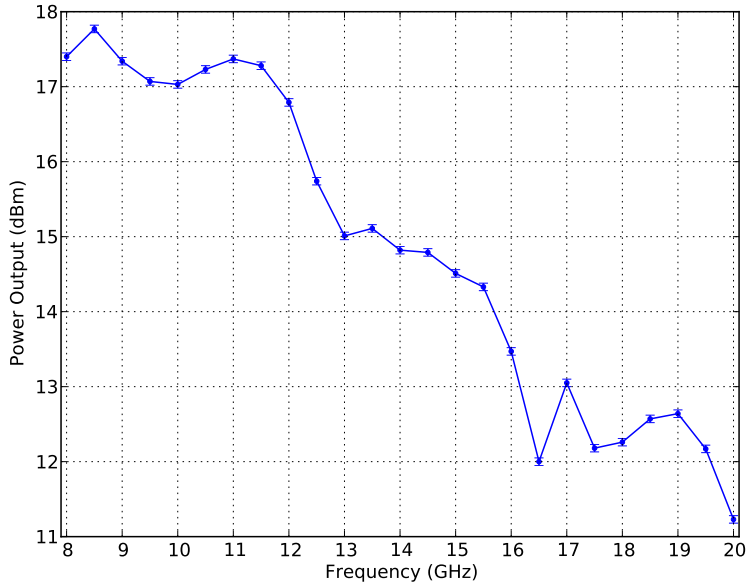


Figure 2.16: Output Power of the MLSP-8020 YIG Oscillator between $8 - 20\ GHz$.

Since the YIG source produced at least $+11\ dBm$ of power across its operating frequency range (which is more than adequate to drive the RPG LO), noise temperature measurements were carried out between $190.0 - 260.0\ GHz$ in $5.0\ GHz$ steps, with the additional inclusion of the problematic frequency of $198.0\ GHz$ and $228.6\ GHz$ which had previously been tested on the FTS.

These measurements were carried out in the Superconducting Detectors Group laboratory at Oxford using a measurement setup as shown in Figure 2.1(a). The signal generator providing the low frequency input tone into the sextupler of the RPG LO was swapped around between the YIG and the Anritsu VCO while all other experimental parameters

were kept the same. A comparison of the results when using the two different signal generators is shown in Figure 2.17.

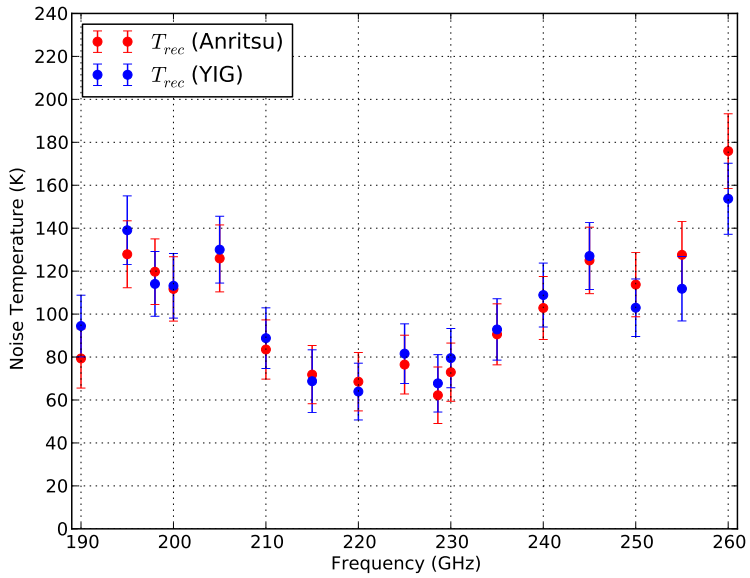


Figure 2.17: Measured SIS receiver noise temperature when using the Anritsu MG3692B VCO and YIG MLSP-8020 signal generator to drive the RPG LO. It can be seen that the receiver performance does not change significantly between the two signal generators. Errors in the results have been propagated by assuming a 10 % uncertainty on the physical temperature of the 77 $K$ cold load.

The measurements presented in Figure 2.17 show that while the Anritsu VCO gives slightly better performance at the lower end of the frequency range (190.0, 195.0 $GHz$) and the YIG is slightly better at the higher frequency end ($250.0 - 260.0$ $GHz$), across the majority of the frequency range tested there is no significant change in receiver performance when using the two different signal generators.

Therefore, it can be concluded that using a low phase noise, YIG based signal generator to drive the RPG LO does not have a significant effect on the SIS receiver performance in this particular case. This result further supports the fact that the unwanted harmonics observed in the FTS and spectrum analyser measurements are indeed produced by the low frequency stage of the LO and are independent of the LO's input signal generator.

## 2.6 The Consequences of Unwanted Harmonic Content in Heterodyne Mixing

The combination of FTS and spectrum analyser measurements presented in this chapter so far has shown that the sextupler unit in the RPG LO generates not only the desired $6^{\text{th}}$ harmonic of the fundamental input frequency, but also a number of additional, large amplitude harmonics such as the $5^{\text{th}}$, $7^{\text{th}}$, $8^{\text{th}}$ and $9^{\text{th}}$. This, in turn, results in a number of large amplitude signals entering the tripler component, separated in frequency by the fundamental tone from the signal generator. It is therefore interesting to consider the expected behaviour at the output of the tripler under these conditions to see if it correlates with the observed results in Figure 2.13, for example. The following harmonic frequency generation analysis is based on Maas (1988) and begins by modelling the tripler as a non-linear component with a current-voltage ($I$-$V$) characteristic given by a power series as

$$I = aV + bV^2 + cV^3 \tag{2.3}$$

where $a$, $b$ and $c$ are constant, real coefficients and $V$ is the excitation voltage applied to the device. It can be assumed that $V$ is a time-varying, two-tone excitation of the form

$$V = v(t) = V_1 \cos(\omega_1 t) + V_2 \cos(\omega_2 t) \tag{2.4}$$

where $\omega_1$ and $\omega_2$ correspond to the angular frequencies of the first and second excitation tones, respectively. While, in the example that will be considered here, up to five tones may be responsible for driving the tripler simultaneously, it will be shown that the expected harmonic content at the output of the tripler can be obtained using a combination of two-tone pairs of frequencies at a time. Hence, the excitation voltage in Equation 2.4 has been modelled as a two-tone signal. By substituting Equation 2.4 into 2.3, the first term of the tripler output current becomes

$$i_a(t) = av(t) = aV_1 \cos(\omega_1 t) + aV_2 \cos(\omega_2 t). \tag{2.5}$$

Doing the same for the second term of Equation 2.3 and applying commonly-used trigonometric formulae for the squares and products of cosines, the quadratic term of the current becomes

$$\begin{aligned} i_b(t) &= bv^2(t) \\ &= \frac{1}{2}b\Big\{V_1^2 + V_2^2 + V_1^2\cos(2\omega_1 t) + V_2^2\cos(2\omega_2 t) \\ &\quad + 2V_1V_2[\cos((\omega_1+\omega_2)t) + \cos((\omega_1-\omega_2)t)]\Big\} \end{aligned} \tag{2.6}$$

while expansion of the third, cubic, term of the current in 2.3 leads to

$$\begin{aligned} i_c(t) = cv^3(t) = \frac{1}{2}c\Big\{&V_1^3\cos(3\omega_1 t) + V_2^3\cos(3\omega_2 t) \\ &+ 3V_1^2V_2[\cos((2\omega_1+\omega_2)t) + \cos((2\omega_1-\omega_2)t)] \\ &+ 3V_1V_2^2[\cos((2\omega_2+\omega_1)t) + \cos((2\omega_2-\omega_1)t)] \\ &+ 3(V_1^3 + 2V_1V_2^2)\cos(\omega_1 t) \\ &+ 3(V_2^3 + 2V_1^2V_2)\cos(\omega_2 t)\Big\}. \end{aligned} \tag{2.7}$$

The total tripler output current is therefore given by the sum of Equations 2.5−2.7 and it can be seen that frequency components are present at multiples of $\omega_1$, $\omega_2$, the sum and difference of $\omega_1$ and $\omega_2$ and also at frequencies corresponding to $2\omega_1 \pm \omega_2$ and $2\omega_2 \pm \omega_1$ as illustrated by the second and third lines of Equation 2.7. By considering the case where the fundamental frequency going into the RPG LO from the signal generator is set to 11 $GHz$, it has been experimentally shown (in Figure 2.14) that the output of the sextupler contains large amplitude tones not only at 66 $GHz$, but also at 55, 77, 88 and 99 $GHz$ as well. Since this is a broadband LO, designed to operate between $\sim 180 - 270$ $GHz$, the input of the tripler must be sensitive to frequencies in the $60 - 90$ $GHz$ range at least, with some fraction of the 55 and 99 $GHz$ harmonics likely driving the component as well. Thus, with reference to the frequency terms derived in Equations 2.5−2.7, it is actually possible to determine a number of the brightest tones generated at the high frequency output of the tripler, as seen in Figure 2.13. These are presented in Table 2.1 which, for every output frequency generated, shows the possible mixing term(s) from Equations 2.5−2.7 that can produce that frequency, as well as the pair of input tones required for that output.

| LO Output Frequency ($GHz$) | Possible Mixing Terms and Pair of Input Frequencies Required | | | |
|---|---|---|---|---|
| | $55,66\ GHz$ | $66,77\ GHz$ | $77,88\ GHz$ | $88,99\ GHz$ |
| 176 | $2\omega_1 + \omega_2$ | – | $2\omega_2$ | $2\omega_1$ |
| 187 | $2\omega_2 + \omega_1$ | – | – | $\omega_1 + \omega_2$ |
| 198 | $3\omega_2$ | $3\omega_1$ | – | $2\omega_2$ |
| 209 | – | $2\omega_1 + \omega_2$ | – | – |
| 220 | – | $2\omega_2 + \omega_1$ | – | – |
| 231 | – | $3\omega_2$ | $3\omega_1$ | – |
| 242 | – | – | $2\omega_1 + \omega_2$ | – |
| 253 | – | – | $2\omega_2 + \omega_1$ | – |
| 264 | – | – | $3\omega_2$ | $3\omega_1$ |
| 275 | – | – | – | $2\omega_1 + \omega_2$ |

Table 2.1: A selection of the brightest LO output harmonics, as seen in the spectrum in Figure 2.13, with the LO nominally set to 198 $GHz$. The possible mixing terms that can generate these harmonics given a particular pair of input frequency tones are also presented.

While the list of mixing possibilities and input tone combinations in Table 2.1 is not exhaustive, it neatly illustrates how the large amplitude harmonic spectrum observed in Figure 2.13 can be predictably generated using a number of possible mixing products derived in Equations 2.5−2.7. The results show that the expected output spectral content of the LO tripler will include the presence of harmonic tones around the desired frequency of 198 $GHz$, separated by the fundamental LO input tone of 11 $GHz$ if such tones are also present at the tripler input. This is exactly the behaviour that is observed. Thus, it can be concluded that the tripler is operating as expected and the main problem with this LO is the harmonic content of the low frequency, $\times 6$ multiplier stage which leads to unwanted tones that are present (and within the input sensitivity range of the tripler) mixing with one another as well as being up converted, resulting in a contaminated spectrum at the high frequency output of the LO. Similarly, if multiple large amplitude LO signals are incident on an SIS mixer, for example, they can down convert not only one another into the IF spectrum, but also result in the down conversion of the same spectral "test" line multiple times, leading to the presence of a number of confusing IF tones. This will be experimentally explored and demonstrated in the following section.

## 2.7 Multiple Tone Down Conversion

It has been shown by the various experimental investigations described in this chapter that at certain frequencies, the spectral content of the RPG LO used to pump an SIS heterodyne receiver system is highly contaminated with large amplitude harmonics. These additional signals are separated from the LO tuning frequency by the frequency of the fundamental tone used to drive the LO and can be generated via the frequency up conversion process described in the previous section.

It was postulated that as well as contributing to a degraded receiver sensitivity, these harmonics may be getting down converted into the IF spectrum of the receiver, along with the desired high frequency RF signal. Furthermore, if the harmonics are of sufficient amplitude, i.e. strong enough to pump the SIS mixer, then they may also down convert RF spectral features to the IF band and cause them to appear multiple times in the IF spectrum, at frequencies that correspond to the difference between the RF feature and the LO harmonic responsible for the down conversion. The observed effect would be similar to pumping an SIS mixer with two pure LOs, separated in their output frequency by one of the fundamental input tones from the low frequency signal generator. This idea is graphically illustrated in Figure 2.18.

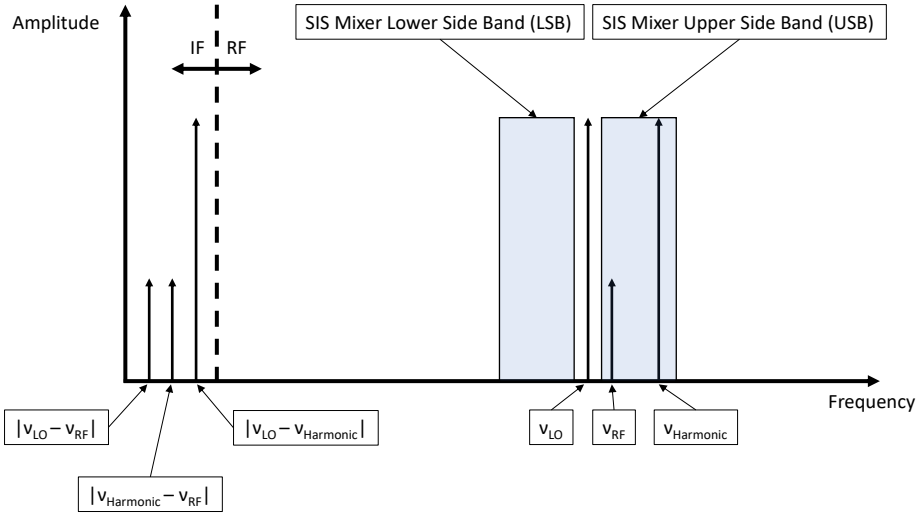


Figure 2.18: An illustration showing how LO harmonics can down convert RF signals into the IF band, thereby introducing confusing tones into the IF spectrum of an SIS mixer.

The diagram in Figure 2.18 shows two LO tones; the desired LO signal at frequency $\nu = \nu_{LO}$ and a large amplitude harmonic at $\nu = \nu_{Harmonic}$ down converting an RF spectral line at $\nu = \nu_{RF}$ into the IF band multiple times. As a result, tones can be seen in the IF spectrum at $\nu = |\nu_{LO} - \nu_{RF}|$, $\nu = |\nu_{Harmonic} - \nu_{RF}|$ and $\nu = |\nu_{LO} - \nu_{Harmonic}|$. The latter two of these would not be present if the mixer were pumped with a spectrally pure LO. By this method, a contaminated LO signal could, in theory, lead to confusing tones arising in the IF spectral output. The experiments described in this section were set up to investigate whether such a scenario would indeed be possible in reality.

To begin with, the SIS mixer was biased at a bias voltage $V_{b\,Mixer} = 2.26\ mV$ which corresponds to the location of the first photon step in the pumped I-V curve and the highest mixer sensitivity. The RPG LO was used to pump the system which was set up as in Figure 2.1(a), with the IF output of the receiver displayed on an Anritsu MS2665C model spectrum analyser. The frequency of the LO input signal was then varied in 0.1 $GHz$ steps while the IF spectral output was carefully monitored. It was found that the majority of the frequencies tested contained a tone in the IF spectrum at the position equal to the frequency of the fundamental LO input tone. A selection of the results obtained is presented in Figure 2.19.

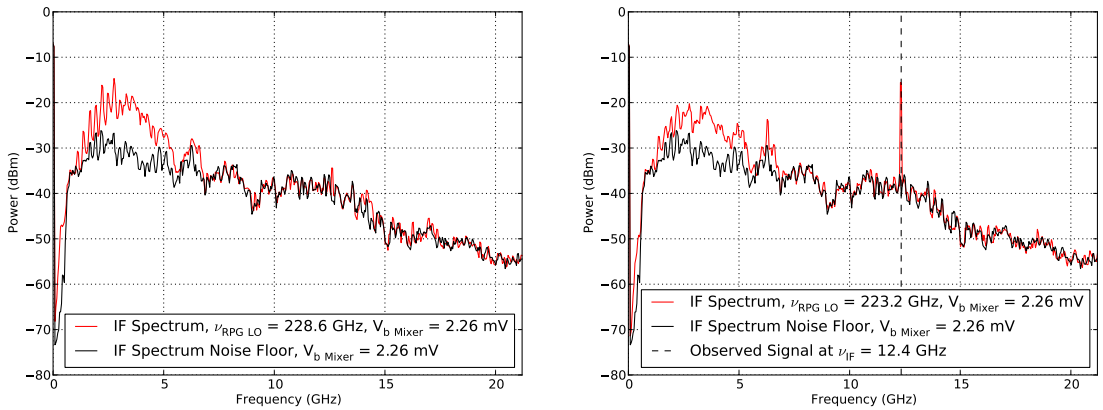


(a) SIS mixer IF spectrum with the RPG LO set to 228.6 $GHz$. The spectral output is clean, with no signals higher than the IF noise floor above $\sim 6.0\ GHz$. The IF signal between $1.0 - 6.0\ GHz$ corresponds to the ambient black-body radiation in the lab that has been down converted to the IF band by the SIS mixer.

(b) SIS mixer IF spectrum with the RPG LO set to 223.2 $GHz$. As well as the down converted black-body radiation, the spectral output contains a signal at 12.4 $GHz$ which is equal to the fundamental frequency tone being used to drive the LO. This is due to a higher order LO harmonic being converted down into the IF band.

Figure 2.19: SIS mixer IF spectral output with the RPG LO set to 228.6 and 223.2 $GHz$.

Figure 2.19(a) shows one of the cleanest IF spectra acquired, when the LO was tuned to 228.6 $GHz$ (12.7 $GHz \times 18$), while Figure 2.19(b) displays a more typical spectrum that contains a signal in the IF band at 12.4 $GHz$ which, in this case, was the frequency of the fundamental tone driving the LO (12.4 $GHz \times 18 = 223.2$ $GHz$).

The presence of a tone at 12.4 $GHz$ in Figure 2.19(b) can be interpreted as an LO harmonic (separated by 12.4 $GHz$ from the LO tuning frequency of 223.2 $GHz$) that has been down converted by the SIS mixer to the IF band, as shown by the presence of a large amplitude harmonic in the IF part of Figure 2.18. This result further demonstrates the fact that the RPG LO is contaminated with harmonics that can be detrimental to receiver performance.

Another similar result, showing a strong peak in the IF spectrum at 11.5 $GHz$, was obtained with the RPG LO set to 207.0 $GHz$ (11.5 $GHz \times 18$). The mixer was once again biased on the first photon step, where it was pumped by the LO. To check that the tone observed was indeed the result of mixer down conversion, the SIS mixer was biased at 0.0 $mV$ while the LO remained powered on. The results of this measurement are shown in Figure 2.20.

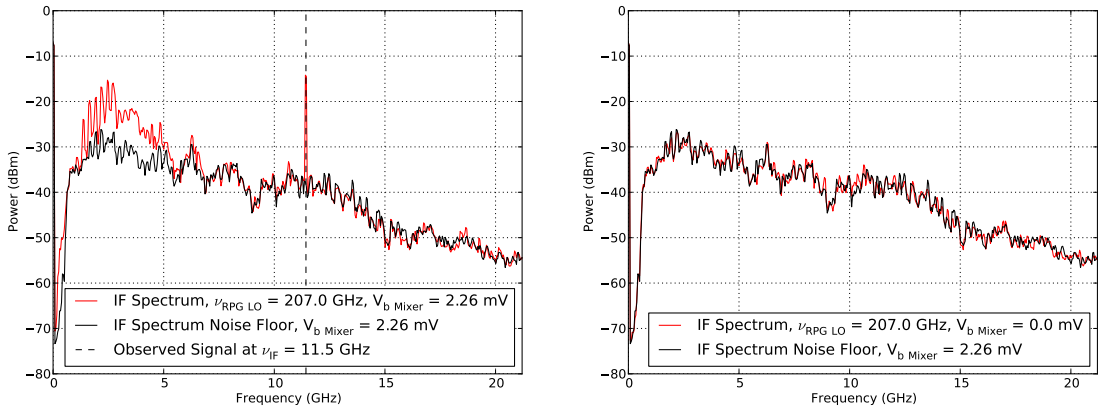


(a) SIS mixer IF spectrum with the RPG LO set to 207.0 $GHz$. The spectral output contains a high amplitude tone at 11.5 $GHz$ when the mixer is biased at 2.26 $mV$.

(b) SIS mixer IF spectrum with the RPG LO set to 207.0 $GHz$. The output tends towards the IF noise floor when the mixer is biased at 0.0 $mV$ and the tone present in Figure 2.20(a) is no longer observed.

Figure 2.20: SIS mixer IF spectral output with the RPG LO set to 207.0 $GHz$ and the mixer biased at $V_{b\,Mixer} = 2.26$ and 0.0 $mV$.

Similar to the IF spectral output in Figure 2.19(b), the spectrum in Figure 2.20(a) shows a strong tone at 11.5 $GHz$ with the SIS mixer biased at $V_{b\,Mixer} = 2.26$ $mV$. When the

mixer is effectively switched off however, i.e. $V_{b\,Mixer} = 0.0\ mV$, the tone disappears and the amplitude of the down converted RF spectrum (red line) tends towards the IF spectrum noise floor which is shown in black. This implies that the tone at 11.5 $GHz$ comes from the mixer output and is the result of down conversion, suggesting that it was originally a high frequency harmonic.

While it is already interesting to observe LO harmonics in the IF spectrum of an SIS mixer based heterodyne receiver when the RPG LO is used to pump the mixer, a further experiment was carried out to test whether it would be possible to down convert an RF signal multiple times into the IF band using the LO signal frequency and one of its harmonics, as outlined in Figure 2.18. This experiment was set up with the RPG LO pumping the mixer and a second, spectrally pure, Gunn diode based LO (Gunn, 1963) acting as a source of RF radiation to emit a low amplitude signal at a carefully selected frequency. This experimental setup is shown in Figure 2.21, with the Gunn LO replacing the hot/cold black-body load typically used in heterodyne receiver noise temperature measurements.

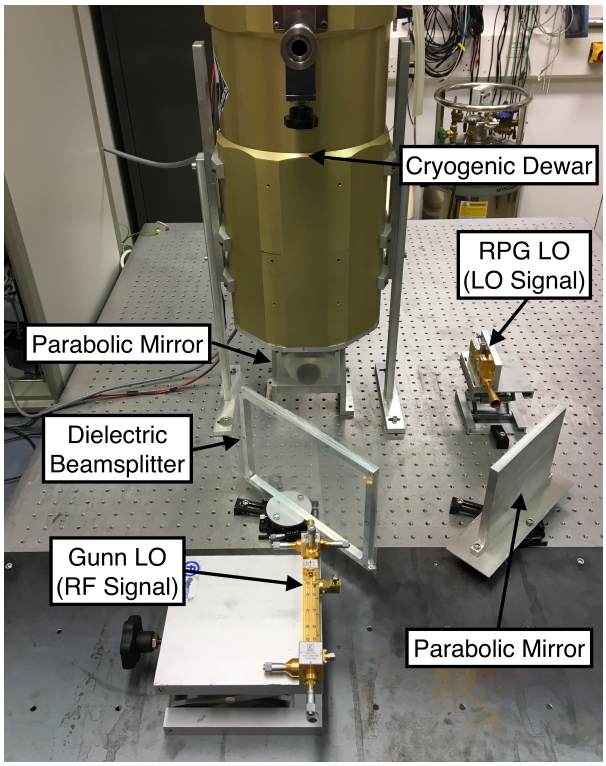


Figure 2.21: Experimental setup showing a Gunn diode based LO being used as a source of RF radiation to down convert signals of a known frequency into the IF band when the SIS mixer is being pumped using the RPG LO.

Using the setup shown in Figure 2.21, the mixer was initially pumped with the RPG LO set to 228.6 $GHz$ because this was one of the cleanest frequencies, as shown in Figure 2.19(a). The Gunn LO was set to 234.2 $GHz$, with an amplitude such that it did not pump the SIS mixer when the RPG LO was switched off. The IF spectral output was then viewed on the spectrum analyser and the result can be seen in Figure 2.22.

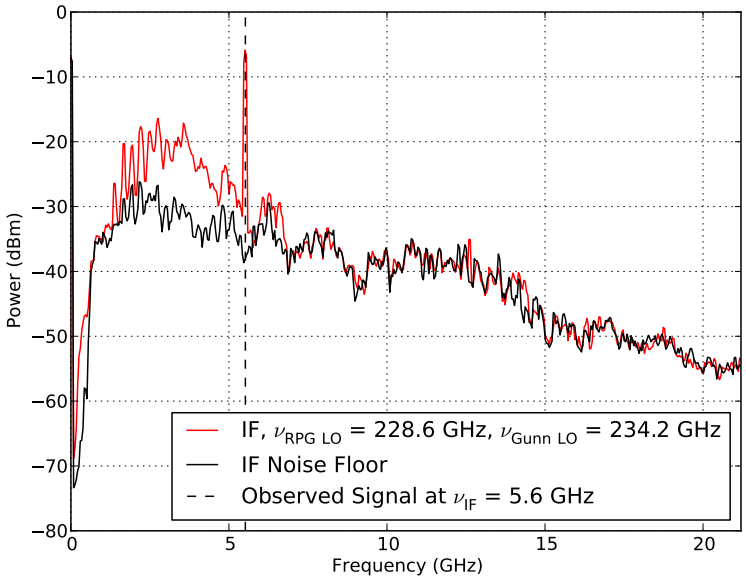


Figure 2.22: SIS mixer IF spectrum with the RPG LO set to 228.6 $GHz$ and the Gunn LO set to 234.2 $GHz$. The spectral output contains a tone at 5.6 $GHz$ when the mixer is biased at 2.26 $mV$, which is equal to the frequency difference of the two LOs.

As well as the down converted, ambient black-body radiation in the lab, the IF output shown in Figure 2.22 contains a tone at $\nu_{IF} = 5.6\ GHz$ which corresponds to the difference between the RPG LO signal frequency and the the frequency of the Gunn ($|\nu_{LO} - \nu_{RF}|$). The fact that there are no other tones present in this spectrum shows that, in this case, the receiver is operating as desired since the RPG LO is spectrally pure at 228.6 $GHz$.

Following this result, the RPG LO was set to 207.0 $GHz$ (11.5 $GHz \times 18$) which was one of the frequencies that contained a strong, additional tone in the IF spectrum at 11.5 $GHz$ when the SIS mixer was pumped using only the RPG LO, as shown in Figure 2.20(a). Meanwhile the Gunn LO was set to 215.6 $GHz$ and the IF spectrum in the presence of both sources at these frequencies is shown in Figure 2.23.

The IF spectrum shown in Figure 2.23 contains large amplitude tones at $\nu_{IF} = 2.9$, 8.6

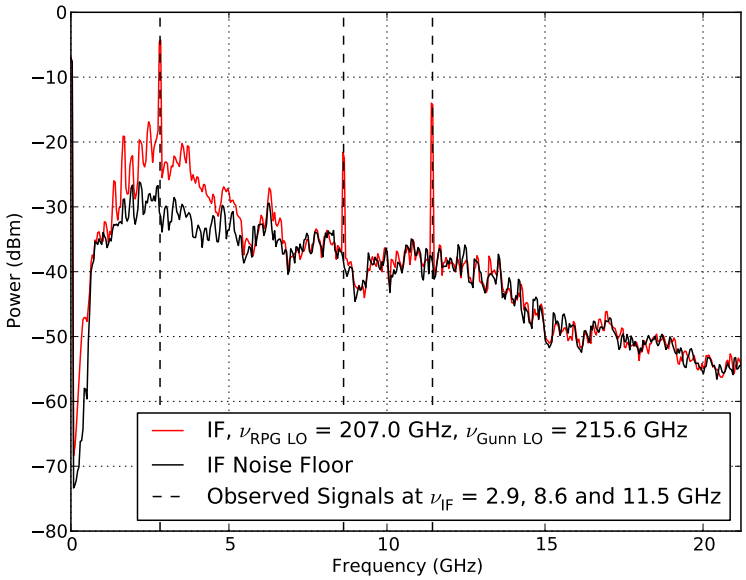


Figure 2.23: SIS mixer IF spectrum with the RPG LO set to 207.0 $GHz$ and the Gunn LO set to 215.6 $GHz$. The spectral output contains tones at 2.9, 8.6 and 11.5 $GHz$ when the mixer is biased at 2.26 $mV$. These tones correspond to the frequency difference of the two LOs (8.6 $GHz$), the frequency difference of the Gunn LO and the 218.5 $GHz$ harmonic of the RPG LO (2.9 $GHz$) and the frequency difference of the RPG LO signal and the 218.5 $GHz$ harmonic (11.5 $GHz$).

and 11.5 $GHz$. The 8.6 $GHz$ signal corresponds to the difference between the frequency of the Gunn source (215.6 $GHz$) and the tuned frequency of the RPG LO (207.0 $GHz$) while the tone at 2.9 $GHz$ is equal to the difference between the Gunn and a frequency of 218.5 $GHz$ (207.0 + 11.5 $GHz$), which is a higher order harmonic of the RPG LO. Furthermore, a tone at 11.5 $GHz$ is also present in the IF spectrum, showing that it is possible for an SIS mixer to down convert large amplitude LO harmonics into the IF band, if they are within the frequency sensitivity range (sideband) of the mixer. This result is interesting as it shows that it is possible for an RF signal to be down converted multiple times into the IF band of an SIS mixer based heterodyne receiver system when it is pumped with a spectrally impure LO. The results of these measurements support the original idea shown schematically in Figure 2.18 and the described effect can lead to various detrimental aspects of receiver performance such as a reduced sensitivity, distorted pumped I-V curves (as seen in Figure 2.3(a)) and confusing down converted tones appearing in the IF spectrum of the receiver.

## 2.8 Conclusions

The harmonic content of LOs affects receiver performance in terms of both noise and spectral output and requires careful consideration and evaluation. The work described in this chapter has, by way of demonstration, investigated the generation of harmonics in a commercially available, coherent, millimetre-wave LO source that is used to pump an SIS mixer in the frequency range of $\sim 190 - 260\ GHz$.

It has been shown that the generation of unwanted harmonics does not occur primarily in the final LO frequency multiplication stage, but actually comes from the spectral impurity of the low frequency multiplier chain, i.e. the sextupler unit also produces significant power at signals corresponding to the $5^{\text{th}}$, $7^{\text{th}}$, $8^{\text{th}}$ and $9^{\text{th}}$ harmonics, in addition to the desired $6^{\text{th}}$ tone. Further evidence indicating a problem with the suxtupler, rather than the fundamental signal generator for example, was given by the fact that there was no significant change in receiver noise temperature performance when the VCO source, that is normally used to drive the LO, was replaced with a YIG oscillator which provides a highly stable input tone with low phase noise characteristics.

As well as this, it has been shown that when an SIS mixer is pumped with a spectrally impure LO, it is possible to down convert high frequency RF signals multiple times into the IF band which can cause spectral lines to appear at multiple locations in the IF spectrum, resulting in the presence of highly confusing signals.

This chapter has therefore highlighted the importance of understanding the spectral content of LOs not only in terms of the effect on receiver noise temperature, but also in terms of how LO sources which produce multiple, large amplitude harmonics at their output that lie within the sideband sensitivity of an SIS mixer can impact the IF output band of the receiver. This is particularly important when corresponding receiver systems are employed for spectroscopic astronomical observations.

# Chapter 3

# Terahertz Frequency Feed Horns

## 3.1 Introduction

The feed horn antenna is a highly important component in astronomical receivers operating in the millimetre/sub-millimetre regime because the properties of the horn determine how well astronomical signals couple into the receiver. Traditionally, corrugated feed horns have been the preferred choice for use as high quality astronomical feeds (Clarricoats & Olver, 1984). Such horns contain azimuthal corrugations within the interior of the horn which present isotropic surface boundary conditions to the propagating electric and magnetic field wavefronts. This suppresses unwanted waveguide modes and results in the propagation of a hybrid $HE_{11}$ mode (Olver et al., 1994) which leads to corrugated feed horns exhibiting excellent antenna beam patterns with low levels of cross-polarisation and sidelobes over a wide frequency bandwidth ($\sim 50\,\%$). The issue with such feeds however, is that because they require multiple corrugations ($\sim 5$) per wavelength to function, they become increasingly more difficult, time consuming and expensive to fabricate at higher frequencies, particularly in the Terahertz (THz) range. This may not be a significant problem for telescopes that employ a single pixel receiver but for new facilities which hope to use multi-pixel focal plane array receiver systems containing between $10 - 10000$ individual feeds, the challenge of fabricating horns robustly could quickly become a serious concern.

A solution to this problem can be achieved by using a smooth-walled, multiple flare-angle-discontinuity horn design which helps to overcome the fabrication issues posed by

corrugated horns at high frequencies. The fact that these horns do not contain any corrugations in their interior means that they do not have to be made using time consuming electroforming processes but can instead be fabricated much more quickly and effectively using a simpler direct machining technique. When carefully designed, these horns can provide an operational bandwidth of $\sim 20$ % which makes them viable alternatives to corrugated feeds at THz frequencies.

Feeds with a flare-angle-discontinuity near the throat of the horn will excite a higher order $TM_{11}$ mode, in addition to the incident $TE_{11}$ mode. This resultant "dual mode" then propagates through the rest of the horn, the length of which is chosen such that the two modes arrive in phase at the aperture. This leads to a highly uniform aperture field distribution and results in sidelobe cancellation and low cross-polarisation in the far-field radiation pattern.

In general, horns with a single discontinuity have a limited operational bandwidth of $\sim 10$ %. However, previous work (Yassin et al., 2007; Leech et al., 2011) has shown that by adding multiple flare-angle-discontinuities, it is possible to increase the operational bandwidth of smooth-walled feed horns up to $\sim 20$ %, thus making them viable for sub-millimetre wavelength astronomy applications. A schematic diagram of such a horn, employing three flare-angle-discontinuities, is shown in Figure 3.1.

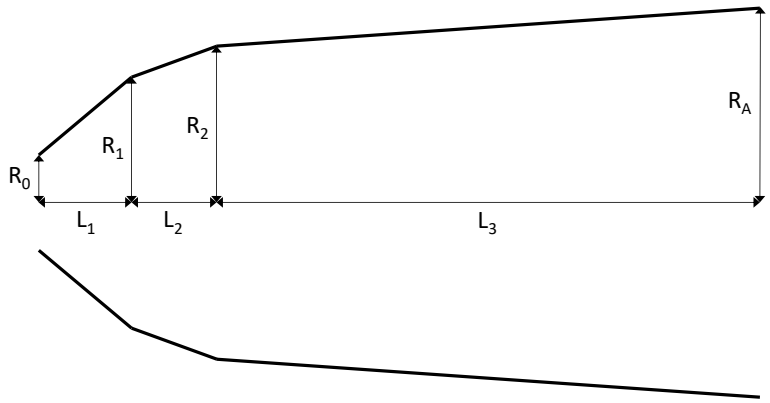


Figure 3.1: A schematic diagram of a 3 section multiple flare-angle feed horn.

Apart from the desired $TM_{11}$ mode, it is important to note that discontinuities near the throat of the horn will excite other higher order modes that will affect the aperture field distribution in a non-trivial, frequency dependent way. This, in turn, makes the design of smooth-walled horns with good performance over a finite bandwidth somewhat challenging. However, it is possible to predict the effect of these modes on the far-field radiation pattern of a particular horn very accurately by using a numerical modal matching technique (Olver et al., 1994; Kittara, 2002). In addition, it is possible to use modal matching in combination with optimisation algorithms to determine desirable horn profiles for a particular application that is constrained to a specified bandwidth.

Given that the smooth-walled design can be an effective alternative to the more complex corrugated feed horn structure, work has been carried out to design and optimise a smooth-walled horn to operate in the THz regime. Since this design features two flare-angle-discontinuities near the throat of the horn, a Genetic Algorithm (GA) (Haupt & Haupt, 2004; Kittara et al., 2007) was employed to optimise their positions and magnitudes.

The work presented in this chapter will first of all summarise the design, fabrication and radiation pattern measurement process for a smooth-walled feed horn operating between $780 - 950\ GHz$. Particular emphasis will be placed on the fabrication tolerances required to achieve good results at these frequencies. In addition, a smooth-walled, 4 pixel feed horn array designed to work between $1300 - 1500\ GHz$ will be shown to exhibit promising experimental results. Finally, a second smooth-walled feed has been designed and fabricated to fit an ALMA style mixer block. This horn has been used in SIS mixer measurements between $800 - 900\ GHz$ and will be described in more detail in Chapter 5.

## 3.2 Feed Horn Design

The horns presented in this chapter were designed and optimised using the commercially available "TICRA CHAMP" software package. This software, based on the work of Kittara et al. (2007), allows the user to specify an initial horn geometry for both smooth-walled and corrugated feed horns, evaluate the far-field radiation patterns at different frequencies and optimise the design using a variety of optimisation techniques. In order to evaluate the

far-field radiation patterns, the software uses a modal matching technique while a genetic algorithm is often used to optimise an initial horn geometry. The principles of operation for the modal matching technique and genetic algorithm optimisation are described in detail in Olver et al. (1994); Kittara (2002); Kittara et al. (2004) and Haupt & Haupt (2004); Kittara et al. (2007) respectively and as such will only briefly be outlined here.

### 3.2.1 The Modal Matching Technique

Modal matching is a useful tool that can be employed to accurately predict the aperture field distribution of a feed horn from which its far-field radiation pattern can then be calculated (James, 1981; Olver & Xiang, 1988). Furthermore, because it is less time consuming when compared to finite element three dimensional solvers, modal matching becomes a highly convenient option to quickly calculate beam patterns across a range of frequencies.

In this section, the principle of operation of modal matching is summarised based on the description in Olver et al. (1994); Kittara (2002) using a conical horn as an example but the general technique can be applied to smooth-walled and corrugated feeds alike.

To begin with, the interior of the horn is represented as a series of cylindrical sections joined together by discontinuities in which the tangential field components of a wave propagating in the z-direction (along the optical axis of the horn) are described in terms of waveguide modes. Using a cylindrical co-ordinate system in this example, these modes can be calculated by first solving the Helmholtz wave equation for the z-components of the E and H-fields inside the horn. For a conical feed, a general solution to the wave equation can be expressed as

$$\psi_z(r, \phi, z, t) = J_n(kr)\cos(n\phi + \phi_0)e^{-\gamma z}e^{i\omega t} \tag{3.1}$$

where $\psi_z$ represents the $E_z$ or $H_z$ field component, $r$ is the radial distance from the z-axis, $\phi$ is the azimuthal angle, $J_n$ is a Bessel function of the first kind of order $n$ and $\phi_0$ is a phase constant. The wave number, $k$, is defined as $k^2 = \gamma^2 + \omega^2\mu\epsilon$ where $\gamma$ is the propagation constant, $\omega$ the radial frequency and $\mu$ and $\epsilon$ are the permeability and electric permittivity of the medium respectively. From this, the E and H-field transverse components of the propagating wave can be expressed in terms of $E_z$ and $H_z$ as

$$E_r = -\frac{1}{k^2}\left(\gamma\frac{\partial E_z}{\partial r} + \frac{i\omega\mu}{r}\frac{\partial H_z}{\partial \phi}\right) \tag{3.2a}$$

$$E_\phi = \frac{1}{k^2}\left(-\frac{\gamma}{r}\frac{\partial E_z}{\partial \phi} + i\omega\mu\frac{\partial H_z}{\partial r}\right) \tag{3.2b}$$

$$H_r = \frac{1}{k^2}\left(\frac{i\omega\mu}{r}\frac{\partial E_z}{\partial \phi} - \gamma\frac{\partial H_z}{\partial r}\right) \tag{3.2c}$$

$$H_\phi = -\frac{1}{k^2}\left(i\omega\mu\frac{\partial E_z}{\partial r} + \frac{\gamma}{r}\frac{\partial H_z}{\partial \phi}\right) \tag{3.2d}$$

Assuming that the wall of the conical horn is a perfect conductor, it will support two sets of orthogonal waveguide modes; the Transverse Electric ($TE_{nm}$) and Transverse Magnetic ($TM_{nm}$) modes where the subscripts $n$ and $m$ are integers denoting cyclic variation with azimuthal angle $\phi$ and the $m^{th}$ root of the Bessel function $J_n$ respectively. For TM modes, $H_z = 0$ since these modes only contain tangential magnetic field components while $E_z = 0$ for TE modes because only tangential electric field components are present here. As well as this, the boundary conditions present on the conducting wall of the horn require that $E_\phi = 0$ for TM modes and $E_\phi = E_z = 0$ for TE modes at $r = a$ where $a$ is the radius of a particular cylindrical section. Using these conditions and applying them to Equation 3.2, it is possible to obtain specific expressions for TE and TM modes inside a cylindrical section of a smooth-walled feed horn. For an electromagnetic wave to propagate from one section of the horn to the next, the total modal fields need to be matched at the interface between two adjacent cylindrical sections. This is usually done by representing the interface with a scattering matrix and considering power conservation such that the power coupling across the interface is related to the scattering matrix as

$$\begin{bmatrix}\mathbf{B}\\ \mathbf{D}\end{bmatrix} = \begin{bmatrix}\mathbf{S}_{11} & \mathbf{S}_{12}\\ \mathbf{S}_{21} & \mathbf{S}_{22}\end{bmatrix}\begin{bmatrix}\mathbf{A}\\ \mathbf{C}\end{bmatrix} \tag{3.3}$$

where $\mathbf{A}$ and $\mathbf{B}$ correspond to input and reflected mode coefficient matrices from the input side of an interface while $\mathbf{C}$ and $\mathbf{D}$ are the equivalent matrices from the output side. This is shown schematically in Figure 3.2 for a wave propagating from left to right where the left hand side represents the interface input while the right hand side is its output.

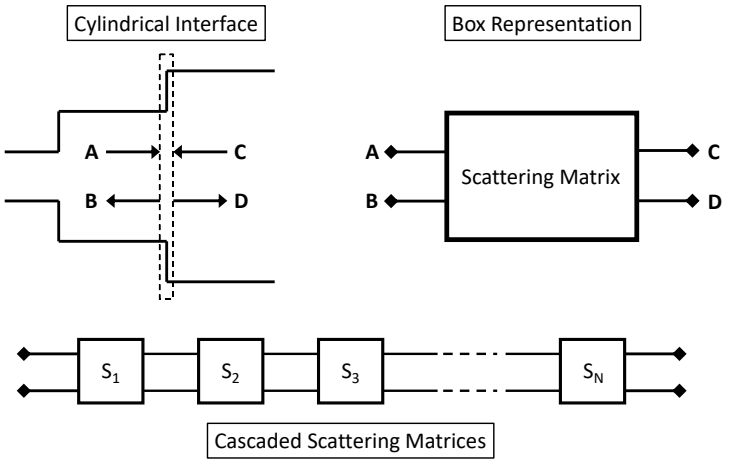


Figure 3.2: A schematic showing how a feed can be modelled using cascaded matrices.

The transverse fields in each of the cylindrical horn sections can be represented as a set of $N$ modes. By considering the example interface in Figure 3.2, the transverse electric and magnetic fields on the left hand side can be expressed as

$$\boldsymbol{E}_L = \sum_{n=1}^{N} \left( A_n e^{-\gamma_n z} + B_n e^{\gamma_n z} \right) \boldsymbol{e}_{nL} \tag{3.4a}$$

$$\boldsymbol{H}_L = \sum_{n=1}^{N} \left( A_n e^{-\gamma_n z} - B_n e^{\gamma_n z} \right) \boldsymbol{h}_{nL} \tag{3.4b}$$

where $A_n$ and $B_n$ are the forward and reflected amplitude coefficients respectively of the $n^{th}$ mode from the input side and $\boldsymbol{e}$ and $\boldsymbol{h}$ are the electric and magnetic transverse modal functions. Similarly, on the right hand side of the interface the corresponding fields are given by

$$\boldsymbol{E}_R = \sum_{m=1}^{M} \left( C_m e^{-\gamma_m z} + D_m e^{\gamma_m z} \right) \boldsymbol{e}_{mR} \tag{3.5a}$$

$$\boldsymbol{H}_R = \sum_{m=1}^{M} \left( C_m e^{-\gamma_m z} - D_m e^{\gamma_m z} \right) \boldsymbol{h}_{mR} \tag{3.5b}$$

with $C_m$ and $D_m$ representing the forward and reflected amplitude coefficients respectively of the $m^{th}$ mode from the output side of the interface. Equating the transverse fields across the interface at $z = 0$ by setting $\boldsymbol{E}_L = \boldsymbol{E}_R$ and $\boldsymbol{H}_L = \boldsymbol{H}_R$ leads to

$$\sum_{n=1}^{N} (A_n + B_n)\, \boldsymbol{e}_{nL} = \sum_{m=1}^{M} (C_m + D_m)\, \boldsymbol{e}_{mR} \tag{3.6a}$$

$$\sum_{n=1}^{N} (A_n - B_n)\, \boldsymbol{h}_{nL} = \sum_{m=1}^{M} (C_m - D_m)\, \boldsymbol{h}_{mR} \tag{3.6b}$$

Multiplying Equations 3.6a and 3.6b by $\boldsymbol{h}_R$ and $\boldsymbol{e}_L$ respectively and integrating over the cross sectional area of the interface leads to a pair of simultaneous matrix equations given by

$$\mathbf{P}(\mathbf{A} + \mathbf{B}) = \mathbf{Q}(\mathbf{C} + \mathbf{D}) \tag{3.7a}$$

$$\mathbf{P}^T(\mathbf{D} - \mathbf{C}) = \mathbf{R}(\mathbf{A} - \mathbf{B}) \tag{3.7b}$$

where matrix $\mathbf{P}$ represents the power coupled between the $i^{th}$ mode on the left hand side of the interface and the $j^{th}$ mode on the right hand side. Meanwhile matrices $\mathbf{Q}$ and $\mathbf{R}$ correspond to the power coupled between modes on the right and left hand side of the interface respectively. Each of these matrices can be expressed as

$$P_{ij} = \int_{S_L} (\boldsymbol{e}_{iL} \times \boldsymbol{h}_{jR}) \cdot \mathbf{ds} \tag{3.8a}$$

$$Q_{jj} = \int_{S_R} (\boldsymbol{e}_{jR} \times \boldsymbol{h}_{jR}) \cdot \mathbf{ds} \tag{3.8b}$$

$$R_{ii} = \int_{S_L} (\boldsymbol{e}_{iL} \times \boldsymbol{h}_{iL}) \cdot \mathbf{ds} \tag{3.8c}$$

It is now possible to rearrange Equation 3.7 into matrix form to obtain the individual elements of the scattering matrix $\mathbf{S}$ for a particular interface which leads to

$$\mathbf{S}_{11} = (\mathbf{R} + \mathbf{P}^T\mathbf{Q}^{-1}\mathbf{P})^{-1} \times (\mathbf{R} - \mathbf{P}^T\mathbf{Q}^{-1}\mathbf{P}) \tag{3.9a}$$

$$\mathbf{S}_{12} = 2 \times (\mathbf{R} + \mathbf{P}^T\mathbf{Q}^{-1}\mathbf{P})^{-1}\mathbf{P}^T \tag{3.9b}$$

$$\mathbf{S}_{21} = 2 \times (\mathbf{Q} + \mathbf{P}\mathbf{R}^{-1}\mathbf{P}^T)^{-1}\mathbf{P} \tag{3.9c}$$

$$\mathbf{S}_{22} = -(\mathbf{Q} + \mathbf{P}\mathbf{R}^{-1}\mathbf{P}^T)^{-1} \times (\mathbf{Q} - \mathbf{P}\mathbf{R}^{-1}\mathbf{P}^T) \tag{3.9d}$$

The scattering matrices describing each interface can then be cascaded together into an overall scattering matrix that describes the entire feed horn as shown schematically in Figure 3.2. The aperture field distribution of the feed can in turn be determined using the overall matrix by computing its output transmission coefficient element ($\mathbf{S}_{21}$), while the return loss of the horn can also be estimated by calculating the reflection coefficient element ($\mathbf{S}_{11}$). Finally, the $\mathbf{S}_{21}$ parameter can be Fourier Transformed to determine the far-field patterns of the horn across a frequency range of interest (Kittara et al., 2004).

### 3.2.2 Genetic Algorithm Optimisation

In order to solve optimisation problems, the Genetic Algorithm (GA) (Haupt & Haupt, 2004; Kittara et al., 2007) procedure uses a natural selection process similar to biological evolution. It begins by converting the parameters used to describe a particular horn geometry ($R_0$, $R_1$, $R_2$, $R_A$, $L_1$, $L_2$ and $L_3$ in Figure 3.1) into a binary string. These binary strings are known as chromosomes and are further converted from binary into their corresponding Gray codes, in which successive integer values differ from each other only by a single bit. The collection of chromosomes that describe a particular horn geometry are known as an individual.

To start with, a population of individuals is created in which the horn parameters are chosen randomly between sensibly specified upper and lower limits. In the case of the horns described here, these limits were specified such that discontinuities were positioned close to the throat of the horn and followed by a long, smooth phasing section.

Next, the fitness of each individual in the population is determined by calculating a frequency dependent cost function from that individual's simulated far-field radiation pattern. This cost function, given by Equation 3.10 (Kittara et al., 2007), is inversely proportional to the fitness of an individual and measures the quality of that individual's far-field radiation pattern given a set of specified pattern criteria.

In general, the radiation pattern requirements for a particular horn will depend on the application and the pattern quality can be characterised by a number of parameters. For a feed horn antenna for example, the desired properties include high beam circularity (i.e. a beamwidth that is independent of polarisation), low cross-polar power, low sidelobe levels, low return loss and a high beam efficiency over a certain bandwidth. It is important

to note that some of these properties are related. For instance, a horn which has good beam circularity will generally also have low cross-polarisation and a feed with high beam efficiency will tend to have low sidelobe levels. For the horns described here, the optimisation parameters were beam circularity and cross-polar power.

$$\delta_f^2 = w_X \left[ \sum_{P=-1}^{P=-30} \left( \frac{\sigma_P}{\sigma_P^{av}} \right)^2 w_P \right] \tag{3.10}$$

In Equation 3.10 (Kittara et al., 2007) (expressed and evaluated as a discrete sum for computational efficiency) $w_X$ corresponds to the peak cross-polar power relative to the main beam peak power, $P$ is the power level in $dB$, $\sigma_P$ is the difference in beamwidths at power level $P$ in the E and H-planes, $\sigma_P^{av}$ is the average beamwidth at power level $P$ and $w_P = 10^{\frac{P}{15}}$ is the weight function for beam circularity. It can be seen that the form of $w_P$ in the cost function of Equation 3.10 provides an exponential weight that slowly varies with power which places the constraint for beam circularity to be better near the centre of the radiation pattern (i.e. at high power levels) than at the edges, where the power is lower.

The frequency dependent cost function in Equation 3.10 can be calculated for a range of frequencies, which then allows an overall cost function for an individual to be determined across a specified bandwidth. This cost function, centred at a frequency $f_0$, is calculated for the desired operating frequency range of the horn, usually in increments of $0.01 \times f_0$, using Equation 3.11 (Kittara et al., 2007)

$$\delta^2 = \sum_f \delta_f^2 \exp \left[ -\frac{(f - f_0)^2}{2\sigma_f^2} \right] \tag{3.11}$$

where the Gaussian-like exponential term is a frequency dependent weight factor centred at $f_0$ that emphasises symmetry with respect to the band centre and $\sigma_f = f_{upper} - f_{lower}$ is the frequency bandwidth.

Once the overall cost function has been calculated for every individual in the population, the fittest individuals (i.e. the ones with the *lowest* overall cost functions) are selected and randomly paired up to become the parents of a new generation of individuals. The new generation is created via a mating process which uses crossover and mutation to produce a

genetically diverse offspring population. The crossover part, shown graphically in Figure 3.3, takes two parent chromosomes that represent a particular horn parameter, divides them at the same random point along their length and swaps the end of each chromosome over before joining them back together. This forms two new offspring chromosomes, with parameter values partially inherited from *both* parents, for the next generation of individuals.

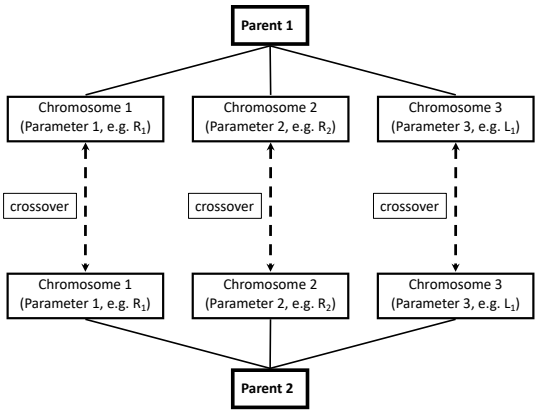


Figure 3.3: A graphical representation of the crossover process used by Genetic Algorithm (Haupt & Haupt, 2004; Kittara et al., 2007). The chromosomes of two parent individuals are randomly split at the same point along their Gray code binary string, swapped over and joined together again to make the chromosomes for the offspring individuals.

Following crossover, there is also a small probability (5 % in the work described here) for the individual bits of the new offspring chromosomes to be flipped. This mimics the random mutation that occurs in biological processes.

Once a new population of horns has been created, the fitness of each individual is computed again and the mating process repeated to make another new generation. This means that multiple iterations of this procedure will lead to an increase in the average fitness of a population of horns.

After the process has been repeated for a sufficiently large number of generations (usually until the change in the average cost function of a population becomes negligible), the fittest horn from the final generation is chosen as the optimum design. In practice, good results tend to be achieved by using $\sim 1000$ generations and $3N$ individuals in the population, where $N$ is the number of free horn parameters that need to be optimised.

One of the main advantages of Genetic Algorithm optimisation is that it avoids convergence to a local minimum by exploring a large parameter space. However, searching for an

optimum solution can be time consuming and thus the GA procedure is usually employed to find the proximity of the global minimum. If necessary, the design can then be further improved by using a Simplex technique (Nelder & Mead, 1965) which is an efficient, iterative minimisation algorithm for problems that do not have a large number of variables.

## 3.3 A 780 - 950 GHz Smooth-Walled Feed Horn

The initial, multiple flare-angle feed horn presented here consists of 3 conical sections which allows for an operational bandwidth of 20 %. It was designed to operate between $780 - 950\ GHz$ and have a Full Width at Half Maximum (FWHM) beamwidth of $\sim 14.67^{\circ}$ at the centre frequency of 865 $GHz$, thus making it suitable for use in cryostats where a narrow beamwidth is required to avoid clipping the cryostat window.

This particular design was optimised using GA for beam circularity and low cross-polarisation levels because horns which satisfy these criteria also tend to have low sidelobes as well as high beam efficiency.

The input and aperture radii ($R_0$, $R_A$) are determined by the cutoff frequency of the input waveguide and the required FWHM beamwidth of the far-field radiation pattern respectively. Here, they were fixed to $R_0 = 0.165$ and $R_A = 0.971\ mm$ while the remaining five parameters were determined using GA.

### 3.3.1 Optimised 3 Section Design

The final dimensions obtained from the GA optimisation procedure are given to the nearest micron in Table 3.1 while the simulated far-field radiation patterns are shown in Figure 3.4. These patterns have good beam circularity, low levels of cross-polar power and low sidelobes across a bandwidth of 20 %.

Following this design process, a horn with the dimensions in Table 3.1 was fabricated out of an aluminium block as described in the following section. The completed feed horn was then taken to the Rutherford Appleton Laboratory so that its far-field radiation patterns could be experimentally measured and thus compared with the theoretical predictions presented in Figure 3.4.

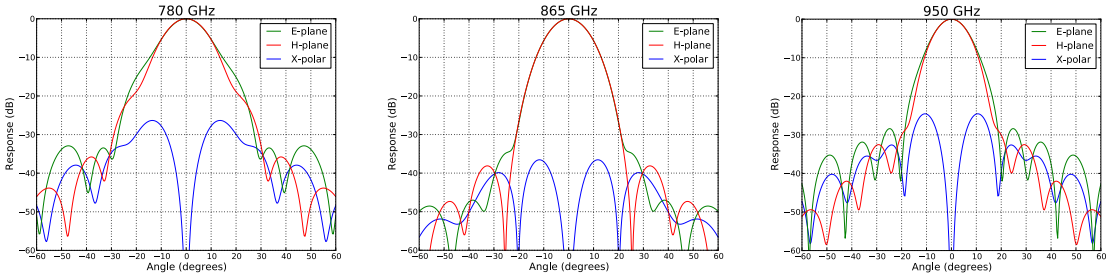


Figure 3.4: Theoretical predictions for E-plane, H-plane and cross-polar far-field radiation patterns at 780, 865 and 950 $GHz$ obtained using GA optimisation. The main beam efficiency is 0.96 at 865 $GHz$.

| Parameter | Length ($mm$) |
|---|---|
| $R_0$ | $0.165 \pm 0.01$ |
| $R_1$ | $0.395 \pm 0.01$ |
| $R_2$ | $0.482 \pm 0.01$ |
| $R_A$ | $0.971 \pm 0.01$ |
| $L_1$ | $0.393 \pm 0.01$ |
| $L_2$ | $0.322 \pm 0.01$ |
| $L_3$ | $6.382 \pm 0.01$ |

Table 3.1: Optimised parameter values for a smooth-walled, 3 section THz feed horn design.

### 3.3.2 Feed Horn Fabrication

Both the horn and a circular to rectangular waveguide transition onto which the feed can be mounted were fabricated by the mechanical workshop at Oxford University using a standard 5-axis Computer Numerical Control (CNC) machine. In order to create the horn, a direct machining technique was employed that uses a drill tool shaped to the inner profile of the horn (Yassin et al., 2007; Leech et al., 2009, 2010). A zoomed in, microscope image of the tool used to create the first iteration of this feed is shown in Figure 3.5(a). It will be shown later in this chapter, that in order to get good experimental agreement with the simulations at these frequencies, the tolerances on the tool dimensions must be $\sim 5 - 10\ \mu m$.

Once the High-Speed Steel (HSS) tool with the correct cutting profile is made (usually manufactured by a machine tool company), it can be used to drill the interior profile of a smooth-walled feed horn directly out of a metal block. The initial horn presented here was fabricated out of aluminium but further implementations of this design were also made using brass and a comparison between the two materials will be presented in Section 3.3.4.

The fabrication process itself begins with the creation of the circular input waveguide by direct drilling from one side of the block. The size of the drill required for this depends on the waveguide and in this case, a 0.33 $mm$ diameter drill bit was used. Once the waveguide is complete, the HSS fabrication tool, such as the one shown in Figure 3.5(a), is used to machine the required horn profile from the opposite side of the metal block.

When fabricating feed horns using this method from two different sides of a metal block, great care must be taken as any misalignment between the input waveguide and the horn itself will lead to deviations from theory in the measured radiation patterns.

Having said that, this method of fabrication has the advantages that it is more robust and reliable than electroforming as it does not require any electroplating or dissolving stages. As well as this, once the machine tool and the metal block have been aligned, it is possible to repeat the process and quickly manufacture any number of identical feed horns, making this technique highly viable for the creation of smooth-walled feed horn arrays for future radio and sub-mm telescopes. The completed feed and its circular to rectangular waveguide transition are shown in Figure 3.5(b). The transition and horn are aligned using dowel pins and as such, any potential misalignment is determined by the accuracy of the dowel pin locations. In this case, the tolerance on dowel pin location was 5 $\mu m$, allowing for a maximum misalignment of just 10 $\mu m$ between the horn and the transition. Considering the 330 $\mu m$ diameter of the circular waveguide of the horn and transition, this is negligible.

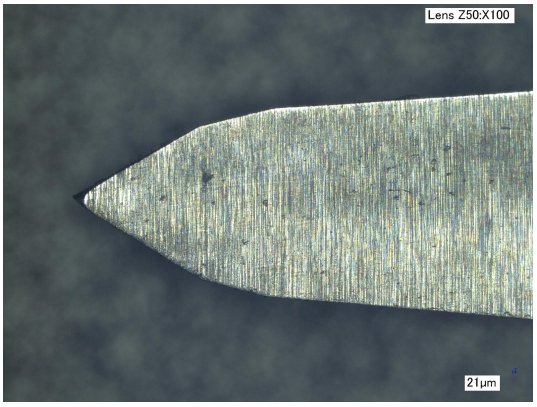


(a) Close up image of the HSS drill tool that was used to fabricate the initial implementation of this horn design.

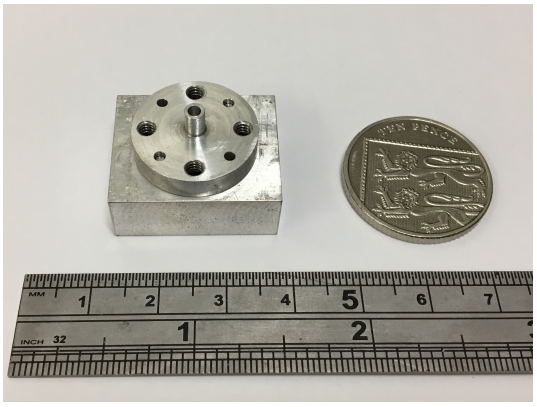


(b) The completed aluminium feed horn and its transition block shown alongside a ruler and coin for scale.

Figure 3.5: Horn fabrication tool and completed aluminium feed with its transition.

### 3.3.3 Beam Pattern Measurement

The radiation pattern measurements were carried out at the Rutherford Appleton Laboratory (RAL) using a far-field antenna test range and a commercially available Millimetre Vector Network Analyser (MVNA) system produced by AB Millimetre. The feed horn under test was mounted on the source side of the system. It was then rotated around its aperture using a computer-controlled rotary stage. The magnitude of the signal was recorded by the detector at each point in the rotational scan which produced the radiation pattern. The entire setup was contained inside an anechoic chamber to minimise stray reflections and to reduce the effects of external sources of noise. The scan range was $\pm 40^\circ$ in the H-plane and $\pm 30^\circ$ in the E-plane, since physical dimensions of the anechoic chamber limited the scan range once the source had been rotated for E-plane measurements. The scan step size was $0.1^\circ$ for all measurements. The source and detector were separated by 35 $mm$ from each other which is $\sim 3D^2/\lambda$ where $D$ is the aperture diameter of the horn and $\lambda$ is the signal wavelength. This ensured that the beam patterns were measured in the far-field regime. The dynamic range obtained at this separation was between $\sim 25 - 35$ $dB$, which was limited both by the available power of the source as well as the sensitivity of the detector. An image of the experimental setup used for these measurements is shown in Figure 3.6.

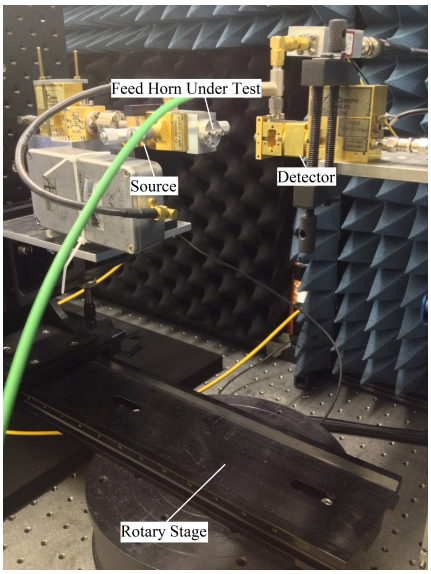


Figure 3.6: Experimental setup used for far-field radiation pattern measurement at RAL. The aperture of the horn is positioned directly above the axis of rotation of the rotary stage and the entire system is housed in an anechoic chamber enclosure.

### 3.3.4 Results

The radiation patterns, measured in E and H-planes between $780 - 945\ GHz$, are presented in Figures 3.7 and 3.8 respectively. These results have been plotted over the theoretical simulations calculated using the previously described modal matching technique. In addition, a Savitzky-Golay filter (Savitzky & Golay, 1964) has been applied to the raw data to act as a low-pass filter and smooth high-frequency thermal noise from the measurements. This can be justified since the thermal noise in the raw data is negligible (down at the $\sim -25 - 30\ dB$ level relative to the measured peak) and the beam profile being measured is an inherently smooth function. The window length for this procedure used 61 data points, corresponding to an angle of 6°, and the samples were fitted with a first order polynomial.

The measurements show reasonable agreement with theoretical predictions down to $\sim -15\ dB$ between $865 - 945\ GHz$, corresponding to a bandwidth of $\sim 10$ %. Within this range, good agreement in both planes also suggests that the beam is circular. However, the sidelobe levels are significantly higher than expected and a degree of asymmetry is present in the measured patterns as well. There are significant differences below 865 $GHz$, where the results show poor agreement with the predicted behaviour of the horn. This suggests that the profile of the fabricated horn did not match the design and implies that the machining tolerances achieved by the drilling technique were, in this instance, not adequate to produce the desired performance. Another possible cause for the differences observed between theory and measurement in Figures 3.7 and 3.8 could, of course, have been misalignment between the horn and the circular to rectangular waveguide transition. However, as stated previously, because the horn and transition had been aligned using dowel pins to ensure a maximum potential misalignment of no more than 10 $\mu m$, it was much more likely that errors in the fabrication tool were the principal cause. Therefore, the horn was split in half along its optical axis using Electrical Discharge Machining (EDM) and its critical dimensions ($R_0$, $R_1$, $R_2$, $R_A$, $L_1$ and $L_2$) were measured using a Keyence VHX-700FE digital microscope. A close up of the split horn can be seen in Figure 3.9 while the measured parameters are presented in Table 3.2.

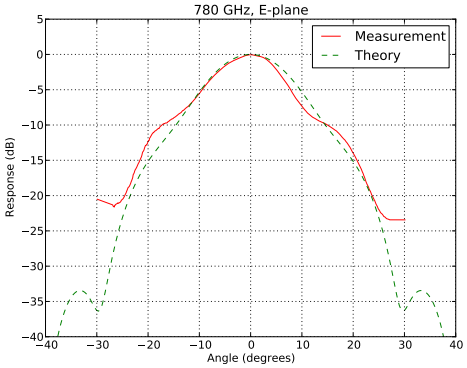


(a) 780 $GHz$.

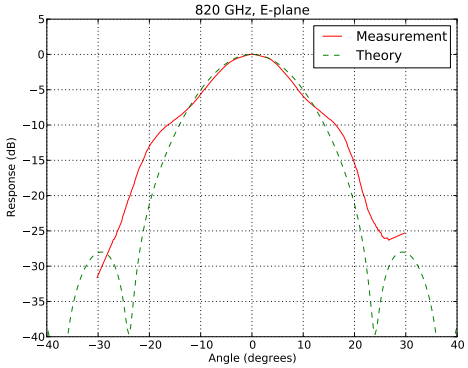


(b) 820 $GHz$.

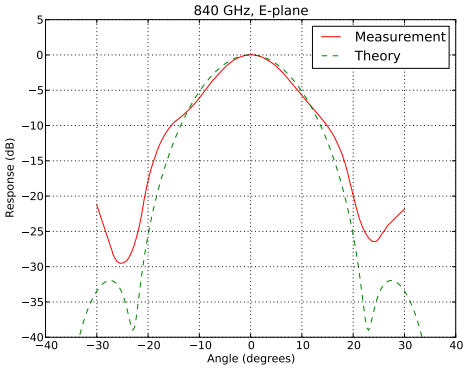


(c) 840 $GHz$.

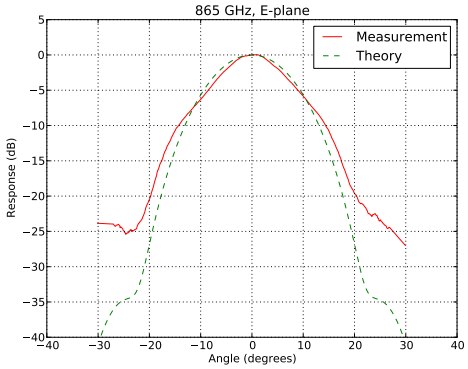


(d) 865 $GHz$.

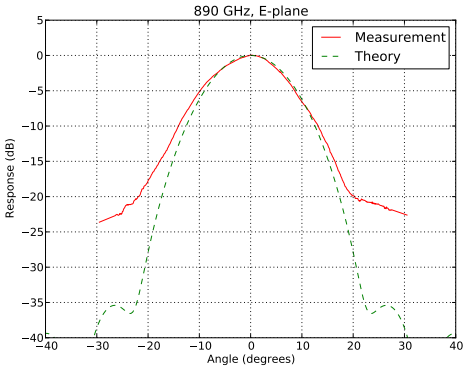


(e) 890 $GHz$.

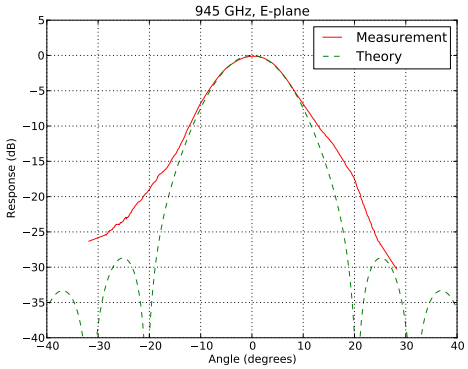


(f) 945 $GHz$.

Figure 3.7: A comparison of the simulated and initial measured radiation patterns in the E-plane of the smooth-walled, aluminium feed horn between $780 - 945$ $GHz$.

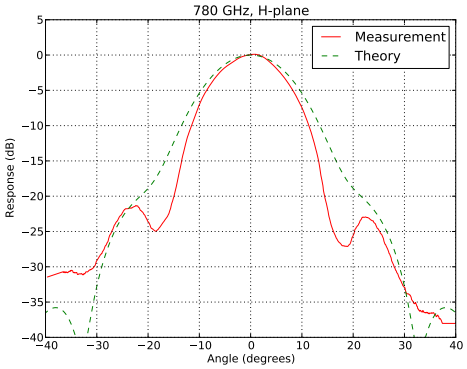


(a) 780 $GHz$.

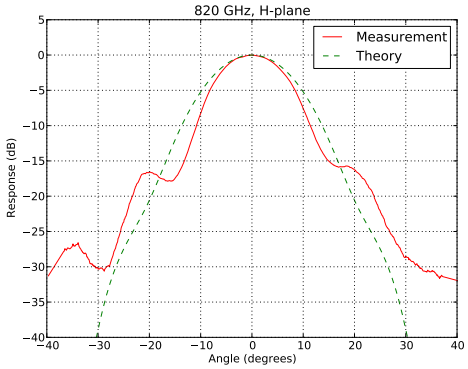


(b) 820 $GHz$.

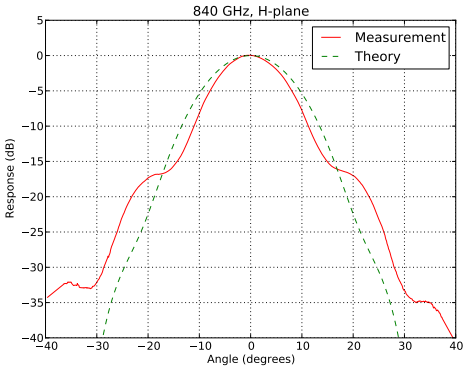


(c) 840 $GHz$.

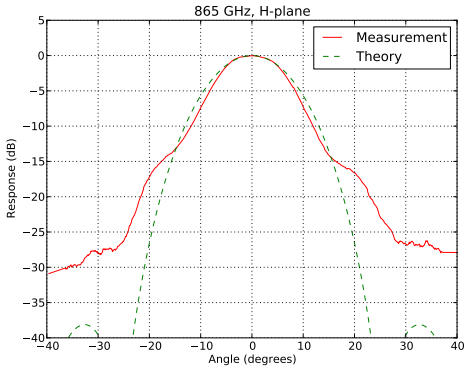


(d) 865 $GHz$.

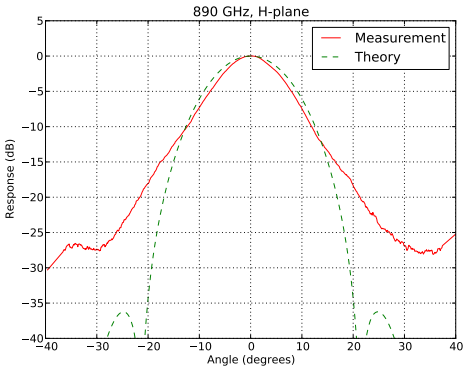


(e) 890 $GHz$.

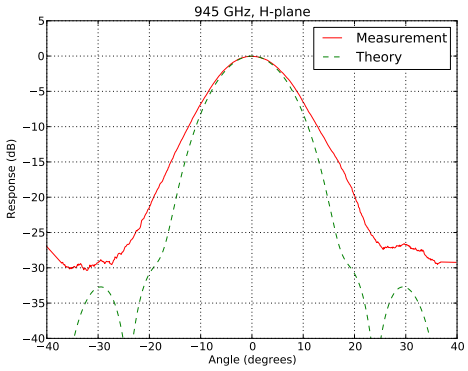


(f) 945 $GHz$.

Figure 3.8: A comparison of the simulated and initial measured radiation patterns in the H-plane of the smooth-walled, aluminium feed horn between $780 - 945\ GHz$. It can be seen that the measured pattern is narrower than predicted, especially at the lower frequencies, because the internal profile of the fabricated horn was significantly different from the design that was modelled.

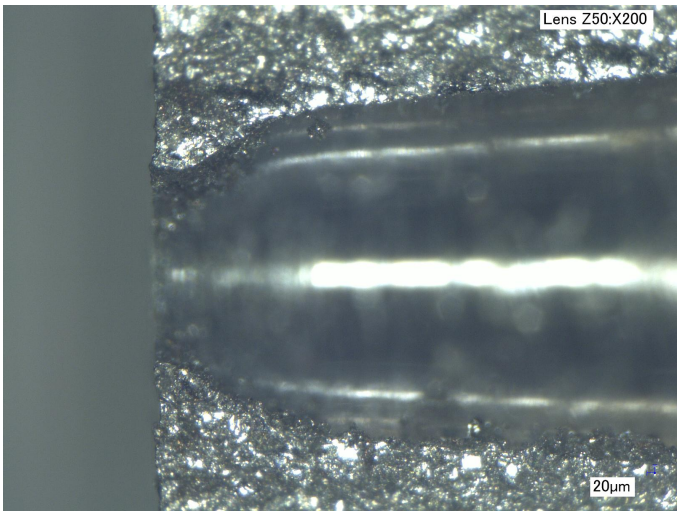


Figure 3.9: Close up microscope image showing the smooth-walled, aluminium feed horn which has been split along its optical axis. It can be seen that the definition of the flare-angle-discontinuities is blurred out and their location poorly defined.

| Parameter | Length ($mm$) |
|---|---|
| $R_0$ | $0.239 \pm 0.0005$ |
| $R_1$ | $0.371 \pm 0.0005$ |
| $R_2$ | $0.411 \pm 0.0005$ |
| $R_A$ | $0.995 \pm 0.0005$ |
| $L_1$ | $0.297 \pm 0.0005$ |
| $L_2$ | $0.125 \pm 0.0005$ |

Table 3.2: Measured dimensions of the fabricated aluminium feed horn after it had been split along its optical axis.

By comparing the design dimensions in Table 3.1 with the measured dimensions in Table 3.2, it can be seen that the fabricated horn is significantly different from the required design. Furthermore, the drill tool used to machine this horn was also measured using the microscope and found, in some cases, to deviate from the design dimensions by over 100 $\mu m$.

Following these findings, a horn with dimensions in Table 3.2 was modelled to test whether it would produce simulated radiation patterns that could recreate the previously obtained experimental measurements. The result of this simulation in the E and H-planes, plotted over the measured beam patterns, is shown in Figures 3.10 and 3.11, respectively. It can be seen that the agreement between theory and measurement in the H-plane is much better.

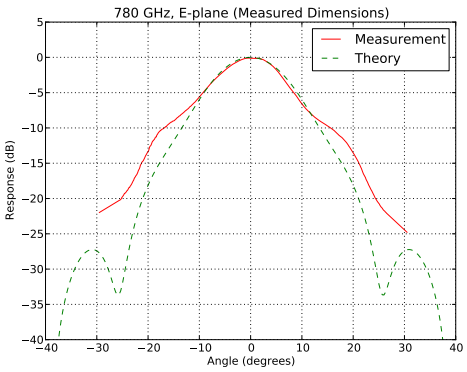


(a) 780 $GHz$.

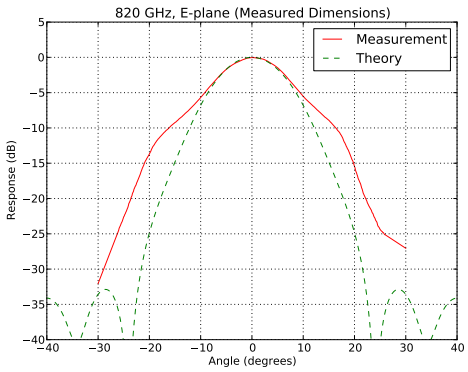


(b) 820 $GHz$.

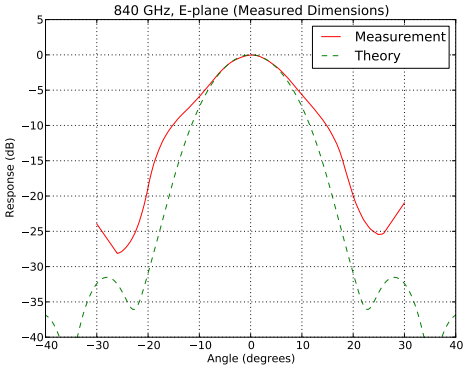


(c) 840 $GHz$.

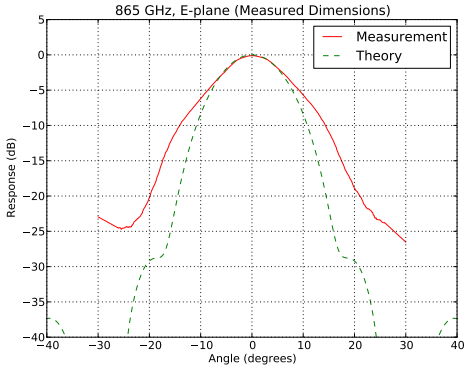


(d) 865 $GHz$.

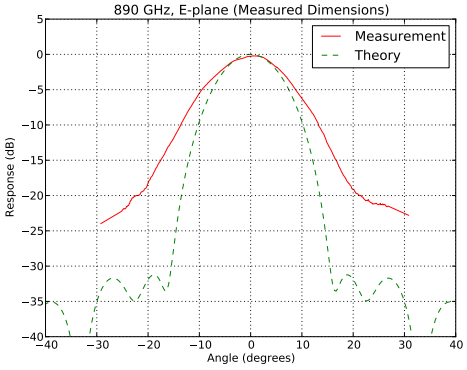


(e) 890 $GHz$.

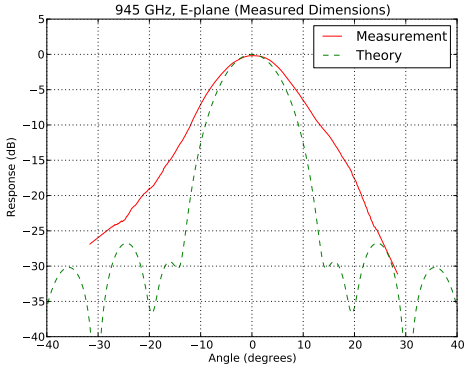


(f) 945 $GHz$.

Figure 3.10: A comparison of the experimental radiation patterns in the E-plane of the aluminium feed horn between $780 - 945$ $GHz$ with simulations after the horn has been split and measured with a microscope.

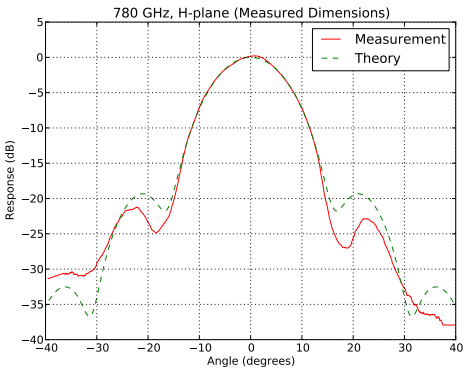


(a) 780 $GHz$.

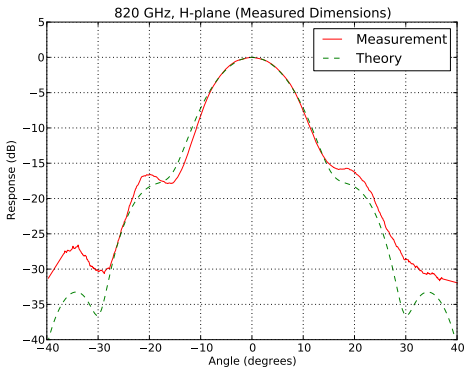


(b) 820 $GHz$.

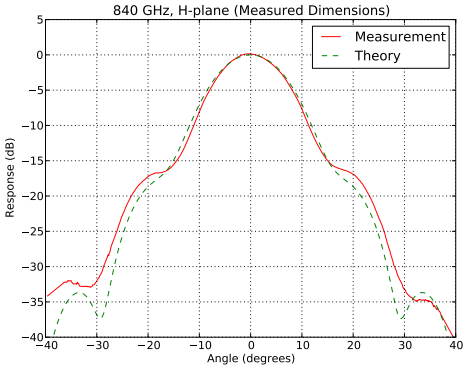


(c) 840 $GHz$.

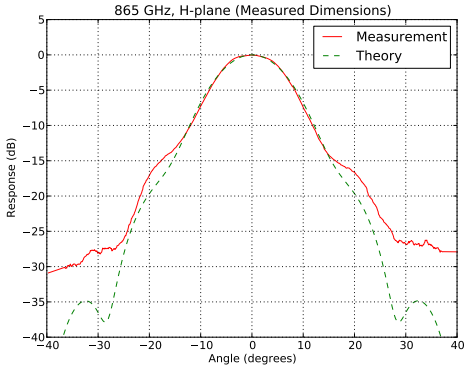


(d) 865 $GHz$.

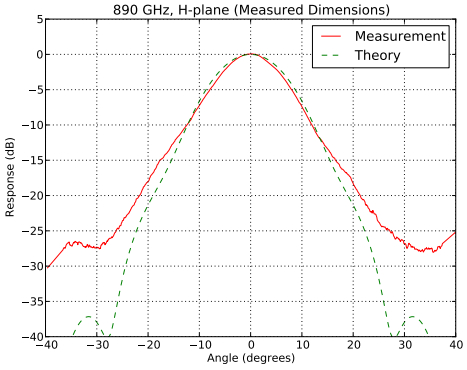


(e) 890 $GHz$.

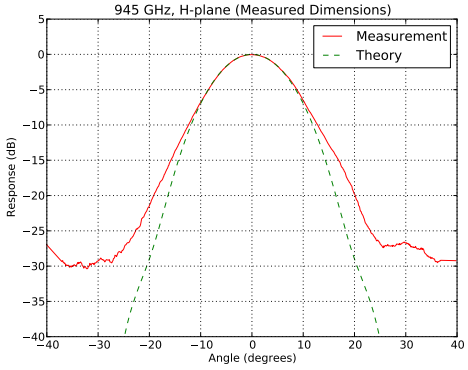


(f) 945 $GHz$.

Figure 3.11: A comparison of the experimental radiation patterns in the H-plane of the aluminium feed horn between $780 - 945$ $GHz$ with simulations after the horn has been split and measured with a microscope.

While the measured beam patterns in Figure 3.10 show differences from the simulations, it is important to remember that because the horn had been split and measured along a particular plane, it may not be representative of the true structure of the feed, which could account for the differences observed. The fact that the experimental radiation patterns could be reproduced in the H-plane by splitting, physically measuring and then modelling the horn supports the idea that inadequate tolerances on the dimensions of the fabrication tool caused some of the deviations between the measured patterns and the desired theoretical predictions shown in Figure 3.4. These results led to the acquisition of new fabrication tools which were extensively measured on the microscope to ensure that their dimensions were correct. A close up image of one of the new fabrication tools is shown in Figure 3.12 while its measured dimensions are presented in Table 3.3. It can be seen that the measured dimensions of this tool are in much better agreement with those specified in Table 3.1.

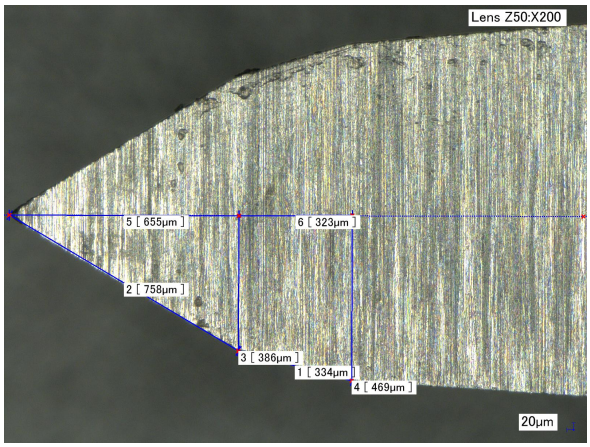


Figure 3.12: Close up microscope image showing a HSS feed horn fabrication drill tool with the correct cutting profile dimensions.

| Parameter | Length ($mm$) |
|---|---|
| $R_0$ | $0.165 \pm 0.01$ |
| $R_1$ | $0.386 \pm 0.0005$ |
| $R_2$ | $0.469 \pm 0.0005$ |
| $L_1$ | $0.375 \pm 0.017$ |
| $L_2$ | $0.323 \pm 0.0005$ |

Table 3.3: Measured dimensions of the feed horn fabrication tool with the correct cutting profile. The parameter $L_1$ has been determined from the measurements in Figure 3.12 assuming an input radius, $R_0$, of $0.165 \pm 0.01$ $mm$.

Apart from the fact that the split horn shown in Figure 3.9 significantly differs from the required dimensions, it can also be seen that the definition of the flare-angle-discontinuities, especially the one corresponding to $R_2$, is rather poor. Given that these discontinuities excite higher order modes in addition to the incident $TE_{11}$ mode which allows the feeds to operate across a wider bandwidth, it is essential that their location is correct if the horn is to work as designed. Therefore, once the new tools had been measured and found to be of the correct size, a series of horn test pieces were drilled in both aluminium and brass, split and measured using the microscope to check the location and definition of the discontinuities. A comparison of these tests is presented in Figure 3.13.

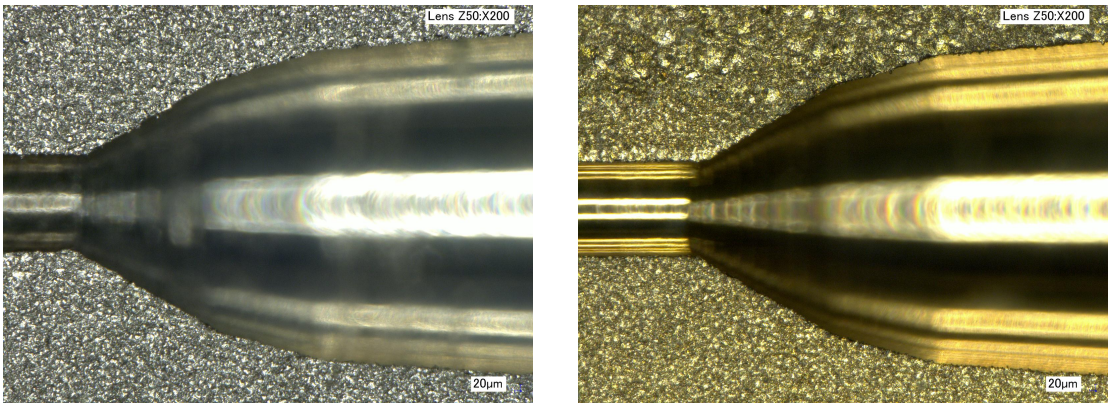


(a) Aluminium horn test piece. (b) Brass horn test piece.

Figure 3.13: A comparison of split horn test pieces in aluminium and brass, fabricated using direct machining. The flare-angle-discontinuity definition is sharper in brass.

The microscope measurements carried out on the horn test pieces in Figure 3.13 show that the positions of the discontinuities and the overall dimensions of the horns made using the new fabrication tools were correct to within 10 $\mu m$ of the design dimensions, in both aluminium and brass.

However, visual inspection and comparison of Figures 3.13(a) and 3.13(b) shows the definition of discontinuities in brass to be sharper, with an approximate surface roughness relative to the ideal "smooth-wall" of the horn profile of $\sim 15 - 20$ $\mu m$ in aluminium compared to only $\sim 5$ $\mu m$ in brass. As such, although aluminium was chosen for the first iteration of the horn due to its ease of machining and lower costs involved, it was decided that the second iteration of this feed horn design should be made using brass. The feed was

again fabricated using the same technique as described in Section 3.3.2 and a completed brass feed horn can be seen in Figure 3.14.

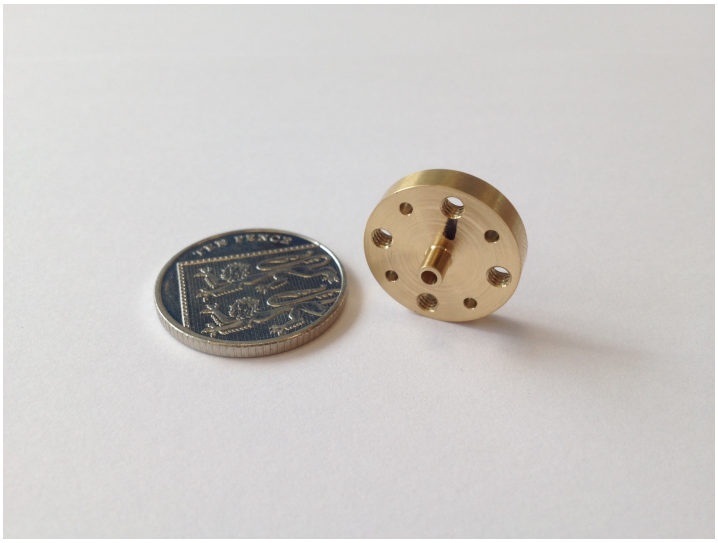

Figure 3.14: A complete, smooth-walled brass feed horn shown alongside a coin for scale.

Once the brass feed shown in Figure 3.14 had been fabricated using a machine tool with the correct cutting profile dimensions, its far-field radiation patterns were once again measured at RAL, as previously described in Section 3.3.3. The results of these measurements in E and H-planes between $780 - 945\ GHz$ are presented in Figures 3.15 and 3.16 respectively. These results have once again been plotted over the theoretical simulations that were calculated using the modal matching technique. As with the plots in Figures 3.7, 3.8 and 3.11, a Savitzky-Golay filter (Savitzky & Golay, 1964) has been applied to the raw data to smooth out high-frequency thermal noise from the measurements. The window length again corresponded to 6° and the samples were fitted with a first order polynomial.

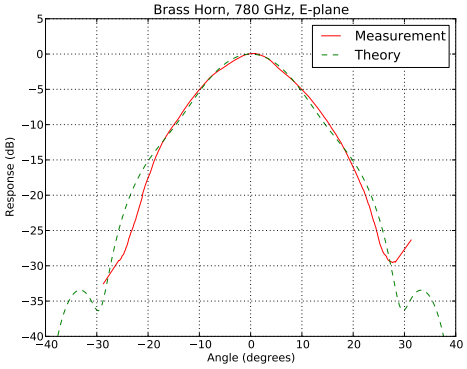


(a) 780 $GHz$.

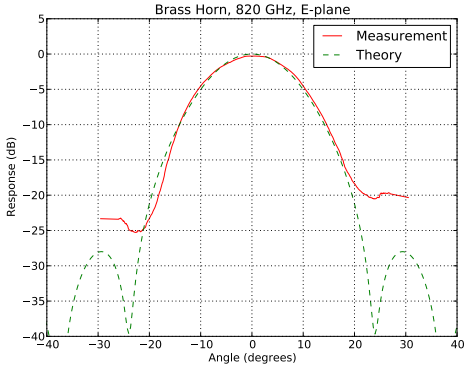


(b) 820 $GHz$.

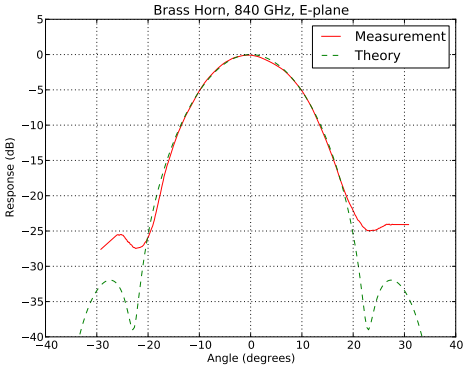


(c) 840 $GHz$.

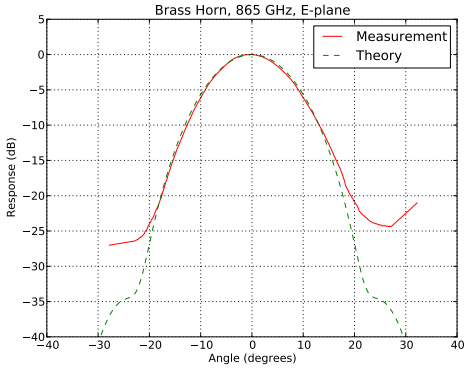


(d) 865 $GHz$.

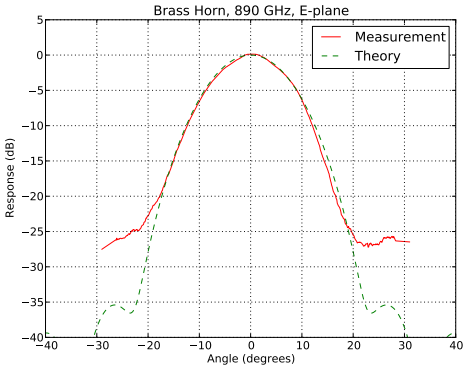


(e) 890 $GHz$.

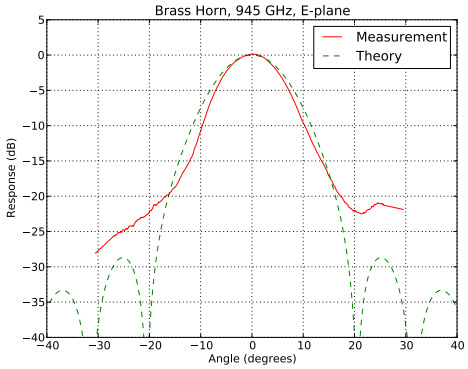


(f) 945 $GHz$.

Figure 3.15: A comparison of the simulated and measured radiation patterns in the E-plane of the smooth-walled brass feed horn between $780 - 945$ $GHz$.

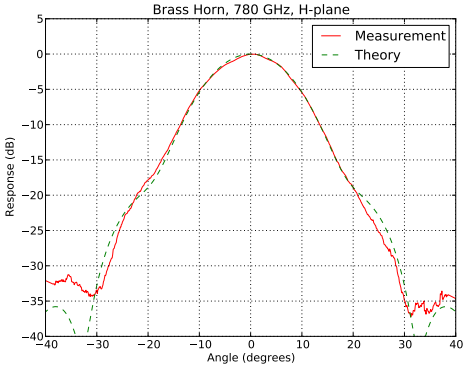


(a) 780 $GHz$.

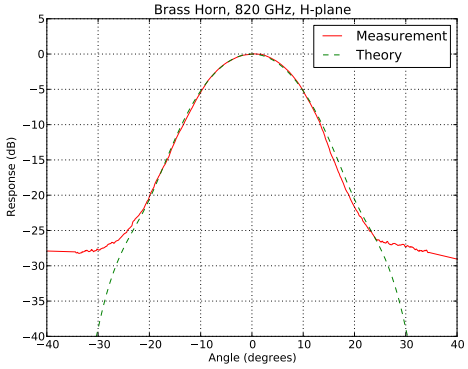


(b) 820 $GHz$.

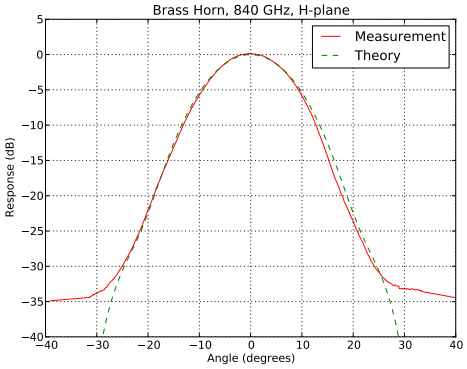


(c) 840 $GHz$.

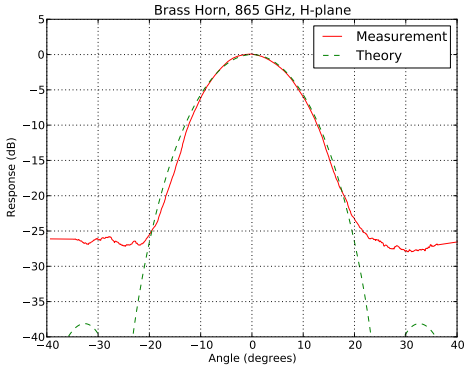


(d) 865 $GHz$.

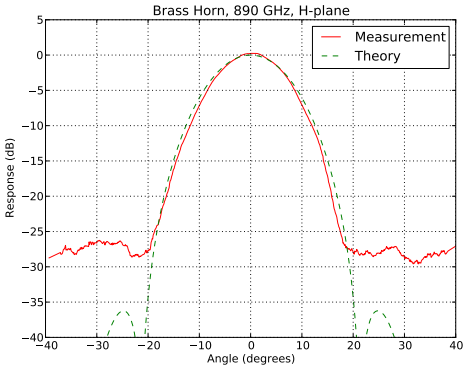


(e) 890 $GHz$.

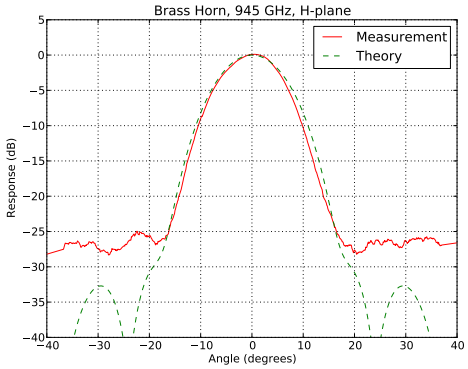


(f) 945 $GHz$.

Figure 3.16: A comparison of the simulated and measured radiation patterns in the H-plane of the smooth-walled brass feed horn between $780 - 945$ $GHz$.

The experimental measurements of the brass feed show very good agreement with the theoretical predictions down to at least $\sim -20\ dB$ across a bandwidth of $\sim 20\ \%$. The only measurement that slightly deviates from its simulation is the E-plane pattern at 945 $GHz$. However, given that this is at the edge of the operating band, it is possible that the tolerances are not quite adequate at this frequency for perfect agreement with theory. For the majority of frequencies tested, the results agree very well in both planes suggesting a highly circular beam and a sidelobe level below $-25\ dB$ across the band indicates excellent beam efficiency.

As well as the co-polar results shown in Figures 3.15 and 3.16, measurements were also performed in the cross-polar configuration where the source and detector are rotated by 90° with respect to each other and by 45° with respect to the rotary scanning stage. This setup allows for maximum coupling of cross-polar radiation with respect to the co-polar peak (Clarricoats & Olver, 1984). The results of these tests between $820 - 945\ GHz$ registered no signal suggesting a lack of dynamic range to capture cross-polar radiation. However, small peaks were measured at 780 $GHz$ which do resemble the simulated cross-polar pattern. This is shown in Figure 3.17.

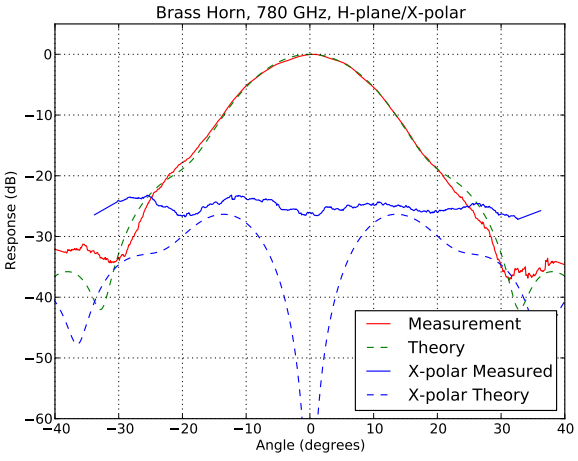


Figure 3.17: A comparison of simulated and experimental cross-polar radiation patterns at 780 $GHz$.

By looking at Figure 3.17, it can be seen that there are two peaks that correspond to the simulated cross-polar pattern. However, given the small amplitude of these peaks and no detected cross-polar signal at other frequencies, it can be concluded that this horn exhibits very low levels of cross-polarisation.

### 3.3.5 Reflection Coefficient

Another important characteristic when specifying the performance of a feed horn is the $S_{11}$ parameter, or Reflection Coefficient (RC). It can be defined as the reciprocal of return loss (IEEE, 1988; Bird, 2009) or, equivalently, as the ratio of reflected power ($P_{ref}$) from a device under test to the power incident on the device ($P_{in}$). This quantity, given by Equation 3.12 (Martin, 1924), is expressed as a negative number in decibels (Martin, 1929), with lower values corresponding to a smaller power loss and generally better performance.

$$RC\ (dB) = 10 \log_{10} \left( \frac{P_{ref}}{P_{in}} \right) \tag{3.12}$$

The reflection coefficient of a feed horn can usually be measured with a Vector Network Analyser (VNA) but due to the high operating frequency range of this horn, it was not possible to experimentally determine the reflection coefficient of the feed in this case. However, a simulation using "ANSYS HFSS" software was carried out to estimate the reflection coefficient between $780 - 960\ GHz$. The result of this is shown in Figure 3.18 and it can be seen that the simulated result predicts a reflection coefficient below $-28\ dB$ across the operating band which should be adequate for most applications. Furthermore, because it has previously been established that multiple flare-angle-discontinuity style horns such as this one generally have low reflection coefficients (Pickett et al., 1984; Kittara et al., 2007), this parameter was not used as a criterion in the design optimisation.

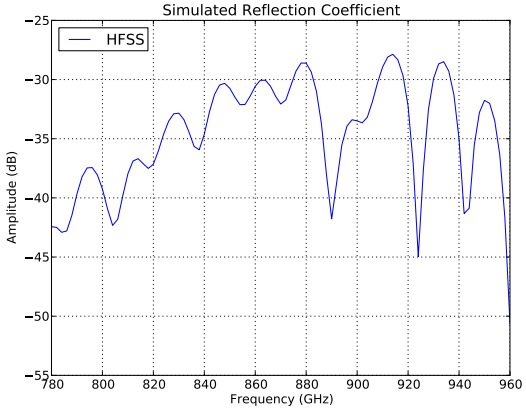


Figure 3.18: A HFSS simulation of the predicted reflection coefficient ($S_{11}$) for the brass feed horn between $780 - 960\ GHz$.

### 3.3.6 The Effect of the Horn Offset Relative to the Waveguide

One of the issues present in some of the measured radiation patterns which can be clearly seen in the plots in Figures 3.7(a) and 3.7(c) is the asymmetry between the two halves of the beam scan. It was suspected that this effect may be being caused by the fact that the direct machining method employed to fabricate these feeds initially drills the circular waveguide from one side of a metal block, while the horn itself is machined from the opposite side which means that the block needs to be rotated by 180° during the fabrication process. This sometimes leads to a small lateral misalignment, or offset, between the circular waveguide and the main body of the horn. This effect is shown in the images in Figures 3.19(a) and 3.19(b) which were taken with the Keyence microscope looking down the apertures of two different feeds. It can be seen that the brass horn in Figure 3.19(b) shows a very small offset ($\sim 15\ \mu m$) between the waveguide and the horn, while the image of the aluminium horn in Figure 3.19(a) shows a misalignment of $\sim 50\ \mu m$ which could be significant. While a misalignment between the feed horn and its waveguide transition could also generate unwanted propagating modes in the horn, with consequences on the radiated field, this misalignment was minimised through a tight, 5 $\mu m$, positional tolerance on the location of the dowel pins used to align the horn and transition.

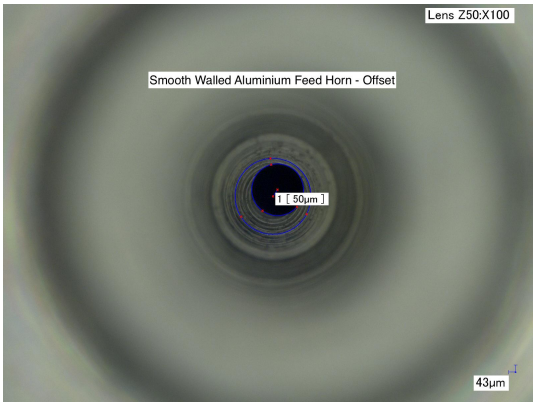


(a) An aluminium feed with a $\sim 50\ \mu m$ offset.

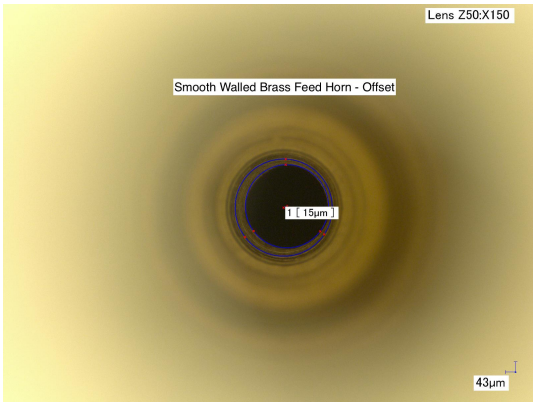


(b) A brass feed with a $\sim 15\ \mu m$ offset.

Figure 3.19: A comparison of the misalignment between the circular input waveguide and the main body of the horn in an aluminium and a brass feed. It can be seen that in this case, the aluminium horn has a greater offset which could be responsible for the asymmetry observed in some of the measured radiation patterns.

To check whether this issue was indeed causing the asymmetry in the measured beam

patterns, the optimised $780-950\ GHz$ feed horn with dimensions from Table 3.1 was modelled using "ANSYS HFSS" software such that the lateral position of the input waveguide was a free parameter which could be changed to replicate the described offset issue. An image of the modelled feed horn and its circular input waveguide is shown in Figure 3.20.

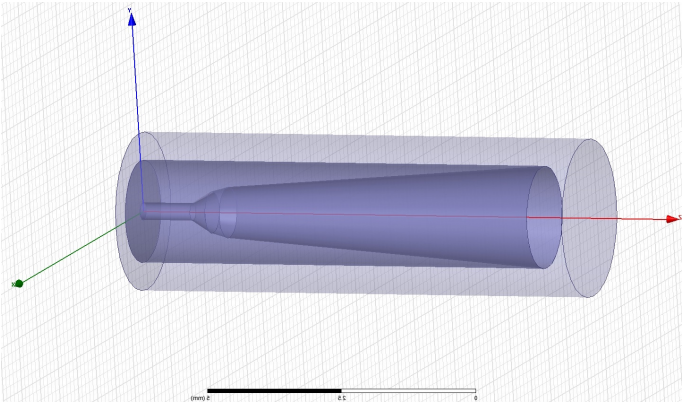

Figure 3.20: A HFSS model of the $780-950\ GHz$ smooth-walled, three-section flare-angle-discontinuity feed horn.

The horn was initially modelled without an offset to check whether the simulated far-field patterns produced by HFSS matched those obtained from CHAMP which is the software that is normally used to generate simulated patterns due to its quicker computation time. An example of a simulated radiation pattern produced by HFSS at 865 $GHz$ is shown in Figure 3.21 which has been plotted over the result from CHAMP at the same frequency.

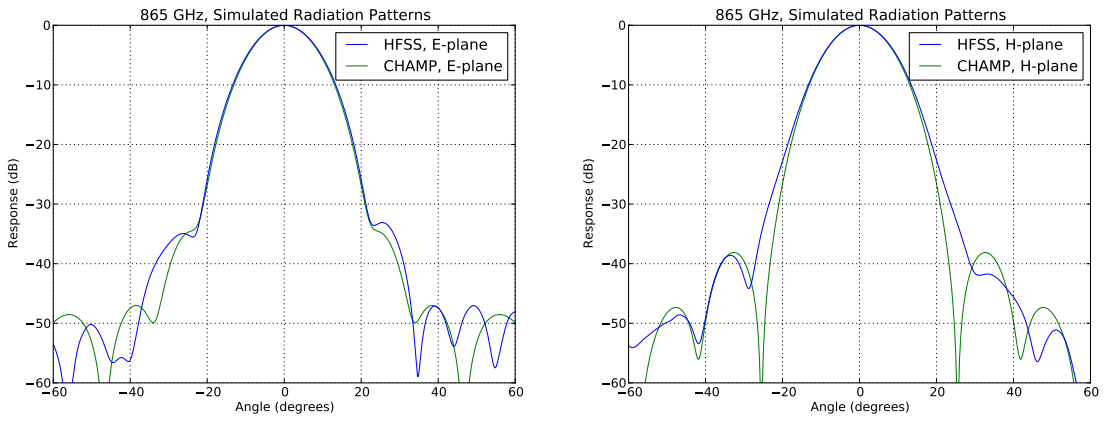


(a) 865 $GHz$, E-plane. (b) 865 $GHz$, H-plane.

Figure 3.21: A comparison of the simulated radiation patterns obtained from HFSS and CHAMP in E and H-planes at 865 $GHz$.

It can be seen that the two results agree very well down to the $\sim -30\ dB$ level in both

planes, with very minor asymmetries in the HFSS solution below this which likely arise from the non axis symmetric meshing that the solver uses to model the three dimensional horn geometry. Following this result, the offset of the waveguide in the HFSS simulation was incrementally stepped to test the effect that this would have on the symmetry of the simulated beam patterns. It was clear that even a small offset on the waveguide position relative to the horn resulted in a small asymmetry in the simulated beam pattern but a particularly interesting result was obtained with a lateral offset of 50 $\mu m$. This simulated pattern has been plotted over the top of the experimental result at 980 $GHz$ which was measured in the E-plane of the aluminium horn with an offset as shown in Figure 3.19(a).

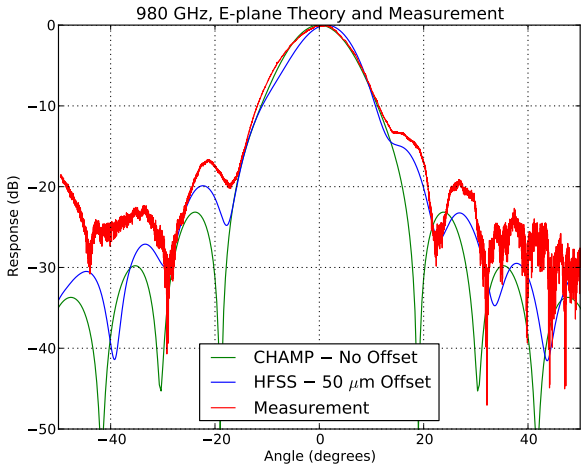


Figure 3.22: A comparison of the measured beam pattern in the E-plane of an aluminium feed with a $\sim 50$ $\mu m$ offset at 980 $GHz$ with a simulated result obtained from HFSS where the circular waveguide has also been offset by 50 $\mu m$. It can be seen that the measurement agress very closely with the simulation.

It can be seen that the HFSS simulation agrees very well with the experimental result in Figure 3.22 which supports the idea that the measured beam pattern asymmetry is caused, to some extent, by the misalignment between the horn and its input waveguide. As such, careful attention needs to be paid to the fabrication process if this method of horn production is to be viable for the manufacture of feed horns in the Terahertz regime. However, if the horns are carefully inspected during the fabrication process and as long as the offset described is kept below $\sim 20$ $\mu m$, smooth-walled feed horns can produce excellent antenna patterns, as seen in Figures 3.15 and 3.16, which can make them highly attractive options for Terahertz frequency applications.

## 3.4 A Smooth-Walled Four-Pixel Feed Horn Array

Multiple pixel feed horn arrays are a popular choice to efficiently couple astronomical and LO signals into SIS mixers or Hot-Electron-Bolometers (HEBs). Such arrays consist of a number of horns and offer high aperture efficiencies, low sidelobe levels and low cross-polarisations required by many astronomical applications (Leech et al., 2011). Because the style and properties of the individual feeds that make up an array determine how well astronomical signals couple to the receiver, the performance of a feed horn array will largely depend on the horn design and the accuracy of fabrication. As such, a prototype feed horn array consisting of four smooth-walled, two-section feeds with a single flare-angle-discontinuity near the throat of each horn has been developed in collaboration with the Harvard-Smithsonian Center for Astrophysics to operate between $1300 - 1500\ GHz$. As with the horns described earlier in this chapter, the feeds in this array were designed by the author using modal matching and Genetic Algorithm (Haupt & Haupt, 2004; Kittara et al., 2007) optimisation. The simulated radiation patterns from the optimised design are shown in Figure 3.23 while the design dimensions are given to the nearest micron in Table 3.4.

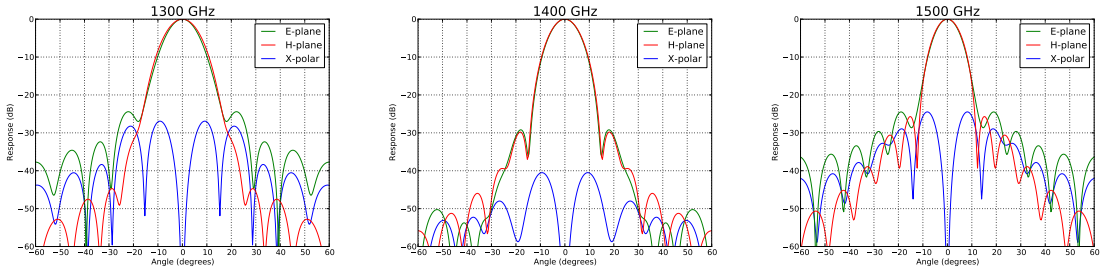


Figure 3.23: Theoretical predictions for E-plane, H-plane and cross-polar far-field radiation patterns at 1300, 1400 and 1500 $GHz$ for the four-pixel feed horn array obtained using GA optimisation.

| Parameter | Length $(mm)$ |
|---|---|
| $R_0$ | $0.112 \pm 0.005$ |
| $R_1$ | $0.304 \pm 0.005$ |
| $R_A$ | $0.764 \pm 0.005$ |
| $L_1$ | $0.420 \pm 0.005$ |
| $L_2$ | $5.110 \pm 0.005$ |

Table 3.4: Optimised parameter values for the horns in the 1400 $GHz$ feed horn array.

It can be seen that the simulated far-field beam patterns have excellent beam circularity, low sidelobe levels and low cross-polarisation between $1300 - 1500\ GHz$, making this array suitable for observations in the supra-Terahertz frequency windows at the Chajnantor plateau shown in Figure 1.1(b), for example. This frequency range corresponds to an operating bandwidth of 15 % which allows a two-section horn design to be employed thus reducing both the design and fabrication complexity, compared to a three-section design.

The array was fabricated, with the author's supervision, out of a brass block by the mechanical workshop at Oxford University using the direct machining technique described in Section 3.3.2 and images of the completed array are shown in Figure 3.24. Following repeated tests, it was found that to achieve good experimental agreement with the simulations at these frequencies, the tolerances on the dimensions of the drill tool must be $\sim 5\ \mu m$.

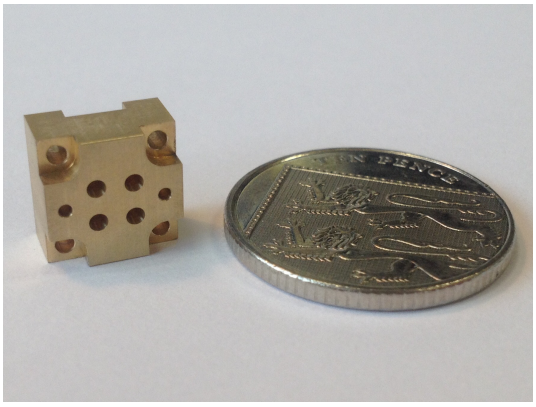

(a) The completed 1400 $GHz$ array, shown beside a coin for scale.

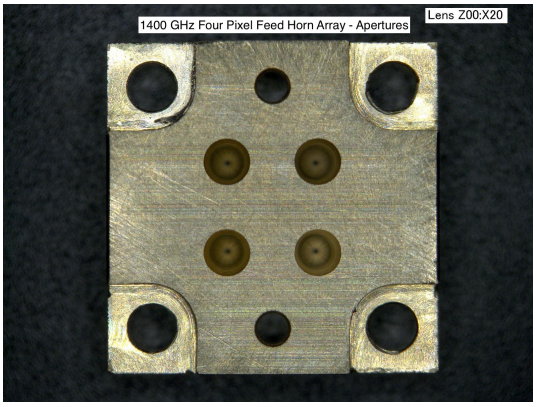


(b) Close up view of the completed 1400 $GHz$ feed horn array.

Figure 3.24: Images of the fabricated four-pixel feed horn array.

The beam pattern measurements were carried out by Andrey Trifonov, a PhD student at the Harvard-Smithsonian Center for Astrophysics using a planar x-y stepper stage. The feed horn array was mounted on the detector side of the system which employed a cryogenic HEB chip cooled to 4.2 $K$. However, since only one of the HEB devices turned out to be alive once the system was cooled down, it was only possible to check the beam patterns for one of the horns during the initial tests.

A conical horn with an aperture diameter of 2.0 $mm$ was used on the transmitter side of the system and the horn and array were separated by $\sim 80\ mm$. At 1500 $GHz$, the Rayleigh distance (given by $R = 2D^2/\lambda$, where $D$ is the aperture diameter and $\lambda$ the wavelength of

radiation) is 40 $mm$ for the conical transmitter horn and 23.35 $mm$ for the horns in the array. Thus, the measurement separation used ensured that both were operating in the far-field regime. A two dimensional beam scan at 1350 $GHz$ is shown in Figure 3.25.

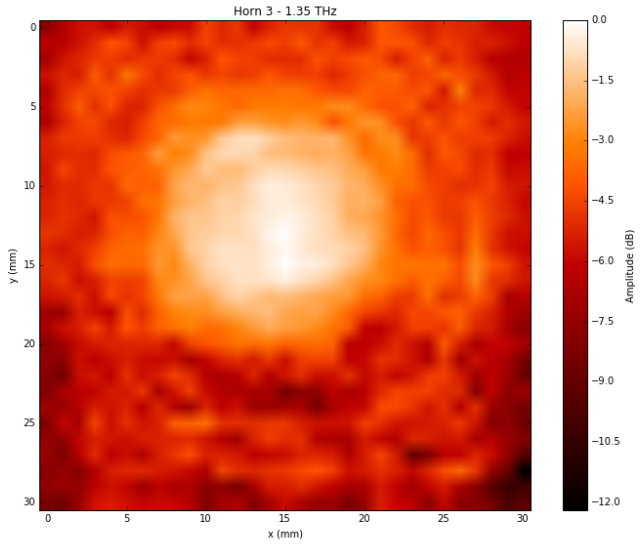


Figure 3.25: The result of a two dimensional beam scan performed at 1350 $GHz$ for one of the horns in the four-pixel array. At a measurement separation of 80 $mm$, the 5 $mm$ displacement increments correspond to an angle of $\sim 3.58°$ between the transmitter and receiver horn.

This result looks promising and it can be seen that the beam has good circularity and symmetry. It can also be seen that there is evidence of a circular ringing structure in the beam scan in Figure 3.25. This is not thought to be a sidelobe of the measured horn however, since it emerges far too close to the centre of the beam. It is possible that this structure is the result of diffraction due to some larger aperture or structure in the measurement setup. However, since these measurements were not performed by the author, it is difficult to comment further and it was not possible to carry out these measurements in Oxford due to a lack of available facilities to carry out such beam pattern scans in the $1300 - 1500$ $GHz$ frequency range. As well as this, measurements were also carried out at 1435 $GHz$ (once again by Andrey Trifonov at the Harvard-Smithsonian Center for Astrophysics) and a quadratic fit to the data, used to smooth out noise, is presented in Figure 3.26. These results have been plotted over the theoretical predictions in the E and H-planes. A quadratic fit was not made to the theoretical predictions.

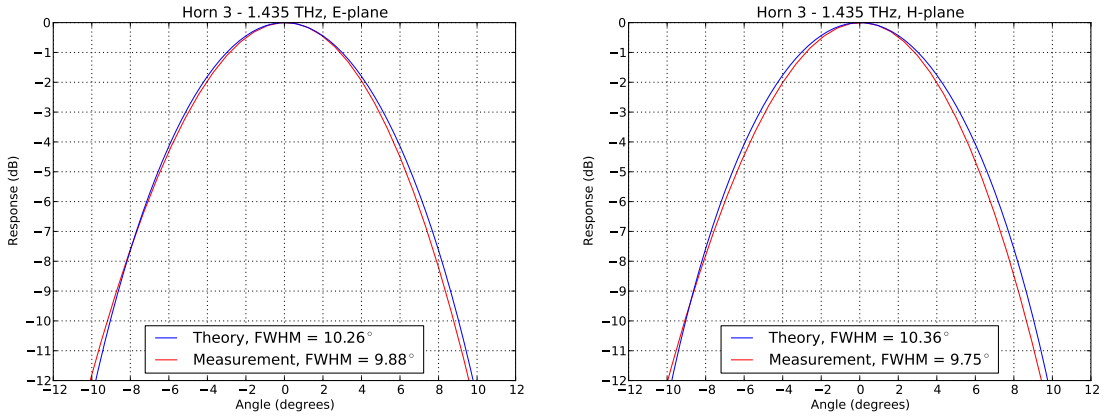


(a) E-plane theory and measurement at 1435 $GHz$. (b) H-plane theory and measurement at 1435 $GHz$.

Figure 3.26: A comparison of the simulated and measured radiation patterns in E and H-planes at 1435 $GHz$ for one of the horns in the four-pixel array.

Figure 3.26 shows that, down to the level of the available dynamic range, the measured beam patterns agree very well with the simulated predictions in both planes. The Full Width at Half Maximum (FWHM) difference between the result and theory is 5.9 % in the H-plane and just 3.7 % in the E-plane. Furthermore, a FWHM difference of 1.3 % between the E and H-planes in the measured data suggests a highly circular beam. This is a very encouraging initial set of results which indicates that the method of horn design and fabrication described in this chapter is effective and viable for creating feed horn arrays that can operate at frequencies well into the Terahertz regime. However, in the future it would be interesting to carry out follow up measurements with the ability to test all four-pixels in the array to check the consistency of the beam patterns against each other as well as the theoretical predictions. Nonetheless, provided that careful attention is paid to the dimensions of the drill tools and that these can be accurately machined to the specified tolerances, there is no reason why this technology cannot be pushed to even higher frequencies, allowing smooth-walled feed horns to offer effective and robust alternatives to corrugated feeds in high frequency radio astronomy applications.

## 3.5 Conclusions

The work presented in this chapter described the design, fabrication and far-field beam pattern measurement of a number of smooth-walled, multiple flare-angle-discontinuity feeds

operating at Terahertz frequencies. The horn design was carried out using modal matching and Genetic Algorithm optimisation that produced excellent simulated far-field beam patterns between $780 - 950\ GHz$ for the three-section design and $1300 - 1500\ GHz$ for the two-section horns used in the four-pixel array.

The feeds were fabricated by the mechanical workshop at Oxford University using a direct machining technique which can robustly create any number of identical horns thus making it suitable for applications such as multiple pixel feed horn arrays. By paying close attention to the fabrication process, it is possible to create smooth-walled feeds that produce excellent measured beam patterns that closely resemble their theoretical predictions as demonstrated in Figures 3.15 and 3.16. To achieve these results, a compliance of $\sim 10\ \mu m$ between the HSS fabrication tool and the horn design has been shown to be sufficient.

Overall, when carefully designed and fabricated, such horns could operate at even higher frequencies thus making them attractive antenna options for the Terahertz regime.

# Chapter 4

# Electron-Beam Lithography for the Development of Schottky Diodes

## 4.1 Introduction

The Schottky barrier diode is one of the most popular devices employed in frequency multipliers and high-frequency Local Oscillator (LO) chains. While in principle any non-linear device can be used as a frequency multiplier or mixer, only a few devices satisfy the necessary practical requirements. For instance, the device used must have a strong non-linearity, uniform electrical properties between individual devices, low noise and an adequate frequency range of operation. A Schottky diode, which consists of a rectifying metal-to-semiconductor junction, is an example of such a device.

Unlike point contact diodes, Schottky diodes are fabricated on an epitaxial substrate using either electron-beam or optical lithography. This type of fabrication results in lower junction capacitance, lower series resistance and a better I-V characteristic than that of point contact diodes. Furthermore, because they are majority carrier devices, Schottky diodes are not subject to the recombination-time limitations that affect *pn* junctions.

In practical applications, the Schottky diode is usually fabricated on a Silicon (Si) or a Gallium Arsenide (GaAs) semiconductor. For high-frequency devices, GaAs is greatly superior because of its higher electron mobility and saturation velocity. This results in a

lower series resistance (for a specified junction capacitance) and means that the performance of GaAs devices exceeds that of silicon. In addition, because GaAs diodes have higher breakdown voltages, their reliability and damage resistance is also better. On the down side, GaAs devices are significantly more expensive than silicon to produce which means that they are usually reserved for more critical applications (Maas, 1992).

For most purposes, Schottky diodes can be fabricated using photolithography. This method involves coating a semiconductor wafer (e.g. GaAs or Si) with a thin ($\sim 400\ nm$) layer of chemical known as "photoresist" that is sensitive to electromagnetic radiation in the ultraviolet part of the spectrum. Once coated with resist, the wafer is placed beneath a mask that contains a specific diode layer as a repeating pattern. The wafer is then exposed to high-energy photons which alters the solubility of the resist in a developer solution. This means that following an exposure, resist on those parts of the wafer that were beneath the gaps in the mask can be removed, leaving behind the required two dimensional shape of the diode layer. A thin amount of metal can then be deposited onto the wafer where it makes contact with the semiconductor surface on the exposed and developed areas. The rest of the resist and metal is removed using a lift-off process to leave behind only the metal that is in contact with the surface of the wafer. By repeating this procedure, the metallic layers of the diode can be built up on top of the semiconductor material.

The main advantage of using a mask for lithography is that it enables many areas of the wafer to be exposed simultaneously, which greatly speeds up the fabrication process. However, there exists a limit to the size of the features that can be achieved using photolithography because of diffraction effects that take place as the feature dimensions on the photomask decrease to the wavelength scale of the exposing radiation. In practice, this means that the minimum component dimensions that can be realised using optical photolithography are $\sim 0.8\ \mu m$ in length. This presents a fundamental problem because some of the feature sizes required for a Terahertz frequency multiplier (namely the diode anodes) can be as small as $\sim 0.4\ \mu m$ in diameter. This means that a different technique from photolithography needs to be employed to fabricate such devices.

Fortunately, electron-beam lithography provides a suitable alternative. Unlike photolithography, this process uses a focused beam of high-energy electrons to directly write a

pattern into the resist, thus exposing the resist-coated wafer. This eliminates the need for a mask and despite taking longer, means it is possible to achieve feature sizes on the order of a few nanometres. For this reason, the Electron-Beam (E-Beam) lithography technique has been employed to fabricate Schottky diodes for use in Terahertz frequency multipliers.

The content presented in this chapter will provide a description of the E-Beam system itself before explaining the general fabrication process used to create Schottky barrier diodes. In addition, a description of work performed using the E-Beam system will be presented which involves sample preparation, system alignment and fabrication of the various diode features including a suspended air-bridge that connects the anode to the rest of the circuit across a surface etched gap. Initial experimental measurements of a selection of diodes will be shown to have promising I-V characteristics. The devices will then be tested in a waveguide block, where they will exhibit excellent RF performance between $225-330\ GHz$, thus validating this fabrication method for producing high-frequency multiplier components.

All of the work described in this chapter was carried out at the Rutherford Appleton Laboratory (RAL) with the Millimetre Technology (MMT) Group and TeraTech, a spin-out company that specialises in high-frequency diode development for astronomical applications. All aspects of work related to the development of Schottky diodes using E-Beam lithography presented here, i.e. Sections 4.4 − 4.8, were carried out by the author of this thesis.

## 4.2 The E-Beam Lithography System

The lithography system that was used for the fabrication process described here consists of a JEOL JSM-5900 Scanning Electron Microscope (SEM) and a XENOS Semiconductor Technologies GmbH E-Beam extension.

An SEM is commonly used to observe microscopic specimen features and surfaces which are too small to resolve using visible light. However, for E-Beam lithography the SEM is a crucial piece of equipment since it provides the source of high-energy electrons that are used to write diode layer patterns into a resist-coated wafer.

To produce an electron-beam (or probe), the SEM uses an electron gun housed at the top of its optical column. In this case, a Thermionic Emission (TE) gun was used which

emits thermoelectrons from a thin ($\sim 0.1\ mm$ diameter) tungsten wire filament (cathode) that is heated to a high ($\sim 2800\ K$) temperature (JEOL, 2018). These thermoelectrons are gathered as an electron-beam and flow into a metal plate (anode) by applying a positive voltage ($1 - 30\ kV$) to it. A hole placed in the centre of the anode allows the beam to flow through it and travel down the column where it is focused to a beam diameter of just a few nanometres on the specimen stage using a combination of magnetic condenser and objective lenses. A scanning coil placed just above the objective lens allows the probe to move across the sample surface and thus expose different areas of the resist-coated wafer.

In addition, the SEM features a motorised specimen stage which allows a sample to be moved in horizontal $(x, y)$ and vertical $(z)$ directions as well as allowing for sample rotation and tilt. The SEM is also equipped with an electron detector that collects secondary electrons containing most of the information about the surface features of a sample.

The optical arrangement inside the microscope column and the space surrounding the sample (i.e. the sample chamber) are kept under vacuum.

A schematic diagram of the SEM column showing the main features of the optical system is shown in Figure 4.1(a) while an image of the motorised specimen stage with a $1\ cm^2$ sample wafer is shown in Figure 4.1(b).

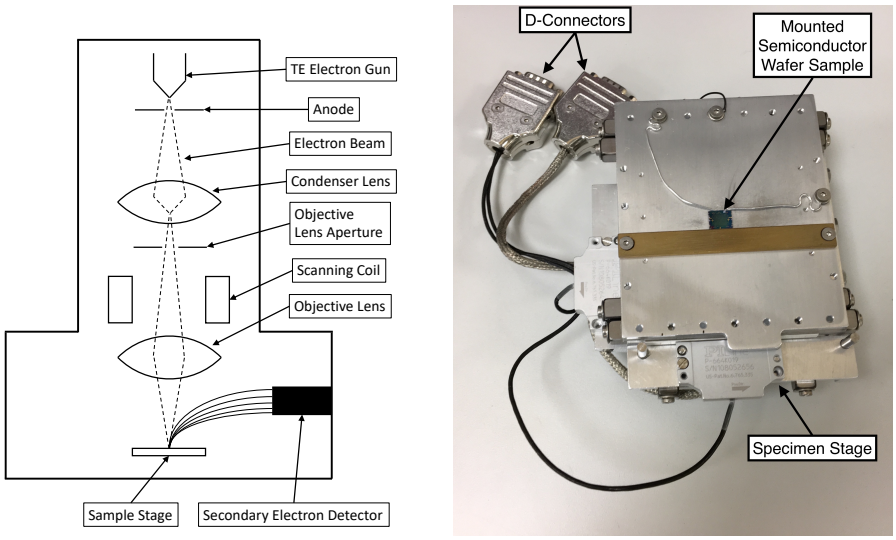


(a) Schematic diagram of the main features of the SEM optical column.

(b) Image of the specimen stage which is used to position a sample inside the specimen chamber.

Figure 4.1: A schematic diagram of the SEM optical column alongside an image of the specimen stage with a wafer sample mounted in the centre.

The XENOS E-Beam extension consists of a voltage-controlled blanker plate, a blanker-tension power-supply, a display and control unit, a XeBaSe central controller and an Exposure Control Program (ECP) software application (XENOS, 2009).

The blanker plate is housed within the SEM column and enables the electron-beam to be toggled on and off with nanosecond precision. This plate is a motorised combination of an electrostatic beam blanker and a Faraday cup that allows measurement of the beam current. It is installed in such a way that it can be moved in and out of the electron-beam of the SEM and there are three key positions to which the blanker can be moved:

1. The "In" position. Here the blanker is placed in the electron-beam of the SEM. This is the operating position of the blanker in which the electron-beam falls through a small gap in the blanker plate and can be toggled on and off using an optical blank signal supplied via an optical fibre cable that connects directly to the blanker box.

2. The "Cup" position. This is used to measure the electrical current of the electron-beam. The beam falls into a Faraday cup and can be measured using a picoammeter connected to the blanker box via a BNC connector.

3. The "Out" position. In this position, the blanker plate and Faraday cup is moved completely out of the electron-beam.

When the XENOS E-Beam system is in use, the electron-beam is switched on and off using a high-tension voltage (up to 150 $V$) that is applied to the blanker plate via the blanker-tension power-supply box. This box is connected to and controlled by the XeBaSe central controller which is another box that acts as a hub connecting up all the components of the E-Beam system including a USB connection to a computer that is running the ECP application.

The E-Beam system also features a display and control unit which is a joystick box that can be used to manually control the stage or blanker when this is not done through a USB interface. The display and control unit also shows the blanker-tension and location or the position of the stage on a two line LCD display.

This lithography system is controlled using its own software - the ECP, which is a

powerful application for pattern design and exposure. The software is very flexible and can be used for completely automatic control of E-Beam lithography systems such as the one described here.

The ECP supports several possibilities to define and edit layouts. The simplest way to define a pattern is to create a text file, which is called a "pattern" or "pat" file. A pat file contains a list of pattern names and the co-ordinates of their locations within a specified working field. An additional file, known as a "control" or "ctl" file, is required to expose those patterns. The commands in a ctl file allow for movement of the stage, pattern exposure, alignment as well as several other tasks. Furthermore, ECP supports a number of additional file formats such as GDSII and DXF (and their conversion to and from ctl and pat files) which adds further flexibility when designing diode layer patters.

An annotated image showing the SEM and the various components of the E-Beam lithography extension system that was used to perform the work described in this chapter is shown in Figure 4.2.

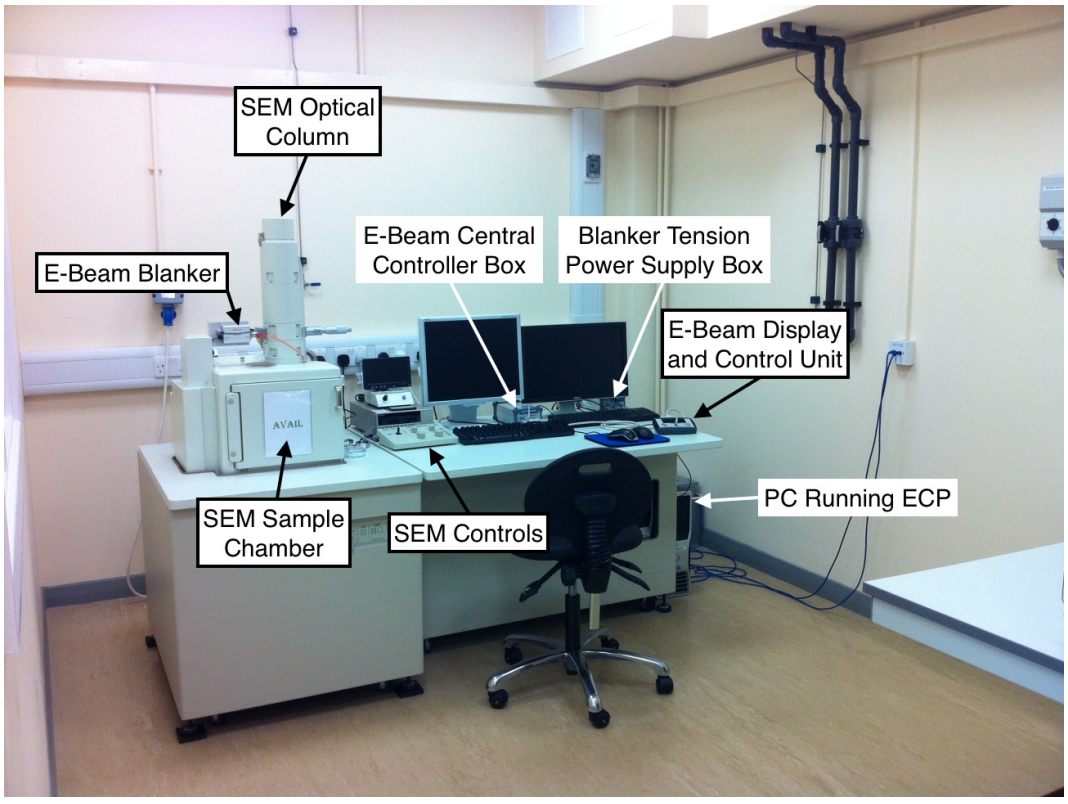


Figure 4.2: An image showing the JEOL JSM-5900 SEM and XENOS E-Beam extension system used for Schottky diode fabrication development.

## 4.3 Diode Fabrication Process

The general Schottky diode fabrication process employed by Teratech at RAL begins with a 1 $cm^2$ Gallium Arsenide (GaAs) wafer that consists of three layers of varying thickness and doping density. At the bottom is a thick, ($> 500\ \mu m$) Semi Insulating (SI) substrate followed by a highly doped ($5 \times 10^{18}\ cm^{-3}$), 2 $\mu m$ thick $n^+$-type buffer layer and a moderately doped ($2 \times 10^{17}\ cm^{-3}$), 0.1 $\mu m$ thick $n$-type epitaxial layer at the top of the wafer. A 0.375 $\mu m$ thick Silicon Dioxide ($SiO_2$) insulating layer is deposited on top of the epitaxial layer.

Once the surface of the wafer has been cleaned (described in detail in Section 4.4), it is coated with a layer of resist so that ohmic pad patterns (separated from each other by $\sim 20\ \mu m$) can be exposed using E-Beam or optical lithography (Alderman et al., 2007).

Following exposure, resist is developed away and the oxide layer etched through using a wet, Buffered Oxide Etch (BOE) process. The exposed $n$-type GaAs layer is anodically thinned to access the underlying $n^+$ layer onto which ohmic contact metals are electroplated (Garfield et al., 1988). The resist, along with the metal on top of it, is then lifted off and an annealing process takes place at $\sim 400\ ^\circ C$ to allow the ohmic contact to form.

With the ohmic contact in place, the wafer is coated once more in resist so that a submicron anode well and a suspended air-bridge can be defined in the resist using E-beam lithography. Following the exposure and resist development stages, the oxide layer beneath the anode well is BOE etched away to expose the $n$-type epitaxial GaAs. A Schottky contact is then formed through a combination of platinum and gold electroplating before the air-bridge is metallised using gold to connect the two diode pads together (Maas, 2003).

Finally, excess resist and metal is lifted off before a channel etch is performed using the BOE process on the $SiO_2$ layer at the top of the wafer while the exposed GaAs is etched through both the $n$ and $n^+$ layers to a depth of $\sim 4\ \mu m$ using a highly directional, $NaOH{:}H_2O_2$ etch process that undercuts the suspended air-bridge (Garfield et al., 1988). This separates the two pads and reduces the parasitic capacitance between the bridge and the $n^+$ layer of the device. Furthermore, the surface channel etch ensures that all of the conduction current passes through the Schottky contact (Bishop et al., 1993). The diode fabrication process showing the main steps involved is schematically illustrated in Figure 4.3.


(a) Side view of the wafer showing the different layers of the initial start material.


(b) Top view of the wafer showing the insulating oxide ($SiO_2$) layer on top of the epitaxial GaAs layer.

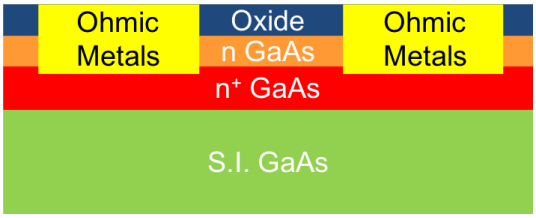


(c) Side view of the wafer once the ohmic metals have been deposited and annealed on top of the $n^+$ GaAs layer.

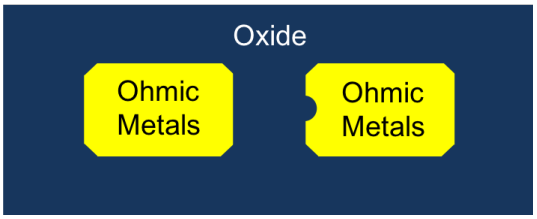


(d) Top view of the wafer showing the shape of the metal pads once the ohmic metals have been deposited and annealed.

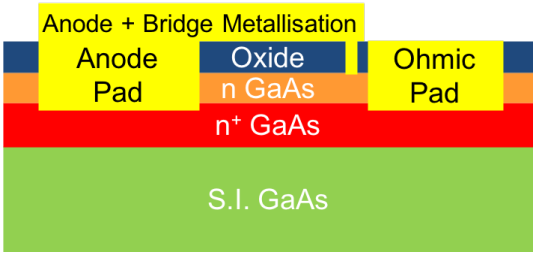


(e) Side view of the wafer after Schottky contact (anode) and bridge metallisation. The anode is metalised on top of the $n$ GaAs layer while the bridge is deposited on top of the oxide.

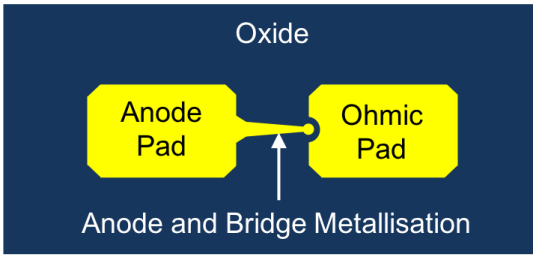


(f) Top view of the wafer after Schottky contact (anode) and bridge metallisation. The anode is metalised on top of the $n$ GaAs layer while the bridge is deposited on top of the oxide.

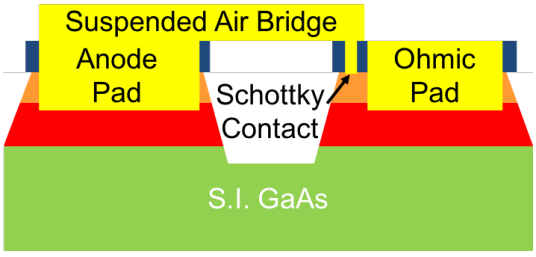


(g) Side view of the wafer after channel etch and sample separation. The bridge is now suspended which reduces the parasitic capacitance between the metal and the surface of the GaAs wafer.

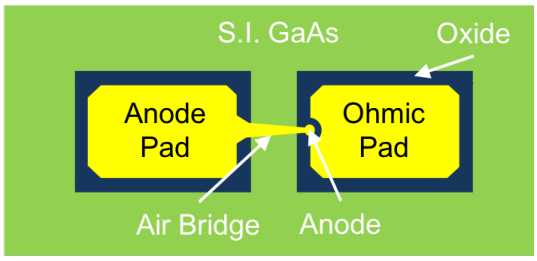


(h) Top view of the wafer after channel etch and sample separation. The bridge is now suspended which reduces the parasitic capacitance between the metal and the surface of the GaAs wafer.

Figure 4.3: Schematic diagram of the main steps involved in the Schottky diode fabrication process employed at RAL. A cross sectional side view of the wafer is shown in the left column while a view of the top of the wafer is presented in the column on the right.

## 4.4 Wafer Preparation and E-Beam Exposure

Before using the E-Beam lithography system to expose structures, it is necessary to correctly prepare the GaAs wafer by removing any resist that may already be on it, carrying out a dehydration bake and coating the wafer in a uniform layer of appropriate E-Beam resist. A low-magnification microscope image showing an example GaAs wafer with global and local alignment marks, as well as previously exposed and metallised identification features on the surface, can be seen in Figure 4.4.

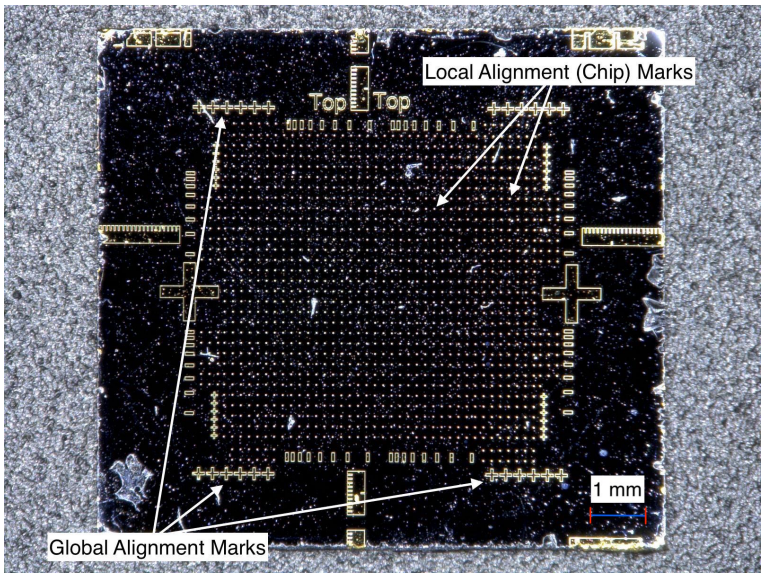


Figure 4.4: A microscope image of an example GaAs wafer that is used for Schottky diode fabrication. Global and local alignment crosses can be seen on the surface of the wafer as well as other metallised features.

### 4.4.1 Cleaning/Stripping a Wafer

This procedure is done in the following way:

- Using a pair of tweezers, carefully place the wafer into a beaker containing a small amount of Acetone.
- Place the beaker, with the wafer inside, into an ultrasonic bath, making sure that the water in the bath is level with the bottom of the metal holder on which the beaker rests.

- Run the ultrasonic bath for 1 minute and the Acetone will remove the resist.
- Using tweezers, remove the wafer from the Acetone and place it inside a beaker containing a small amount of IsoPropyl Alcohol (IPA).
- Place the beaker, containing the wafer and IPA, into the ultrasonic bath and run again for 1 minute. The IPA will remove the Acetone.
- Remove the wafer from the IPA and gently swirl it around in a beaker of de-ionised water for a few seconds. This will remove the IPA.
- Holding the wafer firmly by the edges with tweezers, blow a small amount of nitrogen gas onto it to remove any droplets of water from the surface.
- Place the wafer into a small Petri dish and put it in the oven for a thorough de-hydration bake at 120 $^{\circ}C$. This should last for at least an hour but there is no harm in keeping it there for longer.

### 4.4.2 Coating a Wafer with Resist

Once the de-hydration bake is complete, the clean and dry wafer is ready to be coated with a layer of resist. The resist that was used for most of the fabrication work described in this chapter was PolyMethyl MethAcrylate (495PMMA C3) from MicroChem. The relevant data sheet can be found at Micro Chem Database (2014). The general coating procedure is performed with the aid of a resist spinner in the following manner:

- Bring the wafer to the spinner which is located in a fume cupboard and place it in the centre of the removable, rotary spinner stage.
- Close the lid of the spinner and ensure that there is a strip of sticky tape covering the hole in the centre of the lid.
- Open the nitrogen supply valve to the fume cupboard which also supplies the spinner with nitrogen gas.

- Select the required spin program on the spinner by using the arrow keys and pressing the "Run Mode" button. If necessary, it is possible to add/change the spin parameters by pressing the "Edit Mode" button.
- Press the vacuum button on the spinner which will cause the wafer to stick to the surface of the stage.
- Make sure that the spinner program works as expected by pressing the "Run" (green triangle) button without any resist on the wafer. This should only be done once if coating multiple wafers.
- Once the spinner has been verified to work correctly, load up a pipette with a small amount of resist.
- Peel back the strip of tape on the lid of the spinner and insert the pipette inside, placing it close ($\sim 0.5\ cm$) to the surface of the wafer.
- Keeping the pipette vertical, dispense a few droplets ($\sim 3$) onto the centre of the wafer and a small droplet onto each corner to cover the entire surface of the wafer.
- Promptly remove the pipette from the spinner, recover the hole with the tape and press the "Run" button to spin the resist. In this case, a spin speed of 4000 $rpm$ was chosen for 45 seconds which resulted in a resist thickness of $\sim 250\ nm$.
- Once finished, open the lid, release the vacuum (by pressing the vacuum button again) and carefully remove the wafer from the spinner stage using tweezers.
- Repeat the procedure to coat as many wafers as necessary.
- Once all the wafers have been coated, clean the spinner and stage with Acetone and IPA, making sure not to get any Acetone on the rubber vacuum ring of the stage.
- Close the nitrogen supply valve to the fume cupboard.

Once the wafer has been coated, it can be pre-baked to partially solidify the resist and to remove any excess resist solvents that may be present. This is done by placing the wafer on top of a 180 $^{\circ}C$ hot plate for 1 minute.

### 4.4.3 E-Beam Exposure

After the pre-bake, the wafer is installed in the SEM so that an E-Beam exposure of the resist can be performed. This is carried out as follows:

- Making sure that the SEM is not in use and that the filament is switched off, vent the SEM by holding down the "VENT" button until it lights up. Undo the metal latch on the sample chamber door of the SEM.
- Fetch the sample stage and mount the coated wafer as shown in Figure 4.1(b). If desired, scratch a corner of the wafer with tweezers to create a reference point which may be useful when later looking for structures under a microscope.
- Install the stage inside the SEM sample chamber by gently sliding it into position and connect up the D-connectors.
- Close the door of the sample chamber, fasten the metal latch and evacuate the chamber by holding down the "EVAC" button until it lights up. Change the sign on the door of the chamber to "IN USE".
- Once evacuated, switch on the SEM infrared camera, the Keithley picoammeter and the E-Beam stage and blanker control boxes. Move the blanker to the "Out" position.
- It is important not to move the stage while under partial vacuum as the air conductivity is higher at this pressure and could lead to sparks inside the SEM.
- Set the stage position to the following setup co-ordinates using the SEM interface: $x = -3\ mm$, $y = 3\ mm$ and $z = 43\ mm$. This effectively sets the physical origin co-ordinates from which the E-Beam system can operate.
- Switch on the SEM filament.
- Load up the XENOS pattern generator Exposure Control Program (ECP) and load the "XeDraw2" kernel from "System" $\rightarrow$ "Load XeDraw2 Kernel".

- Reduce the magnification of the SEM and use the coarse focus feature to focus the electron-beam. When combined with the vertical ($z$) position of the stage, the beam should be focused on the surface of the wafer at a working distance of 8 $mm$.
- Find a small feature on the surface of the wafer, increase the magnification and bring the SEM into focus using the fine focus feature.
- Once focused, set the magnification to 300 which gives the required working field size of 300 $\mu m^2$.
- Use the E-Beam joystick stage control to find the bottom left corner of the wafer and move the beam $\sim 3$ $mm$ in from each edge, towards the centre of the wafer.
- Change the position of the E-Beam blanker to "In".
- Load up the required E-Beam control file and map the exposure origin which sets the origin of the exposure in the control file to the current stage co-ordinates. This is done from "Tools" $\rightarrow$ "Map exposure origin".
- Press "Expose..." from the "EBL" menu by going to "EBL" $\rightarrow$ "Expose...". This will begin an exposure with the currently loaded control file.
- Once the pattern is exposed, switch off the filament, move the blanker to the "Out" position and switch off the E-Beam stage and blanker control boxes. Close the ECP software.
- Use the SEM interface to set the $z$ co-ordinate of the stage back to $z = 48$ $mm$.
- Vent the SEM as before, undoing the metal latch.
- Remove the sample stage from the chamber and remove the wafer from the stage.
- Close the door of the SEM specimen chamber, fasten the metal latch, evacuate the chamber and change the sign on the door to "AVAIL".
- Make sure to keep the SEM under vacuum when not in use.

### 4.4.4 Resist Development

Once the exposure is finished, the resist needs to be developed away. The developer used for this process is a mixture of 7 parts IPA to 3 parts water. The initial development process consisted of manually agitating the resist in the developer for 3 minutes using tweezers. However, much better results were obtained by using the ultrasonic bath for 3 minutes instead. After development, the wafer is rinsed in de-ionised water and blow dried using nitrogen gas. At this stage, an optional post-bake can also be performed on the wafer to remove any residual developer and moisture from the resist. This is done by placing the wafer on top of a hot plate at 110 $^{\circ}C$ for 60 seconds. The results of the exposure can then be inspected under a microscope.

## 4.5 Ohmic Layer Development

One of the initial tasks performed using the E-Beam system was the development of ohmic pad features which form the first metallic layer of the Schottky barrier diode, as shown in Figure 4.3. While this process can be (and often is) performed using photolithography, the ultimate goal of this work was to establish a self contained E-Beam fabrication procedure that does not rely on photolithography for any of the steps involved. One of the advantages of using an independent E-Beam process for diode fabrication is that it benefits from superior alignment capabilities compared to optical lithography, which often involves manual alignment of the different diode layers using photomasks. This becomes an important factor as the dimensions of the diode features (especially the sub-micron anodes required for $THz$ frequency applications) decrease to the point that they become difficult to resolve using an optical microscope.

The ohmic pads that were processed using E-Beam lithography which will be described in this section were those of an antiparallel diode structure designed to work at $\sim 1\ THz$. This design was created by Dr. Hui Wang, a researcher working with the MMT group at RAL, and a schematic diagram of the diode geometry can be seen in Figure 4.5.

In this design, the dimensions of the rectangular ohmic pads are $30 \times 10\ \mu m$ with a $5\ \mu m$ mesa gap between them. The semicircular groove for the anode has a diameter of $1.6\ \mu m$

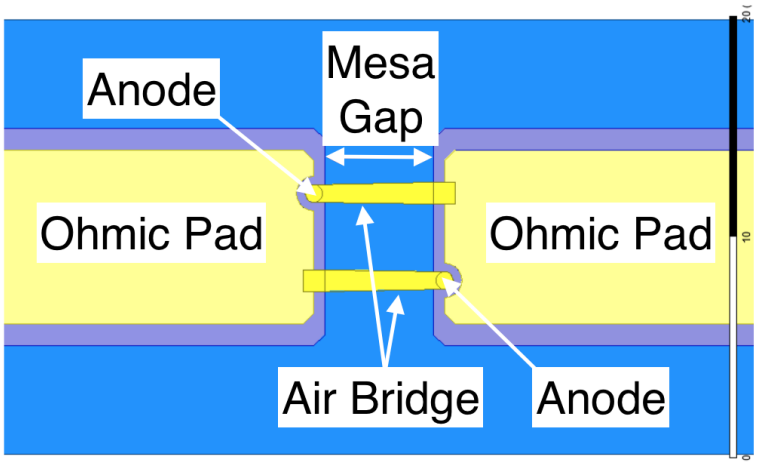


Figure 4.5: Schematic diagram of an antiparallel Schottky diode structure designed to work at $\sim 1\ THz$. The required shape of the ohmic pads, with a small semicircular groove for the anode on each pad can be seen.

while the required diameter of the anode itself is just 0.6 $\mu m$.

To begin with, the ohmic layer pattern file was generated with the ECP pattern editor through a combination of rectangles, trapeziums and semicircular shapes which combined to produce the required geometry shown in Figure 4.5. Once complete, the pattern was exposed onto a GaAs wafer coated with a thin layer of resist as described in Section 4.4. For this exposure, the acceleration voltage on the SEM was set to 30 $kV$ and a spot size of 20 $arb.\ units$ was used. The dwell time at each exposure point was 700 $ns$ which resulted in a dose of $\sim$ 97 $\mu C/cm^2$ with a beam current of $\sim$ 50 $pA$ and a field size of 300 $\mu m^2$. Following the exposure, post-bake and development stages, the results were inspected under an optical (Keyence) microscope and these can be seen in Figure 4.6. In general, this exposure was a success with both ohmic pads exposed in the correct location relative to each other. Furthermore, the results exhibit good definition with clear, smooth edges and the measured dimensions of the pads themselves (and their separation) agree with the specified requirements. However, it is also clear that some fine tuning of the exposure dose was still required since the pads look slightly over-exposed as seen by the rounding of the rectangular corners in Figure 4.6. In addition, the semicircular anode groove was under-exposed and under-developed on this occasion and measurements of the groove dimensions disagree with the requirements. As such, a second exposure of the design was performed

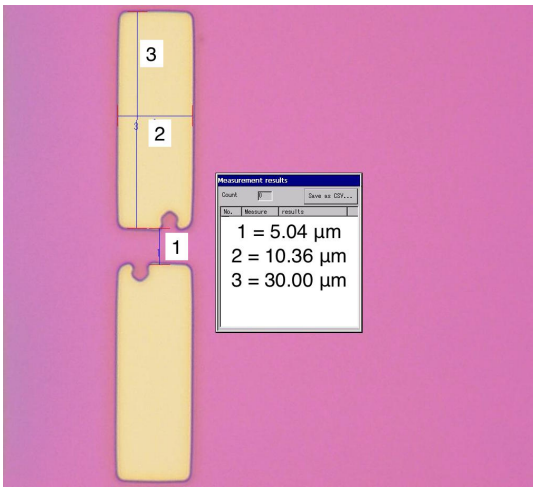


(a) Measured results under 3000 × magnification. The dimensions of the pads match the specifications but there is some over-exposure present which is particularly visible in the corners.

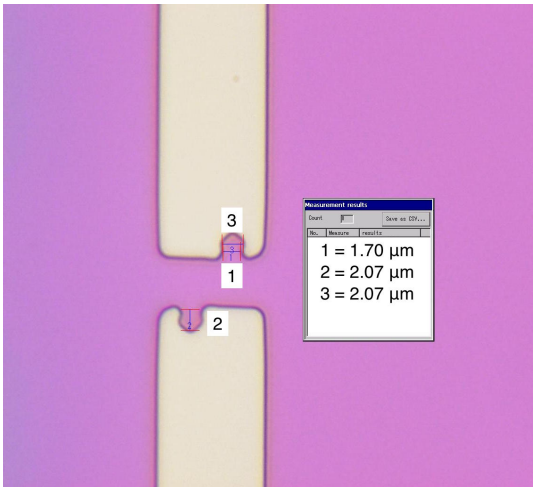


(b) Measured results under 5000 × magnification. The dimensions of the semicircular anode groove do not match the specifications and further work is needed to prevent under-exposure.

Figure 4.6: Optical microscope images of Schottky diode ohmic pads following the first E-Beam exposure. Fine tuning is necessary to prevent over-exposure on the rectangles and under-exposure on the semicircular anode groove.

with the same exposure parameters as before but with the dose adjusted by reducing the dwell time on the rectangular features to 500 $ns$ while the dwell time on the semicircular region was increased to 900 $ns$. The results of this exposure are presented in Figure 4.7.

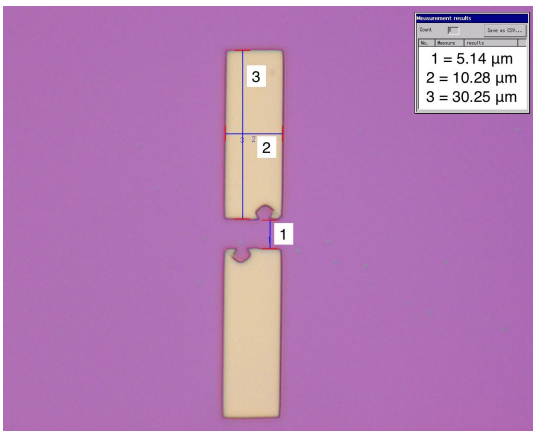


(a) Measured results under 3000 × magnification. The dimensions of the pads match the specifications and exhibit less over-exposure compared to the ones shown in Figure 4.6(a).

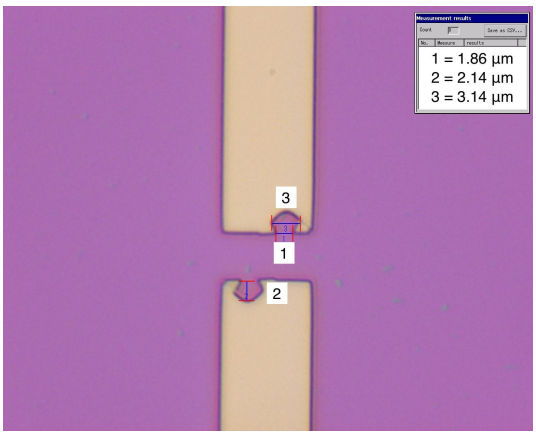


(b) Measured results under 5000 × magnification. The semicircular anode groove is highly under-exposed and deviates significantly from its required dimension and shape.

Figure 4.7: Optical microscope images of Schottky diode ohmic pads following the second E-Beam exposure. The rectangular pads look well developed but despite a longer dwell time, the anode groove is still significantly under-exposed.

The exposure results in Figure 4.7 show much better definition on the rectangular pads with less over-exposure as can be seen by the sharper corners. However, despite using a longer dwell time for the semicircular anode groove it is still significantly under-developed and larger than specified. This effect is even more visible in Figure 4.7 than in the previous result, with the groove not resembling the desired semicircular shape. This may seem like a trivial detail but the shape of the groove will affect the capacitance between the ohmic pad and the anode which will in turn alter the performance of the diode.

To understand why this part of the ohmic layer was not being correctly exposed, an investigation into the E-Beam writing strategy was carried out by exposing an array of semicircular shapes with varying exposure parameters. This led to the discovery that the central part of the semicircles was not being exposed at all, irrespective of the dwell time or exposure dose used. This effect was later found to be caused by a bug in the ECP software which was not opening the blanker when exposing certain types of small shapes or using very short dwell times. The bug was eventually fixed by a software update but in the meantime, the ohmic pad patterns were defined using the GDSII (Graphic Database System) format instead which can be opened in ECP and exported into pattern files to be exposed. The advantage of using this method is that designs can be made using tools other than the ECP editor and approximated using rectangular shapes of various sizes which are not affected by the aforementioned software bug. An example of a GDSII ohmic layer pattern file created with "AutoCAD" and imported into ECP is shown in Figure 4.8.

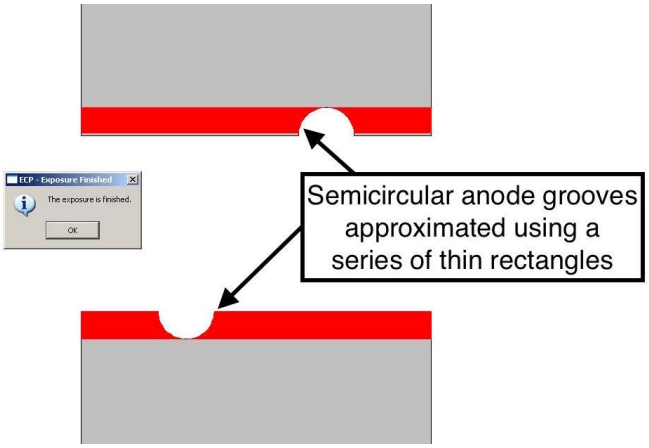


Figure 4.8: Ohmic layer pattern designed using AutoCad and imported into ECP.

Exposure of pattern files created using the GDSII format such as the one shown in Figure 4.8 led to a significant improvement in the shape and definition of the semicircular anode groove while the rest of the ohmic pad also remained well exposed. Following several calibration runs to determine the optimum exposure dose to use, a dwell time of 495 $ns$ (corresponding to a dose of $\sim$ 70 $\mu C/cm^2$) was selected with an acceleration voltage of 30 $kV$, a probe current of $\sim$ 50 $pA$ and the spot size set to 20 $arb.\ units$. With these parameters, an ohmic pad exposure was performed onto a GaAs wafer with the aim of putting metal down onto the developed areas to create ohmic pads as described in Section 4.3. The results of this exposure, following the metallisation stage, are presented in Figure 4.9.

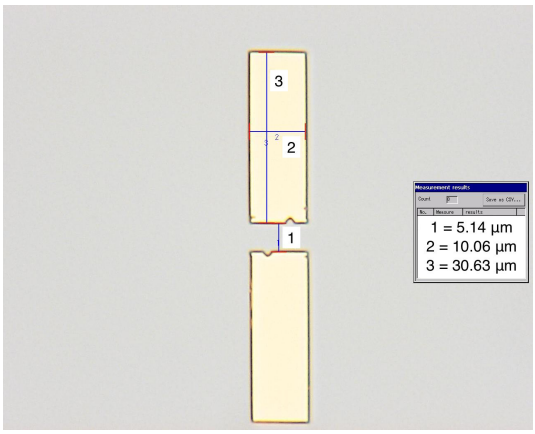


(a) Measured results under 3000 × magnification. The dimensions of the metallised pads match the specifications and exhibit very good definition as can be seen by the straight lines and sharp corners.

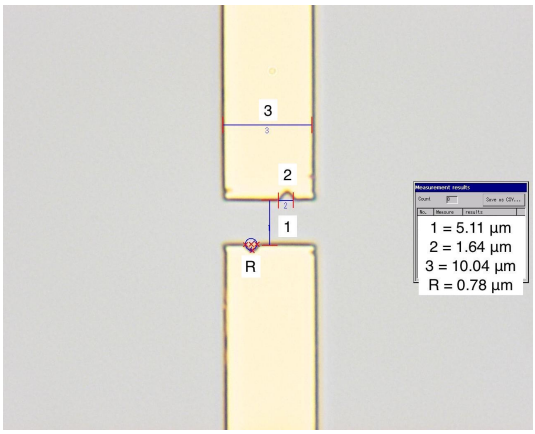


(b) Measured results under 5000 × magnification. The anode grooves have been correctly exposed to exhibit a semicircular shape that matches the required dimension to a few tens of nanometres.

Figure 4.9: Optical microscope images of Schottky diode ohmic pads following E-Beam exposure and metallisation stages. The results show very good definition and agreement with the specified dimensions on both the large rectangular features and the small semicircular anode grooves alike.

The metallised ohmic pads shown in Figure 4.9 exhibit excellent definition on both the rectangular regions as well as the semicircular anode grooves. In addition, the dimensions agree with the required specifications to within a few tens of nanometres. This is a very promising result and also a significant improvement on the exposures shown previously in Figures 4.6 and 4.7. Furthermore, these results were reproducible on the wafer and across different wafers alike showing that the process is reliable and stable. As such, the next step in the diode fabrication process was the development of the sub-micron anode itself.

## 4.6 Sub-Micron Anode Development

Once it was possible to use the E-Beam system to correctly expose and develop the ohmic pads of the diode, it was necessary to establish a process by which sub-micron anodes could also be achieved. This is one of the most crucial steps in the fabrication procedure which requires E-Beam lithography since $THz$ frequency devices require small anode sizes to reduce the overlay capacitance at the anode contact. This is one of the major factors which limits the performance of high-radio-frequency diodes and since optical lithography is constrained to feature sizes of $\sim 0.8\ \mu m$ and above, an E-Beam process for fabricating smaller features must be employed instead.

Therefore, an initial pattern file was created using the ECP editor which consisted of a matrix of circular shapes with each circle representing the Schottky anode contact. The matrix was formed by three rows and nine columns with each row containing a different diameter anode while a varying dwell time was used for the columns. The dwell time was stepped from 2000 to 400 $ns$ in 200 $ns$ increments (left to right) and the three anode diameters were chosen to be 2.0 $\mu m$ (relatively simple to expose), 1.0 $\mu m$ (approximate limit of photolithography) and 0.5 $\mu m$ (approximate size required by the design in Figure 4.5). An exposure of this pattern was performed onto a GaAs wafer coated in a layer of PMMA resist using an acceleration voltage of 30 $kV$, a probe current of $\sim 50\ pA$ and a spot size of 20 $arb.\ units$. The results following the development of the resist can be seen in Figure 4.10.

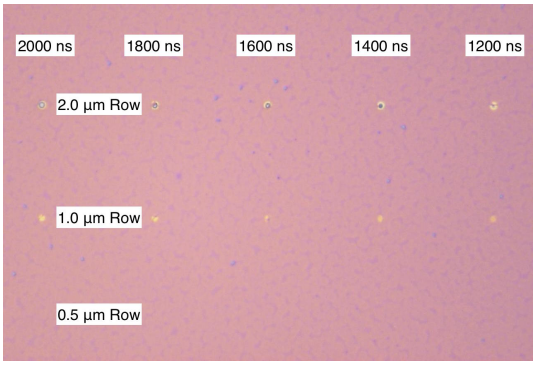


(a) Anode exposure under 2000 × magnification. The 1.0 $\mu m$ row shows partial development while the 0.5 $\mu m$ row has not been developed at all.

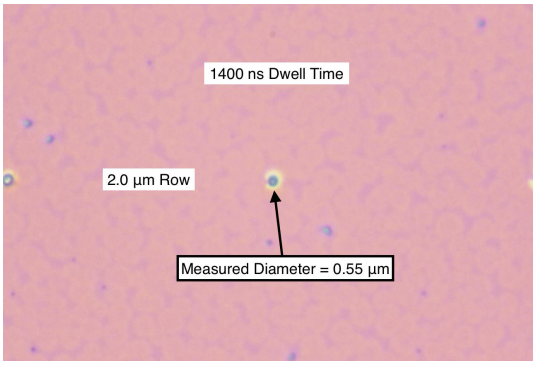


(b) Anode exposure under 5000 × magnification. A 0.55 $\mu m$ diameter anode has been measured but in the 2.0 $\mu m$ row and showing poor definition.

Figure 4.10: Microscope images of anodes following the first E-Beam exposure. Further work is required to improve definition and to develop the 1.0 and 0.5 $\mu m$ diameter rows.

From the results in Figure 4.10(a) it can be seen that the exposure had varying amounts of success with some of the anodes in the 2.0 $\mu m$ diameter row being exposed and partial exposure of anodes in the 1.0 $\mu m$ row. However, none of the anodes from the 0.5 $\mu m$ row have been developed despite using dwell times as long as 2000 $ns$. One of the anodes in the 2.0 $\mu m$ row was measured to have a diameter of 0.55 $\mu m$ when using a dwell time of 1400 $ns$ but it showed poor definition as can be seen in Figure 4.10(b). Furthermore, using a shorter dwell time as a means to control the anode dimension is not an ideal solution since this process is not reliable.

In an attempt to improve on both the anode definition and the general development of smaller features, another pattern of circular anodes was designed using the GDSII file format which had shown a dramatic improvement when developing the ohmic layer of the diode. This pattern consisted of 3 matrices with a different anode diameter in each matrix. A $5 \times 5$ matrix was used for 0.5 and 1.0 $\mu m$ diameter anodes while a $3 \times 3$ matrix was employed for anodes with a 2.0 $\mu m$ diameter. This would allow for a comparison of reproducibility between anodes of the same size. As before, the pattern was exposed onto a GaAs wafer using an acceleration voltage of 30 $kV$, a probe current of $\sim$ 50 $pA$ and a spot size of 20 $arb.\ units$. The dwell time was varied from 200 to 2000 $ns$ in 200 $ns$ increments and after inspecting and measuring the developed results, it was found that 200 $ns$ ($\sim$ 28 $\mu C/cm^2$ dose) produced optimal anodes which are presented in Figure 4.11.

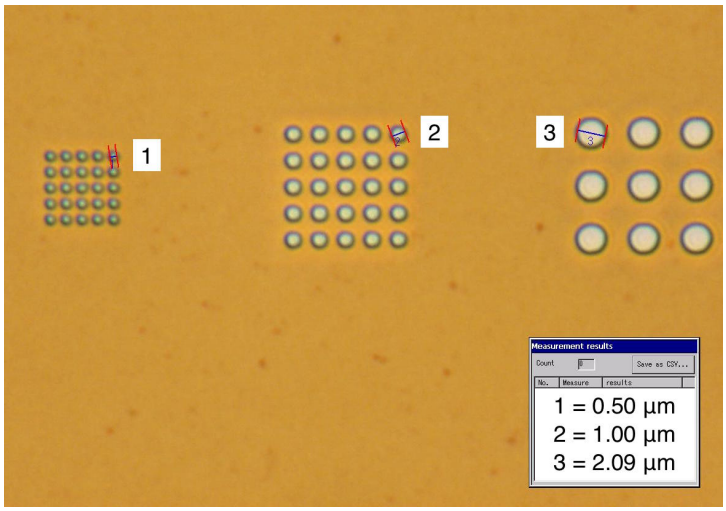


Figure 4.11: A microscope image of anodes following E-Beam exposure of the GDSII pattern file. The results show excellent definition and agreement with all 3 of the specified diameters.

It can be seen that the exposed anodes in Figure 4.11 show much better definition compared to those in Figure 4.10 and all three sizes have successfully been developed. Furthermore, the measured diameters agree very well with the 0.5, 1.0 and 2.0 $\mu m$ specification and the anodes within each matrix are highly reproducible as well. Therefore, it has been shown that using the GDSII file format to define both the anode and ohmic pad layers produced significantly better results than using the ECP editor. Now that it was possible to create sub-micron anodes, the next step in the fabrication process was to align them to the semicircular anode grooves on the ohmic pads.

## 4.7 Alignment

One of the most important aspects of E-Beam fabrication is the ability to successfully and reliably align the various device layers to reference marks on the surface of a wafer. This ensures that diode features are located in the correct place relative to each other.

For the purposes of the work described here, this meant being able to align the Schottky diode ohmic pads to the centre of an exposure field defined by a set of four alignment cross targets and then align sub-micron anodes (as well as a suspended air-bridge) to the semicircular grooves which can be seen in Figures 4.5 and 4.9.

The alignment procedure is carried out by the ECP software in two stages. These are both described in detail in XENOS (2010) and as such will only briefly be outlined here.

To begin with, ECP performs a coarse global alignment mark scan. This is done by manually moving the stage so that one of the large, Global Alignment crosses shown in Figure 4.4 is positioned in the centre of the SEM image scan. When the cross is approximately in the right location, a mark detection is performed which carries out a user-specified series of line scans over the four arms of the cross. The position of the mark is detected by recording the secondary electron signal since the edges of the cross usually show up as distinct peaks in the scan signal. For such marks, a threshold method is employed to determine the edge position from which the centre of the mark is calculated. A number of different parameters (e.g. scan length, scan pitch, number of scans, scan increment, detection threshold and several others) can be used in combination to improve the mark detection. Once one of

the global marks is successfully detected by the system, the stage is moved to its location at which point the exposure origin is mapped. This sets the origin of the local co-ordinate system for the exposure (i.e. the origin of the write field of the wafer) in the control file to the physical co-ordinates of the stage. All of the other co-ordinates used in the exposure are then calculated relative this point. From here, the stage moves to the location of the other global alignment crosses on the wafer and a similar mark detection is performed at each point. With each detection, the software compares the real location of the mark to its expected position and applies any correction factors necessary for offset, rotation and scaling in both the $x$ and $y$ directions.

Once the global alignment has finished, the stage is moved to the location of the first exposure field which is defined by a set of four "local" alignment (chip) marks. These marks can have any arbitrary geometric shape but in the case of the work described here they were simply slightly smaller crosses. At this point, a fine alignment is performed by detecting the four chip marks using a two-dimensional image scan and comparing the scanned result with a pre-defined model of the target mark. The comparison is done by computing the correlation amplitude between the scan and the model and if this is above a user-specified threshold, the mark detection is successful and the field can be calibrated for exposure. When the system performs a series of chip mark detections for the purposes of a fine alignment, the scan is carried out by deflecting the beam to the location of the marks, rather than by moving the stage, which avoids any inaccuracies that may be caused by the motorised stage movement. Following the fine alignment, the required pattern is exposed.

This process was initially performed in an attempt to align a number of anodes to ohmic pads which had previously been exposed and metallised on a GaAs wafer. The result of the exposure can be seen in Figure 4.12(a) which shows that while the anode has been exposed in the correct $y$ location, there is a small ($\sim 3\ \mu m$) offset in the $x$ direction. To check whether this offset was systematic or the result of some gradual drift, a diagonal row of anodes was exposed such that the position of the bottom left anode was specified to be in the centre of the bottom left chip mark. It can be seen from the result in Figure 4.12(b) that all of the anodes are shifted slightly to the right ($x$ direction offset) but correctly exposed in the $y$ direction.

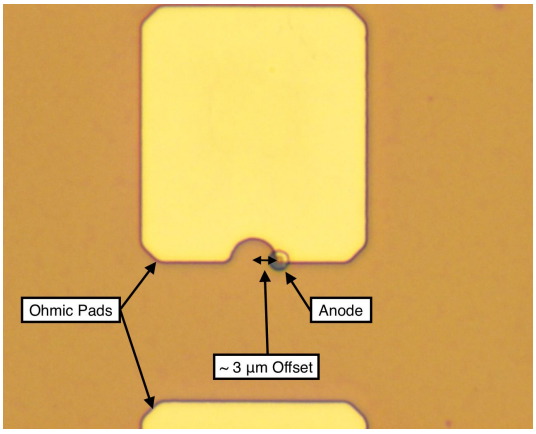


(a) Anode alignment under 5000 × magnification. A small offset can be seen in the $x$ direction.

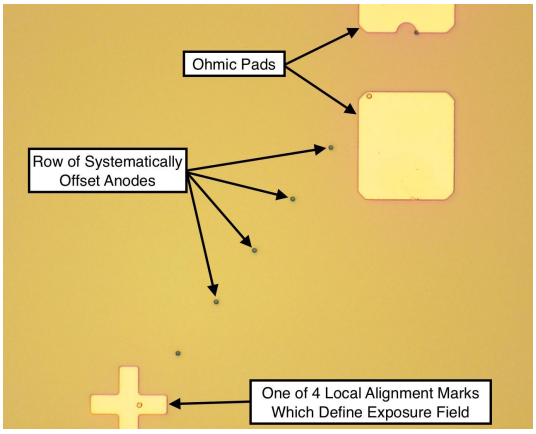


(b) Anode alignment under 2000 × magnification. All anodes are offset by the same amount.

Figure 4.12: Microscope images of an initial attempt to align anodes to the semicircular ohmic pad groove. A small, $\sim 3\ \mu m$ offset is present on all anodes in the $x$ direction.

This offset was eventually determined to be caused by an issue with the image scan which is used to locate the positions of the small chip marks on the wafer. The scanned image was consistently shifted by a few ($\sim 3$) microns in the $x$ direction which caused the exposure error. To overcome this problem, the image scan was used as an effective secondary coarse alignment to determine the approximate chip mark positions following a mechanical stage movement. A line scan over the small crosses (similar to the global mark detection) was then used to determine their true positions. This led to much better alignment results and the removal of the $x$ direction offset as can be seen in the results in Figure 4.13.

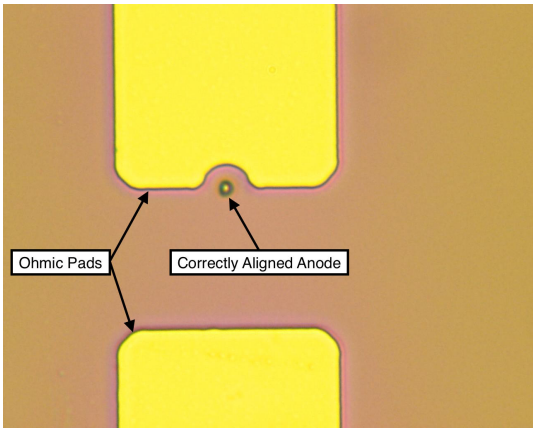


(a) Anode alignment under 5000 × magnification. The anode has been correctly aligned.

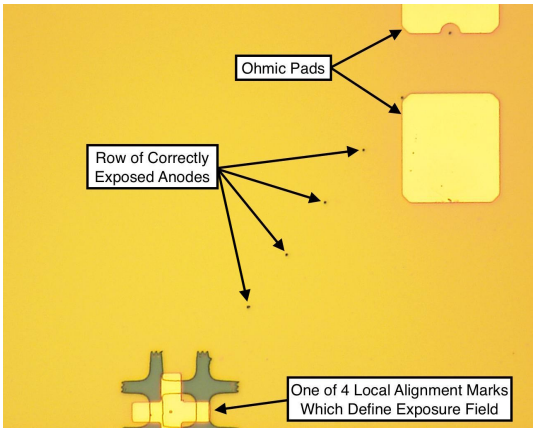


(b) Anode alignment under 2000 × magnification. All anodes have been exposed as specified.

Figure 4.13: Microscope images of anode alignment after using both image and line scans for local chip mark detection. The $x$ direction offset previously observed has been removed.

## 4.8 Suspended Air Bridge Development

With the alignment procedure established such that different diode layers could correctly be aligned to the local chip marks on the wafer (and each other), the next stage of the fabrication process required a technique to create a suspended air-bridge which would connect the Schottky contact to the anode pad across a surface etched gap as shown in Figure 4.3.

These bridges were realised through a bi-layer process in which the wafer is coated with two different types of resist (one on top of the other) that have different molecular weights and therefore require different exposure doses. The resist on the bottom is only exposed over the Schottky contact (anode) area and the area that will become the anode pad while the resist on the top is exposed over the pad, the anode and the region that links the two together. In this manner, the bottom resist can act as a support structure on top of which the bridge is then metallised. Such processing leads to a structure that is actually suspended above the oxide surface of the GaAs wafer following a lift-off process. This helps to further reduce the parasitic capacitance between the bridge and the $n^+$ layer of the wafer which is difficult to achieve through photolithography since this technique fabricates the bridge directly on top of the oxide layer of the wafer.

To implement the bi-layer process, a GaAs wafer was cleaned and prepared as previously described in Section 4.4 before being coated with "950 PMMA A7" resist for the bottom layer and an "MMA 8.5 MAA" copolymer resist for the layer on top. The 950 PMMA A7 was spun for 60 seconds at a speed of 3000 $rpm$ which led to a thickness of $\sim 600\ nm$. After this, the wafer was baked for an hour in an oven at 180 $^{\circ}C$ before having the MMA 8.5 MAA copolymer resist spun on top of the first layer at a speed of 2200 $rpm$ for 60 seconds resulting in a top layer thickness of $\sim 400\ nm$. The wafer was then baked at 180 $^{\circ}C$ for another hour and loaded into the SEM so that a pattern file containing the anode, the anode pad and the bridge could be exposed. The exposure was carried out with an acceleration voltage of 30 $kV$, a beam current of $\sim 50\ pA$, a spot size of 20 $arb.\ units$ and a dwell time of 4000 and 700 $ns$ (or a dose of 555.6 and 97.2 $\mu C/cm^2$) respectively for the bottom and top resist.

After exposure, the resist was developed for 60 seconds in Methyl IsoButyl Ketone (MIBK) developer mixed in a 1 : 3 ratio of MIBK to IPA. The wafer was then rinsed in

IPA for 60 seconds and dried using nitrogen gas. Following the development process, a thin layer of gold was deposited onto the wafer so that the results could be inspected using the SEM prior to lift-off. Two images showing the metallised surface of the GaAs wafer after an exposure involving the bi-layer resist process can be seen in Figure 4.14.

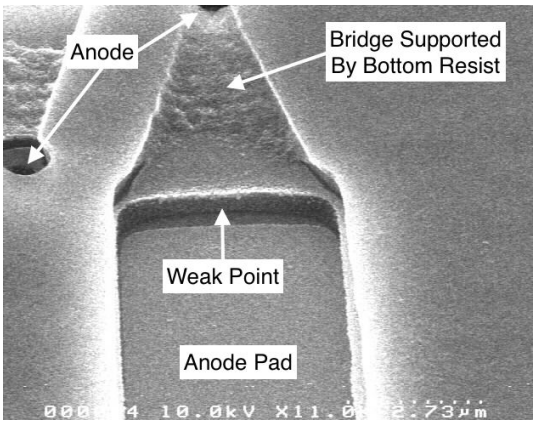


(a) SEM image of Schottky diode bridge structure at 11000 × magnification.

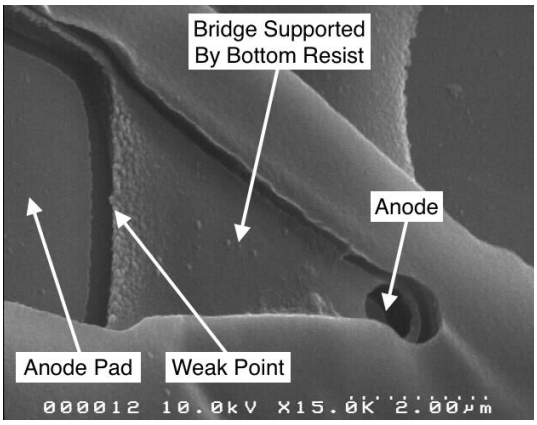


(b) SEM image of Schottky diode bridge structure at 15000 × magnification.

Figure 4.14: SEM images of the diode bridge structure including the anode pad, the anode itself and the bridge that is supported by a bi-layer resist exposure process. A weak point between the bridge and anode pad is suspected to cause the bridges to break after lift-off.

The SEM images in Figure 4.14 show that the exposure was a success with a clearly visible anode, anode pad and a raised region connecting the two which supports the bridge. As such, the wafer was removed from the SEM and a $\sim 300\ nm$ thick layer of gold was electroplated onto its surface which was to form the bridge layer of the device. The undeveloped resist and excess metal was then lifted off in Acetone for $\sim 5$ minutes.

However, when the wafer was inspected following lift-off it was discovered that none of the bridges had been left in place, with just the anode and the anode pad connected to the surface of the GaAs. This was suspected to be caused by the sharp discontinuity between the surface of the wafer and the resist acting as the support structure for the bridge. This is a plausible explanation since the electroplating process is highly directional and deposits metal in a vertical manner which would have created a fragile weak point at the discontinuity which is shown in Figure 4.14.

To reduce the sharpness of the discontinuity, a resist re-flow process was employed following the E-Beam exposure stage which would create a smoother resist profile for the

bridge to be deposited onto. This process was carried out by placing the wafer on top of a 130 $°C$ hot plate for 135 seconds after the exposed resist had been developed. Doing so heats up the resist and causes it to slowly start to flow and round slightly at the edges. This removes sharp discontinuities and fragile weak points following electroplating. However, this is an extremely delicate process because if the resist flows too much then the definition of any exposed shapes will be lost. The results following metallisation of resist that had been subjected to a re-flow process is shown in two SEM images in Figure 4.15.

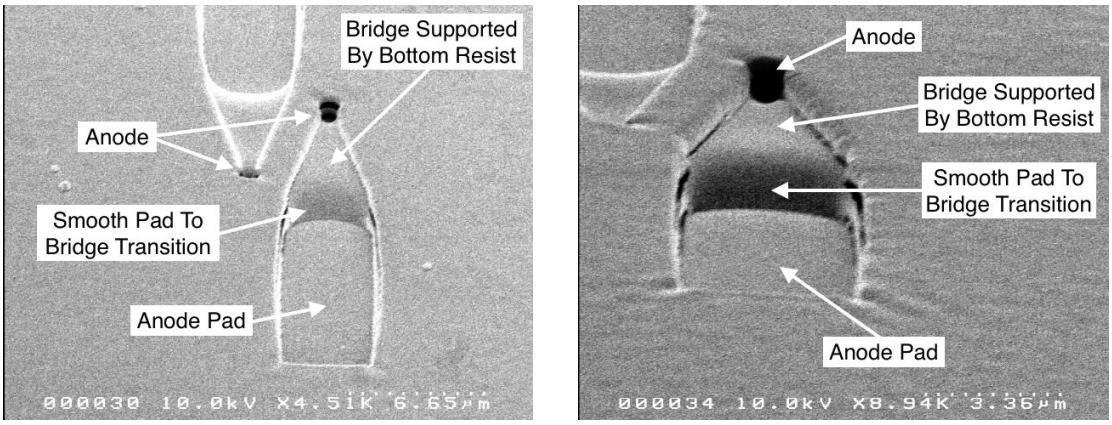


(a) SEM image of Schottky diode bridge structure at 4510 × magnification following resist re-flow.

(b) SEM image of Schottky diode bridge structure at 8940 × magnification following resist re-flow.

Figure 4.15: SEM images of the diode bridge structure including the anode pad, the anode itself and the bridge that is supported by a bi-layer resist exposure process. A smooth transition between the anode pad and bridge has been achieved by re-flowing the resist.

Compared to the images in Figure 4.14 the results in Figure 4.15 show a much smoother transition from the anode pad to the bridge, without any sharp discontinuities. This was achieved by re-flowing the exposed resist following development before a $\sim 300\ nm$ thick layer of gold was once again electroplated onto the surface of the wafer. After the $\sim 5$ minute Acetone lift-off process the wafer was again inspected using the SEM and the results presented in Figure 4.16 show a series of metallic air-bridges successfully suspended $\sim 600\ nm$ above the surface of the GaAs wafer. Furthermore, this process is reproducible with a line of 3 bridges shown in Figure 4.16(a) while the anode diameter in Figure 4.16(b) has been measured to be $\sim 0.6\ \mu m$ as required by the design in Figure 4.5.

This is an encouraging result which demonstrates that E-Beam lithography is a viable tool for manufacturing suspended air-bridges required by $THz$ frequency Schottky diodes.

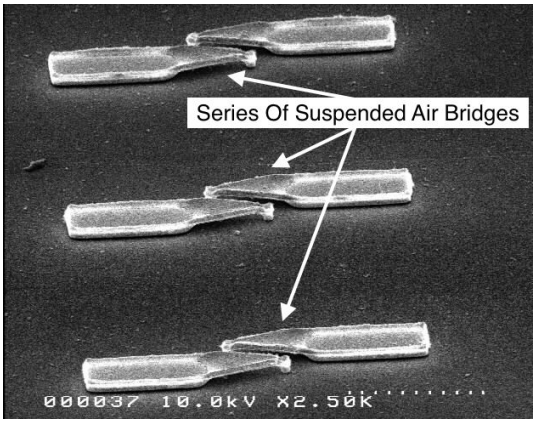


(a) SEM image of Schottky diode bridge structure at 2500 × magnification following resist lift-off.

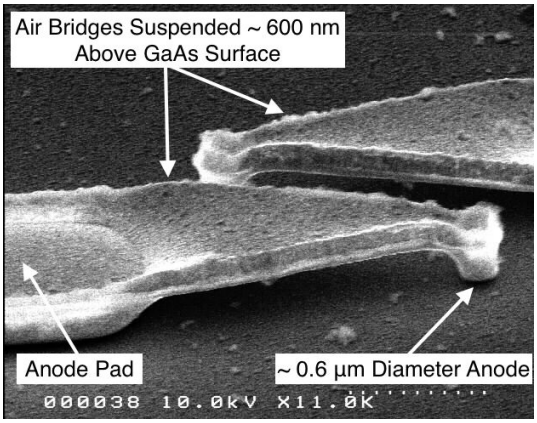


(b) SEM image of Schottky diode bridge structure at 11000 × magnification following resist lift-off.

Figure 4.16: SEM images of the diode bridge structure including the anode pad, the anode itself and an air-bridge that is suspended $\sim 600\ nm$ above the surface of the GaAs wafer.

## 4.9 Experimental Testing of Initial Devices

Having established an E-Beam lithography fabrication process for all the metallic layers of the device including the suspended air-bridge described in the previous section, a number of diodes were fabricated using the process outlined in Section 4.3. These devices were initially made using a combination of E-Beam and photolithography, with the E-Beam process used to define the circular anodes while optical lithography was employed for the ohmic pads and the planar bridge. This was partly due to the fact that it was initially challenging to align the suspended air-bridge to the target crosses on the wafer as it was difficult to see and detect chip marks when implementing the bi-layer resist process. This was eventually overcome by fine tuning the detection threshold parameters but the first working devices were made via a combination of the two lithography techniques.

Once fabricated and channel etched, the diodes were tested on wafer by having their Current-Voltage (I-V) curves measured using a 4-point probe method which uses separate pairs of voltage and current sensing electrodes to make more accurate measurements than the simpler and often employed 2-point technique (Maas, 1992). These measurements were carried out by Dr. Diego Pardo, a researcher working with the MMT group at RAL, for a number of diodes with anode diameters in the range of $0.6 - 1.2\ \mu m$.

The measured I-V characteristic of the diodes was compared to simulated theoretical

predictions for each of the anode diameters and the results are presented in Figure 4.17(a) while a SEM image of one of the devices is shown in Figure 4.17(b). The circles in Figure 4.17(a) represent the current response to an applied bias voltage while the solid lines show theoretical diode performance based on thermionic emission, electron tunnelling and barrier lowering due to the image force which are the three major current transport mechanisms present in Schottky diodes (Padovani & Stratton, 1966; Sze & Ng, 2006).

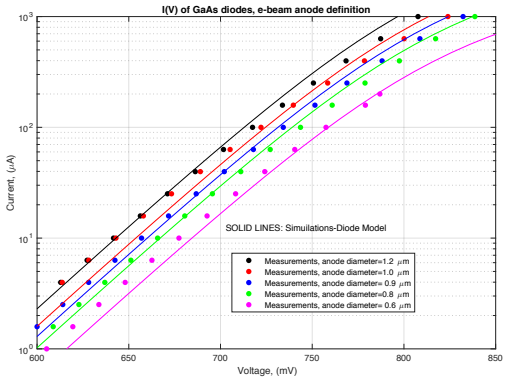


(a) A comparison of measured I-V curves with theoretical predictions for Schottky diodes with anode diameters in the range of $0.6 - 1.2\ \mu m$.

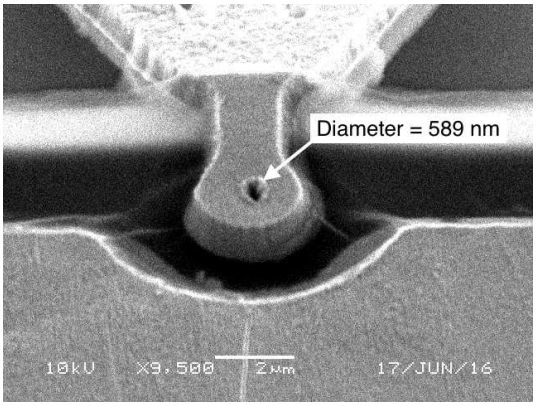


(b) SEM image of Schottky diode made using a combination of E-Beam and photolithography at 9500 × magnification.

Figure 4.17: Measured performance of devices with anode diameters between $0.6 - 1.2\ \mu m$ made using E-Beam and photolithography alongside a SEM image of an example device. Errors on each measurement point are negligible, i.e. within the symbol size.

The measurements in Figure 4.17(a) show very promising results, especially for the smaller 0.6, 0.8 and 0.9 $\mu m$ anode diameters which closely agree with their predicted performance across the bias voltage range tested. There is some discrepancy between simulation and performance of the 1.0 and 1.2 $\mu m$ anode diodes (at lower and upper ends of the voltage range respectively) with work currently ongoing to determine the cause of these issues.

In addition to these devices, a wafer of Schottky diodes was also fabricated using entirely E-Beam processing once it was possible to successfully align the anode and suspended airbridge to the ohmic pads using the bi-layer resist process. Following fabrication and channel etch, these diodes were once again tested on wafer by Dr. Diego Pardo using the 4-point probe technique and the measured I-V curve compared with simulations for anode diameters of 0.8 $\mu m$. The results of these measurements are shown in Figure 4.18(a) with a SEM image of the device presented in Figure 4.18(b).

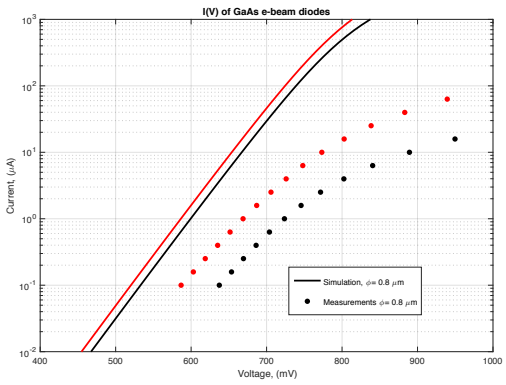


(a) A comparison of measured I-V curves with theory for a 0.8 $\mu m$ anode diameter Schottky diode.

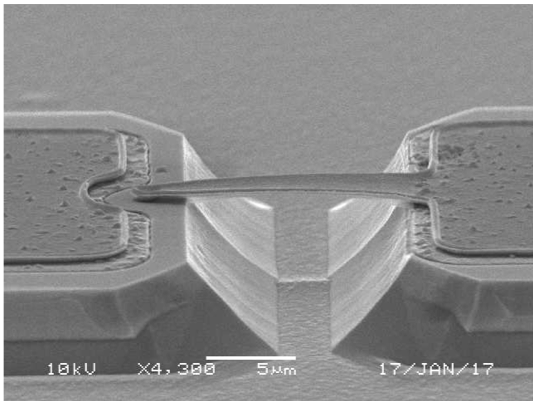


(b) SEM image of Schottky diode made entirely using E-Beam lithography at 4300 × magnification.

Figure 4.18: Measured performance of a Schottky diode made using E-Beam lithography alongside a SEM image of the device. Errors on each measurement point are negligible.

While it has been possible to acquire an I-V curve for a Schottky diode processed solely with E-Beam lithography, there is a significant deviation from the simulated performance shown in the result in Figure 4.18(a), with a consistently lower than expected current observed across the entire voltage range tested.

One possible explanation for this was the fact that the diodes made previously (using a combination of E-Beam and photolithography) were fabricated on a GaAs wafer coated with an insulating layer of parylene rather than $SiO_2$. Parylene is sometimes used instead of an oxide layer because it helps to prevent the device short circuiting during the assembly process. However, it is also easier to etch through than oxide and may therefore be giving better performance. Alternatively, there could have been an issue with the oxide etch process itself which is not always reliable, especially if all the resist is not completely removed. Even a very thin layer of resist (a few $nm$) left behind after development could have a detrimental effect on the oxide etch and lead to the sub-optimal diode performance observed in Figure 4.18(a). However, following further investigation, it was determined that the most significant reason for the diminished performance in Figure 4.18(a) was GaAs wafer damage caused by high-energy electrons impacting the surface of the wafer, thereby damaging the material and altering its conductive properties. This was resolved by tuning the exposure parameter settings such as the electron-beam energy, resist combination and by using a sacrificial layer to limit the depth that the electron-beam could penetrate into the GaAs.

## 4.10 E-Beam Tripler RF Measurements at 300 GHz

Once the E-Beam fabrication parameters had been optimised such that the GaAs wafer properties were not being compromised during exposure, a number of E-Beam devices were fabricated in an antiparallel diode configuration (shown in Figure 4.5) so that their RF performance as frequency multipliers (triplers) could be measured. This is an important step in demonstrating the validity of the diodes as high-frequency LO sources for applications such as heterodyne radio astronomy.

An example of one of these devices can be seen in Figure 4.19. This optical microscope image shows the E-Beam fabricated GaAs diode mounted in a waveguide block along with the low and high-frequency waveguide probes as well as the required impedance-matching circuitry. The whole structure is flip-chip soldered down within a small groove that joins the two waveguides of the block. The circuit benefits from being completely passive, with the antiparallel diode structure generating the odd (in this case third) harmonic without the need for any DC biasing (Kollberg & Rydberg, 1989; Nilsen et al., 1993).

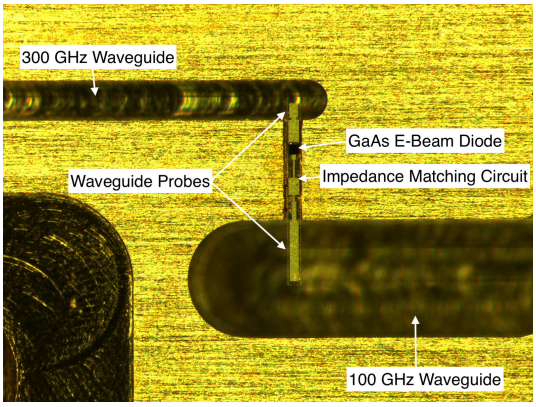


(a) Optical microscope image of an E-Beam fabricated GaAs tripler diode mounted in a 300 $GHz$ waveguide block.

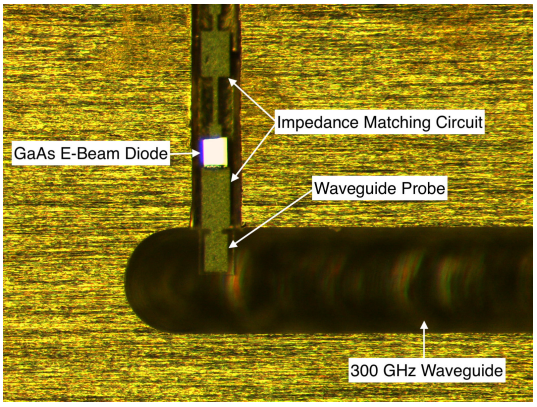


(b) Zoomed in image showing light reflecting off the GaAs diode and the high-frequency side of the waveguide block.

Figure 4.19: Optical microscope images showing one of the E-Beam multiplier diodes along with its impedance-matching circuitry and waveguide probes mounted in a 300 $GHz$ block.

With the tripler diode mounted within the waveguide block as shown in Figure 4.19, the block was incorporated into a Local Oscillator chain such that its input was connected up to a $75 - 110$ $GHz$ TeraTech tripler while its output was linked to an Erickson PM4 power meter using a waveguide transition as shown in Figure 4.20.

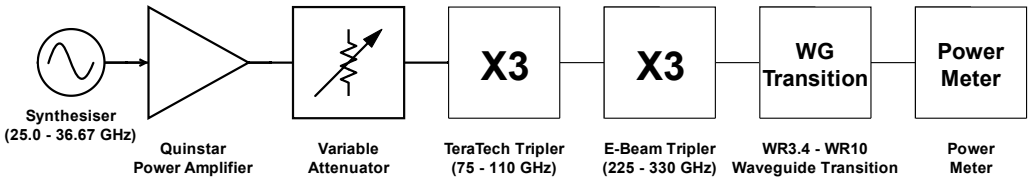


Figure 4.20: Schematic diagram showing the E-Beam tripler incorporated in an LO chain for RF power measurements.

In this configuration, the output power of the GaAs E-Beam device was measured as a function of frequency between $225-330\ GHz$, using a constant input power level of 10 $mW$ going into the E-Beam tripler at every measurement frequency. This was achieved with a commercially available Quinstar power amplifier and a variable attenuator. The results of these measurements, which were carried out by Dr. Byron Alderman at the Rutherford Appleton Laboratory, can be seen in Figure 4.21 and Table 4.1.

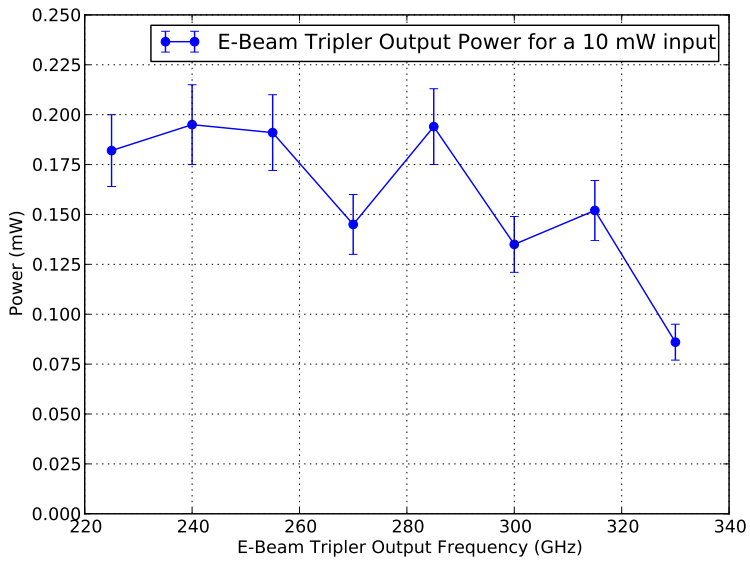


Figure 4.21: Measured output power of a Schottky diode frequency tripler fabricated using E-Beam lithography between $225-330\ GHz$. The multiplier was supplied with a constant input power of 10 $mW$ at every measurement frequency.

The plot in Figure 4.21 shows that the E-Beam tripler, when incorporated into a Local Oscillator chain, exhibits very good RF performance. The measured power is generated by the third harmonic of the diode multiplier. Due to the antiparallel design of the diode,

| Tripler Output Frequency ($GHz$) | Tripler Output Power ($mW$) | Tripler Efficiency (%) [Output Power/10 $mW$] $\times$ 100 |
|---|---|---|
| 225.0 | 0.182 $\pm$ 0.018 | 1.82 |
| 240.0 | 0.195 $\pm$ 0.020 | 1.95 |
| 255.0 | 0.191 $\pm$ 0.019 | 1.91 |
| 270.0 | 0.145 $\pm$ 0.015 | 1.45 |
| 285.0 | 0.194 $\pm$ 0.019 | 1.94 |
| 300.0 | 0.135 $\pm$ 0.014 | 1.35 |
| 315.0 | 0.152 $\pm$ 0.015 | 1.52 |
| 330.0 | 0.086 $\pm$ 0.009 | 0.86 |

Table 4.1: Measured RF output power generated by the E-Beam fabricated Schottky diode tripler between $225 - 330$ $GHz$ along with the corresponding efficiency given a 10 $mW$ power input at each measurement frequency.

even harmonics of the input fundamental are suppressed from propagating in the output waveguide while higher order odd harmonics are filtered out by the diode capacitance (which has been optimised for the third harmonic) as well as the matching circuit following the diode itself (Pavlidis, 2021). These RF measurements were carried out with an Erickson PM4 waveguide power meter that had been cross-referenced with a calibrated power sensor to make sure that the PM4 gave readings that were accurate to within 10 %. As such, an uncertainty of $\pm$10 % has been placed on the measured numbers presented in Figure 4.21 and Table 4.1. The results show that the device is tunable and can operate across a broad frequency range of 105 $GHz$, which corresponds to a bandwidth of approximately 38 % at the central (277.5 $GHz$) frequency of operation. As well as this, the tripler produces between $\sim$ 0.13 and $\sim$ 0.2 $mW$ of RF power in the $225 - 315$ $GHz$ frequency range, which drops to approximately 0.09 $mW$ at 330 $GHz$. As can be seen in Table 4.1, this translates to a tripler efficiency of between 1 and 2 % in the $225-315$ $GHz$ frequency range and $\sim$ 0.9 % at 330 $GHz$. This is comparable to current "state-of-the-art" efficiencies of $1-3$ % reported for similar full-band varistor mode diodes operating at these frequencies (Radiometer Physics, 2021; Virginia Diodes, 2021). While the conversion efficiency of the device presented here is slightly lower than that of similar diodes produced by companies such as VDI, it should be noted that the exact fabrication techniques employed by such commercial companies are not public knowledge and as such, this is an important and novel result for diode development

using E-Beam technology. Furthermore, the measured RF power output presented here should be more than adequate to make this tripler a viable LO source for the majority of heterodyne receiver applications which employ SIS tunnel junction mixers for frequency down conversion.

Overall, the results of this work have demonstrated that the electron-beam lithography technique can be successfully employed to fabricate Schottky diode-based frequency multipliers that operate as effective, high-frequency Local Oscillator sources. Because the feature dimensions that are achievable with this fabrication technique are not diffraction limited to $\sim 0.8\ \mu m$, as is the case with optical photolithography, it provides a highly promising route for realising the ever decreasing anode diameters ($\leq 0.6\ \mu m$) and feature sizes that are required by Schottky diode-based frequency multipliers at frequencies approaching the Terahertz regime.

## 4.11 Conclusions

The work presented in this chapter has demonstrated the use of E-Beam lithography for the development and fabrication of Schottky barrier diodes for use in high radio frequency applications. Because the performance of such devices is strongly limited by the parasitic capacitance at the anode contact which arises at $THz$ frequencies, they require small anode diameters ($\leq 0.6\ \mu m$) which can only be reliably achieved using E-Beam processing since diffraction effects limit feature dimensions of photolithography to $\sim 0.8\ \mu m$ in length. Another source of unwanted capacitance comes from the highly doped $n^+$ layer of the GaAs wafer and the metal bridge that connects the anode to the anode pad. This is usually mitigated using a channel etch to remove GaAs directly below the bridge. However, by employing the bi-layer resist process described in this chapter, it is possible to create an air-bridge that is suspended above the surface of the wafer to further reduce this capacitance.

Apart from the bridge and anode definition, the E-Beam system has also been shown to be effective at writing the ohmic pad layer, which allows the entire device to be created without relying on photolithography. This is useful from a practical point of view since it allows the process to be streamlined and confined to one type of fabrication.

A series of diodes were initially made using a combination of E-Beam and photolithography. They exhibited promising I-V characteristics, especially for the smaller anode diameters of 0.6, 0.8 and 0.9 $\mu m$. In addition, several devices were created using E-Beam lithography alone and, after the exposure parameters had been optimised, an example of one of these devices was incorporated into an RF circuit and mounted within a waveguide block so its performance as part of a Local Oscillator chain could be measured. The RF results showed excellent performance between $225-330\ GHz$ where the E-Beam fabricated, Schottky diode-based frequency tripler produced $\sim 0.1-0.2\ mW$ of power, demonstrating that the multiplier could be used as part of an LO chain in a heterodyne receiver system, such as the ones employed in high-frequency radio astronomy. The power conversion efficiency of the measured device was $\sim 1-2\ \%$, which is comparable to current "state-of-the-art" numbers reported by commercial companies such as RPG and VDI (Radiometer Physics, 2021; Virginia Diodes, 2021). Given that such companies do not tend to make details of their fabrication processes widely available, the work in this chapter has not only helped to bring the technical knowledge of the E-Beam lithography fabrication technique into the public domain, but has also provided an important and viable route for realising the necessary small-feature diodes for multiplier and mixer components at even higher frequencies.

# Chapter 5

# Terahertz Receiver Development

## 5.1 Introduction

In astronomy, the sub-millimetre part of the electromagnetic spectrum remains relatively unexplored which makes it a highly interesting area to study. One of the major facilities designed to observe the universe at sub-mm wavelengths is the Atacama Large Millimetre/sub-millimetre Array (ALMA) which looks set to dominate the field for the foreseeable future (Wootten & Thompson, 2009). As such, there is considerable interest in developing some of the technology used by this telescope to maximise its scientific output.

One of the exciting scientific objectives of ALMA is to observe the cold gas kinematics of Giant Molecular Clouds (GMCs) which collapse to form new stars (Richer, 2005). When stars initially form, the visible light that they emit is absorbed by surrounding gas and dust which makes these stellar nurseries opaque to visible wavelength telescopes. However, since this radiation is later re-emitted at sub-mm wavelengths, it can be detected by facilities such as ALMA in order to improve the understanding of kinematics of star forming regions as well as star formation as a whole.

The ALMA telescope itself is located on the Chajnantor plateau in Chile at a height of $\sim 5000\ m$ above sea level. This is one of the driest observing locations on the planet which is ideal since water vapour heavily attenuates sub-mm signals (Bustos et al., 2014). Nonetheless, because the atmospheric transmission is not perfect, the telescope is designed to work in 10 different, discrete frequency bands which are dictated by the atmospheric

transmission windows at the site. These frequency bands (European Southern Observatory, 2018) are presented in Table 5.1 along with their noise temperature specification and the receiver technology being used.

| ALMA Band | Frequency Range ($GHz$) | Wavelength Coverage ($mm$) | Noise Temperature Specification ($K$) | Receiver Technology |
|---|---|---|---|---|
| 1 | $35-50$ | $6.0-8.5$ | 26 | HEMT |
| 2 | $65-90$ | $3.3-4.5$ | 47 | HEMT |
| 3 | $84-116$ | $2.6-3.6$ | 60 | SIS |
| 4 | $125-163$ | $1.8-2.4$ | 82 | SIS |
| 5 | $163-211$ | $1.4-1.8$ | 105 | SIS |
| 6 | $211-275$ | $1.1-1.4$ | 136 | SIS |
| 7 | $275-373$ | $0.8-1.1$ | 219 | SIS |
| 8 | $385-500$ | $0.6-0.8$ | 292 | SIS |
| 9 | $602-720$ | $0.4-0.5$ | 261 | SIS |
| 10 | $787-950$ | $0.3-0.4$ | 344 | SIS |

Table 5.1: Main properties of the 10 observing bands on the ALMA telescope.

It can be seen that the majority of the observing bands on ALMA (Bands $3-10$) employ Superconductor-Insulator-Superconductor (SIS) mixers as the receiver technology of choice for detecting sub-mm radiation. This is because such detectors are capable of recording the amplitude as well as the phase information of incoming astronomical signals, both of which are necessary for performing interferometry and high resolution spectroscopy which can in turn be used to map the velocities and motions of star forming regions in the local universe.

Because of the considerable scientific interest in sub-mm astronomy, there is subsequent motivation to develop heterodyne receiver systems that can operate at these frequencies with unparalleled sensitivity, making them operational at frequencies approaching and even exceeding 1 $THz$ and ultimately useful to telescopes such as ALMA in the future.

Therefore, the work described in this Chapter will focus on the design and testing of a prototype coherent, heterodyne SIS receiver system which has been developed by the Superconducting Detectors Group at Oxford University. To begin with, the experimental setup will be explained followed by preliminary testing and results using a $\sim 700$ $GHz$ SIS mixer. The Chapter will then present measurements, results and analysis of a $\sim 900$ $GHz$ mixer which will be shown to exhibit excellent performance once corrected for RF losses.

## 5.2 Experimental Setup

The receiver development and testing took place in the Superconducting Detectors Group laboratory at the University of Oxford. The components that make up a heterodyne receiver include a highly non-linear mixing device such as a Superconductor-Insulator-Superconductor (SIS) tunnel junction, a Local Oscillator (LO) which generates a user controlled reference tone, a network of optical components to couple radiation into the mixer and readout electronics to process the output data.

For the receiver system described in this Chapter, most of the components are contained within a cryostat and cooled down which allows the non-linear, superconducting properties of niobium to be utilised for frequency down conversion.

To cool the system down, a Closed Cycle Refrigerator (CCR) from Janis Research Company was employed which provides a convenient way of cooling samples down to $\sim 4\ K$ and can be used to perform a wide variety of optical and electrical experiments between $4 - 300\ K$. CCR systems do not require liquid nitrogen or helium as a source of cooling. Instead, a closed loop of helium gas is compressed and expanded based on the Pulse Tube (PT) thermodynamic cycle (Gifford & Longsworth, 1964). During the expansion phase of each cycle, heat is removed from the cold finger to which a cold plate and an experimental sample, such as an SIS mixer, are attached. A heater and temperature sensor are installed on the cold finger to precisely control the sample temperature.

The cold assembly is encased in a protective aluminium radiation shield which cools down to $\sim 28\ K$ and intercepts room temperature radiation before it reaches the mixer.

The entire setup is contained inside an aluminium vacuum shroud which is bolted to the cold head and includes an evacuation valve, safety pressure relief, electrical feedthroughs and a clamped vacuum seal for convenient access to the cold plate and mixer block.

Because such a system does not require any liquid refrigerants, there is no need for transfers or pre-cools. As well as this, it can achieve slightly lower temperatures than the boiling point of liquid helium and can stay cold for longer because it is not limited by liquid helium evaporation. A typical, lab based experimental setup showing the cryostat and LO is presented in Figure 5.1 while the cold plate optics layout is illustrated in Figure 5.2.

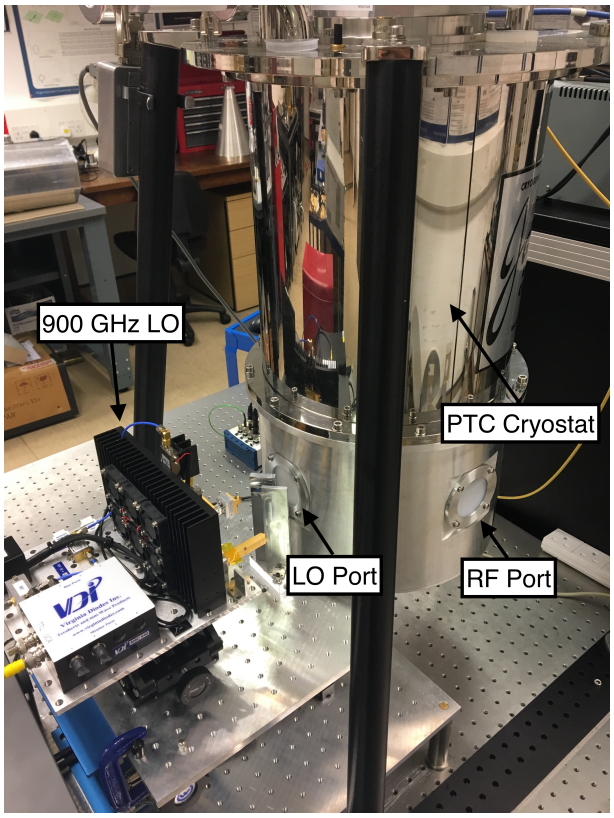


Figure 5.1: Experimental setup for performing SIS mixer measurements at THz frequencies.

The SIS mixer is housed within a gold plated mixer block which is attached to a lightweight aluminium jig using three M3 screws. The aluminium jig, shown in Figure 5.4, also serves as a mount for a cryogenic parabolic mirror and a dielectric beamsplitter. It is primarily used to minimise misalignment between the mixer block and optical components which are also housed inside the cryostat and thus cannot be adjusted while an experiment is in progress.

The aluminium jig is attached to a $\sim 20\ cm$ diameter cold plate which is at a physical temperature of $\sim 2.8\ K$. In order to improve thermal contact between the cold plate, aluminium jig and mixer block, a thin layer of Apiezon-N thermal anchoring grease is usually applied to the surfaces in contact with each other. Furthermore, thermal copper straps can also be attached between the cold plate and the mixer block to further reduce the temperature of the SIS device. With these measures, the mixer block can cool down to as low as $\sim 3.7\ K$. This is well below the superconducting transition temperature of niobium which is widely used as the superconducting material in SIS junctions.

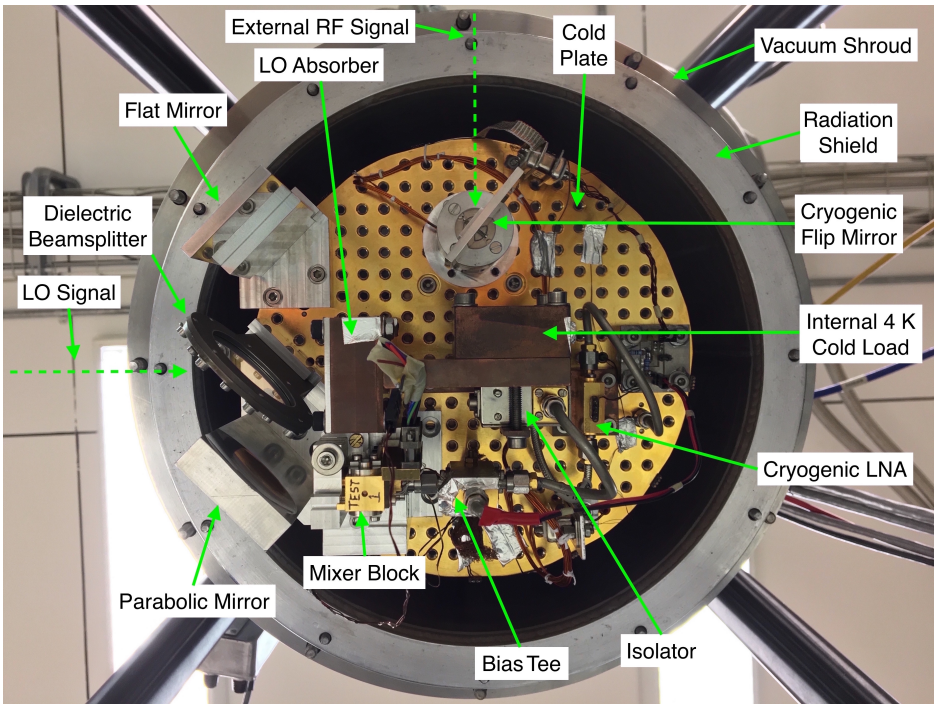


Figure 5.2: Cold plate layout showing the mixer block, cryogenic optics and cold IF chain.

The Radio Frequency (RF) and LO signals are coupled into the mixer block using a smooth-walled feed horn such as the ones described in Chapter 3, with a circular to rectangular waveguide transition machined directly into the mixer block. The down-converted Intermediate Frequency (IF) signal generated at the output of the mixer is directed out of the mixer block via a SubMiniature version A (SMA) connector.

The rest of the cryogenic signal chain consists of an Aeroflex "8810SMF2-18" model bias tee, a $4-8\ GHz$, Raditek cryogenic isolator and a $1-12\ GHz$, Caltech Microwave "CITCRYO1-12A" model low noise amplifier which amplifies the IF signal before it is coupled out of the cryostat and amplified further using two 29 $dB$ warm amplifiers. A $4-6\ GHz$ bandpass filter is also used and normally connected between the warm amplifiers. Finally the IF signal is detected using a Schottky diode based direct power detector the output of which can be displayed on a computer screen. Alternatively, a spectrum analyser can be used to display the spectral content of the IF signal.

The RF signal is coupled into the receiver using one of the windows on the side of the PTC cryostat. One of the main measurements performed with this system is the determination of receiver noise temperature ($T_{rec}$) carried out using the hot/cold load (Y-factor)

measurement technique described in Chapter 1. In the first iteration of the system, both the hot and cold loads were provided by a small piece of Eccosorb (where $T_{hot} = 290\ K$ and $T_{cold} = 77\ K$ for the hot and cold loads respectively), placed just in front of the RF port window on the PTC cryostat. In subsequent iterations however, the cold load was replaced with an aluminium cone coated in a non-reflective, black-body paint which was mounted inside the cryostat where it could cool down to $\sim 4\ K$, thus allowing for a more sensitive Y-factor measurement. Furthermore, using an internal cold load meant that the cold black-body signal had fewer optical components to pass through on its way to the mixer which resulted in a lower loss of cold RF power.

The RF black-body signal entering the system from outside the cryostat first passes through an outer, 5 $cm$ diameter, 2 $mm$ thick High-Density PolyEthylene (HDPE) window which transmits $\sim 92$ % of power at 700 $GHz$ and $\sim 89$ % at 900 $GHz$. A second cryostat window, located on the inner radiation shield, contains a 3 $cm$ diameter 1 $THz$ low-pass Infra-Red (IR) filter purchased from QMC Instruments which is mounted at a slight angle to help the system cool down and prevent the occurrence of standing waves.

The RF signal is then reflected by an aluminium flip mirror which can be rotated to look at either the hot/cold (290 $K$/77 $K$) load outside or the cold 4 $K$ load inside the cryostat.

After the flip mirror is another flat, aluminium mirror which reflects the RF signal through a cryogenic, Mylar beamsplitter before the signal is focused into the mixer horn using a parabolic mirror with focal length of 30 $mm$.

The LO signal is injected from the outside and coupled into the cryostat using a Gaussian telescope configuration. A parabolic mirror with a focal length of 30 $mm$ is used to turn the expanding beam from the LO horn into an approximately parallel beam with a radius of curvature of $\sim -1474\ mm$. A flat mirror is then used to direct the LO signal through the outer cryostat window. Both of these mirrors are made from aluminium and can also be rotated on their mount to give further flexibility when aligning the system optics. The outer cryostat window on the LO side is also made from HDPE and has the same dimensions and transmission properties as the outer window on the RF port. Similarly, the second cryostat window located on the inner radiation shield contains another 3 $cm$ diameter 1 $THz$ low-pass IR filter mounted at a slight angle to the incoming LO signal.

A cryogenic Mylar beamsplitter mounted at 45° to the optical path inside the cryostat itself is then used to reflect the LO signal towards the internal parabolic mirror. The LO signal transmitted through the beamsplitter is absorbed using a conical black-body absorber so as to prevent it bouncing around inside the cryostat. For measurements using the 700 $GHz$ mixer, a 50 $\mu m$ thick beamsplitter was used which reflects $\sim$ 10 % of the incident LO signal while a thickness of 120 $\mu m$ was used to reflect $\sim$ 28 % of the LO signal when testing the 900 $GHz$ mixer.

Finally, the internal cryogenic parabolic mirror focuses the LO signal to a waist located $\sim$ 1.92 $mm$ inside the mixer horn at 700 $GHz$ and $\sim$ 3.16 $mm$ inside the mixer horn at 900 $GHz$, as measured from the horn aperture.

The LO itself is mounted on a small optical plate which can be moved forward, back, left and right. The plate is attached to a rotary mount and a height adjustable jack to give the LO system the maximum number of degrees of freedom which is crucial for alignment and being able to effectively couple LO power to the mixer. For example, the LO signal needs to cover a distance of approximately 21 $cm$ from the LO horn to the mixer horn. Given that the radius of the 700 $GHz$ mixer horn is only 1.27 $mm$, a rotary misalignment of just 0.35° in either direction would lead to the beam missing the mixer horn. The entire LO assembly is attached to a miniature optical table which can be seen in Figure 5.1.

For measurements at 700 $GHz$, a Gunn diode (Gunn, 1963) based LO was employed which needs to be manually tuned over its $607-691$ $GHz$ frequency range of operation. This LO chain consists of a "H203" Gunn oscillator from the Central Laboratory of the Research Councils followed by a Radiometer Physics GmbH (RPG) WR$-8$ crossguide coupler, a modulator, an RPG frequency doubler and tripler and finally a smooth-walled feed horn.

At every frequency, there are several controls that need to be adjusted in order to produce a detectable signal from this LO. These include the Gunn oscillator's micrometer tuner, the backshort, and two tuning dials on both the doubler and tripler. The tuning values for each of these components for the frequency range of operation of the LO are presented in Table 5.2 while the LO power output can be seen in Figure 5.3(a).

For experiments at 900 $GHz$, an LO purchased from Virginia Diodes Inc. (VDI) was used which consists of a signal generator, an amplifier, a frequency tripler, an active fre-

| Frequency | Power | Gunn Controls | | Doubler Controls | | | Tripler Controls | | |
|---|---|---|---|---|---|---|---|---|---|
| $(GHz)$ | $(\mu W)$ | Tuner | Backshort | Bias, $V$ | 1 | 2 | Bias, $V$ | 3 | 4 |
| 607 | 40 | 27.0 | 71.0 | 5.54 | 2.00 | 1.56 | 1.13 | 0.81 | 0.36 |
| 625 | 49 | 21.4 | 92.0 | 5.05 | 1.77 | 1.50 | 1.00 | 0.65 | 0.35 |
| 642 | 60 | 17.5 | 100.0 | 5.46 | 1.59 | 1.40 | 1.64 | 0.71 | 0.08 |
| 650 | 83 | 16.0 | 89.5 | 4.57 | 1.49 | 1.25 | 1.51 | 0.70 | 0.07 |
| 660 | 105 | 14.1 | 67.5 | 5.91 | 1.44 | 1.27 | 1.22 | 0.54 | 0.09 |
| 672 | 110 | 12.6 | 80.0 | 7.39 | 1.37 | 1.24 | 2.25 | 0.60 | 0.08 |
| 682 | 120 | 11.0 | 38.5 | 8.89 | 1.09 | 1.17 | 2.04 | 0.52 | 0.03 |
| 691 | 115 | 10.0 | 36.5 | 7.94 | 0.75 | 1.19 | 1.91 | 0.58 | 0.05 |

Table 5.2: 700 $GHz$ Gunn LO tuning values. The Tuner, Backshort, Doubler and Tripler (1, 2, 3 and 4) Control values correspond to the micrometer settings on each dial.

quency doubler, an active amplifier, two frequency triplers and a diagonal feed horn. This configuration allows the LO to operate over the frequency range of $774 - 954\ GHz$. Since this LO works from a synthesised signal, it does not require manual tuning and can be simply driven using a Voltage Controlled Oscillator (VCO) source. The power output for the VDI LO between $774 - 954\ GHz$ is presented in Figure 5.3(b).

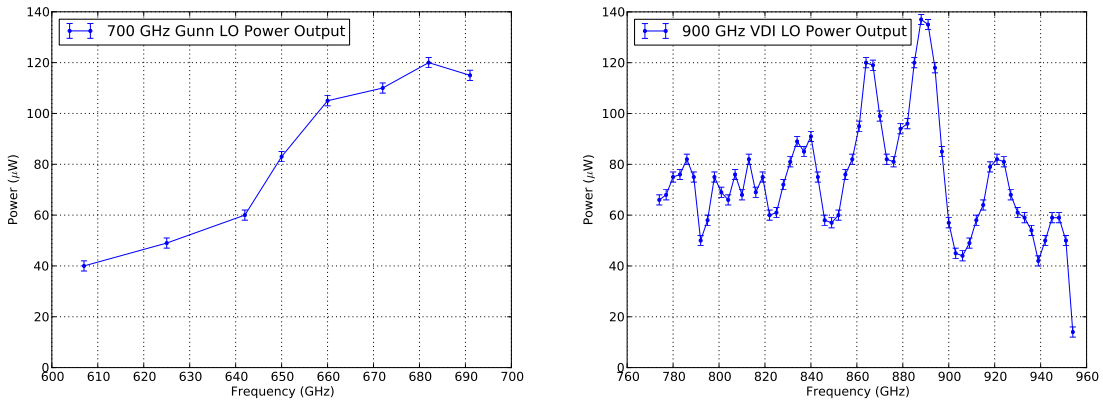


(a) 700 $GHz$ Gunn LO power output.

(b) 900 $GHz$ VDI LO power output.

Figure 5.3: Power output as a function of frequency for the Gunn and VDI LOs.

One of the unique and novel features of this experimental setup is that apart from the LO and the two mirrors used to direct the LO signal into the receiver, the entire optical system is contained inside the cryostat. This helps to reduce the RF noise contribution to the overall receiver noise temperature because the effective noise temperature of the optical components scales with their physical temperature.

## 5.3 SIS Mixer Measurements Between 600 - 700 GHz

To begin with, the receiver system was tested with a 700 $GHz$ Silicon On Insulator (SOI) (Westig et al., 2011) mixer installed in the PTC cryostat as these devices were readily available, robust, easy to install in the mixer block and could be used to demonstrate initial receiver operation, without risking damage to scarce higher frequency devices. SOI mixers can be fabricated on thin ($\sim 15\ \mu m$) silicon substrates which can extend their viability for operation into the Terahertz frequency range. One advantage of using such a thin substrate is that it presents very light loading to the incoming waveguide signal and therefore avoids excitation of higher order modes across a relatively large frequency bandwidth.

For measurements described here, radiation is coupled into the mixer using a smooth-walled, multiple flare-angle feed horn followed by a $320 \times 160\ \mu m$ rectangular waveguide and a unilateral finline taper as the waveguide-to-planar circuitry transition. This provides a broad band and smooth transition from the waveguide impedance to a low slotline impedance (Yassin et al., 2008).

The mixer chip itself is mounted and supported within the mixer block using gold beam leads with a large contact area between the mixer chip and the block. This helps the chip to cool down leading to a larger energy gap, less leakage current and improved performance.

The mixer chip is housed in a groove in the bottom half of a gold plated aluminium mixer block which is split along the E-plane of the rectangular waveguide. The highly non-linear SIS tunnel junction consists of a circular Niobium/Aluminium-Oxide/Niobium (Nb/AlOx/Nb) sandwich structure with a total area of $\sim 1\ \mu m^2$. This corresponds to a normal resistance of $R_n \simeq 20\ \Omega$ and a junction capacitance of $C \simeq 75\ fF$ which leads to $\omega R_n C \simeq 1$ at 650 $GHz$ (Tan et al., 2012).

The system was initially tested using 700 $GHz$ devices due to the considerable risks involved when working with ElectroStatic Discharge (ESD) sensitive components. Because there were a number of 700 $GHz$ SOI mixers available, it was not a huge concern if some of them perished during the experimental testing phase of the receiver development. However, since only one 900 $GHz$ device was available, this left very little margin for error when it came to performing measurements at the higher frequency. An image of a 700 $GHz$ SOI

mixer block mounted on an aluminium jig is shown in Figure 5.4.

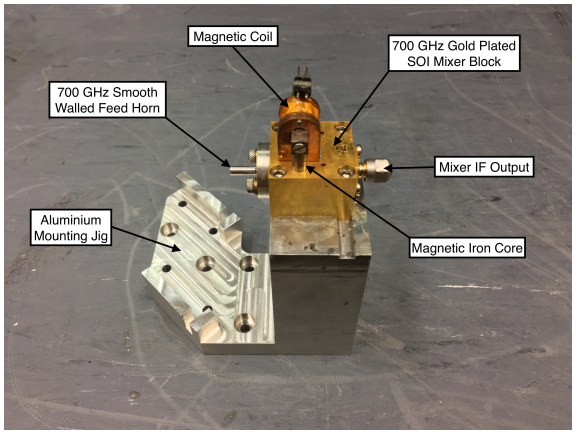


Figure 5.4: 700 $GHz$ mixer block and smooth-walled feed mounted on its aluminium jig. A circular to rectangular waveguide transition is machined directly into the mixer block.

For an SIS mixer to operate as an effective detector, it is necessary to suppress the Josephson tunnelling current which acts as an unstable current source and adds unwanted noise to the mixer. This can be done using a magnetic field supplied by a small, superconducting coil which can be seen in Figure 5.4. The coil contains 2000 turns of 50 $\mu m$ diameter superconducting copper clad NbTi wire which is wound around a 7 $mm$ diameter former. This is sufficient to induce a magnetic field via two ferromagnetic shoes near the mixer chip that can sweep the tunnel junction through several Josephson nulls. For the measurements described here, the field was usually set at the second minimum with a coil current of $\sim 20$ $mA$ since the first minimum does not fully suppress the Josephson current.

### 5.3.1 Initial Measurements

The first objective when working with this system was to correctly align the LO and successfully pump (ideally saturate) the SIS mixer across a number of frequencies so that noise temperature measurements could be performed. As such, this initial testing phase was performed without the IF chain in place but simply with the DC bias sweep connected up to the mixer. Furthermore, the LO was initially injected directly into the cryostat window without the use of the two external mirrors because of the relative difficulty of simultaneously aligning the system optics and tuning the LO to produce a detectable signal.

Therefore, the LO tuning was first optimised at every frequency of interest by directly

coupling the signal into the cryostat and adjusting the various micrometer dials. Once this was done, the LO could be placed at the focus of the external parabolic mirror so that the optics could be adjusted for optimum alignment.

However, despite paying close attention to both LO and the external optical configuration, it proved difficult to pump the SIS mixer. This can be seen in Figure 5.5(a) which shows one of the initial pumped I-V curves at 672 $GHz$. A zoomed in version is presented in Figure 5.5(b) from which it can be seen that while the mixer is registering power, it is not nearly enough to carry out any meaningful experiments.

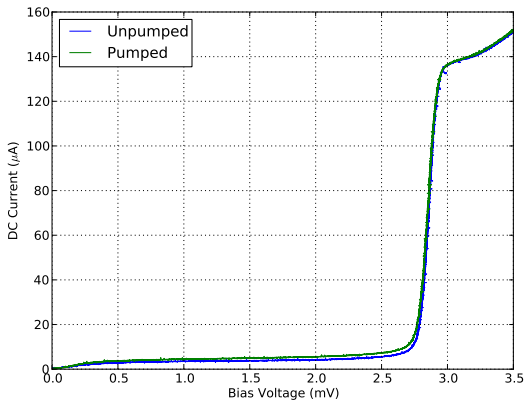


(a) 672 $GHz$ pumped I-V curve obtained during the initial stages of receiver development.

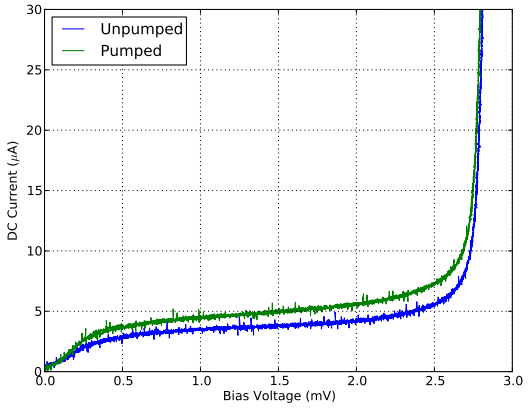


(b) Zoomed in section of (a) showing low LO power coupling to the SIS mixer.

Figure 5.5: An initial "pumped" I-V curve at 672 $GHz$. However, the curve does not show a clear photon step as there is not enough LO power to sufficiently pump the mixer. Uncertainties on the measured DC current are on the order of $\pm 1$ $\mu A$.

Despite multiple adjustments to the external system optics as well as the LO tuning, it proved challenging to couple more LO power into the mixer than shown in Figure 5.5. To investigate this issue, the mixer block was removed from the PTC cryostat and mounted in a different cryogenic system known as the "Square Dewar". Since this system does not contain any internal, cryogenic optics and the mixer horn sits just behind the cryostat window, there is more control over the alignment process as all the optics can be adjusted while an experiment is in progress. This would help to identify whether the power coupling issue was caused by the PTC system optics or a problem with the mixer performance itself. Measurements to obtain pumped I-V curves with the Square Dewar were performed across a frequency range of $607 - 691$ $GHz$ and the results can be seen in Figure 5.6.

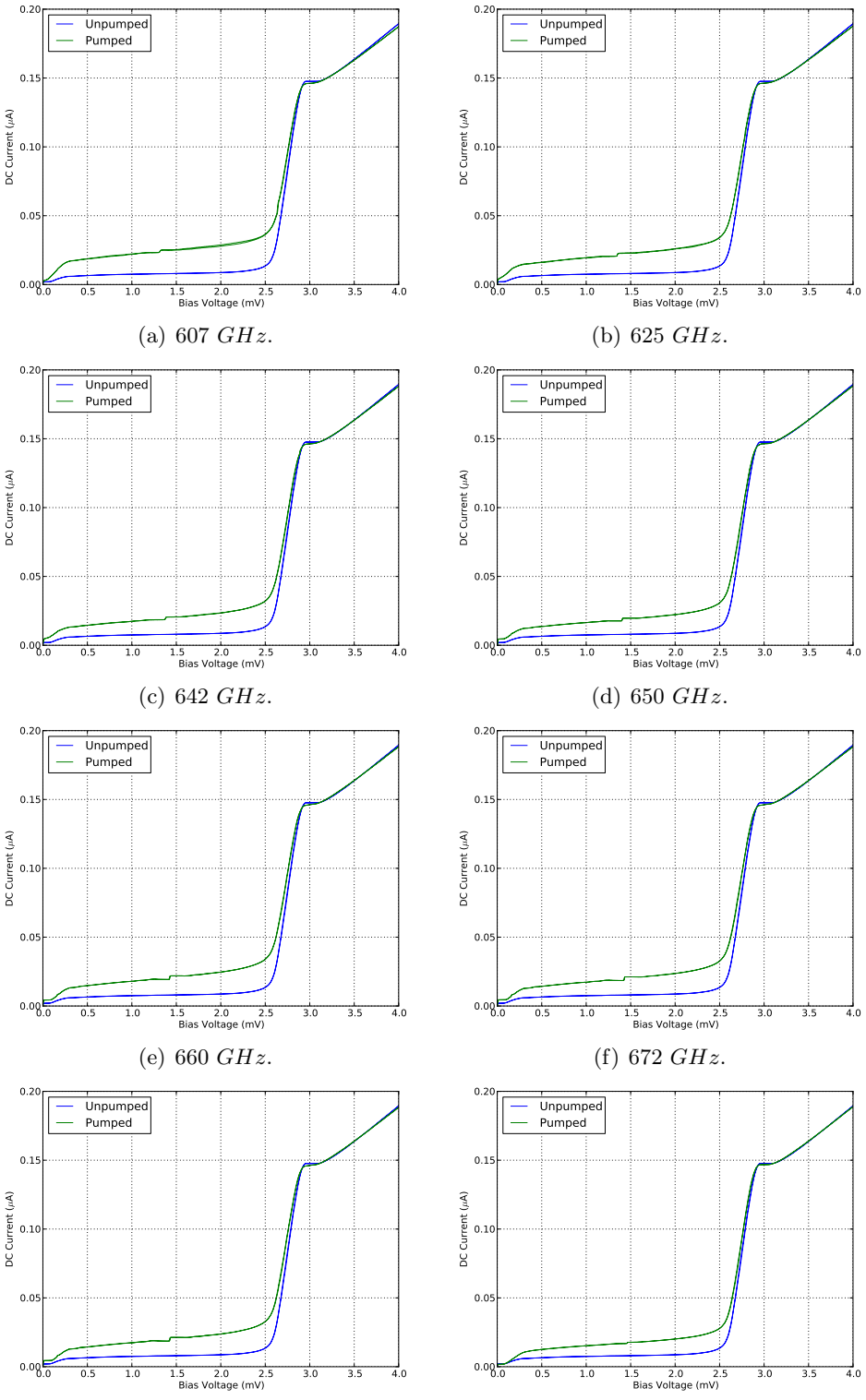


(a) 607 $GHz$. (b) 625 $GHz$.

(c) 642 $GHz$. (d) 650 $GHz$.

(e) 660 $GHz$. (f) 672 $GHz$.

(g) 682 $GHz$. (h) 691 $GHz$.

Figure 5.6: Pumped I-V curves between $607 - 691$ $GHz$ measured in the Square Dewar. Each plot shows a single photon step, rather than multiple steps, as the frequency of incident LO radiation is comparable to the width of the energy gap. Uncertainties on the measured DC current are negligible.

The results in Figure 5.6 show that while the mixer is not saturated, significantly more LO power is coupled into the receiver when using the external optics of the Square Dewar compared to the internal optics on the PTC. Furthermore, unlike the results in Figure 5.5, the pump level in Figure 5.6 would be adequate to begin carrying out noise temperature measurements at least at the lower end of the frequency range of $\sim 607\ GHz$.

Therefore, these measurements suggest that the mixer and the LO work as intended and the power coupling issue lies with the optical setup on the PTC cryostat. One of the components responsible for the lack of power observed could have been the dielectric beamsplitter which may not be behaving as expected when cooled down to cryogenic temperatures. To test this idea, the internal beamsplitter was swapped around with the flat external aluminium mirror that is normally used to reflect LO power into the PTC. The result of this measurement is presented in Figure 5.7 which shows that when the beamsplitter is mounted outside the PTC cryostat, it is possible to adequately pump the mixer and couple enough LO power into the receiver to obtain a good noise temperature.

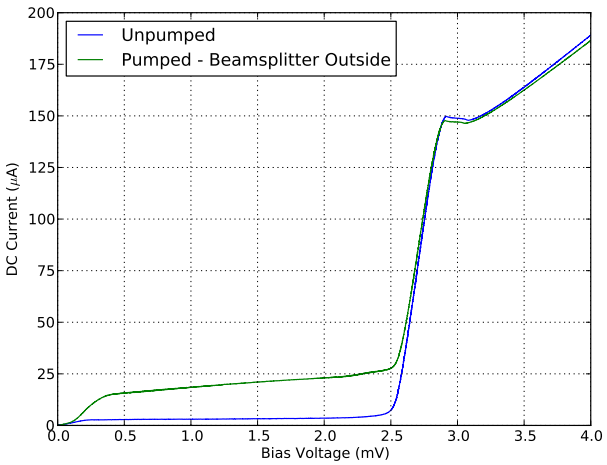


Figure 5.7: Pumped I-V at 607 $GHz$ obtained with an external beamsplitter on the PTC. The plot shows a single photon step, rather than multiple steps, as the frequency of incident LO radiation is comparable to the width of the energy gap. Uncertainties on the measured DC current are on the order of $\pm 0.1\ \mu A$.

To simulate the effect of cooling the beamsplitter down, it was dipped into a liquid nitrogen reservoir and visually compared to its appearance at room temperature. An image of the beamsplitter at room temperature is shown in Figure 5.8(a) while the same beamsplitter at 77 $K$ is presented in Figure 5.8(b).

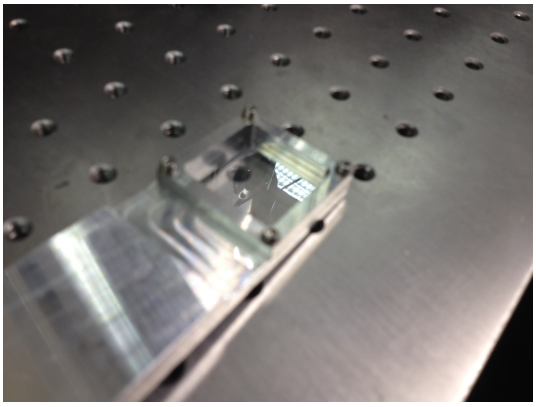

(a) An image of the Mylar beamsplitter at room temperature. A tight, reflective surface is clearly visible.

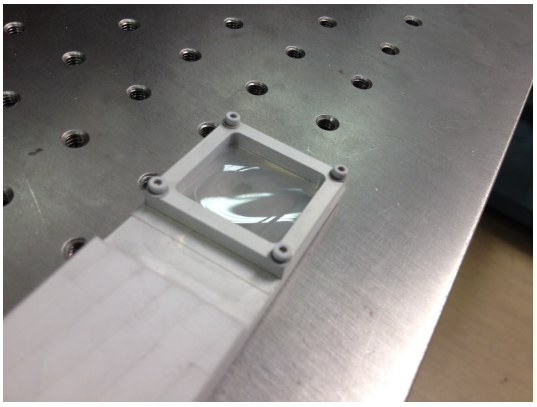

(b) An image of the Mylar beamsplitter at 77 $K$. The surface has become distorted due to the expansion of the beamsplitter.

Figure 5.8: A comparison of the Mylar beamsplitter at 300 and 77 $K$.

It can be seen that when the beamsplitter is cooled, it expands and deforms which means that any incoming wavefront, such as that of the LO, will be distorted and not reflected towards the mixer. This would explain why very little power was initially coupled into the mixer when the beamsplitter was mounted inside the cryostat. Furthermore, since Mylar expands with a decrease in temperature while aluminium (the beamspitter frame material) contracts, the overall expansion effect is amplified further. For example, the Coefficient of Thermal Expansion (CTE) for Mylar and aluminium is $-17$ and 22.2 $\frac{\mu m}{m \cdot K}$ respectively, where the negative sign corresponds to expansion with decreasing temperature. Thus for a square beamsplitter with 27 $mm$ long sides, the Mylar will expand by 102.4 $\mu m$ when cooled from 300 to 77 $K$ while the aluminium frame will contract by 133.7 $\mu m$ meaning that the total effective increase on each of the sides will be $\sim 236.1$ $\mu m$. This corresponds to approximately $\lambda/2$ at 650 $GHz$ and would be enough to prevent the LO signal being effectively coupled into the mixer.

These findings were a serious concern since the system was designed with most of the optics, including the beamsplitter, to be installed inside the cryostat so that the RF noise contribution to the overall system noise temperature could be kept to a minimum. It was therefore necessary to overcome this issue and arrive at a solution to prevent the expansion of the beamsplitter when it is cooled down inside the PTC.

### 5.3.2 Cryogenic Beamsplitter Development

To overcome the thermal expansion issues described in the previous section, the beamsplitter frame needed special consideration and careful design. The main requirements for the new frame are summarised below:

1. The frame material needed to have a low CTE to minimise its thermal contraction as the system cools down.

2. The beamsplitter aperture needed to be wide enough and the frame thin enough so as to not clip the LO beam when mounted at 45° with respect to the optical axis.

3. The frame needed to incorporate a "pre-tensioning" mechanism which could tension the beamsplitter at room temperature to offset the expansion as it cools down.

To address the first point, the new beamsplitter frame was designed to be made using titanium instead of aluminium because the CTE of titanium is 8.41 $\frac{\mu m}{m \cdot K}$ which is almost 3 times lower than that of aluminium.

The second point is important as the original beamsplitter frame shown in Figure 5.8 is 4 $mm$ thick and contains a square Mylar beamsplitter with 27 $mm$ long sides. Since this beamsplitter is mounted inside the PTC at 45° to the incoming LO signal, its *effective* length is $(27-4)\sin(45°) = 16.3\ mm$. Given that the LO beam diameter at the beamsplitter location is 13.89 $mm$, the original frame is just about large enough to accommodate the beam without clipping it. As such, the new frame was designed to have a circular, 40 $mm$ diameter aperture while maintaining a total thickness of 4 $mm$. This leads to an effective diameter of $(40-4)\sin(45°) = 25.45\ mm$ which is wide enough to accommodate the incoming beam down to a $\sim 29\ dB$ taper and couple more LO power into the mixer.

The final point was addressed by including a "floating", 1 $mm$ thick and 3 $mm$ wide, titanium ring within the frame itself. This ring is housed inside a groove in the top half of the beamsplitter frame and sits on top of the Mylar beamsplitter above a second, slightly wider, 4 $mm$ groove in the bottom half of the frame. Eight M1 screws above the ring can be used to apply pressure onto the Mylar thus pre-tensioning the beamsplitter at room temperature before it gets cooled down inside the PTC.

The beamsplitter frame was fabricated by the mechanical workshop at Oxford University and an image of the disassembled frame showing the floating ring and its internal grooves is presented in Figure 5.9(a) while the assembled frame containing a 50 $\mu m$ thick Mylar beamsplitter is shown in Figure 5.9(b).

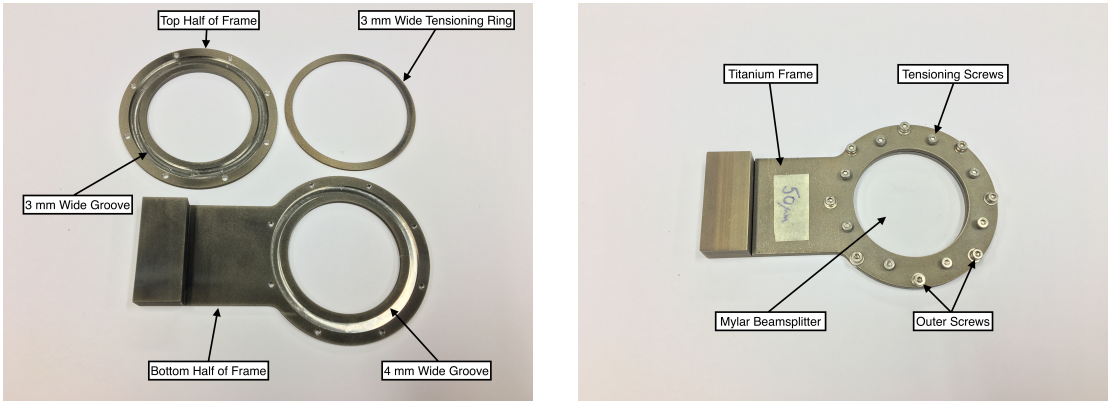


(a) Titanium beamsplitter frame components. (b) An assembled 50 $\mu m$ thick beamsplitter.

Figure 5.9: Images of the frame components and a beamsplitter once it has been assembled.

To mount a beamsplitter in the titanium frame as shown in Figure 5.9(b), a piece of Mylar is cut into a circular, 60 $mm$ diameter shape with eight 2 $mm$ diameter holes around the edge for the outer screws to pass through. The Mylar is then placed over the bottom half of the frame while the top half, with the floating ring housed in the upper groove, is placed over the top. The outer screws are then gently tightened to hold the entire assembly together without pinching the Mylar so that it can still move between the two halves. The M1 screws above the floating ring are then tightened up to apply pressure to the Mylar which pre-tensions the beamsplitter at room temperature. Once this is done the outer screws can be tightened to clamp the two halves of the frame firmly together. A heatgun is then used to heat up the Mylar which causes the surface to tighten up further and smooth out. The beamsplitter is then dipped in a liquid nitrogen reservoir and cooled down before being treated with the heat gun again. This process is repeated two or three times until the Mylar no longer expands when dipped in liquid nitrogen.

Once the beamsplitter had been mounted and installed in the PTC, another attempt to pump the mixer between $607 - 691$ $GHz$ was carried out and the results are presented in Figure 5.10.

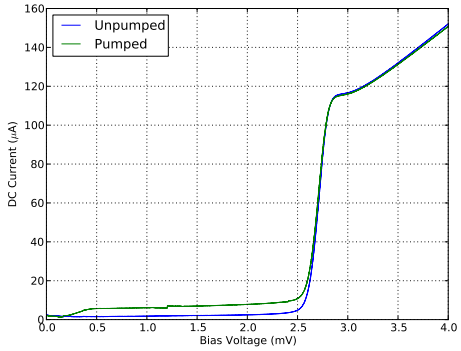


(a) 607 $GHz$.

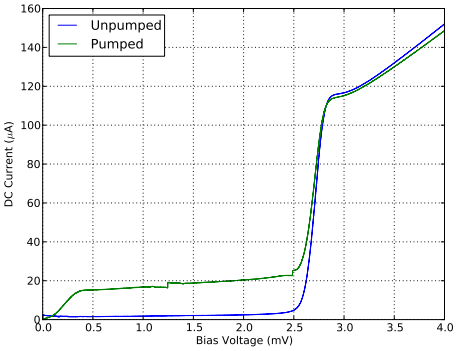


(b) 625 $GHz$.

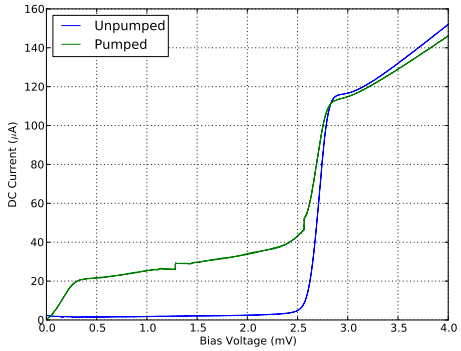


(c) 642 $GHz$.

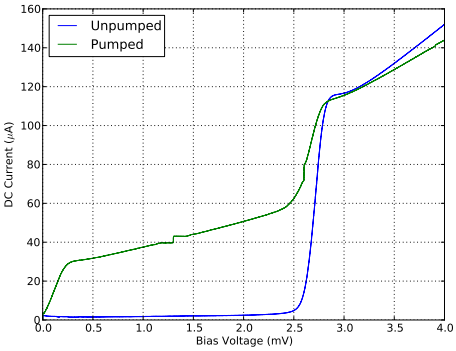


(d) 650 $GHz$.

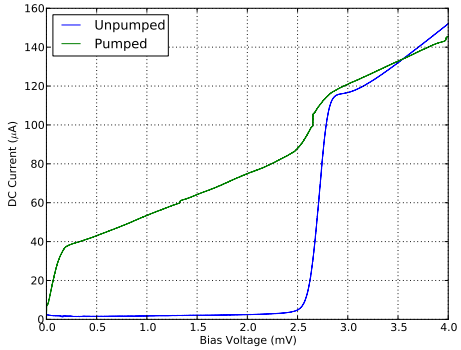


(e) 660 $GHz$.

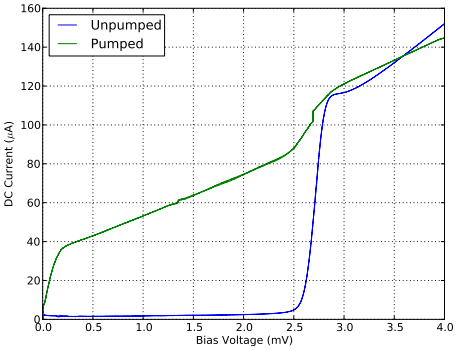


(f) 672 $GHz$.

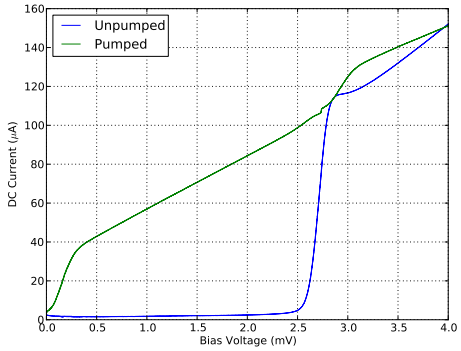


(g) 682 $GHz$.

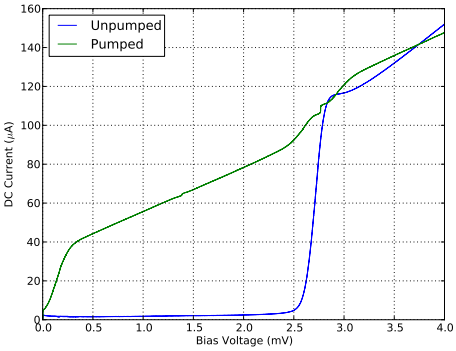


(h) 691 $GHz$.

Figure 5.10: Pumped I-V curves between $607 - 691$ $GHz$ obtained using the PTC and the internally mounted titanium beamsplitter frame.

### 5.3.3 Measurements with an Improved Optical Setup

From Figure 5.10, it is evident that with the new beamsplitter installed the mixer could be adequately pumped between $642 - 691\ GHz$ and even saturated between $660 - 691\ GHz$. The IF chain was therefore installed so that preliminary noise temperature measurements could be performed with the receiver using an SOI device and the $700\ GHz$ Gunn LO.

Given that the IR filters described in Section 5.2 were not yet available, quartz windows were fitted to the inner radiation shield of the PTC instead. This helped the mixer to cool by blocking incident, room temperature radiation from entering the cryogenic part of the receiver. HDPE was still used for the outer windows on the vacuum shroud but cooling the system using HDPE windows on both outer and inner windows led to a relatively high mixer temperature of $\sim 5\ K$. Because the energy gap of niobium at this temperature is very close to the measurement frequency ($V_{gap} \simeq 2.7\ mV$, $\nu_{gap} \simeq 650\ GHz$), the mixer sensitivity degrades rapidly unless it can be kept cold, ideally below $4\ K$. By using quartz windows, the mixer cooled to a physical temperature of $3.74\ K$, with a gap voltage of $V_{gap} \sim 2.8\ mV$, but at the cost of increased RF losses compared to the IR filters that were eventually used.

Nonetheless, once the magnetic coil current had been set on the second Josephson null ($\sim 24.7\ mA$), the IF output of the mixer was found to be responsive to a change in input power which was provided by a "hot" ($\sim 290\ K$) and a "cold" ($\sim 77\ K$) load. A small piece of room temperature Eccosorb acted as the hot load, while another small piece of Eccosorb dipped in a liquid nitrogen reservoir provided the cold load since the internal, cryogenic cold load had not yet been installed. From this, the receiver noise temperature was determined using the Y-factor method, including the hot and cold load noise temperature correction according to the Callen and Welton law (Callen & Welton, 1951; Kerr et al., 1997), described in more detail in Sections 1.5.1 and 1.5.2 of Chapter 1.

The mixer was pumped to about one third of its gap current as it was found to be most sensitive at this pump level and biased at a voltage of $V_b \simeq 2.3\ mV$. The measured pumped I-V and hot/cold output IF curves between $642-691\ GHz$ are shown in Figures 5.11 and 5.12 respectively. A plot of the measured, Double Side Band (DSB) receiver noise temperature and the mixer conversion gain as a function of frequency is presented in Figure 5.13.

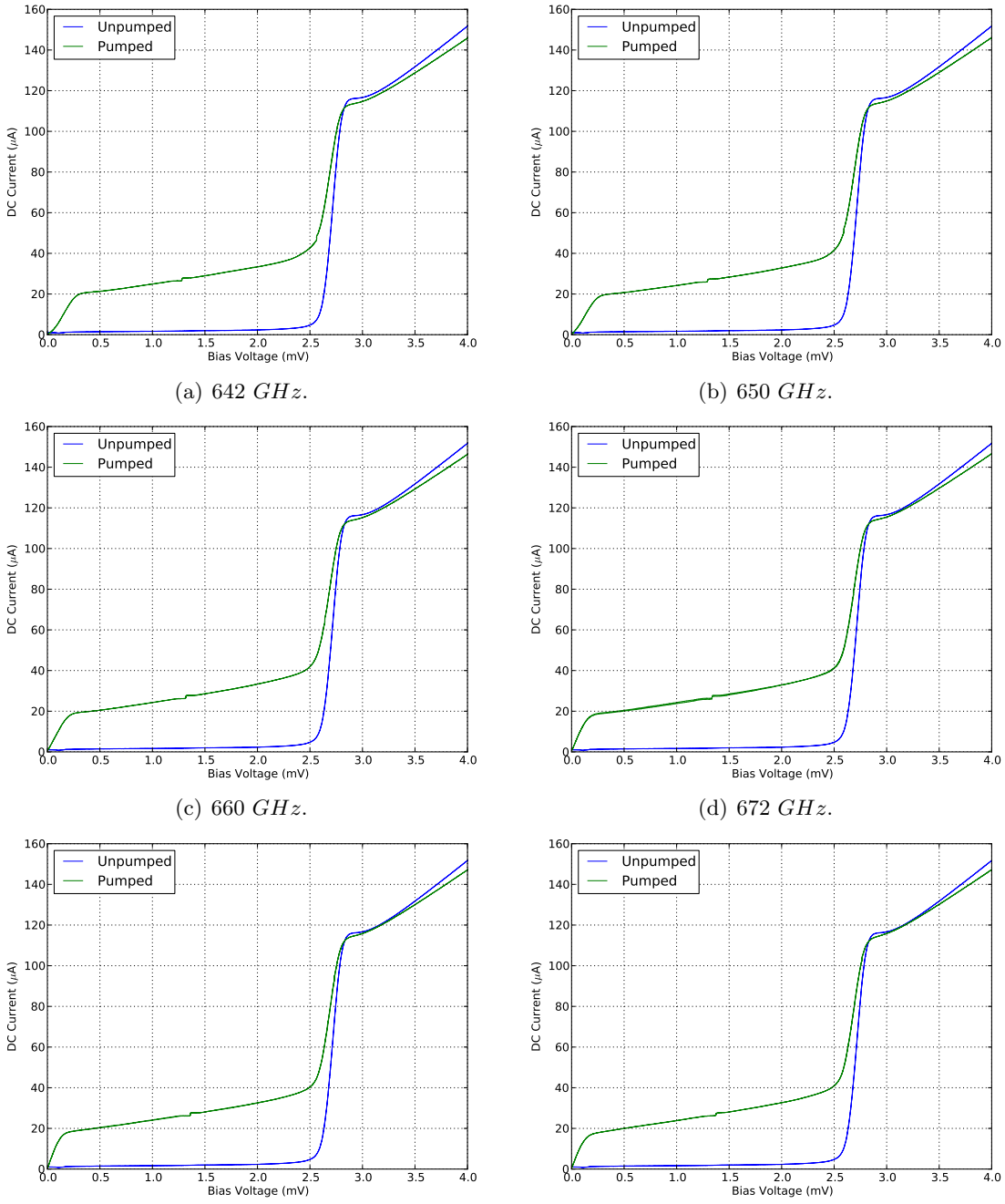


(a) 642 $GHz$.

(b) 650 $GHz$.

(c) 660 $GHz$.

(d) 672 $GHz$.

(e) 682 $GHz$.

(f) 691 $GHz$.

Figure 5.11: Pumped I-V curves that were used for noise temperature measurements between $642 - 691$ $GHz$ with the PTC and an internally mounted beamsplitter.

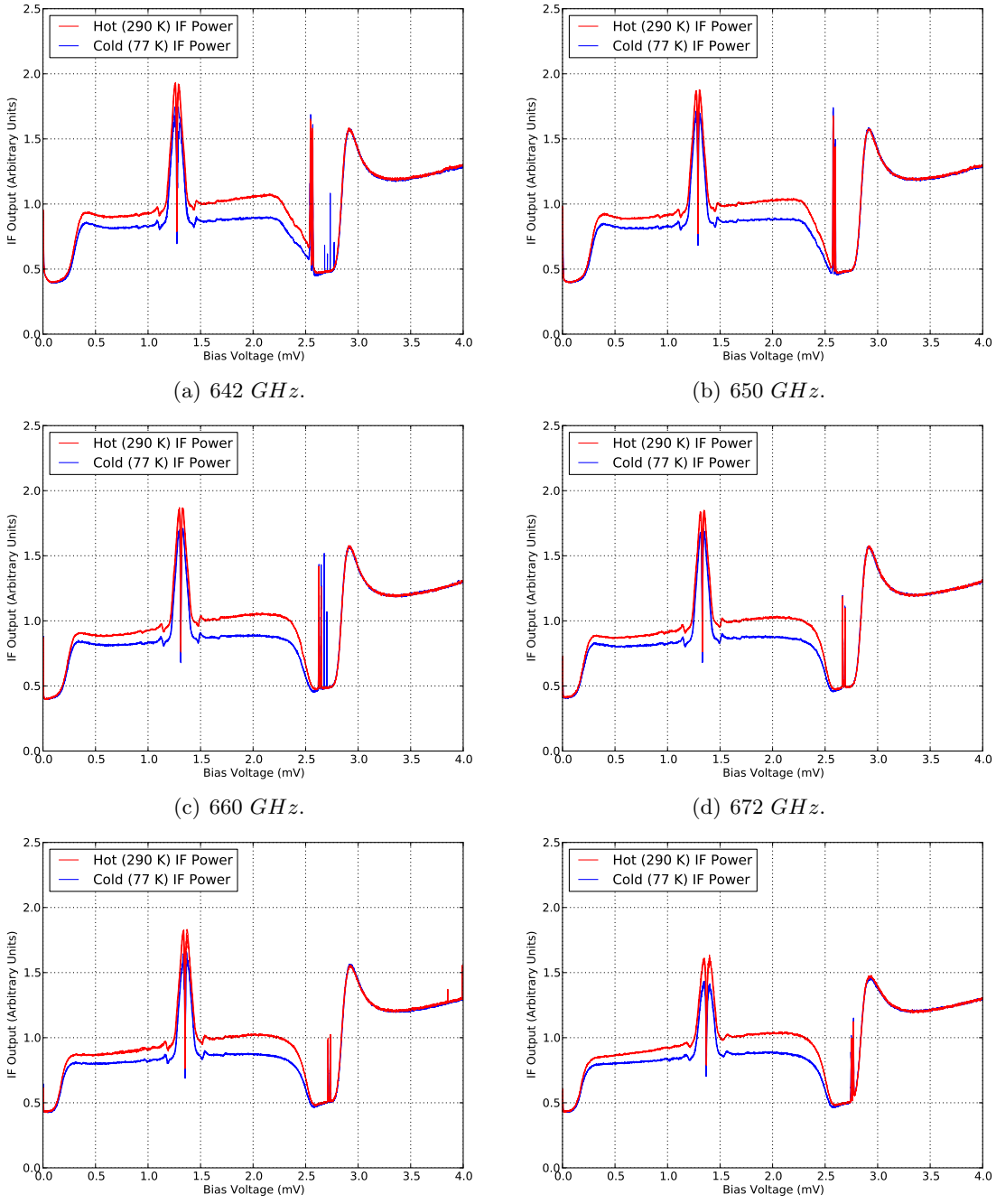


(a) 642 $GHz$. (b) 650 $GHz$.

(c) 660 $GHz$. (d) 672 $GHz$.

(e) 682 $GHz$. (f) 691 $GHz$.

Figure 5.12: Measured output IF curves that were used for noise temperature measurements between $642 - 691$ $GHz$ with the PTC and an internally mounted beamsplitter.

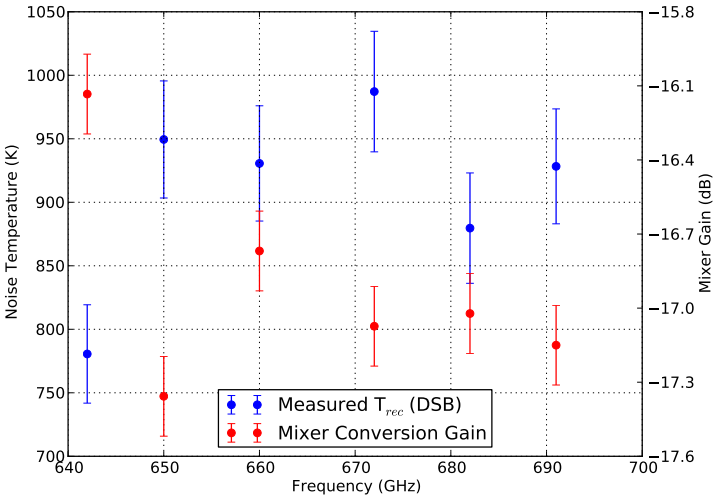


Figure 5.13: Measured DSB receiver noise temperature and mixer conversion gain between $642-691\ GHz$. Errors in the results have been propagated by assuming a 10 % uncertainty on the physical temperature of the 77 $K$ cold load.

The results in Figure 5.13 show reasonable receiver performance given that they have not been corrected for RF losses and that at the time of these measurements, the system was not yet optimally set up. The lowest noise temperature measured was $\sim 780\ K$ at $642\ GHz$, suggesting that the junction may be tuned towards the lower end of the $600-700\ GHz$ frequency range. However, despite attempts to test the system below $642\ GHz$, the relative lack of LO power and subsequent difficulty in pumping the device to the levels shown in Figure 5.11 resulted in significantly degraded performance of $\sim 1100\ K$ at $625\ GHz$.

Furthermore, once the device had been tested in the PTC it was moved to the Square Dewar, where the system optics are optimised for these measurements, so that similar tests could be performed to check the device independently of the PTC setup. The noise temperature measured with the device installed in the Square Dewar was slightly worse ($\sim 200\ K$ higher) across the $642-691\ GHz$ frequency range, implying that the device itself may not be ideal. This, in turn, provided support for the performance of the PTC system.

While superior performance has previously been reported at these frequencies (Baryshev et al., 2015) with noise temperature measurements as low as $\sim 75\ K$ at $650\ GHz$, these results were adequate to demonstrate that the system was operational and could be used as a high frequency heterodyne receiver. As such, a $900\ GHz$ mixer was installed in the PTC and the system adapted in preparation for testing at Terahertz frequencies.

## 5.4 An SIS Receiver Operating Between 800 - 900 GHz

Following measurements at 700 $GHz$, the mixer block described in Section 5.3 was removed so that another device could be installed in the PTC with the aim of experimentally testing the system at higher frequencies. The new mixer, which was provided by colleagues at the Kapteyn Astronomical Institute in the Netherlands, had been measured to have an FTS response in the $780-950$ $GHz$ frequency range. This could make it suitable for applications such as the Band 10 receiver on the ALMA telescope or the high frequency band of the Carbon Heterodyne Array of the Max-Planck Institute Plus (CHAMP+) instrument on the Atacama Pathfinder EXperiment (APEX) telescope (Kasemann et al., 2006).

To enable broadband performance and tune out parasitic junction capacitance, the mixer design employs two, high current density (30 $kA/cm^2$), 0.5 $\mu m^2$ SIS tunnel junctions separated by a quarter-wavelength microstrip (Zmuidzinas et al., 1994; Belitsky et al., 1995).

The junctions themselves consist of a 100 $nm$ thick Niobium (Nb) ground electrode and a 100 $nm$ thick Niobium-Nitride (NbN) top electrode separated by a thin Aluminium-Nitride (AlN) insulation layer to form the Niobium/Aluminium-Nitride/Niobium-Nitride (Nb/AlN/NbN) sandwich structure. These junctions are fabricated on top of a 300 $nm$ thick Niobium-Titanium-Nitride (NbTiN) ground plane with a 250 $nm$ Silicon Dioxide ($SiO_2$) dielectric layer and a 500 $nm$ thick Aluminium (Al) layer that sits on top and forms a microstrip transmission line to connect the junctions to the rest of the superconducting circuit (Khudchenko et al., 2016).

This structure is supported by a 40 $\mu m$ thick quartz substrate placed along the E-plane axis of a reduced height ($300 \times 75$ $\mu m$) rectangular waveguide. The waveguide is fabricated in the back-piece of the mixer block such that when the mixer is mounted, the normal vector to the chip is aligned in the direction of propagation of the incoming RF signal.

In comparison to the 700 $GHz$, Nb/AlOx/Nb device discussed in Section 5.3, the mixer described here will be shown to have a larger gap voltage of $V_{gap} \simeq 3.0$ $mV$ when cooled down in the PTC cryostat. This is useful given that the frequency of 900 $GHz$ radiation corresponds to a gap voltage of $V_{gap} \simeq 3.7$ $mV$. While this is larger than the gap voltage of both types of devices, the use of a niobium-nitride mixer provides a $\sim 0.2$ $mV$ wider voltage

range for biasing the SIS mixer compared to one that employs solely niobium electrodes. This leads to a significant advantage when it comes to mixer operation because of the presence of problematic Shapiro features in the middle of the photon step which can be seen in the IF output of the mixer, as shown in Figure 5.12.

Furthermore, due to the high current density of the aluminium-nitride barrier, these devices have a lower normal resistance of $R_n \simeq 14\ \Omega$ and an estimated junction capacitance of $C \simeq 80\ fF$. This results in a higher $1/R_nC$ ratio providing a wider receiver band and leads to $\omega R_n C \simeq 1$ at 890 $GHz$ (Khudchenko et al., 2016).

Radiation is coupled into the mixer using a smooth-walled feed horn with a rectangular waveguide output. The horn is aligned to the back-piece which houses the mixer chip and held in place using a centring ring. The horn and back-piece assembly slots into an ALMA style mixer block which is equipped with a temperature sensor, magnetic coils to suppress the Josephson tunnelling current and an SMA connector for the DC and IF signals. A schematic diagram of the mixer block (Hesper & Bekema, 2014) is shown in Figure 5.14.

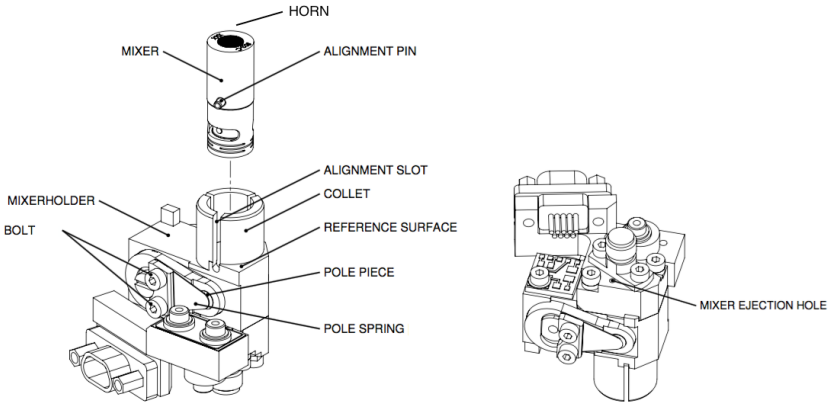


Figure 5.14: Schematic diagram of the ALMA style mixer block along with the horn and back-piece assembly which slots into the mixer holder (Hesper & Bekema, 2014).

The SIS device, back-piece and part of the mixer block were supplied to Oxford by colleagues at the Kapteyn Astronomical Institute in the Netherlands with the rest of the block, including the feed horn and an aluminium mount, being fabricated in-house by the mechanical workshop at Oxford University. A short description of the smooth-walled, multiple flare-angle-discontinuity feed that was employed for measurements with this mixer is given in the following section.

### 5.4.1 A Smooth-Walled ALMA Style Feed Horn

Further to the feed horns described in Chapter 3, an additional horn was developed in collaboration with the Netherlands Institute for Space Research (SRON) to operate between $780 - 950\ GHz$ but with a further constraint that it needed to integrate into the ALMA style mixer block shown in Figure 5.14 and have a narrower Full Width at Half Maximum (FWHM) beamwidth to enable testing and operation inside the PTC cryostat. Similar to the horn in Section 3.3 of Chapter 3, this smooth-walled, three-section flare-angle-discontinuity feed was designed using a combination of modal matching and Genetic Algorithm (GA) optimisation to have a FWHM beamwidth of $\sim 9.37°$ at the centre frequency of 865 $GHz$. This is approximately a third narrower when compared to the FWHM of $\sim 14.67°$ at 865 $GHz$ of the previous horn. The optimised dimensions for this design are given in Table 5.3 while the simulated far-field radiation patterns can be seen in Figure 5.15.

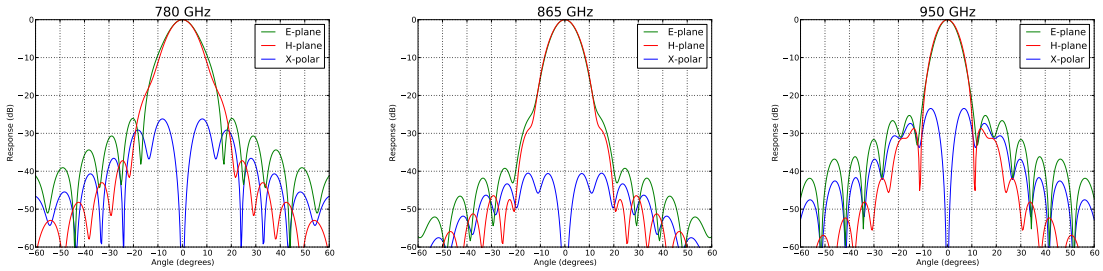


Figure 5.15: Theoretical predictions for E-plane, H-plane and cross-polar far-field radiation patterns at 780, 865 and 950 $GHz$ for an ALMA style feed horn obtained using GA optimisation.

| Parameter | Length ($mm$) |
|---|---|
| $R_0$ | $0.176 \pm 0.01$ |
| $R_1$ | $0.410 \pm 0.01$ |
| $R_2$ | $0.524 \pm 0.01$ |
| $R_A$ | $1.468 \pm 0.01$ |
| $L_1$ | $0.428 \pm 0.01$ |
| $L_2$ | $0.426 \pm 0.01$ |
| $L_3$ | $10.224 \pm 0.01$ |

Table 5.3: Optimised parameter values for a smooth-walled, ALMA style feed horn design.

Figure 5.15 shows this design to exhibit excellent beam circularity, low sidelobes and cross-polar levels below $-25\ dB$ relative to the co-polar peak across the band. The horn itself was fabricated out of brass, along with a circular to rectangular waveguide transition, by the mechanical workshop at Oxford University. As before, a direct machining technique described in Chapter 3 was used to create the main body of the horn. However, one of the challenges that required careful attention during the fabrication process was the unusual interface between the waveguide output of the feed and the back-piece containing the mixer that connects to it. Given that the entire horn and mixer assembly was to fit into a unique ALMA mixer holder, it was not possible to use the UG$-$387/U flange interface that normally connects a waveguide transition to the circular output of a smooth-walled horn at these frequencies. Instead, a custom split-block transition was made using Electrical Discharge Machining (EDM) to form an interlocking jigsaw design which minimises waveguide misalignment and holds the two halves of the transition in place. This transition is dowelled on the side that connects to the circular waveguide output of the horn and screwed into place. The horn and its waveguide interface are shown in Figure 5.16.

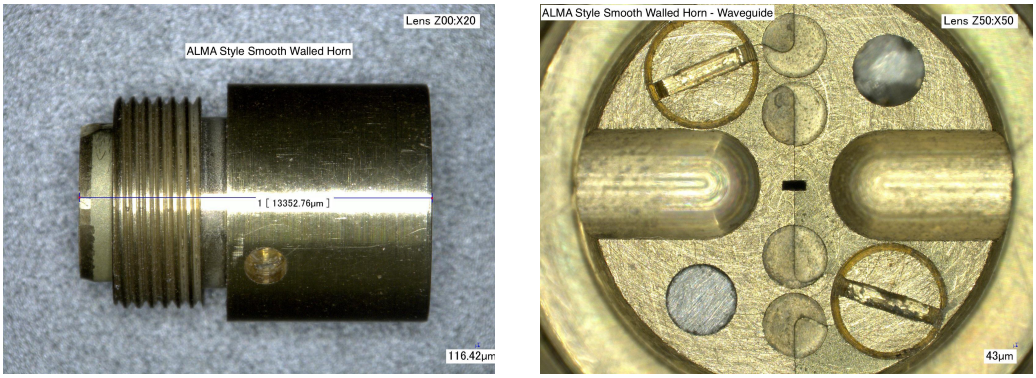


(a) Side view. (b) Rectangular waveguide output.

Figure 5.16: Microscope images of the fabricated smooth-walled ALMA style feed horn.

Given that the dimensions of the rectangular waveguide in Figure 5.16(b) are just $300 \times 150\ \mu m$, it can be seen that the interlocking design of the transition has produced excellent results with virtually no misalignment between the two halves. While the intricate interface meant that it was not possible to measure the beam patterns of this horn using the method described in Chapter 3, once the feed was combined with the 900 $GHz$ mixer described in Section 5.4, it led to promising results as will be shown in the following section.

### 5.4.2 Noise Temperature Measurements

Once the feed had been fabricated, the back-piece containing the 900 $GHz$ mixer was attached using a centring ring and a cap nut. The horn and mixer assembly was then housed in the mixer block shown in Figure 5.14, which was bolted to an aluminium jig similar to the one in Figure 5.4. This jig was modified slightly to accommodate the new mixer block and to place the aperture of the feed at the focal point of the internal parabolic mirror. The block was then installed in the PTC so that noise temperature measurements could be performed using the Nb/AlN/NbN device and 900 $GHz$ VDI LO.

These measurements were carried out with the addition of 1 $THz$ low-pass IR filters installed on the inner radiation shield windows which enabled $90-95$ % of the incident RF signal to be transmitted while allowing the mixer block to cool to $\sim 3.2$ $K$. As previously, HDPE windows were employed on both the LO and RF ports of the outer vacuum shroud. All other windows of the PTC were blanked out with aluminium plates.

The receiver noise temperature was determined using the Y-factor method once again, including the hot and cold load noise temperature correction according to the Callen and Welton law (Callen & Welton, 1951; Kerr et al., 1997), described in Sections 1.5.1 and 1.5.2 of Chapter 1. Room temperature ($\sim 290$ $K$) Eccosorb provided the "hot" load but the "cold" load now came from a small, 30 $mm$ diameter aluminium cone that was coated in a non-reflective, black-body paint and anchored to the PTC cold plate ($\sim 4$ $K$). A flip mirror mounted on top of a cryogenic motor was used to switch between the two loads.

A small series resistance of $\sim 3.5$ $\Omega$, likely caused by the bias circuitry around the junction, was observed when the mixer cooled down. This was determined from the gradient of the DC super current in the unpumped I-V curve and subtracted out of the measurement results. A coil current of $\sim 10$ $mA$ (second null) was used to suppress the Josephson current.

This mixer was most sensitive at a pump level of $\sim 16-20$ % of its gap current and when biased in the range $V_b = 2.0-2.4$ $mV$. The measured pumped I-V and hot/cold IF output curves between $800-900$ $GHz$ are shown in Figures 5.17 and 5.18 respectively. A plot of the measured DSB receiver noise temperature, RF loss corrected noise temperature and mixer conversion gain as a function of frequency is presented in Figure 5.19.

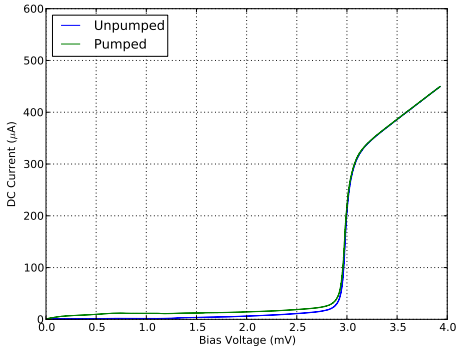


(a) 800 $GHz$.

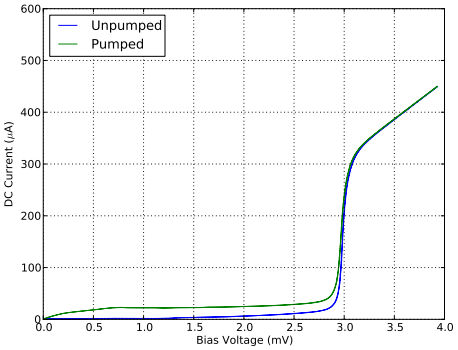


(b) 820 $GHz$.

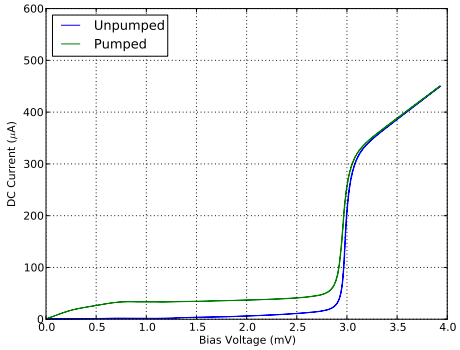


(c) 830 $GHz$.

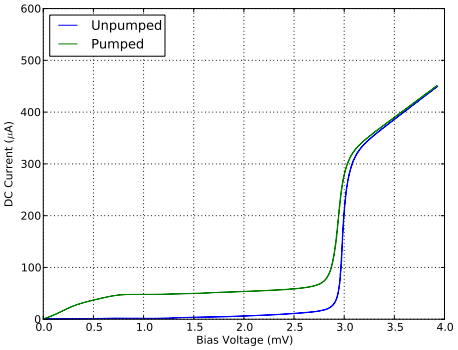


(d) 840 $GHz$.

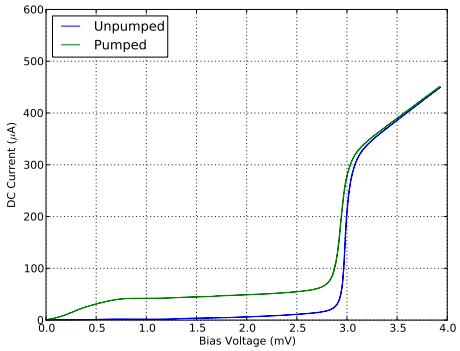


(e) 860 $GHz$.

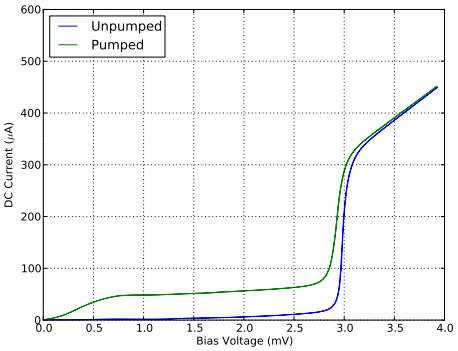


(f) 870 $GHz$.

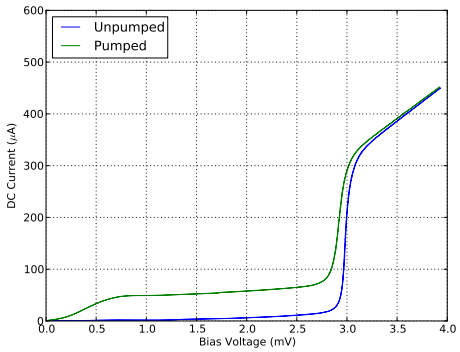


(g) 880 $GHz$.

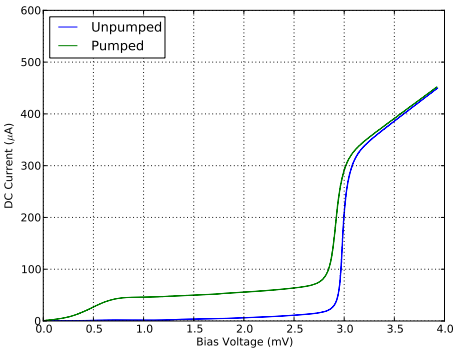


(h) 900 $GHz$.

Figure 5.17: A selection of pumped I-V curves used for noise temperature measurements between $800 - 900\ GHz$ with the PTC and a Nb/AlN/NbN SIS mixer.

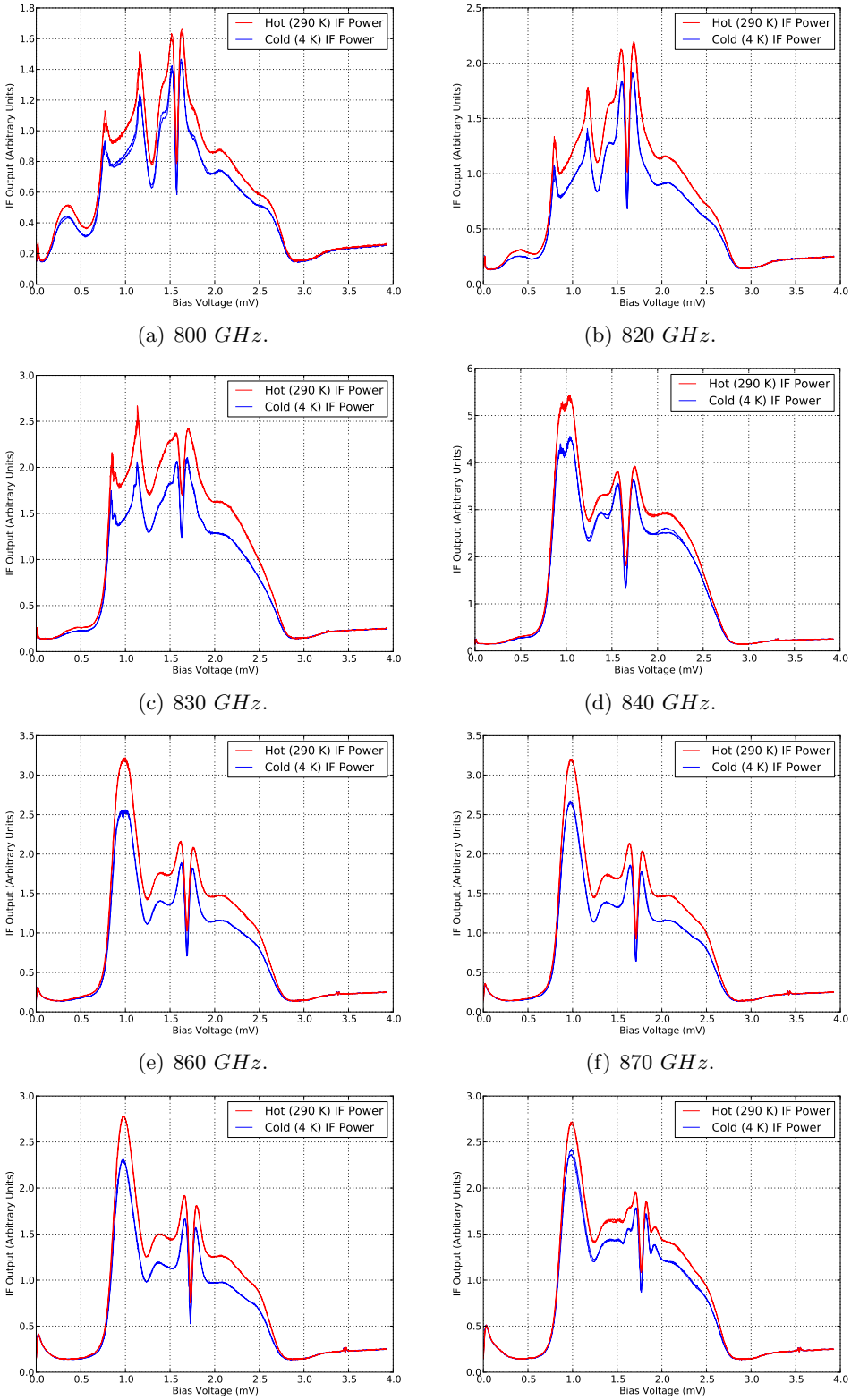


(a) 800 $GHz$. (b) 820 $GHz$.

(c) 830 $GHz$. (d) 840 $GHz$.

(e) 860 $GHz$. (f) 870 $GHz$.

(g) 880 $GHz$. (h) 900 $GHz$.

Figure 5.18: A selection of IF output curves used for noise temperature measurements between $800 - 900\ GHz$ with the PTC and a Nb/AlN/NbN SIS mixer.

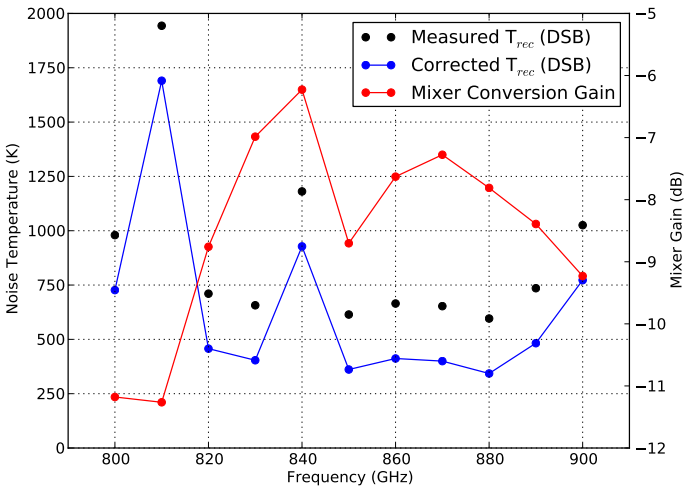


Figure 5.19: Measured DSB receiver noise temperature as well as the noise temperature corrected for RF losses and mixer conversion gain between $800 - 900\ GHz$. Propagating the errors by assuming a 10 % uncertainty on the physical temperature of the 4 $K$ cold load leads to negligible errors in these results.

The measured noise temperature results in Figure 5.19 show good performance across most of the $800 - 900\ GHz$ band. These measurements have been corrected for RF optical losses induced by a $\sim 28$ % reflective beamsplitter and a rectangular waveguide mismatch between the full height (150 $\mu m$) waveguide output of the horn and the reduced height (75 $\mu m$) waveguide input of the mixer back-piece. This waveguide mismatch, which can be seen in detail in Figure 5.20, arose as a result of the practical limitations of machining a circular to rectangular waveguide transition with the required dimensions ($300 \times 75\ \mu m$).

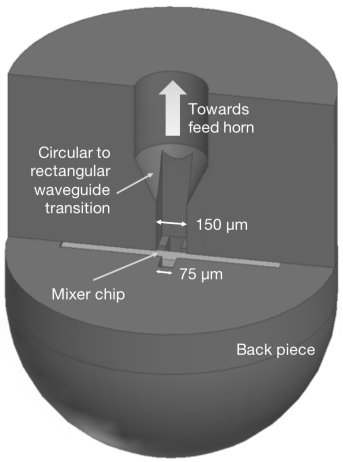


Figure 5.20: Rectangular waveguide mismatch between the reduced height waveguide of the mixer back-piece and the full height circular to rectangular waveguide transition.

Because the waveguide transition was directly machined from a brass block split along the E-plane, it would have been necessary to drill to a depth of 150 $\mu m$ into each side of the block using a drill diameter of less than 75 $\mu m$ in order to fabricate a 300 $\times$ 75 $\mu m$ rectangular waveguide. When working with tools this small and drilling to a depth that is approaching twice their diameter, the tool tends to drift in the metal and the resulting waveguide is skewed relative to the vector normal to the plane along which the block has been split. As such, even a 300 $\times$ 150 $\mu m$ waveguide transition is pushing the limit of the available machining technology. The resulting mismatch presents a discontinuity to the RF signal and leads to a loss of incident power. To estimate this loss, a HFSS simulation was carried out comparing coupling into the mixer when using a full and a reduced height waveguide output from the horn. The result of this simulation can be seen in Figure 5.21.

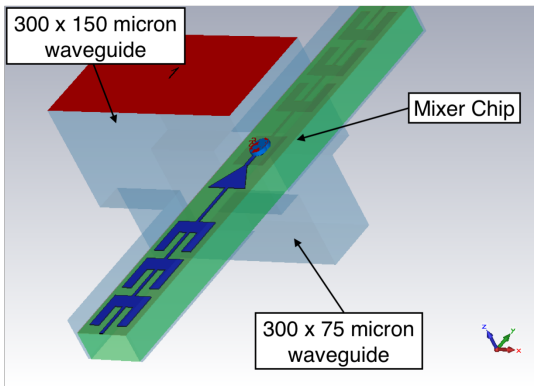


(a) HFSS model screenshot showing the 150 $\mu m$ waveguide, 75 $\mu m$ waveguide and the mixer chip.

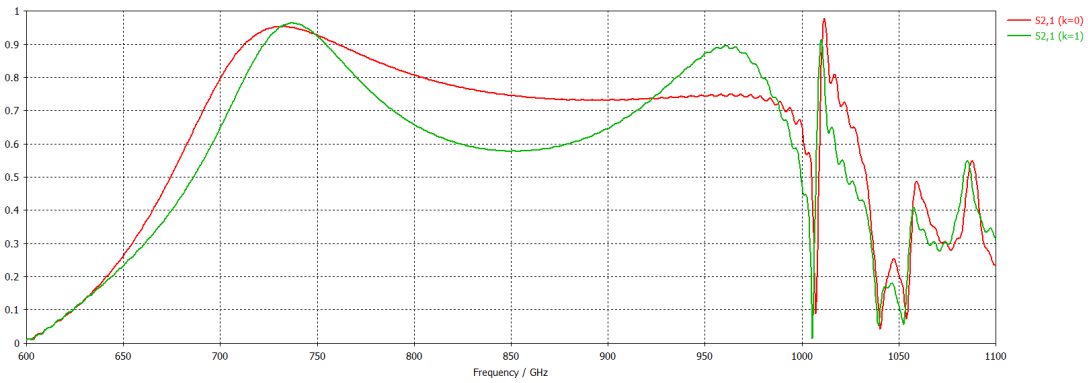


(b) Magnitude of the simulated S21 voltage transmission coefficient as a function of frequency in the presence (green line) and absence (red line) of a waveguide height mismatch.

Figure 5.21: HFSS model and S21 transmission results of the mismatch between the full height waveguide of the transition and the reduced height waveguide of the mixer back-piece.

The modelling work in Figure 5.21 was performed by colleagues at the Kapteyn Astronomical Institute in the Netherlands that supplied the mixer back-piece to Oxford (Baryshev & Khudchenko, 2016). Figure 5.21(a) shows an image of the HFSS model set up such that the mismatch is present while Figure 5.21(b) plots the linear magnitude of the simulated S21 voltage transmission coefficient as a function of frequency for two different cases. First, the case of a reduced, 75 $\mu m$ height waveguide transition that would present no mismatch ($k = 0$, red line) and second, a full, 150 $\mu m$ height waveguide transition that causes the mismatch between the horn and the mixer back-piece ($k = 1$, green line).

To estimate the power coupling difference between the two cases, the S21 voltage transmission coefficient presented in Figure 5.21(b) needs to be squared before the difference can be calculated, since power is proportional to the square of the voltage. With this in mind, the power coupling difference between the two cases has been estimated to be $\sim 11$ % at the higher frequency end of 900 $GHz$, increasing to $\sim 22$ % towards the lower end of 800 $GHz$. Therefore, the mismatch between the $300 \times 150$ $\mu m$ waveguide output of the horn and the $300 \times 75$ $\mu m$ input of the mixer back-piece shown in Figure 5.20 leads to a $\sim 11 - 22$ % power coupling reduction into the SIS mixer within the $800 - 900$ $GHz$ band of interest, which could be even more significant when combined with the mixer conversion gain.

Since it was non-trivial to fabricate the feed horn with a reduced height waveguide transition at the time of these measurements, there are instead plans to modify the design of the mixer back-piece to feature a full height rectangular waveguide input, thus reducing the RF power loss caused by the waveguide mismatch. In addition, a number of other modifications are due to be implemented to the tunnel junction design, including the mixer chip, in order to further improve the receiver performance. For example, it can be seen in the pumped I-V curves presented in Figure 5.17 that the mixer suffers from the junction heating effect in the presence of a strong LO signal, as evidenced by the suppression of the energy gap at frequencies above 820 $GHz$, Figures 5.17(c) $-$ 5.17(h). This effect is most likely caused by a combination of the resistive properties of the mixer (Khudchenko et al., 2016) and the fact that the bottom, Niobium (Nb), electrode of the junction is located between the high gap Niobium-Titanium-Nitride (NbTiN) ground plane and the Niobium-Nitride (NbN) top electrode. As a result, when quasi-particle electrons moving through

the Nb electrode reach the NbTiN ground plane interface, they encounter an energy step presented by the higher gap material, which impedes the energy transport of the current. While it is possible for quasi-particle electrons to move across the energy boundary via Andreev reflections (Andreev, 1964), this charge transfer process can lead to heat trapping in the Nb electrode resulting in an elevated local junction temperature, suppression of the superconductor energy gap and diminished sensitivity in the upper frequency range of the mixer. To overcome this potential issue, the modified mixer design plans to replace the NbTiN ground plane with an Aluminium layer, thus allowing hot electrons to escape via the normal metal. Furthermore, the top wiring layer of the mixer will be replaced with NbN, to make it the same as the superconducting material used for the top electrode of the tunnel junction. These tunnel junctions are expected to have an area of 1 $\mu m^2$ and feature an Aluminium-Oxide insulation layer, instead of the Aluminium-Nitride one that is currently employed (Tan et al., 2018).

As well as this, the mixer chip circuit will be altered to include a radial waveguide probe, rather than the triangular one present in the current design, which will allow for coverage of a broader frequency bandwidth. Additionally, the radial probe will be extended to $\sim$ 35 % of the waveguide height to increase RF signal coupling from the waveguide to the SIS junction circuit. The radial probe will be connected to the virtual grounding pad, RF chokes and the IF bonding pads using a high impedance line to form an integrated bias-tee arrangement (Risacher et al., 2003). A preliminary design of the new mixer chip is shown in Figure 5.22 while the predicted conversion gain and noise temperature performance, simulated using a combination of HFSS and SuperMix (Ward et al., 1999) modelling packages, can be seen in Figure 5.23. Both the proposed mixer design in Figure 5.22 and the simulated results in Figure 5.23 have been reproduced from Tan et al. (2018).

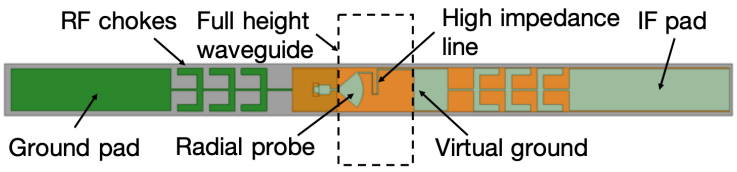


Figure 5.22: Preliminary design of an improved SIS mixer chip employing a radial probe coupled to a full height rectangular waveguide (Tan et al., 2018).

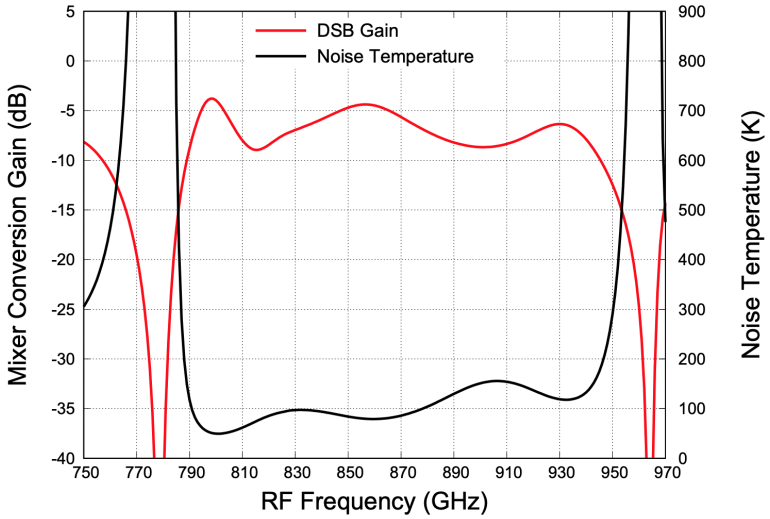


Figure 5.23: Predicted gain and noise temperature performance of the modified SIS mixer chip design, simulated using HFSS and SuperMix software packages (Tan et al., 2018).

The proposed modifications to the tunnel junction and mixer chip design can be seen to significantly improve the receiver sensitivity, with predicted noise temperature performance between $790 - 940\ GHz$ approaching a few multiples of the quantum limit at these frequencies, as shown in Figure 5.23. However, it can also be seen that the simulated Double Side Band (DSB) gain is not yet ideal, ranging between $\sim -5$ and $-10\ dB$ across the band. This remains an active area of study, with ongoing work to further optimise the mixer conversion gain and cover the full $780 - 950\ GHz$ frequency band of interest (Tan et al., 2018).

The lowest measured noise temperature in Figure 5.19 was $\sim 600\ K$ at $880\ GHz$ with a total estimated RF noise contribution of $\sim 420\ K$ as determined by the intersecting lines method described in Ke & Feldman (1994). As such, the measured results are clearly $\sim 2-3$ times worse than the ALMA Band 10 noise specification requirements of $T_{DSB} < 230\ K$ over 80 % of the band and $T_{DSB} < 344\ K$ over 100 % of the band at any frequency. However, it should be noted that these are highly stringent requirements and even after considerable effort by the National Astronomical Observatory of Japan (NAOJ) team that worked on the development the ALMA Band 10 cartridge, a request was made to change the $T_{DSB} < 230\ K$ noise temperature specification to cover only 60 %, rather than 80 %, of the central band due to the technical challenges involved (Hills, 2012). It is therefore not

entirely surprising that given the various technical and experimental challenges involved with the prototype system described here, a noise temperature result consistent with the ALMA specification has not been met.

However, with the exception of 840 $GHz$, the receiver was found to exhibit good performance between $820 - 890$ $GHz$ with corrected, "ideal" noise temperatures below 500 $K$ in this range. This is consistent with previous tests of such devices at these frequencies reported by Khudchenko et al. (2016) which obtained values of $\sim 250$ $K$ at 800 $GHz$ and $\sim 550$ $K$ at around 940 $GHz$ once corrected for an 88 % transparent beamsplitter.

The increased noise temperature at the lower end of the frequency range (800 $GHz$) could be explained by the fact that it was barely possible to pump the device here as shown in the plot of the pumped I-V curve in Figure 5.17(a). As such, the mixer was not operating at its most sensitive pump level which led to a reduced IF response shown in Figure 5.18(a) and a higher noise temperature. It is not yet completely clear why the performance degrades at the higher frequency end (900 $GHz$) given that the mixer can be adequately pumped here but one possible explanation comes from the recent work of Traini et al. (2020), which investigates the effect of LO power heating on tunnel junctions and the resulting impact on the performance of SIS mixers at Terahertz frequencies. The paper shows that in the presence of an increasing LO signal, the effective junction temperature can rise significantly above the temperature of the mixer block which leads to suppression of the superconducting energy gap and a substantial increase in the noise temperature of the receiver. The effect of LO heating on mixer performance is particularly detrimental when the mixer temperature is greater than $\sim 0.3 \times T_c$, where $T_c$ is the critical temperature of the junction which in the case of the device described here and in Traini et al. (2020) is $\simeq 9.9$ $K$. Therefore, to mitigate this effect, it would have been necessary to cool the mixer below 3 $K$ which was not possible with this particular setup. In addition, the paper finds that for a given pump level between $800 - 900$ $GHz$, the effective junction temperature increases at a rate of 0.53 $K/100$ $GHz$. When combined with the 3.2 $K$ base temperature of the PTC, which is greater than $0.3 \times T_c$ for this device, as well as the relatively large LO signal required to pump the mixer, this effect could provide a feasible explanation for the rise in receiver noise temperatures observed towards the upper end of the measured frequency range.

The worst performance can be seen at 810 $GHz$ and 840 $GHz$, both of which produce sharp spikes in an otherwise smooth noise temperature profile. The exact cause of this behaviour is not yet fully understood, but possible explanations include the mixer not being optimally tuned as well as increased Local Oscillator noise (Traini et al., 2020) at these frequencies.

Even though the stringent ALMA noise temperature specifications have not been met with the measured results presented here, it can be concluded that the initial iteration of the 900 $GHz$ SIS receiver is showing promising results as an experimental testbed for high frequency cryogenic receiver development. However, in order to improve the performance of this system and bring it to the level of current state-of-the-art facilities such as ALMA Band 10, for example, the additional modifications described in this chapter are required. This is currently an active and ongoing area of research.

## 5.5 Conclusions

The work presented in this Chapter has focused on the development of a coherent, heterodyne receiver suitable for operation at Terahertz frequencies. The system was developed with all of the RF and most of the LO signal coupling optics inside a Pulse Tube Cooled cryostat to reduce RF losses as well as an internally mounted cryogenic cold load for more sensitive Y-factor noise temperature measurements.

The receiver was initially tested between $600 - 700$ $GHz$ where it showed reasonable performance once it was possible to pump the SIS device using a pre-tensioned, internally mounted cryogenic Mylar beamsplitter. The system was then modified and upgraded before being tested between $800 - 900$ $GHz$ using a Nb/AlN/NbN twin tunnel junction SIS mixer combined with a custom smooth-walled feed horn. While the measured receiver noise temperatures between $800 - 900$ $GHz$ were $\sim 2 - 3$ times worse than the ALMA Band 10 noise specification requirements of $T_{DSB} < 230$ $K$ over 80 % of the band and $T_{DSB} < 344$ $K$ over 100 % of the band, there are several reasons for this which have been described in detail in this chapter and which are still being investigated.

However, once corrected for a $\sim$ 28 % reflective beamsplitter and a waveguide height

mismatch between the output of the horn and the input of the mixer back-piece, the receiver demonstrated noise temperature results consistent with similar tests of such devices presented by Khudchenko et al. (2016).

In the near future, there are plans to investigate and improve the performance of the receiver between $800-900\ GHz$ by fabricating a full height ($300\times150\ \mu m$) mixer back-piece to remove the waveguide mismatch (Tan et al., 2018) as well as to determine the exact cause of diminished performance observed at 810 and 840 $GHz$.

Nonetheless, this experimental testbed has successfully demonstrated a "proof of concept" coherent, heterodyne receiver design with the following novel features:

- internally mounted RF signal coupling optics, including a pre-tensioned cryogenic Mylar beamsplitter,
- an internally mounted cryogenic cold load,
- a custom, easy to machine, smooth-walled feed horn,
- a modular design which allows for simple modification and allows laboratory-based testing of different mixers.

As such, with the feasible upgrades described, the system should be able to demonstrate noise performance consistent with the ALMA Band 10 specification while being easy to modify and upgrade if required to accommodate a supra-Terahertz mixer.

With the advent of new technology and SIS junctions with larger energy gaps, the aim is to ultimately push the system to higher frequencies of 1.1 and 1.3 $THz$, as dictated by atmospheric transmission windows, which could make the receiver a useful instrument upgrade for high frequency radio telescopes such as ALMA in years to come.

# Chapter 6

# Concluding Remarks

## 6.1 Summary

The field of high frequency radio astronomy is currently enjoying an exciting era of powerful, ground based facilities such as the Atacama Large Millimetre/sub-millimetre Array (ALMA) and the Atacama Pathfinder EXperiment (APEX) telescope which are already on-line and collecting data in the sub-millimetre part of the electromagnetic spectrum.

Given that such facilities require a significant amount of time and effort to establish, including a variety of international collaborations, there is considerable motivation to advance the technology on which they operate to maximise their ability to provide a wide range of useful scientific data for the foreseeable future.

ALMA, for example, is currently designed to observe the universe in 10 different, discrete frequency bands which are dictated by the atmospheric transmission windows at the Chajnantor Plateau. Bands 1 and 2 ($35-50$ and $65-90\ GHz$) employ High Electron Mobility Transistor (HEMT) detectors while Superconductor-Insulator-Superconductor (SIS) mixer technology is used for Bands $3-10$ ($84-950\ GHz$).

Although it is already possible to achieve near quantum limited detection sensitivity at the lower frequencies, with an average Band 3 receiver noise temperature performance of 33.2 $K$, considerable challenges remain in achieving similar results at the high frequency end, especially near 1 $THz$ and beyond.

There are several reasons for this; to begin with, difficulty in fabricating and producing

powerful $THz$ frequency LO sources, with high conversion gains and well defined harmonic content, often makes it difficult to pump SIS devices to their optimum sensitivity levels. In addition, SIS mixers employed in sub-mm frequency heterodyne receivers are usually made with niobium as the superconducting material of choice which has an energy gap of $\sim 675\ GHz$ at a physical temperature of $\sim 3.7\ K$. While in principle it is possible to detect radiation up to double the gap frequency (i.e. 1350 $GHz$ in this example), photons with energy above the gap will break superconducting Cooper pairs leading to surface impedances which degrade the mixer sensitivity. Research into new, "high-gap" materials such as niobium nitride and niobium titanium nitride for use in SIS mixers is currently going on with the aim to push the detecting capabilities of SIS mixer receivers well into the $THz$ regime. Furthermore, the fact that the physical dimensions of quasi-optical components (such as the feed horn antenna) decrease with increasing frequency means that there are added fabrication challenges when making these components such that they perform as required when used in a high frequency receiver system. All of these issues combined make it non-trivial to achieve quantum-limited sensitivity at $THz$ frequencies.

As such, the work presented in this thesis has attempted to address a number of important technological aspects of sub-mm wave detection, with the aim of developing the current technology for potential use by sub-mm telescope facilities in the future.

To begin with, an introduction to the area of sub-mm astronomy was presented in Chapter 1 and the principle of coherent heterodyne detection using SIS mixer based receivers described, which are required to perform high resolution spectroscopic measurements at sub-millimetre wavelengths.

The work in Chapter 2 focused on the harmonic content of Local Oscillator (LO) sources and how this can affect receiver performance in terms of noise and spectral output. It was shown that by pumping an SIS mixer using a commercially available, spectrally impure LO operating between $\sim 180 - 270\ GHz$, it was possible for RF signals to be down converted into the IF band multiple times which caused the same spectral line to appear at several locations in the IF spectrum leading to the presence of highly confusing spectral artefacts.

It was deduced that the generation of unwanted harmonics emanating from the LO did not occur in the final LO frequency multiplication stage, but rather came from the spectral

impurity of the low frequency multiplier chain. This was shown to affect the receiver performance in terms of noise and spectral content, thus requiring careful consideration and evaluation. This is particularly important when receivers employing such sources are used for astronomical observations.

The content presented in Chapter 3 looked at the design, fabrication and far-field beam pattern measurement of a number of smooth walled, multiple flare angle discontinuity feed horns operating in the $THz$ frequency regime. These feeds were designed using a combination of modal matching and genetic algorithm optimisation techniques which led to high quality simulated beam patterns for a three section design between $780-950\ GHz$ and a two section design employed in a four pixel feed horn array operating between $1300-1500\ GHz$.

The horns were fabricated by the mechanical workshop at Oxford University using a direct machining technique which can robustly create any number of identical feeds thus making it suitable for applications such as multiple pixel feed horn arrays. By ensuring that the fabrication tool dimensions were within $\sim 10\ \mu m$ of the design specifications, it was possible to create feeds with excellent measured beam patterns which closely resembled their theoretical predictions. This makes such horns highly attractive antenna option alternatives to the more complex corrugated feed horn structure at Terahertz frequencies.

Another important aspect of receiver technology was examined in Chapter 4 which demonstrated the use of E-Beam lithography for the fabrication of Schottky barrier diodes for high radio frequency applications. Because such devices are extensively used in multiplier and mixer components alike, advancing the fabrication technology to create novel devices can have useful results for sub-mm astronomy such as the development of more efficient and stable LO sources.

The E-Beam system was successfully used not only to write the ohmic pad layer of the diode, but to also define sub-micron anode features and to employ a novel bi-layer resist process for the creation of suspended air-bridge structures which are necessary for the successful operation of these devices at high radio frequencies.

The initial diodes were made using a combination of E-Beam and photolithography and these were shown to exhibit promising I-V characteristics, especially for the smaller anode diameters of 0.6, 0.8 and 0.9 $\mu m$. In addition, Schottky devices were also created

using E-Beam lithography alone and once the exposure parameters had been fine tuned, a frequency multiplier diode was installed in a waveguide block and its RF performance measured. The device produced an output power of approximately $0.1 - 0.2\ mW$ across a broad, $225 - 330\ GHz$ frequency range which corresponds to a conversion efficiency of between $\sim 1 - 2\ \%$. This is an excellent result which is comparable to current "state-of-the-art" performance for such devices. This validates the E-Beam fabrication technique and provides a platform on which future iterations of this process can be pursued to ultimately realise the small-feature devices required for use in multiplier and mixer circuits suitable for astronomy applications at $THz$ frequencies and beyond.

Finally, Chapter 5 focused on the development of a prototype coherent, heterodyne receiver suitable for operation at Terahertz frequencies. One of the major novel features of this system was that it was developed with all of the RF and most of the LO signal coupling optics inside a Pulse Tube Cooled cryostat. This helps to reduce RF losses not only because the components are at a lower physical temperature but also because signals have a shorter optical travel path through the highly attenuating atmosphere. Furthermore, the system employed an internally mounted cryogenic cold load for more sensitive Y-factor noise temperature measurements.

The receiver was initially tested between $600 - 700\ GHz$ where it showed reasonable performance once it was possible to pump the SIS device using a pre-tensioned, internally mounted cryogenic Mylar beamsplitter. The system was then modified and upgraded before being tested between $800 - 900\ GHz$ using a Nb/AlN/NbN twin tunnel junction SIS mixer combined with a custom smooth walled feed horn. The results produced encouraging noise temperature measurements once corrected for a $\sim 28\ \%$ reflective beamsplitter and a waveguide dimension mismatch between the output of the horn and the mixer back-piece.

## 6.2 Future Work

In the future, further development in the following key areas could be pursued to further advance the heterodyne receiver technology described in this thesis to higher frequencies and make it viable for supra-Terahertz astronomy applications:

1. Build upon the diode design and E-Beam fabrication process presented in Chapter 4 to realise high conversion efficiency multiplier diodes operating at even higher frequencies. Once this is achieved the diodes can be installed in multiplier circuits and mounted inside waveguide blocks to create highly efficient, stable and spectrally pure LO sources for $THz$ frequency applications and beyond.

2. Improve the performance of the 900 $GHz$ SIS heterodyne receiver described in Chapter 5 by fabricating the full height ($300 \times 150$ $\mu m$) mixer back-piece required to remove the waveguide mismatch between the output waveguide of the horn and the input waveguide of the mixer.

3. Test and characterise the Pulse Tube Cooled heterodyne receiver system described in Chapter 5, including the novel internal optical setup, at frequencies above 1 $THz$ once suitable SIS devices are available.

# References


Alderman, B., Sanghera, H., Price, C., Thomas, B. & Matheson, D. N., 2007. Fabrication of Reproducible Air-bridged Schottky Diodes for use at Frequencies Near 200 GHz. *2007 Joint 32nd International Conference on Infrared and Millimeter Waves and the 15th International Conference on Terahertz Electronics*, 848–849.

Andreev, A. F., 1964. Thermal conductivity of the intermediate state of superconductors. *Sov. Phys. JETP*, **19**, 1228–1231.

Bardeen, J., Cooper, L. N. & Schrieffer, J. R., 1957. Microscopic Theory of Superconductivity. *Physical Review*, **106**(1), 162–164.

Baryshev, A. M., Hesper, R., Mena, F. P., Klapwijk, T. M., van Kempen, T. A. et al., 2015. The ALMA Band 9 receiver - Design, construction, characterization, and first light. *A&A*, **577**, A129.

Baryshev, A. M. & Khudchenko, A., 2016. Horn-Mixer Waveguide Mismatch Simulations. Private Communication.

Belitsky, V. Y., Jacobsson, S. W., Filippenko, L. V. & Kollberg, E. L., 1995. Broadband twin-junction tuning circuit for submillimeter SIS mixers. *Microwave and Optical Technology Letters*, **10**(2), 74–78.

Bird, T. S., 2009. Definition and Misuse of Return Loss [Report of the Transactions Editor-in-Chief]. *IEEE Antennas and Propagation Magazine*, **51**(2), 166–167.

Bishop, W. L., Crowe, T. W. & Mattauch, R. J., 1993. PLANAR GaAs SCHOTTKY DIODE FABRICATION: PROGRESS AND CHALLENGES. *Proceedings of the Fourth International Symposium on Space Terahertz Technology*, 415–429.

Bustos, R., Rubio, M., Otárola, A. & Nagar, N., 2014. Parque Astronómico de Atacama: An Ideal Site for Millimeter, Submillimeter, and Mid-Infrared Astronomy. *Publications of the Astronomical Society of the Pacific*, **126**, 1126–1132.

Callen, H. B. & Welton, T. A., 1951. Irreversibility and Generalized Noise. *Physical Review*, **83**(1), 34–40.

Castetter, D., 2018. An Introduction to YIG Tuned Oscillators. URL `https://www.microwave.gr/content/yigintro.pdf`.

Clarricoats, P. J. B. & Olver, A. D., 1984. *Corrugated Horns for Microwave Antennas*. Peter Peregrinus Ltd.

Devyatov, I. A., Kuzmin, L. S., Likharev, K. K., Migulin, V. V. & Zorin, A. B., 1986. Quantum-statistical theory of microwave detection using superconducting tunnel junctions. *Journal of Applied Physics*, **60**(5), 1808–1828.

Ellison, B., 2021. Side Band Separation Schematic. Private Communication.

European Southern Observatory, 2018. ALMA Receiver Bands. URL `http://www.eso.org/public/teles-instr/alma/receiver-bands/`.

Friis, H. T., 1944. Noise Figures of Radio Receivers. *Proceedings of the IRE*, **32**(7), 419–422.

Garfield, D. G., Mattauch, R. J. & Bishop, W. L., 1988. DESIGN, FABRICATION, AND TESTING OF A NOVEL PLANAR SCHOTTKY BARRIER DIODE FOR MILLIMETER AND SUBMILLIMETER WAVELENGTHS. *Conference Proceedings '88.. IEEE Southeastcon*, 154–160.

Gifford, W. E. & Longsworth, R. C., 1964. Pulse Tube Refrigeration. *Journay of Engineering for Industry*, **86**(3), 264–268.

Golay, M. J. E., 1947. Theoretical Consideration in Heat and Infra-Red Detection, with Particular Reference to the Pneumatic Detector. *The Review Of Scientific Instruments*, **18**(5), 347–356.

Gunn, J. B., 1963. Microwave oscillations of current in III-V semiconductors. *Solid State Communications*, **1**(4), 88 – 91.

Haupt, R. L. & Haupt, S. E., 2004. *Practical Genetic Algorithms*. Wiley-Blackwell.

Hector, A., Ellison, B. N., Yassin, G., Tan, B. K. & Leech, J., 2015a. Investigating the Origin of Harmonics in a 230 GHz Local Oscillator. *Proceedings of the Twenty Sixth International Symposium on Space Terahertz Technology*.

Hector, A., Trifonov, A. V., Tong, E., Grimes, P. & Yassin, G., 2017. A Smooth Walled Four Pixel Feed Horn Array Operating at 1.4 THz. *Proceedings of the Twenty Eighth International Symposium on Space Terahertz Technology*.

Hector, A., Yassin, G., Ellison, B. N., Leech, J. & Henry, M., 2015b. A SMOOTH-WALLED FEED HORN OPERATING IN THE TERAHERTZ REGIME. *Proceedings of the Thirty Sixth ESA Antenna Workshop on Antennas and RF Systems for Space Science*.

Henry, M., 2014. W-Band Filter Transmission. Private Communication.

Hesper, R. & Bekema, M., 2014. ALMA Band 9 Cartridge Top Level Assembly and Service Manual.

Hills, R., 2012. Change Request for the Band 10 Cartridge Noise Performance (DRAFT!). URL `https://safe.nrao.edu/wiki/pub/ALMA/11May12Agenda/Band10_ASAC_2012.pdf`.

IEEE, 1988. *IEEE Standard Dictionary of Electrical and Electronic Terms, Fourth Edition*. New York, IEEE Press.

James, G. L., 1981. Analysis and Design of $TE_{11}$-to-$HE_{11}$ Corrugated Cylindrical Waveguide Mode Converters. *IEEE Transactions on Microwave Theory and Techniques*, **29**(10), 1059–1066.

JEOL, 2018. Scanning Electron Microscope A To Z.

Kasemann, C., Gsten, R., Heyminck, S., Klein, B., Klein, T., Philipp-May, S., Korn, A., Schneider, G., Henseler, A., Baryshev, A. & Klapwijk, T., 2006. CHAMP+: a powerful array receiver for APEX. *Proceedings of SPIE, Millimeter and Submillimeter Detectors and Instrumentation for Astronomy III*, **6275**, 62750N.

Ke, Q. & Feldman, M. J., 1994. A Technique for Noise Measurements of SIS Receivers. *IEEE Transactions on Microwave Theory and Techniques*, **42**(4), 752–755.

Kerr, A. R., Feldman, M. J. & Pan, S. K., 1997. Receiver Noise Temperature, the Quantum Noise Limit, and the Role of the Zero-Point Fluctuations. *Proceedings of the Eighth International Symposium on Space Terahertz Technology*, 101–111.

Kerr, A. R., Pan, S. K., Claude, S. M. X., Dindo, P., Lichtenberger, A. W., Effland, J. E. & Lauria, E. F., 2014. Development of the ALMA Band-3 and Band-6 Sideband-Separating SIS Mixers. *IEEE Transactions on Terahertz Science and Technology*, **4**(2), 201–212.

Khudchenko, A., Baryshev, A. M., Rudakov, K. I., Dmitriev, P. M., Hesper, R., de Jong, L. & Koshelets, V. P., 2016. High-Gap Nb-AlN-NbN SIS Junctions for Frequency Band 790−950 GHz. *IEEE Transactions on Terahertz Science and Technology*, **6**(1), 127–132.

Kittara, P., 2002. *The Development of a 700 GHz SIS Mixer with Nb Finline Devices: Nonlinear Mixer Theory, Design Techniques and Experimental Investigation*. Ph.D. thesis, University of Cambridge.

Kittara, P., Grimes, P., Yassin, G., Withington, S., Jacobs, K. & Wulff, S., 2004. A 700-GHz SIS Antipodal Finline Mixer Fed by a Pickett-Potter Horn-Reflector Antenna. *IEEE Transactions on Microwave Theory and Techniques*, **52**(10), 2352–2360.

Kittara, P., Jiralucksanawong, A., Yassin, G., Wangsuya, S. & Leech, J., 2007. The Design of Potter Horns for THz Applications Using a Genetic Algorithm. *Int. J. Inf. Millim. Waves*, **28**, 1103–1114.

Kollberg, E. & Rydberg, A., 1989. Quantum-barrier-varactor diodes for high-efficiency millimetre-wave multipliers. *Electronics Letters*, **25**(25), 1696–1698.

Lee, M. M., Nagao, T., De Breuck, C., Carniani, S., Cresci, G., Hatsukade, B., Kawabe, R., Kohno, K., Maiolino, R., Mannucci, F., Marconi, A., Nakanishi, K., Saito, T., Tamura, Y., Troncoso, P., Umehata, H. & Yun, M., 2019. First [N II]122 $\mu$m Line Detection in a QSO-SMG Pair BRI 1202-0725 at z = 4.69. *The Astrophysical Journal Letters*, **883**(2), L29.

Leech, J., Tan, B. K., Yassin, G., Kittara, P., Jiralucksanawong, A. & Wangsuya, S., 2010. Measured performance of a 230 GHz prototype focal-plane feedhorn array made by direct drilling of smooth-walled horns. *Proceedings of the Twenty First International Symposium on Space Terahertz Technology*, 114–119.

Leech, J., Tan, B. K., Yassin, G., Kittara, P., Wangsuya, S., Treuttel, J., Henry, M., Oldfield, M. L. & Huggard, P. G., 2011. Multiple flare-angle horn feeds for sub-mm astronomy and cosmic microwave background experiments. *Astronomy & Astrophysics*, **532**, A61.

Leech, J., Yassin, G., Tan, B. K., Tacon, M., Kittara, P., Jiralucksanawong, A. & Wangsuya, S., 2009. A new, simple method for fabricating high performance sub-mm focal plane arrays by direct machining using shaped drill bits. *Proceedings of the Twentieth International Symposium on Space Terahertz Technology*, 214–218.

Maas, S. A., 1988. *Nonlinear Microwave Circuits*. Artech House.

Maas, S. A., 1992. *Microwave Mixers*. Artech House.

Maas, S. A., 2003. *Nonlinear Microwave and RF Circuits*. Artech House.

Malin, C. & European Southern Observatory, 2013. The Atacama Large Millimeter/submillimeter Array (ALMA) by night, under the Magellanic Clouds. URL https://www.eso.org/public/images/ann13016a/.

Martin, D. & Puplett, E., 1970. Polarised Interferometric Spectrometry for the Millimetre and Submillimetre Spectrum. *Infrared Physics*, **10**, 105–109.

Martin, W. H., 1924. The Transmission Unit and Telephone Transmission Reference Systems. *Transactions of the American Institute of Electrical Engineers*, **XLIII**, 797–801.

Martin, W. H., 1929. Decibel-The Name for the Transmission Unit. *The Bell System Technical Journal*, **8**(1), 1–2.

Micro Chem Database, 2014. PMMA Resist Data Sheet. URL http://microchem.com/pdf/PMMA_Data_Sheet.pdf.

Micro Lambda Wireless Inc., 2018. YIG Tuned Oscillators. URL http://www.microlambdawireless.com/uploads/files/pdfs/ytodefinitions2.pdf.

Nelder, J. A. & Mead, R., 1965. A Simplex Method for Function Minimization. *Computer Journal*, **7**, 308–313.

Nilsen, S., Gronqvist, H., Hjelmgren, H., Rydberg, A. & Kollberg, E., 1993. Single barrier varactors for submillimeter wave power generation. *IEEE Transactions on Microwave Theory and Techniques*, **41**(4), 572–580.

Nyquist, H., 1928. Certain Topics in Telegraph Transmission Theory. *Transactions of the American Institute of Electrical Engineers*, **47**(2), 617–644.

Olver, A. D., Clarricoats, P. J. B., Kishk, A. A. & Shafai, L., 1994. *Microwave Horns and Feeds*. Bookcraft, Bath.

Olver, A. D. & Xiang, J., 1988. Wide angle corrugated horns analysed using spherical modal-matching. *IEE Proceedings H - Microwaves, Antennas and Propagation*, **135**(1), 34–40.

Padovani, F. A. & Stratton, R., 1966. Field and Thermionic Field Emission in Schottky Barriers. *Solid-State Electronics*, **9**(7), 695–707.

Pavlidis, D., 2021. *Fundamentals of Terahertz Devices and Applications*. Wiley-Blackwell.

Pickett, H. M., Hardy, J. C. & Farhoomand, J., 1984. Characterization of a Dual-Mode Horn for Submillimeter Wavelengths. *IEEE Transactions on Microwave Theory and Techniques*, **32**(8), 936–937.

Radiometer Physics, 2021. RPG FrequencyMultipliersFullband FM3-220-330 Product-DataSheet.pdf. URL `https://www.radiometer-physics.de/download/datasheets/mmwave-and-terahertz-products/frequency-multipliers/fullband-multipliers`.

Richer, J., 2005. Scientific requirements of ALMA, and its capabilities for key-projects: Galactic. *Proceedings of The Dusty and Molecular Universe: A Prelude to Herschel and ALMA*, **577**, 33–38.

Risacher, C., Vassilev, V., Pavolotsky, A. & Belitsky, V., 2003. Waveguide-to-microstrip transition with integrated bias-T. *IEEE Microwave and Wireless Components Letters*, **13**(7), 262–264.

Rogovin, D. & Scalapino, D. J., 1974. Fluctuation phenomena in tunnel junctions. *Annals of Physics*, **86**(1), 1–90.

Savitzky, A. & Golay, M. J. E., 1964. Smoothing and Differentiation of Data by Simplified Least Squares Procedures. *Analytical Chemistry*, **36**(8), 1627–1639.

SciPy, 2017. Discrete Fourier Transform. URL `https://docs.scipy.org/doc/numpy-1.13.0/reference/routines.fft.html`.

Shannon, C., 1949. Communication in the Presence of Noise. *Proceedings of the Institute of Radio Engineers*, **37**(1), 10–21.

Shu, F. H., Adams, F. C. & Lizano, S., 1987. Star formation in molecular clouds - Observation and theory. *ARA&A*, **25**, 23–81.

Solomon, P. M., Radford, S. J. E. & Downes, D., 1992. Molecular gas content of the primaeval galaxy IRAS 10214+4724. *Nature*, **356**, 318–319.

Sze, S. M. & Ng, K. K., 2006. *Physics of Semiconductor Devices*. Wiley-Blackwell.

Tan, B. K., Mahashabde, S., Hector, A., Yassin, G., Khudchenko, A., Hesper, R., Baryshev, A. M., Dmitriev, P., Rudakov, K. & Koshelets, V. P., 2018. Investigation of the Performance of an SIS Mixer with Nb-AlN-NbN Tunnel Junctions in the 780-950 GHz Frequency Band. *Proceedings of the Twenty Ninth International Symposium on Space Terahertz Technology*.

Tan, B. K., Yassin, G., Grimes, P., Leech, J., Jacobs, K. & Groppi, C., 2012. A 650 GHz Unilateral Finline SIS Mixer Fed by a Multiple Flare-Angle Smoot-Walled Horn. *IEEE Transactions on Terahertz Science and Technology*, **2**(1), 40–49.

Traini, A., Tan, B. K., Garrett, J. D., Khudchenko, A., Hesper, R., Baryshev, A. M., Dmitriev, P. N., Koshelets, V. P. & Yassin, G., 2020. The Influence of LO Power Heating of the Tunnel Junction on the Performance of THz SIS Mixers. *IEEE Transactions on Terahertz Science and Technology*, **10**(6), 721–730.

Tucker, J. R., 1979. Quantum Limited Detection in Tunnel Junction Mixers. *IEEE Journal of Quantum Electronics*, **15**(11), 1234–1258.

Virginia Diodes, 2021. WR3.4X3 Multiplier Specifications. URL `https://www.vadiodes.com/en/frequency-multipliers/?id=168`.

Ward, J., Rice, F., Chattopadhyay, G. & Zmuidzinas, J., 1999. SuperMix: A flexible software library for high-frequency circuit simulation, including SIS mixers and superconducting elements. *Proceedings of the Tenth International Symposium on Space Terahertz Technology*, 269–281.

Wengler, M., 1992. Submillimeter-Wave Detection with Superconducting Tunnel Diodes. *Proceedings of the IEEE*, **80**(11), 1810–1826.

Westig, M. P., Jacobs, K., Stutzki, J., Schultz, M., Justen, M. & Honingh, C. E., 2011. Balanced superconductor-insulator-superconductor mixer on a 9 $\mu$m silicon membrane. *Superconductor Science and Technology*, **24**(8), 085012.

Wilson, R. W., Jefferts, K. B. & Penzias, A. A., 1970. Carbon Monoxide in the Orion Nebula. *ApJ*, **161**, L43.

Woody, D. P., Miller, R. E. & Wengler, M. J., 1985. 85 – 115-GHz Receivers for Radio Astronomy. *IEEE Transactions on Microwave Theory and Techniques*, **33**(2), 90–95.

Wootten, A. & Thompson, A. R., 2009. The Atacama Large Millimeter/Submillimeter Array. *Proceedings of the IEEE*, **97**(8), 1463–1471.

XENOS, 2009. XeBaSe Instruction Manual.

XENOS, 2010. ECP Instruction Manual.

Yassin, G., Grimes, P. K., King, O. G. & North, C. E., 2008. Waveguide-to-planar circuit transition for millimetre-wave detectors. *Electronics Letters*, **44**(14), 866–867.

Yassin, G., Kittara, P., Jiralucksanawong, A., Wangsuya, S., Leech, J. & Jones, M., 2007. A High Performance Horn for Large Format Focal Plane Arrays. *Proceedings of the Eighteenth International Symposium on Space Terahertz Technology*, 199–210.

Yassin, G. et al., 2014. Supra-THz SIS and HEB Receivers and System Specifications. *To be published*.

Zhou, Y., 2013. *A Millimeter Unilateral Finline SIS Mixer with a Wide IF Bandwidth*. Ph.D. thesis, University of Oxford.

Zhou, Y., Yassin, G., Grimes, P., Leech, J., Jacobs, K. & Groppi, C., 2012. Performance of a 230 GHz finline SIS Mixer with a Wide IF Bandwidth. *Proceedings of the Twenty Third International Symposium on Space Terahertz Technology*, 116–121.

Zmuidzinas, J., LeDuc, H. G., Stern, J. A. & Cypher, S. R., 1994. Two-junction tuning circuits for submillimeter SIS mixers. *IEEE Transactions on Microwave Theory and Techniques*, **42**(4), 698–706.